Synthesis and In Vitro Evaluation of ^{18}F-Labelled ACE2 Small Molecule Inhibitors for PET Imaging Studies

A thesis submitted to the Board of the Faculty of Physical Sciences, in partial fulfilment of the requirements for the degree of Doctor of Philosophy at the University of Oxford

Xiaoyun Wang

St. Peter's College

University of Oxford

Trinity Term 2025

Author's Declaration

The work presented in this thesis was conducted under the supervision of Prof. Véronique Gouverneur at the Department of Chemistry, University of Oxford. All of the work is my own, unless otherwise stated, and has not been submitted for any other degree at this or any other university.

Xiaoyun Wang

Table of Contents

Abstract ... **iii**
Acknowledgements ... **v**
Abbreviations ... **vi**
Chapter 1. Introduction ... **1**
1.1 Overview of COVID-19 ... 2
1.2 SARS-CoV-2 and ACE2 ... 4
1.2.1 The Structure of SARS-CoV-2 ... 4
1.2.2 The Structure of ACE2 and Its Function ... 5
1.2.3 The Interaction of ACE2 with SARS-CoV-2 ... 8
1.2.4 Mechanism of Entry of SARS-CoV-2 at the Cell Surface ... 9
1.3 ACE2 as a COVID-19 Biomarker ... 10
1.3.1 ACE2 in COVID-19 Research ... 10
1.3.2 COVID-19 and ACE2 Expression ... 12
1.3.3 ACE2 in Other Diseases ... 15
1.4 Known ACE2 Inhibitors ... 17
1.4.1 Peptide-Based ACE2 Inhibitors ... 17
1.4.2 The Small Molecule ACE2 Inhibitor MLN-4760 ... 20
1.4.3 Other Small Molecule ACE2 Inhibitors ... 29
1.5 Positron Emission Tomography ... 32
1.5.1 Development of PET Imaging ... 32
1.5.2 Principles of PET Imaging ... 33
1.5.3 Fluorine-18 in PET Imaging ... 37
1.6 Conclusion ... 42
1.7 References ... 43
Chapter 2: Design, Synthesis, and Evaluation of Fluorinated MLN-4760 Analogues ... **64**
2.1 Introduction ... 65
2.2 In Silico Design of MLN-4760 Analogues ... 68
2.2.1 Docking Validation and Analogue Selection ... 68
2.2.2 Molecular Dynamics and RBFE Analysis ... 71
2.3 Synthesis of Fluorinated MLN-4760 Analogues ... 74
2.3.1 Validation of the Existing Synthetic Route with Analogue (*S,S*)-**2.1** . 74

2.3.2 Development of an Optimised Synthetic Strategy for MLN-4760 Analogues 81
2.4 In Vitro ACE2 Inhibition Analysis 100
2.5 Conclusion and Future Outlook 106
2.6 Reference 107
Chapter 3: Development of Radiolabelled [^{18}F]MLN-4760 Analogues 110
3.1 Introduction 111
3.1.1 Current PET Radiotracers for ACE2 Imaging 112
3.1.2 Aromatic ^{18}F-Fluorination 119
3.2 Radiosynthesis of [^{18}F]MLN-4760 Analogues 125
3.2.1 Robustness Screening Experiments for [^{18}F]MLN-4760 Analogues 125
3.2.2 Synthesis of Bpin Precursors for ^{18}F-Fluorination 129
3.2.3 Radiosynthesis of the [^{18}F]MLN-4760 Analogues 131
3.3 Conclusion and Future Outlook 137
3.4 References 138
Chapter 4. Experimental 143
4.1 General Information 144
4.2 Procedures and Characterisation for Chapter 2 146
4.3 X-ray Crystallography Data for Chapter 2 182
4.4 In Silico Experimental Procedure for Chapter 2 (Conducted by Dr. L. Hosseini-Gerami and Dr. M. Thomas) 184
4.3.1 Protein and Ligand Preparation 184
4.3.2 Validation of Computational Docking for ACE2 184
4.3.3 Estimation of Analogue Binding Affinity by Docking 187
4.3.4 Validation of Molecular Dynamics for ACE2 189
4.3.5 Relative binding free energy protocol 190
4.3.6 Validation of relative binding free energy for ACE2 192
4.3.7 Estimation of radiolabelled analogue binding affinity by RBFE 194
4.5 In Vitro Experimental Procedure for Chapter 2 (Conducted by J. He) .. 197
4.6 Procedures and Characterisation for Chapter 3 200
4.7 Radiosynthesis Procedure for Chapter 3 208
4.7.1 General Information 208
4.7.2 Radiochemistry protocols 209
4.8 References 217

Abstract

This thesis aims to develop ^{18}F-labelled ACE2 inhibitors as PET tracers for the non-invasive visualisation of ACE2 expression, with potential applications in COVID-19 and other ACE2-related pathologies.

Chapter I provides a general introduction to ACE2, its role in disease, and the rationale for fluorine-18-labelled inhibitors as PET tracers.

Chapter II details the design and synthesis of novel fluorinated analogues of MLN-4760. It starts with the in silico selection of fluorinated MLN-4760 analogues guided by molecular docking, and discusses new synthetic strategies developed to overcome limitations of the existing route. The synthesis of selected analogues is described, and their ACE2 inhibitory activity is evaluated in vitro through IC_{50} measurements.

Chapter III examines the role of PET in imaging ACE2 expression and reviews existing tracer studies. The radiolabelling of ACE2-targeting analogues is described, including precursor synthesis, fluorine-18 incorporation, and optimisation of labelling conditions.

Chapter IV provides full experimental procedures and characterisation data for the compounds discussed in this thesis.

Acknowledgements

I would like to begin by thanking Professor Véronique Gouverneur for her supervision and support throughout this project. I have learned a great deal during my time in her group and appreciate the opportunity to carry out this work under her guidance.

At the start of this project, I was grateful for the help of Dr. Gianluca Destro and Dr. Zijun Chen, who guided me through the early stages and helped me settle into the lab. I would also like to thank Dr. Joseph Ford and Dr. Sebastiano Ortalli for their valuable guidance and support in the radiolabelling laboratory. Thanks to the members of F11 for the time spent working together and supporting one another throughout the DPhil. I am also thankful to Professor Franklin Aigbirhio and Professor Andreas Bender and their groups from University of Cambridge for their collaboration on this project and for their insightful input and support.

I would like to thank St Peter's College for its support and all the college supervisors and staff for their assistance over the years.

I am especially grateful to my parents Zhen Wang and Dongdong Qi for their unwavering support throughout my PhD, both financially and emotionally. Their belief in me made this journey possible. I would also like to thank my husband, Dr. Zhongyi Hu, who has completed his doctorate at Oxford. Sharing this experience with him and having his constant encouragement has been a tremendous source of strength.

Abbreviations

[^{18}F]FDG	2-[^{18}F]Fluoro-2-deoxy-*D*-glucose
ACE	Angiotensin-Converting Enzyme
ACE2	Angiotensin-Converting Enzyme 2
ACEI	Angiotensin-Converting Enzyme Inhibitor
ADAM17	A Disintegrin and Metalloprotease 17
AI	Artificial Intelligence
ARB	Angiotensin Receptor Blocker
ARDS	Acute Respiratory Distress Syndrome
Arg	Arginine
AT1R	Angiotensin II Type 1 Receptor
AT2R	Angiotensin II Type 2 Receptor
β^+	Positron
Boc	*tert*-Butoxycarbonyl
COPD	Chronic Obstructive Pulmonary Disease
COVID-19	Coronavirus Disease 2019
CPDA	Carboxypeptidase A
CQ	Chloroquine
cryo-EM	Cryo-Electron Microscopy
CT	Computed Tomography
Cys	Cysteine
d.r.	Diastereomeric Ratio
DIAD	Diisopropyl Azodicarboxylate
DIPEA	N,N-Diisopropylethylamine

e^-	Electron
E	Envelope Protein
FBP	Filtered Back-Projection
γ	Gamma Photon
Glu	Glutamate
GLUT	Glucose Transporter
HCQ	Hydroxychloroquine
HEXXH	Histidine (H) Glutamic Acid (E) Variable Amino Acids (X)
His	Histidine
HIV	Human Immunodeficiency Virus
IC_{50}	Half-Maximal Inhibitory Concentration
ICU	Intensive Care Unit
keV	Kiloelectronvolt
K_i	Inhibitor Constant
LBD	Ligand-Binding Domain
LOR	Line of Response
μ	Micro (10^{-6})
M	Membrane Protein
mACE2	Membrane-bound Angiotensin-Converting Enzyme 2
MD	Molecular Dynamics
MRI	Magnetic Resonance Imaging
n	Nano (10^{-9})
n.d.	Not Determined
N	Nucleocapsid Protein

NAAE	*N*-(2-Aminoethyl)-1-Aziridine-Ethanamine
NMR	Nuclear Magnetic Resonance
2-Ns	2-Nitrobenzenesulfonyl
p	Pico (10^{-12})
p, α, d, n	Proton (*p*), Alpha Particle (*α*), Deuteron (*d*), Neutron (*n*)
PET	Positron Emission Tomography
PETT II	Positron Emission Transaxial Tomograph Prototype II
Phe	Phenylalanine
PMT	Photomultiplier Tube
PPh_3	Triphenylphosphine
Pro	Proline
QC	Quality Control
RAAS	Renin-Angiotensin-Aldosterone System
RBFE	Relative Binding Free Energy
RBD	Receptor-Binding Domain
RCY	Radiochemical yield
rhACE2	Recombinant Human Angiotensin-Converting Enzyme 2
RNA	Ribonucleic Acid
rt	Room Temperature
RT-PCR	Reverse Transcription Polymerase Chain Reaction
S	Spike Protein
sACE2	Soluble ACE2
SARS-CoV-2	Severe Acute Respiratory Syndrome Coronavirus 2
SCXRD	Single-crystal X-ray Diffraction

SiPM	Silicon Photomultiplier
S_N2	Bimolecular Nucleophilic Substitution
SUV	Standardised Uptake Value
$t_{1/2}$	Half-life
TLC	Thin-Layer Chromatography
TMPRSS2	Transmembrane Serine Protease 2
TOF	Time-of-Flight
WHO	World Health Organization

Chapter 1. Introduction

1.1 Overview of COVID-19

This chapter begins by outlining the biological relevance of severe acute respiratory syndrome coronavirus 2 (SARS-CoV-2) and its host receptor, angiotensin-converting enzyme 2 (ACE2), which prompted the initial conception of this project. Although the aim of this work is not to develop treatments for Coronavirus Disease 2019 (COVID-19), the pandemic highlighted the central role of ACE2 in viral entry and renewed interest in its wider physiological and pathological functions. In this context, ACE2 is considered as a biomarker whose expression may be relevant not only to COVID-19 but also to a range of other diseases in which ACE2 dysregulation has been implicated. To enable non-invasive, quantitative assessment of ACE2 expression in vivo, this chapter also introduces the principles of positron emission tomography (PET) imaging and the rationale for developing ^{18}F-labelled radiotracers.

COVID-19 is a respiratory disease caused by SARS-CoV-2 that emerged in late 2019 and led to a pandemic, which the World Health Organization (WHO) officially declared a global health crisis in March 2020.[1-6] The virus spread rapidly worldwide, resulting in significant illness, mortality, and disruption to social and economic systems.[6] COVID-19 is transmitted through respiratory droplets, aerosols, and contaminated surfaces, contributing to its rapid transmission.[7] Table 1.1 outlines the timeline of events from the initial outbreak to the approval of vaccines and treatments, highlighting the substantial efforts made to control the pandemic.

Time	Event/Development	Description	Ref.
Dec 2019	First Cases in Wuhan, China	Initial cluster of pneumonia cases identified, later confirmed as SARS-CoV-2.	2
Jan 2020	SARS-CoV-2 Sequencing Published	Chinese scientists published the genetic sequence of the virus.	4
Feb 2020	ACE2 Identified as SARS-CoV-2 Receptor	ACE2 identified as the primary entry receptor for SARS-CoV-2, allowing the virus to bind and enter human cells.	8
Mar 2020	WHO Declared COVID-19 a Global Pandemic	Rapid spread of COVID-19 led to global public health emergency declaration.	1, 3
Jun 2020	Dexamethasone Shown Effective in Severe Cases	First effective treatment for severe COVID-19 cases identified.	9
Dec 2020	Vaccines Approved for Emergency Use	Pfizer-BioNTech and Moderna vaccines and later the Oxford–AstraZeneca vaccine received emergency use authorisation.	10
2022	Booster Shots and Variants	Booster doses rolled out to combat new variants (Delta, Omicron).	11
Until now	Ongoing Vaccine and Treatment Research	Continuous updates to vaccines and antiviral drugs to tackle emerging variants and improve treatment.	12

Table 1.1: Key milestones in the development of COVID-19 and its treatment. SARS-CoV-2 = severe acute respiratory syndrome coronavirus 2; ACE2 = angiotensin-converting enzyme 2; WHO = World Health Organization; COVID-19 = coronavirus disease 2019.

COVID-19 exhibits a variety of symptoms, ranging from mild (e.g. fever, cough, and fatigue) to severe (e.g. shortness of breath, pneumonia, and multiorgan failure) in vulnerable populations.[13-16] This range of symptom severity, as summarised in Table 1.2, has highlighted the urgent need for effective treatments and preventive measures. Recent review articles on COVID-19 drug discovery have summarised the progress in therapeutic development since 2020, highlighting the main drug discovery strategies, preclinical evaluation models, representative therapies targeting both viral and host pathways, and the evolution of key treatments currently in clinical use for managing the disease.[17] Additionally, the recognition of long COVID symptoms, such as persistent fatigue, cognitive difficulties, and respiratory

issues, has driven ongoing research into effective management strategies for both acute and chronic forms of the virus.[18]

Symptom Severity	Selected Treatments	Ref.
Fever, cough, sore throat, fatigue, headaches	Exploration of repurposed drugs (e.g., hydroxychloroquine, remdesivir)	19, 20
Shortness of breath, chest pain, confusion	Antivirals (remdesivir), Dexamethasone (anti-inflammatory)	9, 19
Severe pneumonia, acute respiratory distress syndrome, organ failure	Monoclonal antibodies (e.g., bamlanivimab), antivirals	3, 21, 22
Fatigue, cognitive impairment, breathing problems, joint pain, cardiovascular complications, memory loss, sleep disorders, anxiety, depression, etc.	Rehabilitation, supportive care, clinical research into long COVID	23-25

Table 1.2: Severity of COVID-19 symptoms and associated treatments.

1.2 SARS-CoV-2 and ACE2

1.2.1 The Structure of SARS-CoV-2

COVID-19 is caused by SARS-CoV-2, an enveloped, positive-sense, single-stranded ribonucleic acid (RNA) virus from the coronavirus family.[2-5] The structure of SARS-CoV-2 is illustrated in Figure 1.1. Central to its infectivity is the spike (S) protein, which forms a trimer on the viral surface.[26] Each monomer within this trimer is comprised of two subunits: the S1 subunit contains the receptor-binding domain (RBD) that binds to the host cell receptor, while the S2 subunit facilitates fusion with the host cell membrane, enabling viral entry.[27-30]

Beyond the spike protein, SARS-CoV-2 includes additional structural proteins vital for its function and stability. The envelope (E) protein acts as a viroporin, enabling

ion transport and contributing to viral assembly,[31] while the membrane (M) protein, the most abundant structural protein, drives viral assembly and budding.[32] The nucleocapsid (N) protein surrounds the RNA genome, playing a critical role in its packaging and facilitating the replication process within host cells.[33] Together, these structural components support the virus' infectivity and propagation in host organisms.[34]

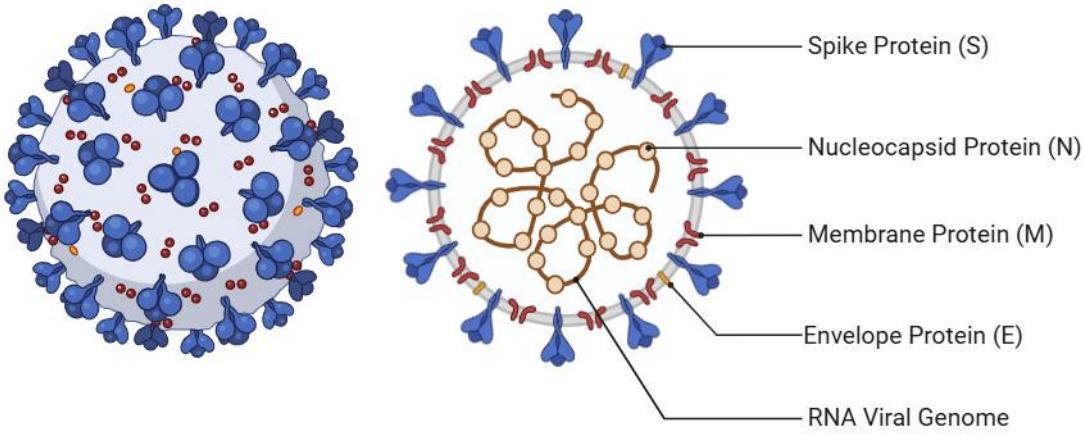

Figure 1.1: An annotated representation of SARS-CoV-2.

1.2.2 The Structure of ACE2 and Its Function

The angiotensin-converting enzyme 2 (ACE2) is a protein consisting of 805 amino acids, features a transmembrane domain and a zinc-binding motif located at positions 374–378, characteristic of its role as a metalloprotease.[35-39] ACE2 has been classified as a zinc-dependent carboxypeptidase that plays an essential role in the renin-angiotensin-aldosterone system (RAAS), which regulates blood pressure

and fluid balance.[35-39] Figure 1.2 illustrates the ACE2 structure, its role in RAAS, and its broader biological significance.

ACE2 is primarily expressed in the lungs, heart, kidneys, and intestines, acting as a counter-regulatory enzyme to angiotensin-converting enzyme (ACE).[35, 40, 41] While ACE converts angiotensin I (Asp-Arg-Val-Tyr-Ile-His-Pro-Phe-His-Leu) into angiotensin II (Asp-Arg-Val-Tyr-Ile-His-Pro-Phe), a vasoconstrictor that raises blood pressure, ACE2 hydrolyses angiotensin II into angiotensin-(1-7) (H-Asp-Arg-Val-Tyr-Ile-His-Pro-OH).[42-45] Angiotensin-(1-7) binds to MAS receptors, promoting vasodilation, and exerting anti-inflammatory and anti-fibrotic effects, thereby supporting cardiovascular, renal, and pulmonary health.[43, 46-50]

Following the 2003 SARS outbreak, ACE2 was identified as a functional receptor for coronaviruses, mediating viral entry and cell fusion.[51, 52] Later during the COVID-19 pandemic, its critical role as the receptor for SARS-CoV-2 attracted renewed attention, due to its significance in viral pathogenesis. The virus utilises the RBD of its spike protein to bind ACE2, allowing the virus to enter host cells.[8, 53-56] This interaction could be exploited for developing new therapeutics that could potentially block ACE2 binding and prevent viral entry.

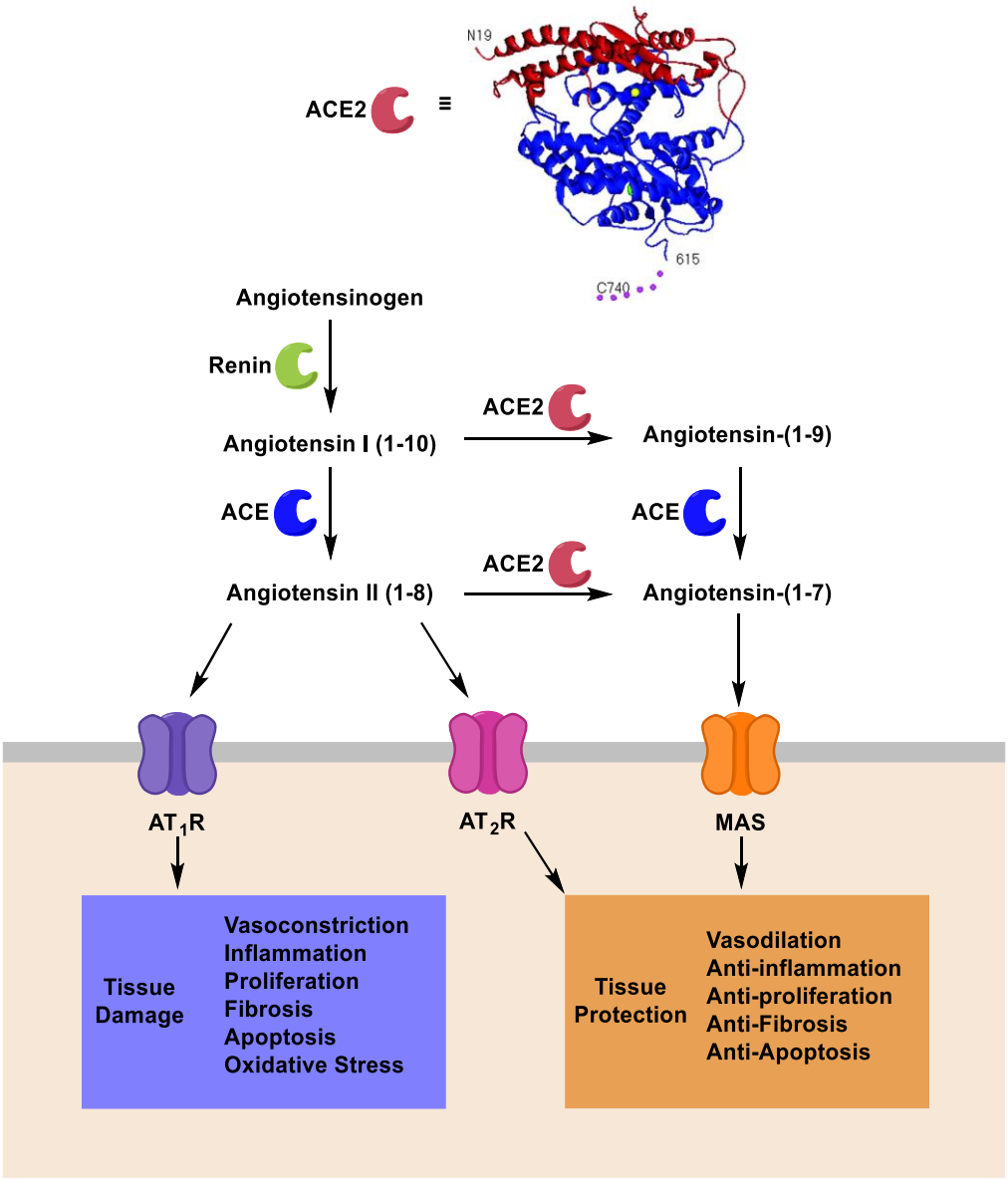

Figure 1.2: the RAAS system illustrating the role of ACE2 in converting angiotensin II into angiotensin-(1-7), counterbalancing AT1R (angiotensin II type 1 receptor) effects like vasoconstriction and fibrosis, while promoting AT2R (angiotensin II type 2 receptor) functions such as vasodilation and anti-inflammation. Above, the ribbon diagram of the ACE2 crystal structure, showing its secondary structure and two subdomains forming the active site cleft: Subdomain I (red, N-terminus with zinc-binding site) and Subdomain II (blue, C-terminus). The active site zinc ion is shown as a yellow sphere, and the chloride ion as a green sphere. *Figure adapted with permission of P. Towler et al., ACE2 X-ray structures reveal a large hinge-bending motion important for inhibitor binding and catalysis, Journal of Biological Chemistry, 2004, Vol. 279, Issue 17, Pages 17996-18007;* [57] *permission conveyed through Copyright Clearance Center, Inc.*

1.2.3 The Interaction of ACE2 with SARS-CoV-2

The interaction of the SARS-CoV-2 spike protein with ACE2 has been extensively studied using advanced techniques such as cryo-electron microscopy (cryo-EM) and X-ray crystallography.[26, 53, 56, 58-63] In 2020, Lan and co-workers, and Shang and co-workers, simultaneously published the earliest crystal structures of the SARS-CoV-2 RBD–ACE2 complex using X-ray crystallography, providing atomic-level insights into the virus-host interaction.[26, 63] These studies have established the precise binding mechanism, revealing how specific amino acid interactions between ACE2 and the spike RBD contribute to the strong affinity of the virus for host cells. [26, 53, 56, 58-62] As shown in Figure 1.3, the SARS-CoV-2 RBD of the spike protein primarily interacts with the N-terminal helix of ACE2, stabilised by hydrophilic side-chain networks involving 20 residues on ACE2 and 17 residues on the RBD.[26, 63, 64] Notably, the binding mode of ACE2 is almost identical for both SARS-CoV and SARS-CoV-2, as many of the interacting residues are either completely conserved or with only minor variations between the two RBDs.[26, 51, 63, 65, 66] Interestingly, the catalytic activity of ACE2 is not essential for its function as a viral receptor and its active site does not overlap with the viral binding site.[65]

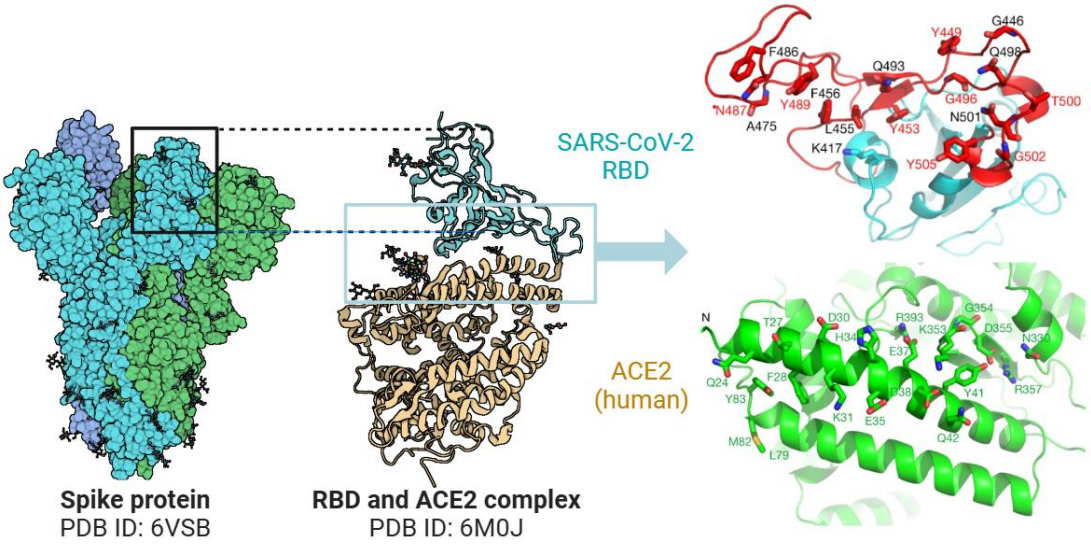

Figure 1.3: The receptor binding and interaction of the SARS-CoV-2 RBD–ACE2 complex, resolved using X-ray crystallography (PDB ID: 6VSB and 6M0J).[26, 53] The interaction interface between the binding sites, with contacting residues displayed as sticks. Residues involved in ACE2 binding for both the SARS-CoV-2 and SARS-CoV RBD–ACE2 complexes are marked with red labels. *Figure adapted with permission of J. Lan et al., Structure of the SARS-CoV-2 spike receptor-binding domain bound to the ACE2 receptor, Nature, 2020, Vol. 581, Issue 7807, Pages 215-220;* [26] *permission conveyed through Copyright Clearance Center, Inc.*

1.2.4 Mechanism of Entry of SARS-CoV-2 at the Cell Surface

The entry of SARS-CoV-2 into host cells via the cellular surface begins when the RBD of the S1 subunit in the S protein binds with high affinity to the ACE2 receptor on the cell surface, as illustrated in Figure 1.4.[26, 29, 53-56, 63, 64] This binding is crucial for viral attachment and triggers a series of conformational changes within the spike protein.[28, 29, 64] These changes, facilitated by the action of transmembrane serine protease 2 (TMPRSS2), activate the S2 subunit, which enables the fusion of the viral envelope with the host cell membrane.[27, 64] Following membrane fusion, the viral

RNA is released into the host cell, where it hijacks the cellular machinery of the host to replicate and propagate the infection.[64, 67, 68]

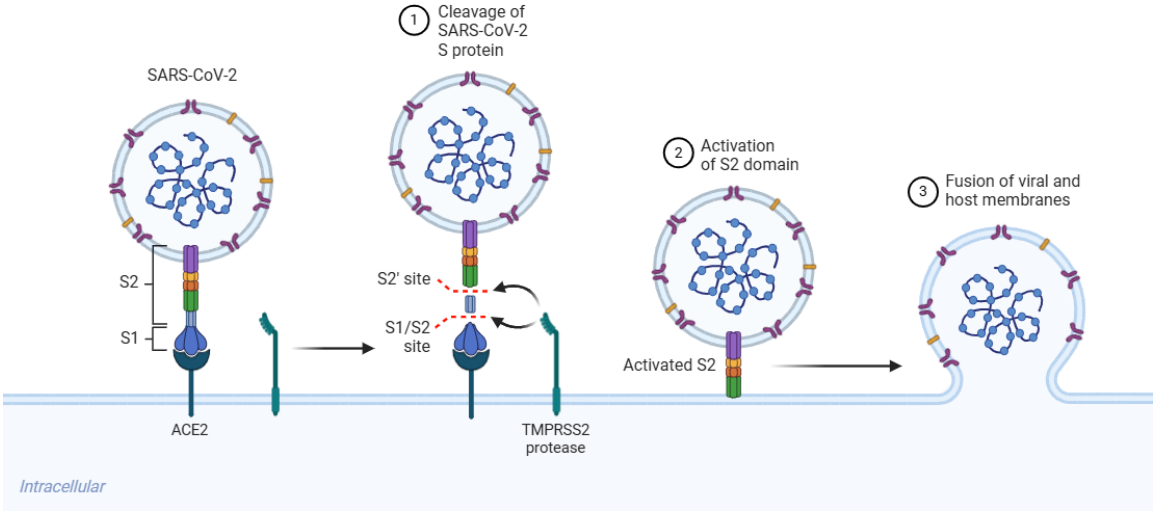

Figure 1.4: Mechanism of SARS-CoV-2 entry via ACE2 at the cell surface. *Figure reproduced with permission of E. Hartenian et al., The molecular virology of coronaviruses, Journal of Biological Chemistry, 2020, Vol. 295, Issue 37, Pages 12910-12934;* [69] *permission conveyed through Copyright Clearance Center, Inc.*

1.3 ACE2 as a COVID-19 Biomarker

1.3.1 ACE2 in COVID-19 Research

1.3.1.1 Therapeutic Strategies Targeting ACE2

ACE2 serves as the primary entry receptor for SARS-CoV-2, positioning it as a key biomarker in COVID-19 research with both diagnostic and therapeutic relevance. For therapeutic applications, various strategies have been developed to modulate ACE2 activity or block its interaction with the viral spike protein as shown in Table 1.3. Initial pharmacological efforts explored the use of existing RAAS modulators

such as angiotensin-converting enzyme inhibitors (ACEIs) and angiotensin receptor blockers (ARBs). ACEIs inhibit the conversion of angiotensin I to angiotensin II by blocking ACE, while ARBs antagonise the angiotensin II type 1 receptor (AT1R), and preclinical studies in rodent models indicated that administration of ACEIs or ARBs can lead to a two- to fivefold increase in ACE2 expression in cardiac and renal tissues.[70] This raised concerns about heightened susceptibility to SARS-CoV-2, given the role of ACE2 as the viral entry receptor. However, large-scale clinical analyses have not supported this hypothesis. A retrospective study of 1,128 hypertensive COVID-19 patients in Wuhan found that in-hospital use of ACEIs or ARBs was associated with decreased mortality compared to non-users.[71] The impact of ACEIs and ARBs on COVID-19 outcomes remains inconclusive, with several studies reporting no significant association between their use and disease severity or mortality.[71-75]

Recombinant human ACE2 (rhACE2) proteins demonstrated efficacy as soluble competitors by binding the SARS-CoV-2 viral spike protein, thereby preventing its interaction with membrane-bound ACE2 on host cells.[76] This mechanism has been shown to reduce viral replication by up to 5,000-fold and markedly suppresses early-stage infection in human blood vessel and kidney organoids.[76] Neutralising antibodies targeting the spike protein-ACE2 interface present another promising approach by preventing the spike protein from binding to ACE2, thereby effectively halting the viral entry process.[77] Complementary to this strategy, viral fusion

inhibitors block the fusion of the viral and host cell membranes, further disrupting the infection cycle and reducing viral replication.[78]

Therapeutic Approach	Mechanism of Action	Ref.
ACEIs and ARBs	ACEIs inhibit ACE and ARBs block AT1R, both potentially upregulating ACE2 expression. However, evidence regarding their impact on COVID-19 outcomes remains inconclusive.	[70, 72, 74]
rhACE2	Binds to the SARS-CoV-2 spike protein, blocking viral entry.	[76]
Neutralising antibodies against spike-ACE2	Prevent spike protein-ACE2 binding.	[77]
Viral Fusion Inhibitors	Block fusion of viral and host cell membranes.	[78]

Table 1.3: Therapeutic strategies targeting ACE2. ACEIs = angiotensin-converting enzyme inhibitors; ARBs = angiotensin II receptor blockers; rhACE2 = recombinant human angiotensin-converting enzyme 2; ACE = angiotensin-converting enzyme; ACE2 = angiotensin-converting enzyme 2; COVID-19 = coronavirus disease 2019.

1.3.2 COVID-19 and ACE2 Expression

ACE2 expression levels are relevant to disease susceptibility, severity, and post-infection effects. Three key aspects to consider are: (1) baseline ACE2 levels and vulnerability to COVID-19, (2) ACE2 expression changes during infection and their impact on severity, and (3) the role of altered ACE2 levels in long-term COVID-19 symptoms.

(1) ACE2 Expression and COVID-19 Susceptibility

ACE2 expression, influenced by various conditions and comorbidities, plays a key role in tissue susceptibility to SARS-CoV-2.[79] High-risk organs, including the lungs, heart, kidneys, and intestines, exhibit ACE2 expression in over 1% of cells.[80] Elevated ACE2 levels are commonly observed in individuals with diabetes, hypertension, and cardiovascular diseases, potentially increasing their risk of severe COVID-19.[81] Patients using ACEIs and ARBs, which upregulate ACE2, may also be more susceptible to infection.[81, 82] Similarly, diabetic patients with increased lung ACE2 expression have shown higher Intensive Care Unit (ICU) admission rates.[83, 84] Smoking and chronic obstructive pulmonary disease (COPD) further elevate ACE2 expression in the lungs, heightening the risk of severe respiratory complications.[85, 86] Additionally, as plasma ACE2 levels are higher in men and increase with age this may indicate demographic influences on COVID-19 susceptibility.[87] Recognising these variations in ACE2 expression is essential for identifying high-risk populations and developing targeted therapeutic strategies.

(2) Changes in ACE2 Expression During Infection

SARS-CoV-2 infection alters ACE2 expression, impacting disease severity. ACE2 exists as membrane-bound (mACE2) and soluble (sACE2) isoforms, with mACE2 cleaved by an enzyme ADAM17 to generate sACE2.[88] Studies on SARS-CoV and SARS-CoV-2 have shown that viral spike protein binding promotes mACE2 endocytosis and degradation, reducing surface expression.[89, 90] This downregulation

disrupts the RAAS balance by decreasing the conversion of angiotensin II to angiotensin-(1–7). The resultant accumulation of angiotensin II exacerbates inflammation and tissue damage, contributing to severe COVID-19 outcomes.[89, 90]

Infection-induced RAAS dysregulation also increases mACE2 shedding, elevating plasma sACE2 levels.[91] Tissue damage further releases sACE2 into circulation, suggesting its potential as a mortality marker.[79] Clinical studies confirm elevated sACE2 levels in hospitalised COVID-19 patients, with a strong correlation to disease severity.[92-96] Measuring plasma sACE2 could thus aid in predicting COVID-19 outcomes and linking disease severity to risk factors such as hypertension and cardiovascular disease.[97] While the precise relationship between ACE2 expression and infection outcomes remains unclear, monitoring both mACE2 and sACE2 is critical for understanding COVID-19 progression.

(3) Post-Infection ACE2 Expression and Long COVID

ACE2 dysregulation post-infection has been implicated in long COVID, as viral binding depletes ACE2, disrupting RAAS balance and contributing to tissue damage secondary to sepsis.[98, 99] This imbalance is suspected in long COVID, but no predictive biomarker has been identified.[100] ACE2 deficiency has been linked to persistent symptoms such as fatigue, cognitive impairment, and respiratory issues, particularly in patients with diabetes, hypertension, cardiovascular diseases, or cancer.[100] Severe COVID-19 may significantly impair renin-angiotensin-aldosterone

system, but even mild or asymptomatic cases could contribute to long COVID through alternative pathways.[101] COVID-19 is thus not merely a viral pneumonia but a condition with complex pathophysiological consequences.[101] Further research is required to clarify post-infection ACE2 regulation and explore strategies to mitigate long-term effects.

1.3.3 ACE2 in Other Diseases

Beyond its implication in SARS-CoV and SARS-CoV-2, ACE2 has been extensively studied for its potential role as a biomarker in various pathologies, including cancer.[43, 102] ACE2 is broadly expressed across various cell types, including pulmonary and intestinal epithelial cells, vascular endothelial and smooth muscle cells, kidney tubular cells, and cardiomyocytes (Figure 1.5).[41] As ACE2 plays a role in regulating the RAAS by converting angiotensin, a mediator of vascular homeostasis, vasomotor regulation, and blood pressure control, its expression could also be linked to cardiovascular and renal diseases.[38] Decreased ACE2 expression has been linked to heart failure, hypertension, diabetes, coronary artery disease, and myocardial infarction recovery.[103] Figure 1.5 further highlights the diseases related to organs such as the lungs, heart, and vascular system, which are more severely affected by COVID-19 infections due to the disruption of ACE2 expression and altered RAAS function.[83, 104-106] In oncology, ACE2 upregulation has been associated with enhanced antitumour immune responses, reduced tumour malignancy, and improved survival rates, making it valuable for tracking cancer progression.[107, 108]

Given its multifunctional significance, monitoring ACE2 expression offers valuable insights as a biomarker for tracking disease progression.

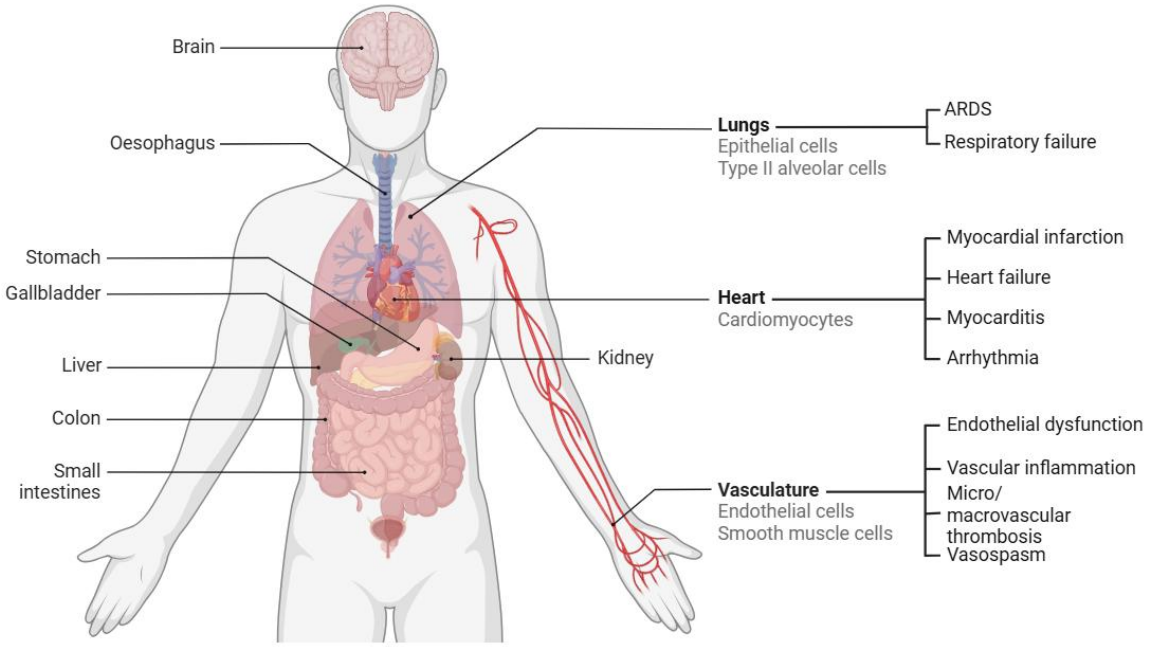

Figure 1.5: ACE2 receptor distribution in various human tissues, emphasising the lungs, heart, and vasculature. *Figure reproduced with permission of P. M. Ryan and N. Caplice, COVID-19 and relative angiotensin-converting enzyme 2 deficiency: role in disease severity and therapeutic response, Open Heart, 2020, Vol. 7, Issue 1, Pages e001302;*[109] *permission conveyed through Copyright Clearance Center, Inc.*

1.4 Known ACE2 Inhibitors

To date, only a limited number of ACE2 inhibitors have been explored and two such inhibitors are well-established: DX600, a peptide-based inhibitor, and MLN-4760, a small-molecule inhibitor.

1.4.1 Peptide-Based ACE2 Inhibitors

DX600 is a well-established and potent peptide inhibitor widely used in ACE2 research, with its structure shown in Figure 1.6. DX600 was designed to bind specifically to ACE2 by mimicking sequences similar to the its natural substrate, angiotensin I, thereby effectively blocking its catalytic function.[110] It exhibits a mixed competitive and non-competitive inhibition mechanism, with a reported inhibition constant (K_i) of 2.8 nM. DX600 specifically targets ACE2 and is not hydrolysed by it. It does not inhibit ACE activity, and effectively blocks ACE2 activity towards angiotensin I, indicating potential functionality in vivo.[110] As a potent ACE2-specific peptide inhibitor, DX600 has proven invaluable for elucidating the in vivo functions of ACE2, studying its physiological roles, and tracing its expression in imaging techniques.[110]

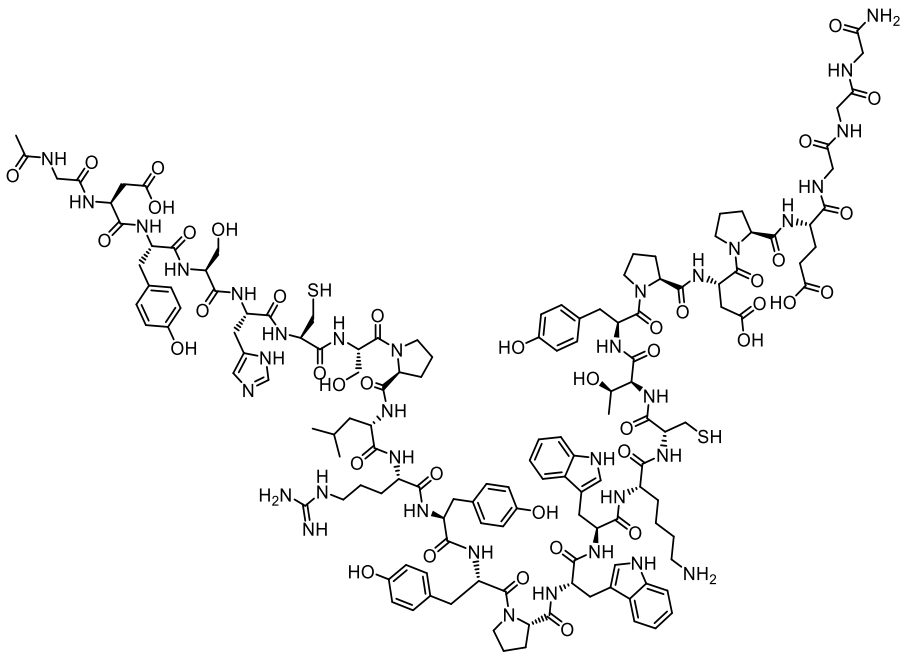

Figure 1.6: Structure of DX600.

DX600 remains the most widely used peptide inhibitor of ACE2 and research into active-site-targeting peptide inhibitors is relatively limited. In 2023, a new class of ACE2 inhibitors was identified using bacteriophage display, leading to the discovery of bicyclic peptides with high affinity and selectivity.[111] Among these, BCY20862 (sequence: ACVRS[4MePhe]CSSLLPRIHCA) exhibits potent inhibition, with a reported K_i of 0.22 nM and >81,000-fold selectivity for ACE2 over ACE, and its binding to ACE2 is illustrated in Figure 1.7A. Structural characterisation using X-ray crystallography revealed that BCY20862 binding to ACE2 (PDB: 8BN1) induced a conformational rearrangement, resulting in a ligand-specific closure mechanism.

Following the emergence of COVID-19, research focus shifted towards developing inhibitors that modulate the interaction between ACE2 and the SARS-CoV-2 spike

protein, rather than directly inhibiting the enzymatic activity of ACE2.[112, 113] For example, a novel peptide KYPAY (K5), characterised by its boomerang structure, was developed to bind to the ACE2 ligand-binding domain (LBD) and block its interaction with the SARS-CoV-2 spike protein as shown in Figure 1.7B.[112] The inhibitory effects of K5 were assessed through molecular simulations, adsorption kinetics analyses and cellular experiments.[112] Although these studies are highly relevant to COVID-19-related research, this type of LBD-inhibitors target the allosteric site rather than the catalytic active site of ACE2, which may not directly influence the enzymatic function of ACE2.[65]

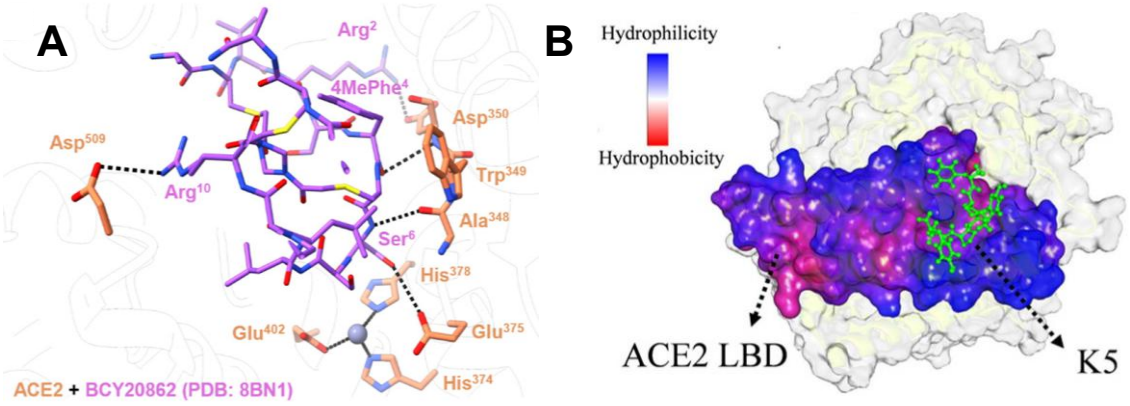

Figure 1.7: A) Binding conformation of BCY20862 with ACE2, highlighting electrostatic interactions near the catalytic site with hydrogen bonds shown as dashed lines. B) A representative snapshot from a 200 ns molecular dynamics simulation illustrating the binding of K5 to the ACE2 ligand-binding domain in aqueous solution. *Figure A reproduced with permission of M. A. Harman et al., Structure-guided chemical optimization of bicyclic peptide (bicycle) inhibitors of angiotensin-converting enzyme 2, Journal of Medicinal Chemistry, 2023, Vol. 66, Issue 14, Pages 9881–9893; permission conveyed through Copyright Clearance Centre, Inc. Figure B reproduced under CC BY 4.0 license from Y. Wei, Z. Liu, M. Zhang, X. Zhu, and Q. Niu, Inhibition of ACE2–S Protein Interaction by a Short Functional Peptide with a Boomerang Structure*, *Molecules*, *2024, Vol. 29, Issue 13, Page 3022 (http://creativecommons.org/licenses/by/4.0).*

1.4.2 The Small Molecule ACE2 Inhibitor MLN-4760

MLN-4760 ((*S*,*S*)-2-[1-carboxy-2-[3-(3,5-dichlorobenzyl)-3*H*-imidazol-4-yl]-ethylamino]-4-methylpentanoic acid), also known as GL-1001, is the first rationally designed small-molecule ACE2 inhibitor and remains one of the most potent and well-characterised inhibitors to date, with its structure displayed in Figure 1.8. As the central focus of this thesis, this section will provide a comprehensive overview of MLN-4760 by examining three key aspects: (1) its design and development, (2) its crystal structure and binding interactions with ACE2, and (3) its current applications.

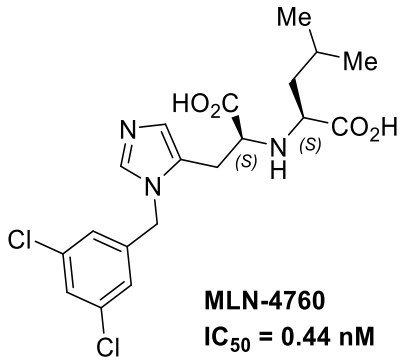

Figure 1.8: Structure of MLN-4760.

(1) Design and Development of MLN-4760

MLN-4760 was developed by Millennium Pharmaceuticals in 2002 through a rational design process guided by substrate screening data to design an effective ACE2 inhibitor.[44, 114] Its design targeted the ACE2 active site, drawing inspiration from the C-terminal dipeptide of Angiotensin I (Ang I), which is a natural substrate of ACE2 and features a histidine-leucine motif that is non-hydrolysable and a centrally located

carboxylate to coordinate with the zinc cofactor.[114] These features, combined with stabilising hydrophobic interactions, formed the basis for the development of the inhibitor as demonstrated in Figure 1.9.

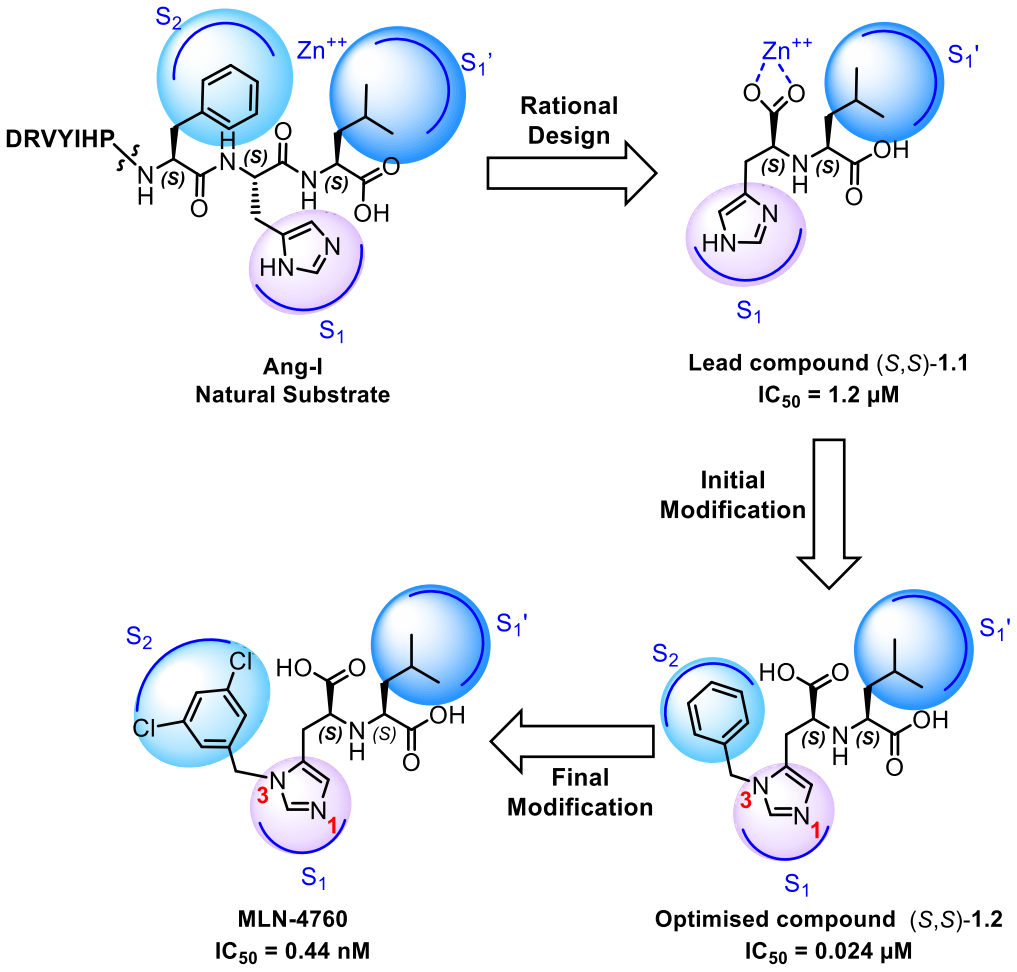

Figure 1.9: Rational design progress of MLN-4760.[114]

The initial lead compound (*S,S*)-**1.1** exhibited moderate micromolar activity (IC_{50} = 1.2 µM). As of its other stereoisomers, (*R,R*)-**1.1** was inactive, and the other two diastereomers demonstrated comparable potency. (*S,S*)-**1.1** exhibited superior

selectivity against related enzymes, such as ACE and carboxypeptidase A (CPDA) (both IC_{50} > 50 μM), making it the preferred candidate. The imidazole ring, characteristic of histidine-based inhibitors, maintains the orientation of the molecule within the ACE2 active site. Subsequent modifications focused on this imidazole core. Introduction of an N3 benzyl substituent in optimised compound (*S,S*)-**1.2** significantly enhanced potency (IC_{50} = 24 nM), likely due to strengthened interactions with the S2 pocket of ACE2. In contrast, the addition of a benzyl group at the N1 position reduced potency compared to the unsubstituted compound (IC_{50} = 10 μM).

Further optimisation explored modifications on the aromatic ring to improve potency and selectivity. *Meta*-substitution on the phenyl ring proved to be productive, leading to the development of the (*S*,*S*)-configured 3,5-dichloro derivative, MLN-4760. This modification achieved picomolar-level potency (IC_{50} = 0.44 nM) and exceptional selectivity (> 5000-fold) over other related enzymes like ACE and CPDA (ACE IC_{50} = 100 μM; CPDA IC_{50} = 27 μM). The stereochemical configuration of MLN-4760 is crucial for its tight binding to ACE2, achieved primarily through stabilising interactions with the S1, S1', and S2 pockets of the ACE2 active site. This unique binding profile makes MLN-4760 a highly potent and selective ACE2 inhibitor.

(2) Binding Interactions of MLN-4760 with ACE2

The binding interactions between MLN-4760 and ACE2 were elucidated by Towler and co-workers in 2004 using X-ray crystallography, marking the first crystal structures of both the native and inhibitor-bound forms of the extracellular metallopeptidase domain of ACE2 as presented in Figure 1.10.[57]

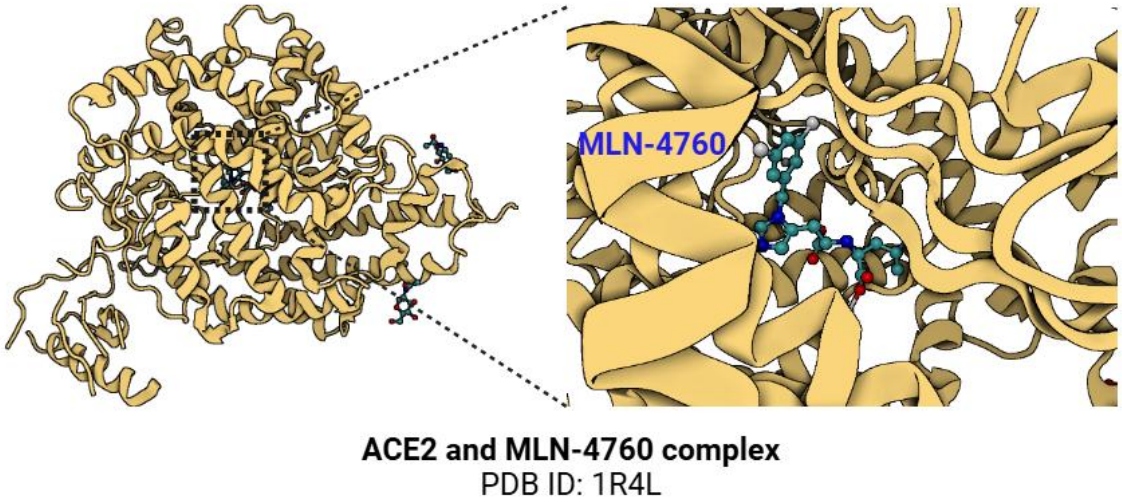

Figure 1.10: X-ray crystal structure of ACE2 and MLN-4760 complex shown and an image enlarged with ACE2 active site binding with the inhibitor showing binding interaction (PDB ID: 1R4L).[57]

The binding interactions of MLN-4760 with ACE2 is shown in Figure 1.11. The inhibitor displaces a water molecule in the native structure to form a coordination sphere with the zinc ion via residues His374, His378, and Glu402, thereby stabilising the interaction. Hydrogen bonding plays a crucial role in further stabilising the MLN-4760-ACE2 complex. The terminal carboxylate group of MLN-4760 forms hydrogen bonds with Arg273, His505, and His345. Each hydrogen bond is estimated to contribute approximately -2 to -20 kJ mol^{-1} to the overall binding enthalpy, depending

on bond geometry and solvent effects.[115] These interactions enhance binding affinity by lowering the Gibbs free energy of complex formation, compensating for the entropic penalty associated with conformational ordering of the ligand and protein upon complexation. Additionally, Pro346 and His345 stabilise the secondary amine group of the inhibitor, while Thr371 and Tyr515 interact with the imidazole group and the zinc-coordinated carboxylate group, respectively. The carboxyl group of Glu375 is positioned within hydrogen-bonding distance of one of the oxygen atoms of the zinc-bound carboxylate of MLN-4760, although it likely remains ionised at physiological pH 7.4. The isobutyl group of MLN-4760 occupies the S1 subsite, while the 3,5-dichlorobenzylimidazole group fits into the S1′ subsite. Side chains of Phe274, Asn149, Thr371, Met360, and the disulphide bond between Cys344 and Cys361, create a hydrophobic environment that further stabilises the inhibitor within the active site. Additional interactions stabilising the 3,5-dichlorobenzyl group of MLN-4760 involve the side chains of Asn149, Asp368, and Glu145, as well as the carbonyl groups of Cys344 and Cys361. A notable conformational change occurs upon MLN-4760 binding, where a 16° hinge-bending "clamshell" motion closes the active site cleft around the inhibitor, further enhancing the binding efficiency.

The MLN-4760 design was inspired by the His-Leu motif of angiotensin I, but its binding orientation within the ACE2 active site deviates from initial predictions which is displayed in Figure 1.9.[114] The dichlorobenzyl group of the substituted imidazole occupies the S1′ subsite, while the leucine moiety is positioned in the S1 subsite as depicted in Figure 1.11. This deviation occurs because the S1′ subsite, being larger

and more spacious than the S1 subsite, readily accommodates the bulky 3,5-dichlorobenzylimidazole group. Although MLN-4760 contains two carboxylate groups capable of coordinating with the catalytic zinc ion in the ACE2 active site, which could theoretically result in multiple binding modes and potential interactions with other zinc metalloproteases, it binds specifically and deeply within the active site cleft of ACE2, engaging both subdomains I and II.

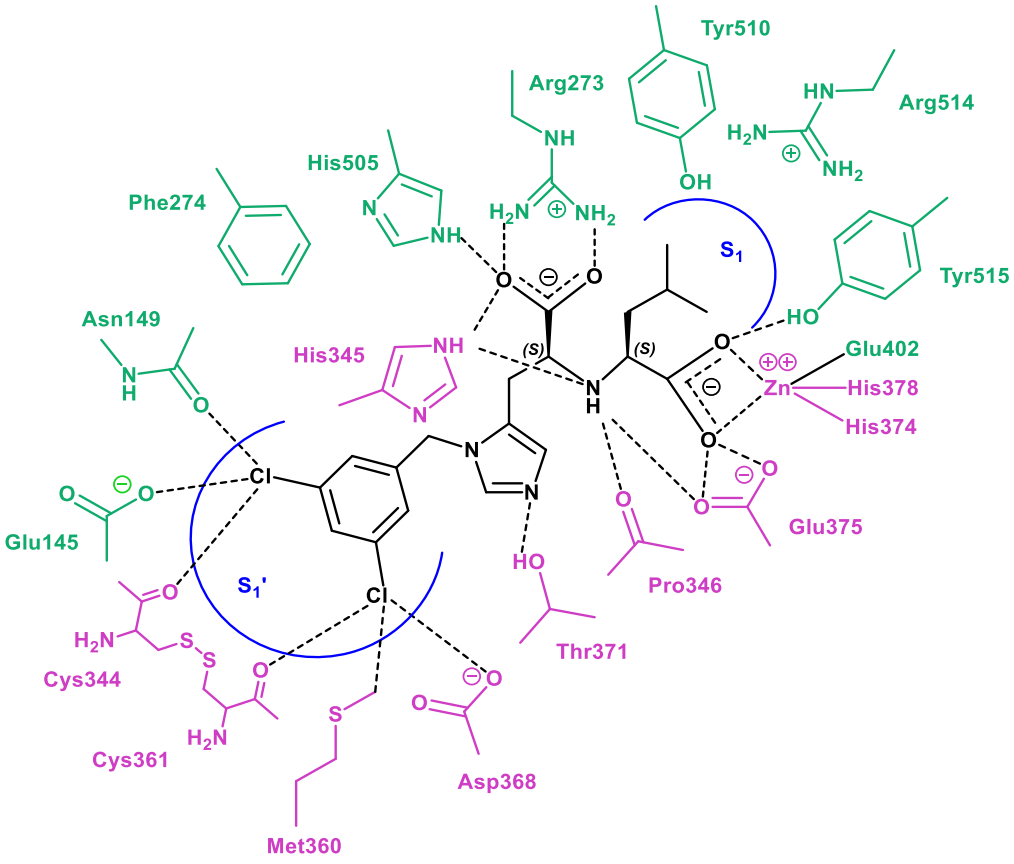

Figure 1.11: A schematic representation of the binding interactions between MLN-4760 and ACE2. MLN-4760 is shown in black, with residues from subdomain I in purple and those from subdomain II in green. *Figure reproduced with permission of P. Towler et al., ACE2 X-ray structures reveal a large hinge-bending motion important for inhibitor binding and catalysis, Journal of Biological Chemistry, 2004, Vol. 279, Issue 17, Pages 17996-18007;*[57] *permission conveyed through Copyright Clearance Centre, Inc.*

The key binding interactions of inhibitors also provide crucial insights into the catalytic mechanism underlying peptide hydrolysis by ACE2 as demonstrated in Figure 1.12. A proposed catalytic mechanism suggests that, upon substrate binding, a substrate-induced hinge-bending motion occurs, effectively closing the active site and aligning essential catalytic residues. This conformational rearrangement facilitates the nucleophilic attack of a zinc-bound water molecule on the carbonyl carbon of the reactive amide bond, leading to the formation of a tetrahedral intermediate. Concurrently, a proton from the attacking water is transferred to Glu375, while His505 donates a proton to the nitrogen atom of the departing amino acid residue. The resulting sp^3-hybridised nitrogen is stabilised through hydrogen-bonding interactions with Pro346, His505, and His345. Subsequent collapse of the tetrahedral intermediate cleaves the amide C–N bond. Simultaneously, the liberated nitrogen atom abstracts a proton from Glu375, thereby completing the peptide bond cleavage. The carboxyl group of the product may then transfer a proton back to His505, either directly via exchange between carboxyl oxygen atoms or indirectly through solvent.

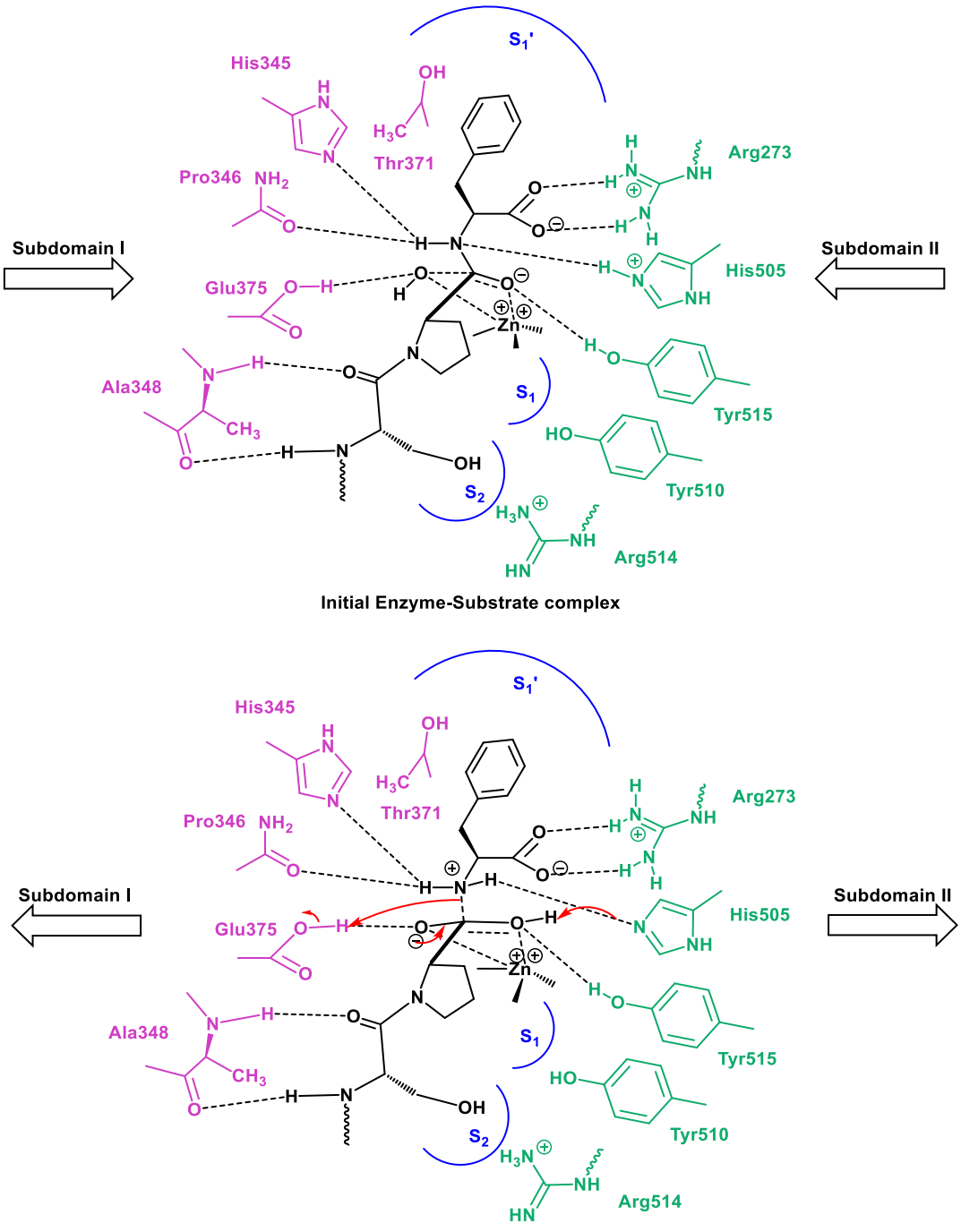

Figure 1.12: Proposed mechanism for peptide hydrolysis by ACE2. Peptide substrate is shown in black, with residues from subdomain I in purple and those from subdomain II in green. *Figure adapted with permission of P. Towler et al., ACE2 X-ray structures reveal a large hinge-bending motion important for inhibitor binding and catalysis, Journal of Biological Chemistry, 2004, Vol. 279, Issue 17, Pages 17996-18007;*[57] *permission conveyed through Copyright Clearance Centre, Inc.*

(3) Current Applications of MLN-4760

As a potent and selective ACE2 inhibitor, MLN-4760 has been used to investigate ACE2 function. Its ability to block the ACE2 active site has advanced our understanding of the role of ACE2 in various physiological and pathological conditions, especially in kidney and cardiovascular diseases.[116-118]

In the context of COVID-19, MLN-4760 has been studied for its potential effect on the interaction between ACE2 and the SARS-CoV-2 spike protein. A study shows that while MLN-4760 binds strongly to ACE2 and alters its conformation, it does not block or enhance the binding affinity between the viral spike protein and ACE2, suggesting that it likely has no direct effect on viral entry.[119] Interestingly, when the SARS-CoV-2 spike protein binds to ACE2 already complexed with MLN-4760, it induces structural rearrangements within ACE2 that reverse the effect of the inhibitor binding and ACE2 enzyme returns to its active form.[119] This observation underscores the complexity of inhibitor design targeting ACE2 in the context of viral interaction.

In imaging applications, MLN-4760 represents a promising scaffold for the development of radiolabelled derivatives. This is important given that ACE2 imaging remains relatively underexplored as most current efforts have focused on radiolabelled derivatives of the peptide DX600, which will be discussed in detail in Chapter 3.

1.4.3 Other Small Molecule ACE2 Inhibitors

At the onset of the COVID-19 pandemic, research efforts focused on identifying inhibitors that specifically targeted the ACE2–SARS-CoV-2 binding interface, which is distinct from the catalytic site of ACE2.[120] Initial strategies focused on repurposing existing drugs, such as ARBs and ACEIs, but these compounds demonstrated limited selectivity and potency towards ACE2.[35, 36, 121] In parallel, computational studies were conducted to identify clinically approved drugs with potential ACE2 inhibitory activity. In a structure-based virtual screening study, eight drug candidates were identified as promising inhibitors, including quisinostat **1.3** shown in Figure 1.13.[122] These compounds may stabilise a closed, substrate- or inhibitor-bound conformation of ACE2, potentially relocating key exterior residues recognised by SARS-CoV-2.[122] Another molecular docking study suggested that chloroquine **1.4** and its metabolite hydroxychloroquine **1.5**, originally used for malaria and rheumatic diseases, can interact with different ACE2 domains involved in coronavirus spike protein binding, suggesting their potential in the treatment of SARS-CoV-2 infection.[123] These findings emphasise the potential of drug repurposing in identifying ACE2 inhibitors, although further experimental validation is needed to confirm their clinical efficacy.

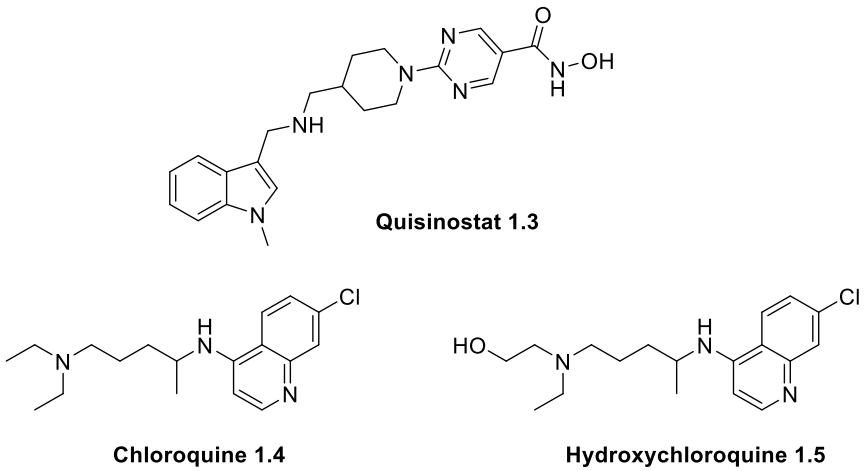

Figure 1.13: Selected drugs repurposed for the treatment of COVID-19.

MLN-4760 is the most extensively characterised ACE2 inhibitor to date, and only a few other small-molecule inhibitors have been investigated. One such competitive inhibitor is a series of phosphinic dipeptides and tripeptides, with general structures Z-Xaa(PO_2-CH_2)YaaOH and Ac-Zaa-Xaa(PO_2-CH_2)YaaOH, have shown promising inhibitory activity against ACE2.[124] Among these, the most potent is the tripeptide **1.6** displayed in Figure 1.14A with a K_i value of 0.4 nM for ACE2, exhibiting exceptional selectivity by distinguishing ACE2 from CPDA, both members of the family of zinc-dependent metallopeptidases, with a selectivity factor exceeding three orders of magnitude. Another competitive ACE2 inhibitor shown in Figure 1.14A is nicotianamine **1.7**, also known as soybean ACE2 inhibitor, which is the active compound isolated from soybean. It has ACE2 inhibitory activity with an IC_{50} value of 84 nM against recombinant human ACE2.[125]

Another noteworthy ACE2 inhibitor is the allosteric inhibitor *N*-(2-aminoethyl)-1-aziridine-ethanamine (NAAE **1.8**), first identified after the SARS outbreak as shown

in Figure 1.14B.[126] NAAE targets the virus-binding allosteric site on ACE2, exhibiting dose-dependent inhibition with an IC_{50} of 57 ± 7 μM. It effectively disrupts spike protein-mediated cell fusion by altering the ACE2 residues that interact with the SARS-CoV spike protein. While NAAE may be of interest for probing SARS-CoV-2 binding to ACE2, it is not a potent inhibitor of ACE2 enzymatic activity.

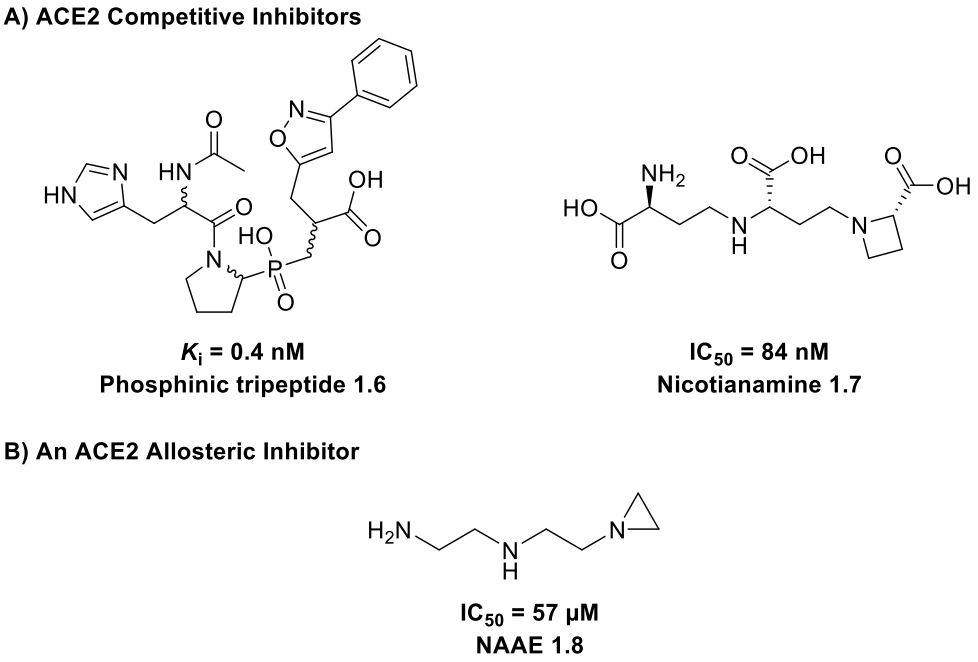

Figure 1.14: Selected small-molecule inhibitors of ACE2: A) competitive inhibitors and B) an allosteric inhibitor.

It is important to note that prolonged inhibition of ACE2 may lead to ACE2 deficiency. As discussed in Section 1.2 regarding the role of ACE2 in the renin-angiotensin-aldosterone system, this imbalance could result in elevated levels of angiotensin II, which may contribute to heart failure and lung injury. Consequently, further investigations into ACE2 inhibitors as a therapeutic approach have been limited.[127]

1.5 Positron Emission Tomography

1.5.1 Development of PET Imaging

Positron emission tomography (PET) is a non-invasive nuclear imaging technique that enables real-time visualisation of metabolic and physiological processes within the body.[128-130] Unlike anatomical imaging modalities such as magnetic resonance imaging (MRI), computed tomography (CT), X-ray, and ultrasound, which primarily provide structural details, PET captures functional dynamics at the molecular level.[130-132] This real-time capability makes PET particularly valuable in diagnosing and managing various diseases, notably in oncology, cardiology, and neurology.[129, 132-134]

PET imaging requires the use of a radiotracer, which is a molecule labelled with a suitable positron emitting radionuclide, such as fluorine-18. The introduction of fluorine-18 labelled 2-deoxy-2-[^{18}F]fluoro-*D*-glucose ([^{18}F]FDG), as depicted in Figure 1.15, by Tatsuo Ido and colleagues in 1978 transformed PET imaging.[135] [^{18}F]FDG is widely employed for the quantitative evaluation of glucose metabolism in vivo and has become an essential tool in routine oncological imaging for the detection, staging, and monitoring of various cancers.[136] By the 1990s, PET had become an established clinical tool, with studies demonstrating its high sensitivity for cancer detection.[136] Advances in technology have further enhanced PET performance, with modern scanners achieving spatial resolutions below 3 mm and time resolutions under 200 ps.[136]

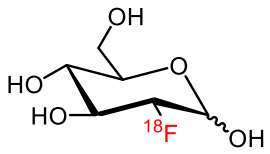

Figure 1.15: Structure of [^{18}F]FDG.

Today, PET imaging is frequently combined with CT or MRI, forming PET/CT and PET/MRI systems that integrate metabolic information from PET with the high-resolution structural detail of CT or MRI, enabling precise correlation between molecular activity and structural information. This fusion enhances diagnostic accuracy and broadens the clinical and research applications of PET, particularly in oncology, neurology, and cardiology. Furthermore, the integration of PET with artificial intelligence and its emerging role as a bioimaging tool continue to attract significant attention.[136]

1.5.2 Principles of PET Imaging

The process of PET imaging is summarised in Figure 1.16.[129] It begins with the production of positron-emitting radionuclides. These radionuclides are typically generated using a cyclotron, which produces a beam of high-energy protons that can bombard a target material to yield positron-emitting isotopes.[137] Following radionuclide production, the radioisotope is incorporated into a biomolecule of interest to yield a radiotracer. For instance, [^{18}F]FDG is synthesised via nucleophilic substitution using an acetyl-protected mannose triflate precursor.[138] The choice of radiotracer depends on the biological process under investigation, such as [^{18}F]FDG for glucose metabolism, [^{18}F]fluoromisonidazole for hypoxia, or [^{11}C]methionine for

the evaluation of brain tumours. Before administration, the synthesised radiotracer undergoes stringent quality control to ensure radiochemical purity, sterility and molar activity. Once the radiotracer passes quality control, it is administered intravenously to the patient and accumulates in target tissues based on its biochemical properties. The injected amount of radiotracer is typically in the nmol range, depending on the molar activity and the sensitivity of the PET scanner used.[139] The uptake and biodistribution of the tracer depend on various physiological factors, such as blood flow, receptor density, and metabolic activity.

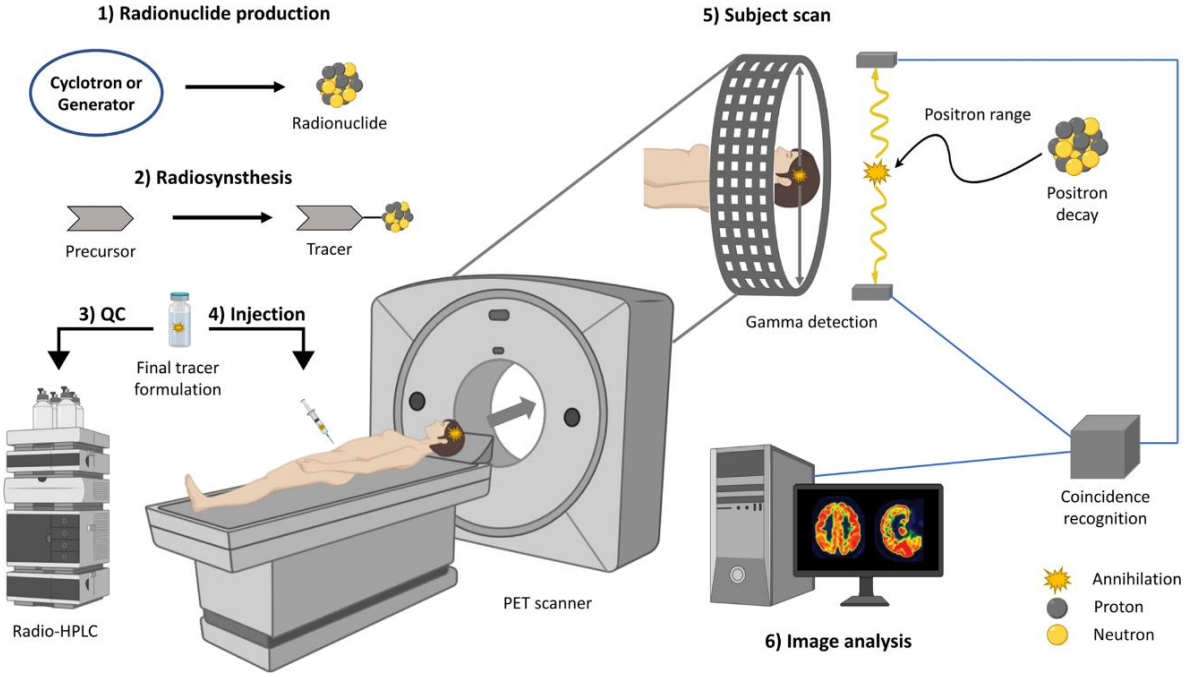

Figure 1.16: Key stages of the PET imaging process: 1) radionuclide production, 2) radiotracer synthesis, 3) quality control (QC), 4) intravenous administration of the tracer, 5) PET scanning—positron emission, annihilation, and coincidence detection, and 6) image reconstruction and quantitative analysis. *Figure reproduced with permission from J. Rong, A. Haider, T. E. Jeppesen, L. Josephson and S. H. Liang, Radiochemistry for Positron Emission Tomography, Nature Communications, 2023, Vol. 14, Issue 1, Pages 3257;*[129] *permission conveyed through Copyright Clearance Center, Inc.*

In the body, the radionuclide spontaneously undergoes β^+ decay, emitting a positron (β^+). The resulting positron then travels a short distance (~1 mm in tissue for fluorine-18) and undergoes multiple inelastic collisions, over which it loses its kinetic energy, followed by a final annihilation of the positron with an electron (e^-). As shown in Figure 1.17, this process produces two 511 keV gamma (γ) photons, which are emitted in nearly opposite directions (~180° apart).

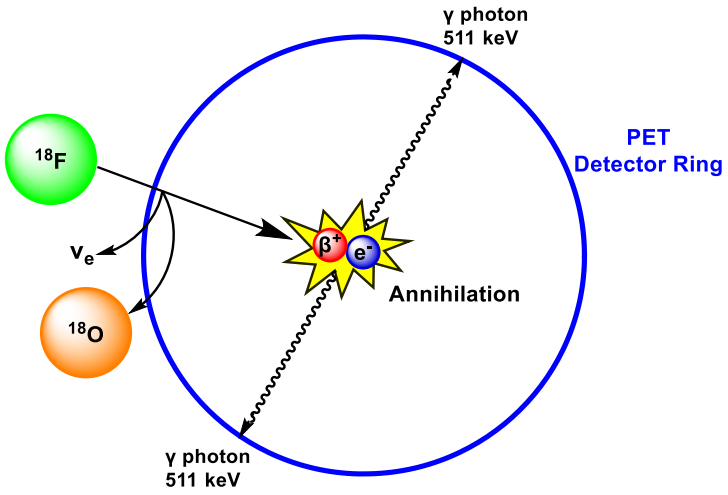

Figure 1.17: Positron decay of ^{18}F, followed by annihilation and detection by PET.

A ring of scintillation detectors with a diameter of 60–90 cm detects these annihilation photons, and identifies photon pairs detected simultaneously, establishing a line of response along which the annihilation event occurred. Finally, image reconstruction algorithms process the acquired coincidence data to generate a three-dimensional representation of radiotracer distribution.

1.5.2.1 Key Parameters in Radiosynthesis

Unlike conventional chemical synthesis, where structural characterisation typically relies on nuclear magnetic resonance (NMR) spectroscopy, PET radiotracer analysis is constrained by the nanomolar to sub-nanomolar concentrations of radioactive material. Therefore, analytical techniques sensitive to radioactivity such as radio-high performance liquid chromatography (radio-HPLC) and radio-thin layer chromatography (radio-TLC) are widely used. In radio-HPLC, which couples HPLC with a radioactivity detector, the identity of the radiolabelled compound is confirmed by comparing its retention time to that of a non-radiolabelled reference standard. For example, the ^{18}F-labelled product and its corresponding ^{19}F analogue. Integration of the radioactive signal enables quantification of the radiochemical yield. Radio-TLC, typically combined with digital autoradiography for detection, is particularly effective in [^{18}F]fluoride-based labelling reactions, where unreacted fluoride remains at the baseline of the silica or alumina plate, allowing for rapid assessment of labelling efficiency.[140]

In PET radiochemistry, a distinct set of analytical parameters is employed, differing from those used in conventional synthetic chemistry. The definitions introduced here align with the established guidelines proposed by the radiochemistry community.[141, 142] Radiochemical yield (RCY) refers to the percentage of starting radioactivity converted into the desired radiolabelled compound. It may refer to either an isolated or crude product, and the method of calculation should be specified. Throughout this

thesis, RCY values obtained by integration of preparative HPLC radioactive peaks are reported as RCY_{HPLC}.[141, 142]

Radiochemical purity (RCP) denotes the percentage of radioactivity in a sample that originates from the intended radiolabelled compound. It is typically assessed by radio-HPLC and reported as the fraction of the desired radioactive product relative to all detected radioactive species.[141, 142]

1.5.3 Fluorine-18 in PET Imaging

1.5.3.1 PET Radionuclides

PET employs a variety of positron-emitting radionuclides, including fluorine-18 (^{18}F) carbon-11 (^{11}C), nitrogen-13 (^{13}N), oxygen-15 (^{15}O), gallium-68 (^{68}Ga), copper-64 (^{64}Cu), and zirconium-89 (^{89}Zr). Their key properties are summarised in Table 1.4.

The half-life ($t_{1/2}$) of a radionuclide, defined as the time required for 50% of its radioactive nuclei to decay, is a critical parameter influencing its practical utility in PET imaging. It determines the feasible timeframe for radiotracer synthesis, quality control, transportation, and imaging, as well as the total radiation dose delivered to the patient. Short-lived radionuclides such as oxygen-15 ($t_{1/2}$ = 2.03 min) and nitrogen-13 ($t_{1/2}$ = 9.97 min) are well suited for imaging rapid physiological processes, though their utility is constrained by the need for on-site cyclotron production and rapid radiochemical synthesis due to their rapid decay.[143] Longer-lived radionuclides, such as fluorine-18 ($t_{1/2}$ = 109.8 min), allow for more complex radiochemical

transformations and extended quality control procedures. Radionuclides with even longer half-lives, such as copper-64 ($t_{1/2}$ = 12.7 h) and zirconium-89 ($t_{1/2}$ = 78.4 h), may be less suitable for conventional clinical PET but are valuable for studying slower biological processes, such as protein–ligand interactions or antibody-based imaging, where extended circulation times are required to achieve high-contrast images.[144]

Radionuclide	Half-Life $t_{1/2}$	Maximum Positron Energy E_{max} (MeV)	Main Production Method
Carbon-11 (^{11}C)	20.4 min	0.96	Cyclotron (^{14}N(p,α)^{11}C)
Nitrogen-13 (^{13}N)	9.97 min	1.20	Cyclotron (^{16}O(p,α)^{13}N)
Oxygen-15 (^{15}O)	2.03 min	1.73	Cyclotron (^{15}N(d,n)^{15}O)
Fluorine-18 (^{18}F)	109.8 min	0.64	Cyclotron (^{18}O(p,n)^{18}F)
Copper-64 (^{64}Cu)	12.7 h	0.65	Cyclotron (^{64}Ni(p,n)^{64}Cu)
Zirconium-89 (^{89}Zr)	78.4 h	0.90	Cyclotron (^{89}Y(p,n)^{89}Zr)
Gallium-68 (^{68}Ga)	67.8 min	1.92	Generator (^{68}Ge → ^{68}Ga)

Table 1.4: Comparison of common PET radionuclides.

The maximum positron energy (E_{max}) affects the spatial resolution of PET images.[145] After emission, a positron travels a finite distance, known as the positron range, before annihilating with an electron to produce detectable gamma photons. Higher-energy positrons, like those emitted by gallium-68 (E_{max} = 1.92 MeV), have longer positron ranges in tissue, leading to greater spatial uncertainty and reduced image resolution. In contrast, fluorine-18 (E_{max} = 0.64 MeV) emits lower-energy positrons with shorter ranges, enabling higher-resolution imaging.

Regarding production methods, most PET radionuclides are generated using a cyclotron, a type of particle accelerator that accelerates protons to high energies and directs them onto a target. When a proton collides with a stable isotope in the target, a nuclear reaction occurs, resulting in the formation of a radionuclide. For example, fluorine-18 is produced by bombarding an oxygen-18-enriched target, typically in the form of [^{18}O]water, with protons. This reaction is denoted as ^{18}O(*p,n*)^{18}F, where *p* indicates a proton and *n* a neutron. In other notations, *d* and *α* represent a deuteron and alpha particle, respectively. Some radionuclides, such as gallium-68, are obtained via a radionuclide generator system. A generator operates on the principle of radioactive decay, in which a long-lived parent isotope decays into a shorter-lived daughter isotope suitable for PET imaging. In the ^{68}Ge/^{68}Ga generator, the parent nuclide ^{68}Ge decays to yield ^{68}Ga, which can then be eluted from a column using hydrochloric acid solution.[132]

1.5.3.2 Significance of Fluorine-18

Fluorine-18 (^{18}F) is one of the most widely utilised radionuclides in PET imaging owing to its highly favourable nuclear and chemical properties. As outlined in the previous section, it offers advantageous nuclear characteristics, including a moderate half-life ($t_{1/2}$ = 109.8 min), relatively low maximum positron energy (E_{max} = 0.64 MeV), and a short positron range in tissue (mean ≈ 0.6 mm), all of which contribute to high-resolution imaging. Its production via the ^{18}O(*p,n*)^{18}F nuclear reaction is both reliable and commercially scalable, primarily yielding [^{18}F]fluoride

([^{18}F]F^-) for use in labelling reactions. Furthermore, fluorine-18 decays almost exclusively by positron emission (97%), reducing radiation burden to the patient. Its decay leads to the formation of stable oxygen-18, further contributing to its favourable radiological safety profile.[146]

From a chemical perspective, fluorine possesses a unique combination of properties that make it highly valuable in medicinal chemistry. Approximately 20–25% of all marketed small-molecule pharmaceuticals contain at least one fluorine atom.[147] As the most electronegative element (Pauling electronegativity = 3.98), fluorine induces strong inductive effects when introduced into organic molecules. The carbon–fluorine (C–F) bond, with a bond dissociation energy of approximately 105.4 kcal/mol, is one of the strongest bond in organic chemistry. Fluorine has a van der Waals radius (1.47 Å) comparable to that of hydrogen (1.20 Å) and oxygen (1.52 Å), enabling it to function as a bioisostere capable of modulating molecular properties.[148]

One of fluorine's most valuable applications in drug development is its ability to enhance metabolic stability. Fluorine substitution for hydrogen at metabolically labile sites in biomolecules subject to cytochrome P450-mediated oxidation often reduces the rate of metabolic degradation.[147, 149] Fluorine also modulates acidity and lipophilicity of molecules. For example, the pK_a of acetic acid (4.76) decreases to 0.52 in trifluoroacetic acid. Such shifts in ionisation affect solubility, permeability, and target binding under physiological conditions. For instance, fluorine substitution has been shown to improve blood–brain barrier penetration, as seen in central nervous

system drugs such as fluorinated Human Immunodeficiency Virus (HIV) protease inhibitors.[150] Moreover, fluorine can modulate receptor binding affinity by affecting dipolar interactions, enhancing hydrogen bonding networks, and stabilising conformations.[147, 149] These multifaceted effects make fluorination a powerful strategy in the rational design of drug candidates. Consequently, the incorporation of fluorine-18 into radiotracers allows for the development of biologically relevant probes that retain favourable pharmacological profiles.

1.6 Conclusion

This chapter has provided a comprehensive background on COVID-19, with a focus on the critical role of the ACE2 receptor in SARS-CoV-2 infection. The structural and functional characteristics of ACE2 were discussed, alongside the mechanisms of viral entry and the relevance of ACE2 expression in COVID-19 pathology and other diseases. Various therapeutic strategies targeting ACE2 were explored, including peptide-based and small-molecule inhibitors, with a focus on MLN-4760 as a lead compound. The chapter also introduced the principles and development of PET imaging, highlighting the significance of fluorine-18 as a key radionuclide. Together, these sections establish a scientific rationale for the design of fluorine-18-labelled ACE2 inhibitors as PET tracers.

By integrating computational modelling, synthetic chemistry, and radiochemistry, this research aims to develop and evaluate fluorine-18-labelled ACE2 inhibitors for PET imaging to enable non-invasive visualisation of ACE2 expression, with potential applications in understanding COVID-19 and other diseases involving ACE2 dysregulation.

1.7 References

(1) Cucinotta, D.; Vanelli, M. WHO declares COVID-19 a pandemic. *Acta Biomed.* **2020**, *91* (1), 157.

(2) Zhu, N.; Zhang, D.; Wang, W.; Li, X.; Yang, B.; Song, J.; Zhao, X.; Huang, B.; Shi, W.; Lu, R. A novel coronavirus from patients with pneumonia in China, 2019. *N. Engl. J. Med.* **2020**, *382* (8), 727–733.

(3) Clinical management of severe acute respiratory infection when novel coronavirus (2019-nCoV) infection is suspected: interim guidance. *World Health Organization* **2020**.

(4) Wu, F.; Zhao, S.; Yu, B.; Chen, Y.-M.; Wang, W.; Song, Z.-G.; Hu, Y.; Tao, Z.-W.; Tian, J.-H.; Pei, Y.-Y. A new coronavirus associated with human respiratory disease in China. *Nature* **2020**, *579* (7798), 265–269.

(5) Huang, C.; Wang, Y.; Li, X.; Ren, L.; Zhao, J.; Hu, Y.; Zhang, L.; Fan, G.; Xu, J.; Gu, X. Clinical features of patients infected with 2019 novel coronavirus in Wuhan, China. *Lancet* **2020**, *395* (10223), 497–506.

(6) WHO Director-General's opening remarks at the media briefing on COVID-19. *World Health Organization* **2022**.

(7) Jayaweera, M.; Perera, H.; Gunawardana, B.; Manatunge, J. Transmission of COVID-19 virus by droplets and aerosols: A critical review on the unresolved dichotomy. *Environ. Res.* **2020**, *188*, 109819.

(8) Zhou, P.; Yang, X.-L.; Wang, X.-G.; Hu, B.; Zhang, L.; Zhang, W.; Si, H.-R.; Zhu, Y.; Li, B.; Huang, C.-L. A pneumonia outbreak associated with a new coronavirus of probable bat origin. *Nature* **2020**, *579* (7798), 270–273.

(9) Group, R. C. Dexamethasone in hospitalized patients with Covid-19. *N. Engl. J. Med.* **2021**, *384* (8), 693–704.

(10) Fortner, A.; Schumacher, D. First COVID-19 vaccines receiving the US FDA and EMA emergency use authorization. *Discoveries* **2021**, *9* (1).

(11) Schultz, B. M.; Melo-González, F.; Duarte, L. F.; Gálvez, N. M.; Pacheco, G. A.; Soto, J. A.; Berríos-Rojas, R. V.; González, L. A.; Moreno-Tapia, D.; Rivera-Pérez, D. A booster dose of CoronaVac increases neutralizing antibodies and T cells that recognize Delta and Omicron variants of concern. *MBio* **2022**, *13* (4), e01423–01422.

(12) Zhu, C.; Pang, S.; Liu, J.; Duan, Q. Current Progress, Challenges and Prospects in the Development of COVID-19 Vaccines. *Drugs* **2024**, 1–21.

(13) Alimohamadi, Y.; Sepandi, M.; Taghdir, M.; Hosamirudsari, H. Determine the most common clinical symptoms in COVID-19 patients: a systematic review and meta-analysis. *J. Prev. Med. Hyg.* **2020**, *61* (3), E304.

(14) Chan, J. F.-W.; Yuan, S.; Kok, K.-H.; To, K. K.-W.; Chu, H.; Yang, J.; Xing, F.; Liu, J.; Yip, C. C.-Y.; Poon, R. W.-S. A familial cluster of pneumonia associated with the 2019 novel coronavirus indicating person-to-person transmission: a study of a family cluster. *Lancet* **2020**, *395* (10223), 514–523.

(15) Wu, Z.; McGoogan, J. M. Characteristics of and important lessons from the coronavirus disease 2019 (COVID-19) outbreak in China: summary of a report of 72

314 cases from the Chinese Center for Disease Control and Prevention. *JAMA* **2020**, *323* (13), 1239–1242.

(16) Pascarella, G.; Strumia, A.; Piliego, C.; Bruno, F.; Del Buono, R.; Costa, F.; Scarlata, S.; Agrò, F. E. COVID-19 diagnosis and management: a comprehensive review. *J. Intern. Med.* **2020**, *288* (2), 192–206.

(17) Chan, J. F.-W.; Yuan, S.; Chu, H.; Sridhar, S.; Yuen, K.-Y. COVID-19 drug discovery and treatment options. *Nat. Rev. Microbiol.* **2024**, 1–17.

(18) Raveendran, A.; Jayadevan, R.; Sashidharan, S. Long COVID: an overview. *Diabetes Metab. Syndr.* **2021**, *15* (3), 869–875.

(19) Beigel, J. H.; Tomashek, K. M.; Dodd, L. E.; Mehta, A. K.; Zingman, B. S.; Kalil, A. C.; Hohmann, E.; Chu, H. Y.; Luetkemeyer, A.; Kline, S. Remdesivir for the treatment of Covid-19. *N. Engl. J. Med.* **2020**, *383* (19), 1813–1826.

(20) Group, R. C. Effect of hydroxychloroquine in hospitalized patients with Covid-19. *N. Engl. J. Med.* **2020**, *383* (21), 2030–2040.

(21) Chen, P.; Nirula, A.; Heller, B.; Gottlieb, R. L.; Boscia, J.; Morris, J.; Huhn, G.; Cardona, J.; Mocherla, B.; Stosor, V. SARS-CoV-2 neutralizing antibody LY-CoV555 in outpatients with Covid-19. *N. Engl. J. Med.* **2021**, *384* (3), 229–237.

(22) Taylor, P. C.; Adams, A. C.; Hufford, M. M.; De La Torre, I.; Winthrop, K.; Gottlieb, R. L. Neutralizing monoclonal antibodies for treatment of COVID-19. *Nat. Rev. Immunol.* **2021**, *21* (6), 382–393.

(23) Sudre, C. H.; Murray, B.; Varsavsky, T.; Graham, M. S.; Penfold, R. S.; Bowyer, R. C.; Pujol, J. C.; Klaser, K.; Antonelli, M.; Canas, L. S. Attributes and predictors of long COVID. *Nat. Med.* **2021**, *27* (4), 626–631.

(24) Nalbandian, A.; Sehgal, K.; Gupta, A.; Madhavan, M. V.; McGroder, C.; Stevens, J. S.; Cook, J. R.; Nordvig, A. S.; Shalev, D.; Sehrawat, T. S. Post-acute COVID-19 syndrome. *Nat. Med.* **2021**, *27* (4), 601–615.

(25) Lopez-Leon, S.; Wegman-Ostrosky, T.; Perelman, C.; Sepulveda, R.; Rebolledo, P. A.; Cuapio, A.; Villapol, S. More than 50 long-term effects of COVID-19: a systematic review and meta-analysis. *Sci. Rep.* **2021**, *11* (1), 1–12.

(26) Lan, J.; Ge, J.; Yu, J.; Shan, S.; Zhou, H.; Fan, S.; Zhang, Q.; Shi, X.; Wang, Q.; Zhang, L. Structure of the SARS-CoV-2 spike receptor-binding domain bound to the ACE2 receptor. *Nature* **2020**, *581* (7807), 215–220.

(27) Hoffmann, M.; Kleine-Weber, H.; Schroeder, S.; Krüger, N.; Herrler, T.; Erichsen, S.; Schiergens, T. S.; Herrler, G.; Wu, N.-H.; Nitsche, A. SARS-CoV-2 cell entry depends on ACE2 and TMPRSS2 and is blocked by a clinically proven protease inhibitor. *Cell* **2020**, *181* (2), 271–280. e278.

(28) Hoffmann, M.; Kleine-Weber, H.; Pöhlmann, S. A multibasic cleavage site in the spike protein of SARS-CoV-2 is essential for infection of human lung cells. *Mol. Cell* **2020**, *78* (4), 779–784. e775.

(29) Shang, J.; Wan, Y.; Luo, C.; Ye, G.; Geng, Q.; Auerbach, A.; Li, F. Cell entry mechanisms of SARS-CoV-2. *Proc. Natl. Acad. Sci. U.S.A.* **2020**, *117* (21), 11727–11734.

(30) Walls, A. C.; Park, Y.-J.; Tortorici, M. A.; Wall, A.; McGuire, A. T.; Veesler, D. Structure, function, and antigenicity of the SARS-CoV-2 spike glycoprotein. *Cell* **2020**, *181* (2), 281–292. e286.

(31) Mandala, V. S.; McKay, M. J.; Shcherbakov, A. A.; Dregni, A. J.; Kolocouris, A.; Hong, M. Structure and drug binding of the SARS-CoV-2 envelope protein transmembrane domain in lipid bilayers. *Nat. Struct. Mol. Biol.* **2020**, *27* (12), 1202–1208.

(32) Siu, Y.; Teoh, K.; Lo, J.; Chan, C.; Kien, F.; Escriou, N.; Tsao, S.; Nicholls, J.; Altmeyer, R.; Peiris, J. The M, E, and N structural proteins of the severe acute respiratory syndrome coronavirus are required for efficient assembly, trafficking, and release of virus-like particles. *J. Virol.* **2008**, *82* (22), 11318–11330.

(33) Zeng, W.; Liu, G.; Ma, H.; Zhao, D.; Yang, Y.; Liu, M.; Mohammed, A.; Zhao, C.; Yang, Y.; Xie, J. Biochemical characterization of SARS-CoV-2 nucleocapsid protein. *Biochem. Biophys. Res. Commun.* **2020**, *527* (3), 618–623.

(34) Yao, H.; Song, Y.; Chen, Y.; Wu, N.; Xu, J.; Sun, C.; Zhang, J.; Weng, T.; Zhang, Z.; Wu, Z. Molecular architecture of the SARS-CoV-2 virus. *Cell* **2020**, *183* (3), 730–738. e713.

(35) Donoghue, M.; Hsieh, F.; Baronas, E.; Godbout, K.; Gosselin, M.; Stagliano, N.; Donovan, M.; Woolf, B.; Robison, K.; Jeyaseelan, R. A novel angiotensin-converting enzyme–related carboxypeptidase (ACE2) converts angiotensin I to angiotensin 1-9. *Circul. Res.* **2000**, *87* (5), e1–e9.

(36) Tipnis, S. R.; Hooper, N. M.; Hyde, R.; Karran, E.; Christie, G.; Turner, A. J. A human homolog of angiotensin-converting enzyme: cloning and functional expression as a captopril-insensitive carboxypeptidase. *J. Biol. Chem.* **2000**, *275* (43), 33238–33243.

(37) Turner, A. Exploring the structure and function of zinc metallopeptidases: old enzymes and new discoveries. *Biochem. Soc. Trans.* **2003**, *31* (3), 723–727.

(38) Burrell, L. M.; Johnston, C. I.; Tikellis, C.; Cooper, M. E. ACE2, a new regulator of the renin–angiotensin system. *Trends Endocrinol. Metab.* **2004**, *15* (4), 166–169.

(39) Singh, K. D.; Karnik, S. S. Angiotensin receptors: structure, function, signaling and clinical applications. *J. Cell Signal.* **2016**, *1* (2).

(40) Hikmet, F.; Méar, L.; Edvinsson, Å.; Micke, P.; Uhlén, M.; Lindskog, C. The protein expression profile of ACE2 in human tissues. *Mol. Syst. Biol.* **2020**, *16* (7), e9610.

(41) Hamming, I.; Timens, W.; Bulthuis, M. L. C.; Lely, A. T.; Navis, G. J. v.; van Goor, H. Tissue distribution of ACE2 protein, the functional receptor for SARS coronavirus. A first step in understanding SARS pathogenesis. *J. Pathol.* **2004**, *203* (2), 631–637.

(42) Erdös, E. G. Conversion of angiotensin I to angiotensin II. *Am. J. Med.* **1976**, *60* (6), 749–759.

(43) Hamming, I.; Cooper, M. E.; Haagmans, B. L.; Hooper, N. M.; Korstanje, R.; Osterhaus, A. D.; Timens, W.; Turner, A.; Navis, G.; van Goor, H. The emerging role of ACE2 in physiology and disease. *J. Pathol.* **2007**, *212* (1), 1–11.

(44) Vickers, C.; Hales, P.; Kaushik, V.; Dick, L.; Gavin, J.; Tang, J.; Godbout, K.; Parsons, T.; Baronas, E.; Hsieh, F. Hydrolysis of biological peptides by human angiotensin-converting enzyme-related carboxypeptidase. *J. Biol. Chem.* **2002**, *277* (17), 14838–14843.

(45) Keidar, S.; Kaplan, M.; Gamliel-Lazarovich, A. ACE2 of the heart: from angiotensin I to angiotensin (1–7). *Cardiovasc. Res.* **2007**, *73* (3), 463–469.

(46) Ferrario, C. M.; Chappell, M. C.; Tallant, E. A.; Brosnihan, K. B.; Diz, D. I. Counterregulatory actions of angiotensin-(1-7). *Hypertension* **1997**, *30* (3), 535–541.

(47) Oudit, G. Y.; Crackower, M. A.; Backx, P. H.; Penninger, J. M. The role of ACE2 in cardiovascular physiology. *Trends Cardiovasc. Med.* **2003**, *13* (3), 93–101.

(48) Zhong, J.; Guo, D.; Chen, C. B.; Wang, W.; Schuster, M.; Loibner, H.; Penninger, J. M.; Scholey, J. W.; Kassiri, Z.; Oudit, G. Y. Prevention of angiotensin II–mediated renal oxidative stress, inflammation, and fibrosis by angiotensin-converting enzyme 2. *Hypertension* **2011**, *57* (2), 314–322.

(49) Chamsi-Pasha, M. A.; Shao, Z.; Tang, W. W. Angiotensin-converting enzyme 2 as a therapeutic target for heart failure. *Curr. Heart Fail. Rep.* **2014**, *11*, 58–63.

(50) Mascolo, A.; Urbanek, K.; De Angelis, A.; Sessa, M.; Scavone, C.; Berrino, L.; Rosano, G. M. C.; Capuano, A.; Rossi, F. Angiotensin II and angiotensin 1–7: which is their role in atrial fibrillation? *Heart Fail. Rev.* **2020**, *25*, 367–380.

(51) Li, W.; Moore, M. J.; Vasilieva, N.; Sui, J.; Wong, S. K.; Berne, M. A.; Somasundaran, M.; Sullivan, J. L.; Luzuriaga, K.; Greenough, T. C. Angiotensin-converting enzyme 2 is a functional receptor for the SARS coronavirus. *Nature* **2003**, *426* (6965), 450–454.

(52) Dimitrov, D. S. The secret life of ACE2 as a receptor for the SARS virus. *Cell* **2003**, *115* (6), 652–653.

(53) Wrapp, D.; Wang, N.; Corbett, K. S.; Goldsmith, J. A.; Hsieh, C.-L.; Abiona, O.; Graham, B. S.; McLellan, J. S. Cryo-EM structure of the 2019-nCoV spike in the prefusion conformation. *Science* **2020**, *367* (6483), 1260–1263.

(54) Xu, X.; Chen, P.; Wang, J.; Feng, J.; Zhou, H.; Li, X.; Zhong, W.; Hao, P. Evolution of the novel coronavirus from the ongoing Wuhan outbreak and modeling of its spike protein for risk of human transmission. *Sci. China Life Sci.* **2020**, *63* (3), 457–460.

(55) Basu, A.; Sarkar, A.; Maulik, U. Molecular docking study of potential phytochemicals and their effects on the complex of SARS-CoV2 spike protein and human ACE2. *Sci. Rep.* **2020**, *10* (1), 17699.

(56) Yan, R.; Zhang, Y.; Li, Y.; Xia, L.; Guo, Y.; Zhou, Q. Structural basis for the recognition of SARS-CoV-2 by full-length human ACE2. *Science* **2020**, *367* (6485), 1444–1448.

(57) Towler, P.; Staker, B.; Prasad, S. G.; Menon, S.; Tang, J.; Parsons, T.; Ryan, D.; Fisher, M.; Williams, D.; Dales, N. A. ACE2 X-ray structures reveal a large hinge-bending motion important for inhibitor binding and catalysis. *J. Biol. Chem.* **2004**, *279* (17), 17996–18007.

(58) Yan, R.; Zhang, Y.; Li, Y.; Ye, F.; Guo, Y.; Xia, L.; Zhong, X.; Chi, X.; Zhou, Q. Structural basis for the different states of the spike protein of SARS-CoV-2 in complex with ACE2. *Cell Res.* **2021**, *31* (6), 717–719.

(59) Shi, W.; Cai, Y.; Zhu, H.; Peng, H.; Voyer, J.; Rits-Volloch, S.; Cao, H.; Mayer, M. L.; Song, K.; Xu, C. Cryo-EM structure of SARS-CoV-2 postfusion spike in membrane. *Nature* **2023**, *619* (7969), 403–409.

(60) Xu, C.; Wang, Y.; Liu, C.; Zhang, C.; Han, W.; Hong, X.; Wang, Y.; Hong, Q.; Wang, S.; Zhao, Q. Conformational dynamics of SARS-CoV-2 trimeric spike glycoprotein in complex with receptor ACE2 revealed by cryo-EM. *Sci. Adv.* **2021**, *7* (1), eabe5575.

(61) Zhou, T.; Tsybovsky, Y.; Gorman, J.; Rapp, M.; Cerutti, G.; Chuang, G.-Y.; Katsamba, P. S.; Sampson, J. M.; Schön, A.; Bimela, J. Cryo-EM structures of SARS-CoV-2 spike without and with ACE2 reveal a pH-dependent switch to mediate endosomal positioning of receptor-binding domains. *Cell Host Microbe* **2020**, *28* (6), 867–879. e865.

(62) Wang, Q.; Zhang, Y.; Wu, L.; Niu, S.; Song, C.; Zhang, Z.; Lu, G.; Qiao, C.; Hu, Y.; Yuen, K.-Y. Structural and functional basis of SARS-CoV-2 entry by using human ACE2. *Cell* **2020**, *181* (4), 894–904. e899.

(63) Shang, J.; Ye, G.; Shi, K.; Wan, Y.; Luo, C.; Aihara, H.; Geng, Q.; Auerbach, A.; Li, F. Structural basis of receptor recognition by SARS-CoV-2. *Nature* **2020**, *581* (7807), 221–224.

(64) Jackson, C. B.; Farzan, M.; Chen, B.; Choe, H. Mechanisms of SARS-CoV-2 entry into cells. *Nat. Rev. Mol. Cell Biol.* **2022**, *23* (1), 3–20.

(65) Li, W.; Zhang, C.; Sui, J.; Kuhn, J. H.; Moore, M. J.; Luo, S.; Wong, S. K.; Huang, I. C.; Xu, K.; Vasilieva, N. Receptor and viral determinants of SARS-coronavirus adaptation to human ACE2. *EMBO J.* **2005**, *24* (8), 1634–1643.

(66) Li, F.; Li, W.; Farzan, M.; Harrison, S. C. Structure of SARS coronavirus spike receptor-binding domain complexed with receptor. *Science* **2005**, *309* (5742), 1864–1868.

(67) V'kovski, P.; Kratzel, A.; Steiner, S.; Stalder, H.; Thiel, V. Coronavirus biology and replication: implications for SARS-CoV-2. *Nat. Rev. Microbiol.* **2021**, *19* (3), 155–170.

(68) Bayati, A.; Kumar, R.; Francis, V.; McPherson, P. S. SARS-CoV-2 infects cells after viral entry via clathrin-mediated endocytosis. *J. Biol. Chem.* **2021**, *296*.

(69) Hartenian, E.; Nandakumar, D.; Lari, A.; Ly, M.; Tucker, J. M.; Glaunsinger, B. A. The molecular virology of coronaviruses. *J. Biol. Chem.* **2020**, *295* (37), 12910–12934.

(70) Ferrario, C. M.; Jessup, J.; Chappell, M. C.; Averill, D. B.; Brosnihan, K. B.; Tallant, E. A.; Diz, D. I.; Gallagher, P. E. Effect of angiotensin-converting enzyme inhibition and angiotensin II receptor blockers on cardiac angiotensin-converting enzyme 2. *Circulation* **2005**, *111* (20), 2605–2610.

(71) Zhang, P.; Zhu, L.; Cai, J.; Lei, F.; Qin, J.-J.; Xie, J.; Liu, Y.-M.; Zhao, Y.-C.; Huang, X.; Lin, L. Association of inpatient use of angiotensin-converting enzyme inhibitors and angiotensin II receptor blockers with mortality among patients with hypertension hospitalized with COVID-19. *Circul. Res.* **2020**, *126* (12), 1671–1681.

(72) Zhang, X.; Yu, J.; Pan, L.-y.; Jiang, H.-y. ACEI/ARB use and risk of infection or severity or mortality of COVID-19: a systematic review and meta-analysis. *Pharmacol. Res.* **2020**, *158*, 104927.

(73) Di Castelnuovo, A.; Costanzo, S.; Antinori, A.; Berselli, N.; Blandi, L.; Bonaccio, M.; Cauda, R.; Gialluisi, A.; Guaraldi, G.; Menicanti, L. RAAS inhibitors are not associated with mortality in COVID-19 patients: findings from an observational

multicenter study in Italy and a meta-analysis of 19 studies. *Vascul. Pharmacol.* **2020**, *135*, 106805.

(74) Kai, H.; Kai, M. Interactions of coronaviruses with ACE2, angiotensin II, and RAS inhibitors—lessons from available evidence and insights into COVID-19. *Hypertens. Res.* **2020**, *43* (7), 648–654.

(75) Yang, G.; Tan, Z.; Zhou, L.; Yang, M.; Peng, L.; Liu, J.; Cai, J.; Yang, R.; Han, J.; Huang, Y. Effects of angiotensin II receptor blockers and ACE (angiotensin-converting enzyme) inhibitors on virus infection, inflammatory status, and clinical outcomes in patients with COVID-19 and hypertension: a single-center retrospective study. *Hypertension* **2020**, *76* (1), 51–58.

(76) Monteil, V.; Kwon, H.; Prado, P.; Hagelkrüys, A.; Wimmer, R. A.; Stahl, M.; Leopoldi, A.; Garreta, E.; Del Pozo, C. H.; Prosper, F. Inhibition of SARS-CoV-2 infections in engineered human tissues using clinical-grade soluble human ACE2. *Cell* **2020**, *181* (4), 905–913. e907.

(77) Chen, Y.; Zhao, X.; Zhou, H.; Zhu, H.; Jiang, S.; Wang, P. Broadly neutralizing antibodies to SARS-CoV-2 and other human coronaviruses. *Nat. Rev. Immunol.* **2023**, *23* (3), 189–199.

(78) Freidel, M. R.; Armen, R. S. Research Progress on Spike-Dependent SARS-CoV-2 Fusion Inhibitors and Small Molecules Targeting the S2 Subunit of Spike. *Viruses* **2024**, *16* (5), 712.

(79) Beyerstedt, S.; Casaro, E. B.; Rangel, É. B. COVID-19: angiotensin-converting enzyme 2 (ACE2) expression and tissue susceptibility to SARS-CoV-2 infection. *Eur. J. Clin. Microbiol. Infect. Dis.* **2021**, *40* (5), 905–919.

(80) Zou, X.; Chen, K.; Zou, J.; Han, P.; Hao, J.; Han, Z. Single-cell RNA-seq data analysis on the receptor ACE2 expression reveals the potential risk of different human organs vulnerable to 2019-nCoV infection. *Front. Med.* **2020**, *14*, 185–192.

(81) Fang, L.; Karakiulakis, G.; Roth, M. Are patients with hypertension and diabetes mellitus at increased risk for COVID-19 infection? *Lancet Respir. Med.* **2020**, *8* (4), e21.

(82) Peng, M.; He, J.; Xue, Y.; Yang, X.; Liu, S.; Gong, Z. Role of Hypertension on the Severity of COVID-19: A Review. *J. Cardiovasc. Pharmacol.* **2021**, *78* (5), e648–e655.

(83) Zhou, F.; Yu, T.; Du, R.; Fan, G.; Liu, Y.; Liu, Z.; Xiang, J.; Wang, Y.; Song, B.; Gu, X. Clinical course and risk factors for mortality of adult inpatients with COVID-19 in Wuhan, China: a retrospective cohort study. *Lancet* **2020**, *395* (10229), 1054–1062.

(84) Wijnant, S. R.; Jacobs, M.; Van Eeckhoutte, H. P.; Lapauw, B.; Joos, G. F.; Bracke, K. R.; Brusselle, G. G. Expression of ACE2, the SARS-CoV-2 receptor, in lung tissue of patients with type 2 diabetes. *Diabetes* **2020**, *69* (12), 2691–2699.

(85) Leung, J. M.; Yang, C. X.; Tam, A.; Shaipanich, T.; Hackett, T.-L.; Singhera, G. K.; Dorscheid, D. R.; Sin, D. D. ACE-2 expression in the small airway epithelia of smokers and COPD patients: implications for COVID-19. *Eur. Respir. J.* **2020**, *55* (5).

(86) Alqahtani, J. S.; Oyelade, T.; Aldhahir, A. M.; Alghamdi, S. M.; Almehmadi, M.; Alqahtani, A. S.; Quaderi, S.; Mandal, S.; Hurst, J. R. Prevalence, severity and

mortality associated with COPD and smoking in patients with COVID-19: a rapid systematic review and meta-analysis. *PLoS One* **2020**, *15* (5), e0233147.

(87) Kornilov, S. A.; Lucas, I.; Jade, K.; Dai, C. L.; Lovejoy, J. C.; Magis, A. T. Plasma levels of soluble ACE2are associated with sex, Metabolic Syndrome, and its biomarkers in a large cohort, pointing to a possible mechanism for increased severity in COVID-19. *Crit. Care* **2020**, *24*, 1–3.

(88) Lambert, D. W.; Yarski, M.; Warner, F. J.; Thornhill, P.; Parkin, E. T.; Smith, A. I.; Hooper, N. M.; Turner, A. J. Tumor necrosis factor-α convertase (ADAM17) mediates regulated ectodomain shedding of the severe-acute respiratory syndrome-coronavirus (SARS-CoV) receptor, angiotensin-converting enzyme-2 (ACE2). *J. Biol. Chem.* **2005**, *280* (34), 30113–30119.

(89) Lu, Y.; Zhu, Q.; Fox, D. M.; Gao, C.; Stanley, S. A.; Luo, K. SARS-CoV-2 down-regulates ACE2 through lysosomal degradation. *Mol. Biol. Cell* **2022**, *33* (14), ar147.

(90) Kuba, K.; Imai, Y.; Rao, S.; Gao, H.; Guo, F.; Guan, B.; Huan, Y.; Yang, P.; Zhang, Y.; Deng, W. A crucial role of angiotensin converting enzyme 2 (ACE2) in SARS coronavirus–induced lung injury. *Nat. Med.* **2005**, *11* (8), 875–879.

(91) Ramchand, J.; Burrell, L. M. Circulating ACE2: a novel biomarker of cardiovascular risk. *Lancet* **2020**, *396* (10256), 937–939.

(92) Lundström, A.; Ziegler, L.; Havervall, S.; Rudberg, A. S.; von Meijenfeldt, F.; Lisman, T.; Mackman, N.; Sandén, P.; Thålin, C. Soluble angiotensin-converting enzyme 2 is transiently elevated in COVID-19 and correlates with specific inflammatory and endothelial markers. *J. Med. Virol.* **2021**, *93* (10), 5908–5916.

(93) Nagy Jr, B.; Fejes, Z.; Szentkereszty, Z.; Sütő, R.; Várkonyi, I.; Ajzner, É.; Kappelmayer, J.; Papp, Z.; Tóth, A.; Fagyas, M. A dramatic rise in serum ACE2 activity in a critically ill COVID-19 patient. *Int. J. Infect. Dis.* **2021**, *103*, 412–414.

(94) van Lier, D.; Kox, M.; Santos, K.; van der Hoeven, H.; Pillay, J.; Pickkers, P. Increased blood angiotensin converting enzyme 2 activity in critically ill COVID-19 patients. *ERJ Open Res.* **2021**, *7* (1).

(95) Patel, S. K.; Juno, J. A.; Lee, W. S.; Wragg, K. M.; Hogarth, P. M.; Kent, S. J.; Burrell, L. M. Plasma ACE2 activity is persistently elevated following SARS-CoV-2 infection: implications for COVID-19 pathogenesis and consequences. *Eur. Respir. J.* **2021**, *57* (5).

(96) Fagyas, M.; Fejes, Z.; Sütő, R.; Nagy, Z.; Székely, B.; Pócsi, M.; Ivády, G.; Bíró, E.; Bekő, G.; Nagy, A. Circulating ACE2 activity predicts mortality and disease severity in hospitalized COVID-19 patients. *Int. J. Infect. Dis.* **2022**, *115*, 8–16.

(97) Kragstrup, T. W.; Singh, H. S.; Grundberg, I.; Nielsen, A. L.-L.; Rivellese, F.; Mehta, A.; Goldberg, M. B.; Filbin, M. R.; Qvist, P.; Bibby, B. M. Plasma ACE2 predicts outcome of COVID-19 in hospitalized patients. *PLoS One* **2021**, *16* (6), e0252799.

(98) Costa, L. B.; Perez, L. G.; Palmeira, V. A.; Macedo e Cordeiro, T.; Ribeiro, V. T.; Lanza, K.; Simoes e Silva, A. C. Insights on SARS-CoV-2 molecular interactions with the renin-angiotensin system. *Front. Cell Dev. Biol.* **2020**, *8*, 559841.

(99) El-Arif, G.; Farhat, A.; Khazaal, S.; Annweiler, C.; Kovacic, H.; Wu, Y.; Cao, Z.; Fajloun, Z.; Khattar, Z. A.; Sabatier, J. M. The renin-angiotensin system: a key role in SARS-CoV-2-induced COVID-19. *Molecules* **2021**, *26* (22), 6945.

(100) Cojocaru, E.; Cojocaru, C.; Vlad, C.-E.; Eva, L. Role of the Renin-Angiotensin System in long COVID's cardiovascular injuries. *Biomedicines* **2023**, *11* (7), 2004.

(101) Khazaal, S.; Harb, J.; Rima, M.; Annweiler, C.; Wu, Y.; Cao, Z.; Abi Khattar, Z.; Legros, C.; Kovacic, H.; Fajloun, Z. The pathophysiology of long COVID throughout the renin-angiotensin system. *Molecules* **2022**, *27* (9), 2903.

(102) Turner, A. J.; Nalivaeva, N. N. Angiotensin-converting enzyme 2 (ACE2): Two decades of revelations and re-evaluation. *Peptides* **2022**, *151*, 170766.

(103) Tikellis, C.; Thomas, M. Angiotensin-converting enzyme 2 (ACE2) is a key modulator of the renin angiotensin system in health and disease. *Int. J. Pept.* **2012**, *2012* (1), 256294.

(104) Wang, D.; Hu, B.; Hu, C.; Zhu, F.; Liu, X.; Zhang, J.; Wang, B.; Xiang, H.; Cheng, Z.; Xiong, Y. Clinical characteristics of 138 hospitalized patients with 2019 novel coronavirus–infected pneumonia in Wuhan, China. *JAMA* **2020**, *323* (11), 1061–1069.

(105) Guan, W.-j.; Ni, Z.-y.; Hu, Y.; Liang, W.-h.; Ou, C.-q.; He, J.-x.; Liu, L.; Shan, H.; Lei, C.-l.; Hui, D. S. Clinical characteristics of coronavirus disease 2019 in China. *N. Engl. J. Med.* **2020**, *382* (18), 1708–1720.

(106) Shi, S.; Qin, M.; Shen, B.; Cai, Y.; Liu, T.; Yang, F.; Gong, W.; Liu, X.; Liang, J.; Zhao, Q. Association of cardiac injury with mortality in hospitalized patients with COVID-19 in Wuhan, China. *JAMA Cardiol.* **2020**, *5* (7), 802–810.

(107) Zhang, Z.; Li, L.; Li, M.; Wang, X. The SARS-CoV-2 host cell receptor ACE2 correlates positively with immunotherapy response and is a potential protective factor for cancer progression. *Comput. Struct. Biotechnol. J.* **2020**, *18*, 2438–2444.

(108) Dai, Y.-J.; Hu, F.; Li, H.; Huang, H.-Y.; Wang, D.-W.; Liang, Y. A profiling analysis on the receptor ACE2 expression reveals the potential risk of different type of cancers vulnerable to SARS-CoV-2 infection. *Ann. Transl. Med.* **2020**, *8* (7).

(109) Ryan, P. M.; Caplice, N. COVID-19 and relative angiotensin-converting enzyme 2 deficiency: role in disease severity and therapeutic response. *Open Heart* **2020**, *7* (1), e001302.

(110) Huang, L.; Sexton, D. J.; Skogerson, K.; Devlin, M.; Smith, R.; Sanyal, I.; Parry, T.; Kent, R.; Enright, J.; Wu, Q.-l. Novel peptide inhibitors of angiotensin-converting enzyme 2. *J. Biol. Chem.* **2003**, *278* (18), 15532–15540.

(111) Harman, M. A.; Stanway, S. J.; Scott, H.; Demydchuk, Y.; Bezerra, G. A.; Pellegrino, S.; Chen, L.; Brear, P.; Lulla, A.; Hyvönen, M. Structure-Guided Chemical Optimization of Bicyclic Peptide (Bicycle) Inhibitors of Angiotensin-Converting Enzyme 2. *J. Med. Chem.* **2023**, *66* (14), 9881–9893.

(112) Wei, Y.; Liu, Z.; Zhang, M.; Zhu, X.; Niu, Q. Inhibition of ACE2–S Protein Interaction by a Short Functional Peptide with a Boomerang Structure. *Molecules* **2024**, *29* (13), 3022.

(113) Boshah, H.; Samkari, F.; Valle-Pérez, A. U.; Alsawaf, S. M.; Aldoukhi, A. H.; Bilalis, P.; Alshehri, S. A.; Susapto, H. H.; Hauser, C. A. Evaluation of Potential Peptide-Based Inhibitors against SARS-CoV-2 and Variants of Concern. *Biomed Res. Int.* **2023**, *2023* (1), 3892370.

(114) Dales, N. A.; Gould, A. E.; Brown, J. A.; Calderwood, E. F.; Guan, B.; Minor, C. A.; Gavin, J. M.; Hales, P.; Kaushik, V. K.; Stewart, M. Substrate-based design of

the first class of angiotensin-converting enzyme-related carboxypeptidase (ACE2) inhibitors. *J. Am. Chem. Soc.* **2002**, *124* (40), 11852–11853.

(115) Chen, D.; Oezguen, N.; Urvil, P.; Ferguson, C.; Dann, S. M.; Savidge, T. C. Regulation of protein-ligand binding affinity by hydrogen bond pairing. *Sci. Adv.* **2016**, *2* (3), e1501240.

(116) Soler, M.; Wysocki, J.; Ye, M.; Lloveras, J.; Kanwar, Y.; Batlle, D. ACE2 inhibition worsens glomerular injury in association with increased ACE expression in streptozotocin-induced diabetic mice. *Kidney Int.* **2007**, *72* (5), 614–623.

(117) Ye, M.; Wysocki, J.; William, J.; Soler, M. J.; Cokic, I.; Batlle, D. Glomerular localization and expression of angiotensin-converting enzyme 2 and angiotensin-converting enzyme: implications for albuminuria in diabetes. *J. Am. Soc. Nephrol.* **2006**, *17* (11), 3067–3075.

(118) Kluknavsky, M.; Micurova, A.; Cebova, M.; Şaman, E.; Cacanyiova, S.; Bernatova, I. MLN-4760 induces oxidative stress without blood pressure and behavioural alterations in SHRs: Roles of Nfe2l2 gene, nitric oxide and hydrogen sulfide. *Antioxidants* **2022**, *11* (12), 2385.

(119) Nami, B.; Ghanaeian, A.; Ghanaeian, K.; Houri, R.; Nami, N.; Ghasemi-Dizgah, A.; Caluseriu, O. The interaction of the severe acute respiratory syndrome coronavirus 2 spike protein with drug-inhibited angiotensin converting enzyme 2 studied by molecular dynamics simulation. *J. Hypertens.* **2021**, *39* (8), 1705–1716.

(120) Al Adem, K.; Shanti, A.; Stefanini, C.; Lee, S. Inhibition of SARS-CoV-2 entry into host cells using small molecules. *Pharmaceuticals* **2020**, *13* (12), 447.

(121) Ahmad, I.; Pawara, R.; Surana, S.; Patel, H. The repurposed ACE2 inhibitors: SARS-CoV-2 entry blockers of Covid-19. *Top. Curr. Chem.* **2021**, *379*, 1–49.

(122) Teralı, K.; Baddal, B.; Gülcan, H. O. Prioritizing potential ACE2 inhibitors in the COVID-19 pandemic: Insights from a molecular mechanics-assisted structure-based virtual screening experiment. *J. Mol. Graph. Model.* **2020**, *100*, 107697.

(123) Badraoui, R.; Adnan, M.; Bardakci, F.; Alreshidi, M. M. Chloroquine and hydroxychloroquine interact differently with ACE2 domains reported to bind with the coronavirus spike protein: mediation by ACE2 polymorphism. *Molecules* **2021**, *26* (3), 673.

(124) Mores, A.; Matziari, M.; Beau, F.; Cuniasse, P.; Yiotakis, A.; Dive, V. Development of potent and selective phosphinic peptide inhibitors of angiotensin-converting enzyme 2. *J. Med. Chem.* **2008**, *51* (7), 2216–2226.

(125) Takahashi, S.; Yoshiya, T.; Yoshizawa-Kumagaye, K.; Sugiyama, T. Nicotianamine is a novel angiotensin-converting enzyme 2 inhibitor in soybean. *Biomed. Res.* **2015**, *36* (3), 219–224.

(126) Huentelman, M. J.; Zubcevic, J.; Hernández Prada, J. A.; Xiao, X.; Dimitrov, D. S.; Raizada, M. K.; Ostrov, D. A. Structure-based discovery of a novel angiotensin-converting enzyme 2 inhibitor. *Hypertension* **2004**, *44* (6), 903–906.

(127) Jia, H.; Neptune, E.; Cui, H. Targeting ACE2 for COVID-19 therapy: opportunities and challenges. *Am. J. Respir. Cell Mol. Biol.* **2021**, *64* (4), 416–425.

(128) Townsend, D. W. *Positron Emission Tomography*; SPIE, 1985.

(129) Rong, J.; Haider, A.; Jeppesen, T. E.; Josephson, L.; Liang, S. H. Radiochemistry for positron emission tomography. *Nat. Commun.* **2023**, *14* (1), 3257.

(130) Phelps, M. E. PET: the merging of biology and imaging into molecular imaging. *J. Nucl. Med.* **2000**, *41* (4), 661–681.

(131) Phelps, M. E. Positron emission tomography provides molecular imaging of biological processes. *Proc. Natl. Acad. Sci. U.S.A.* **2000**, *97* (16), 9226–9233.

(132) Phelps, M. E. Molecular imaging and its biological applications. *Eur. J. Nucl. Med. Mol. Imag.* **2004**, *31*, 1544.

(133) Ametamey, S. M.; Honer, M.; Schubiger, P. A. Molecular Imaging with PET. *Chem. Rev.* **2008**, *108* (5), 1501–1516. DOI: 10.1021/cr0782426.

(134) Gambhir, S. S. Molecular imaging of cancer with positron emission tomography. *Nat. Rev. Cancer* **2002**, *2* (9), 683–693.

(135) Ido, T.; Wan, C. N.; Casella, V.; Fowler, J.; Wolf, A.; Reivich, M.; Kuhl, D. Labeled 2-deoxy-D-glucose analogs. 18F-labeled 2-deoxy-2-fluoro-D-glucose, 2-deoxy-2-fluoro-D-mannose and 14C-2-deoxy-2-fluoro-D-glucose. *J. Labelled Compd. Radiopharm.* **1978**, *14* (2), 175–183.

(136) Belcari, N.; Bisogni, M.; Del Guerra, A. Positron emission tomography: its 65 years and beyond. *Riv. Nuovo Cimento* **2023**, *46* (11), 693–785.

(137) Cherry, S. R.; Sorenson, J. A.; Phelps, M. E. *Physics in Nuclear Medicine*; Elsevier Saunders, 2012.

(138) Fowler, J. S.; Ido, T. Initial and subsequent approach for the synthesis of 18FDG. *Semin. Nucl. Med.* **2002**, *32* (1), 6–12.

(139) Luurtsema, G.; Pichler, V.; Bongarzone, S.; Seimbille, Y.; Elsinga, P.; Gee, A.; Vercouillie, J. EANM guideline for harmonisation on molar activity or specific activity

of radiopharmaceuticals: impact on safety and imaging quality. *EJNMMI Radiopharm. Chem.* **2021**, *6*, 1–16.

(140) Rokka, J.; Grönroos, T. J.; Viljanen, T.; Solin, O.; Haaparanta-Solin, M. HPLC and TLC methods for analysis of [18F] FDG and its metabolites from biological samples. *J. Chromatogr. B* **2017**, *1048*, 140–149.

(141) Coenen, H. H.; Gee, A. D.; Adam, M.; Antoni, G.; Cutler, C. S.; Fujibayashi, Y.; Jeong, J. M.; Mach, R. H.; Mindt, T. L.; Pike, V. W. Consensus nomenclature rules for radiopharmaceutical chemistry—Setting the record straight. *Nucl. Med. Biol.* **2017**, *55*, v–xi.

(142) Coenen, H. H.; Gee, A. D.; Adam, M.; Antoni, G.; Cutler, C. S.; Fujibayashi, Y.; Jeong, J. M.; Mach, R. H.; Mindt, T. L.; Pike, V. W. Status of the 'consensus nomenclature rules in radiopharmaceutical sciences' initiative. *Nucl. Med. Biol.* **2019**, *71*, 19.

(143) Miller, P. W.; Long, N. J.; Vilar, R.; Gee, A. D. Synthesis of 11C, 18F, 15O, and 13N radiolabels for positron emission tomography. *Angew. Chem. Int. Ed.* **2008**, *47* (47), 8998–9033.

(144) Yoon, J.-K.; Park, B.-N.; Ryu, E.-K.; An, Y.-S.; Lee, S.-J. Current perspectives on 89Zr-PET imaging. *Int. J. Mol. Sci.* **2020**, *21* (12), 4309.

(145) Levin, C. S.; Hoffman, E. J. Calculation of positron range and its effect on the fundamental limit of positron emission tomography system spatial resolution. *Phys. Med. Biol.* **1999**, *44* (3), 781.

(146) Le Bars, D. Fluorine-18 and medical imaging: Radiopharmaceuticals for positron emission tomography. *J. Fluor. Chem.* **2006**, *127* (11), 1488–1493.

(147) Purser, S.; Moore, P. R.; Swallow, S.; Gouverneur, V. Fluorine in medicinal chemistry. *Chem. Soc. Rev.* **2008**, *37* (2), 320–330.

(148) Meanwell, N. A. Fluorine and fluorinated motifs in the design and application of bioisosteres for drug design. *J. Med. Chem.* **2018**, *61* (14), 5822–5880.

(149) Gillis, E. P.; Eastman, K. J.; Hill, M. D.; Donnelly, D. J.; Meanwell, N. A. Applications of fluorine in medicinal chemistry. *J. Med. Chem.* **2015**, *58* (21), 8315–8359.

(150) Amano, M.; Yedidi, R. S.; Salcedo-Gómez, P. M.; Hayashi, H.; Hasegawa, K.; Martyr, C. D.; Ghosh, A. K.; Mitsuya, H. Fluorine modifications contribute to potent antiviral activity against highly drug-resistant HIV-1 and favorable blood-brain barrier penetration property of novel central nervous system-targeting HIV-1 protease inhibitors in vitro. *Antimicrob. Agents Chemother.* **2022**, *66* (2), e01715–01721.

Chapter 2: Design, Synthesis, and Evaluation of Fluorinated MLN-4760 Analogues

2.1 Introduction

As introduced in Chapter 1, ACE2 is a critical target for both therapeutic and diagnostic applications, particularly in the context of SARS-CoV-2 infection. The small-molecule ACE2 inhibitor MLN-4760 ((*S*,*S*)-2-(1-carboxy-2-(3-(3,5-dichlorobenzyl)-3*H*-imidazol-4-yl)-ethylamino)-4-methylpentanoic acid) has demonstrated high potency (IC_{50} = 0.44 nM) and selectivity over other enzymes like ACE and CPDA.[1] Despite its favourable biochemical profile, the original synthesis of MLN-4760 presents challenges for radiotracer development, due to inflexibility with respect to analogue generation and the synthetic inefficiencies associated with early-stage functionalisation. To overcome these limitations, this chapter details the development of a divergent and more versatile synthetic route for fluorinated MLN-4760 analogues, which can be extended to radiolabelling applications, and is depicted in Figure 2.1. The development started with in silico prioritisation of candidate structures using molecular modelling and binding affinity predictions, followed by the synthesis of four MLN-4760 analogues using an optimised route. These compounds were subsequently subjected to in vitro evaluation to assess ACE2 inhibitory potency. Together, these efforts support the rational design of ACE2 inhibitors suitable for development as fluorine-18-labelled PET radioligands.

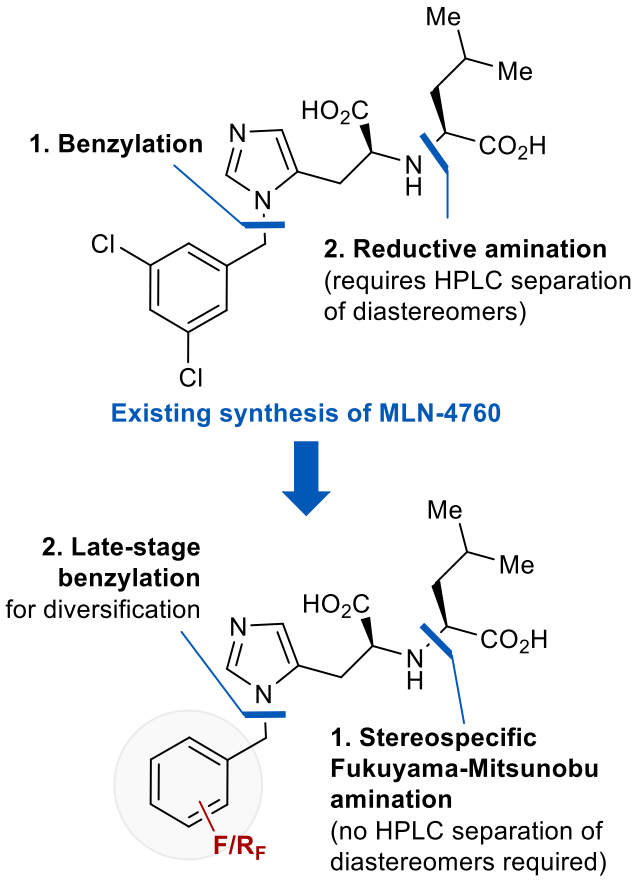

Figure 2.1: Synthetic development of fluorinated MLN-4760 analogues.

Section 2.2 outlines the in silico studies conducted to identify four fluorinated analogues of MLN-4760, as illustrated in Figure 2.2, with favourable ACE2 binding affinity, and the aim of developing potent candidates for PET radiotracer applications. This computational work was carried out by Dr. Morgan Thomas and Dr. Layla Hosseini-Gerami of the Bender Group, University of Cambridge.

Section 2.3 begins with the synthesis of fluorinated MLN-4760 analogues following the literature-reported route.[1] However, limitations associated with this approach,

particularly low yields and poor diastereoselectivity, prompted the development of an improved synthetic strategy. The optimised route addresses key challenges in the preparation of these analogues, incorporating a late-stage benzylation strategy to streamline analogue generation. This new approach enables efficient synthesis to a range of fluorinated MLN-4760 derivatives.

Section 2.4 presents the in vitro evaluation of four fluorinated MLN-4760 analogues using an ACE2 inhibition assay, providing initial evidence for their potential as ACE2-targeted PET radiotracers. The study was conducted by Jieyu He from the Aigbirhio Group at the University of Cambridge.

The work described in this chapter forms the basis of a paper published in the *Journal of Organic Chemistry*: Wang, X.; He, J.; Hosseini-Gerami, L.; Thomas, M.; Thompson, S.; Ford, J.; Gouverneur, V. *Synthesis and Inhibitory Assessment of ACE2 Inhibitors for SARS-CoV-2: An In Silico and In Vitro Study*. *J. Org. Chem*. **2025**, *90* (30), 10941–10947. https://doi.org/10.1021/acs.joc.5c00918.[2]

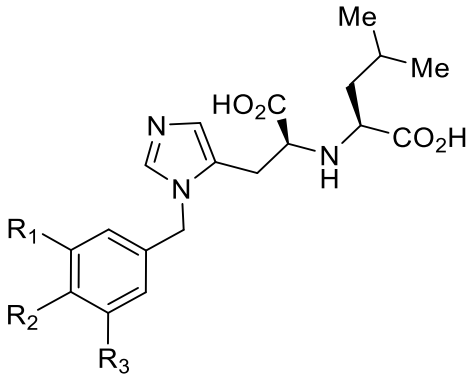

	R_1	R_2	R_3
MLN-4760	Cl	H	Cl
(*S*,*S*)-**2.1**	H	F	H
(*S*,*S*)-**2.2**	Me	H	F
(*S*,*S*)-**2.3**	Cl	H	F
(*S*,*S*)-**2.4**	OMe	H	OC_2H_4F

Figure 2.2: Structure of proposed fluorinated MLN-4760 analogues.

2.2 In Silico Design of MLN-4760 Analogues

To investigate MLN-4760 analogues as ACE2-targeted PET radiotracers through in silico design, we developed a structure-guided computational workflow. This integrated strategy combined molecular docking, molecular dynamics simulations, and relative binding free energy (RBFE) calculations to predict binding affinities and prioritise candidates for synthesis and subsequent in vitro evaluation. In contrast to traditional *de novo* small molecule discovery, the workflow enabled rapid screening of fluorinated MLN-4760 analogues, while strategically guiding the selection of radiolabelling sites to minimise interference with ACE2 binding.

2.2.1 Docking Validation and Analogue Selection

The X-ray crystal structure of ACE2 in complex with MLN-4760 (PDB ID: 1R4L) was employed as the structural template for molecular docking studies, providing a structurally resolved framework to guide ligand–receptor modelling.[3] The structure was refined to optimise hydrogen bonding networks and ensure overall structural integrity, enhancing its suitability for in silico modelling as shown in Figure 2.3. Ligand docking was performed using Glide, a molecular docking module developed by Schrödinger, Inc. that predicts binding poses and estimates ligand–receptor interaction strength. Glide uses an empirical scoring function composed of multiple energetic terms, including hydrogen bonding, electrostatic interactions, hydrophobic interactions, and protein-ligand van der Waals energy contributions, to rank ligand conformations. To validate the docking protocol, MLN-4760 was re-docked into the

ACE2 active site, yielding a pose consistent with its crystallographic conformation. Further validation involved retrospective docking of known MLN-4760 analogues, for which reported ACE2 inhibition data (pIC_{50}) are available as detailed in Table 2.1.[1] Among the docking score components, the van der Waals interaction energy ($Glide_{Evdw}$) served as a key predictive component. This metric reflects the contribution of van der Waals forces between the ligand and the binding pocket, which are particularly important in the hydrophobic S1' subsite of ACE2 as depicted in Figure 2.3. A simple linear regression model was fit between experimental pIC_{50} and $Glide_{Evdw}$ scores as shown in Equation 1 with β = -2.12 and α = -14.77. This model enabled estimation of binding affinities for the majority of the calculated experimental pIC_{50} values falling within 1 log unit of their reported values from the literature.[1] Based on the top-ranked docking poses obtained for each structure, a focused library of 31 fluorinated MLN-4760 analogues was rationally designed for further computational evaluation.

$$pIC_{50} = \beta \times Glide_{evdw} + \alpha \quad (1)$$

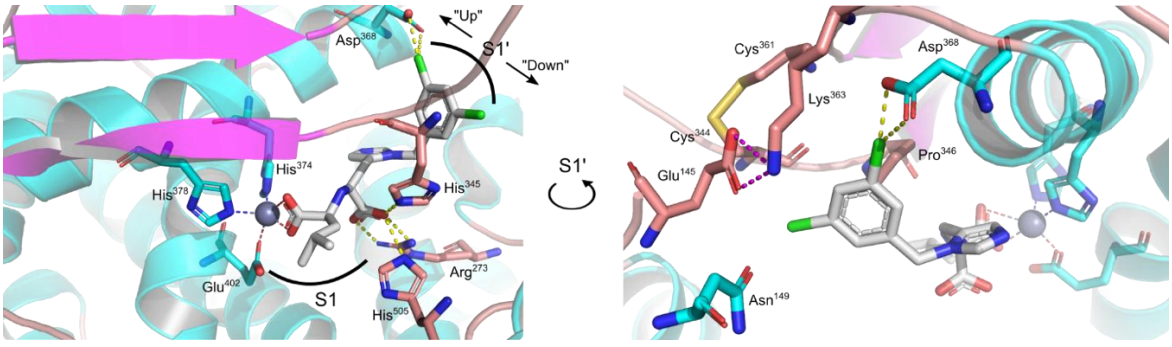

Figure 2.3: X-ray crystal structure of ACE2 in complex with inhibitor MLN-4760 (PDB ID: 1R4L), highlighting sub-pockets S1 and S1' relevant for analogue design. Left: view through the S1 subsite at zinc coordination of MLN-4760. Right: view through the S1' subsite and nearby residues, notably Asp368 interacting with the 3,5-dichlorobenzyl moiety.

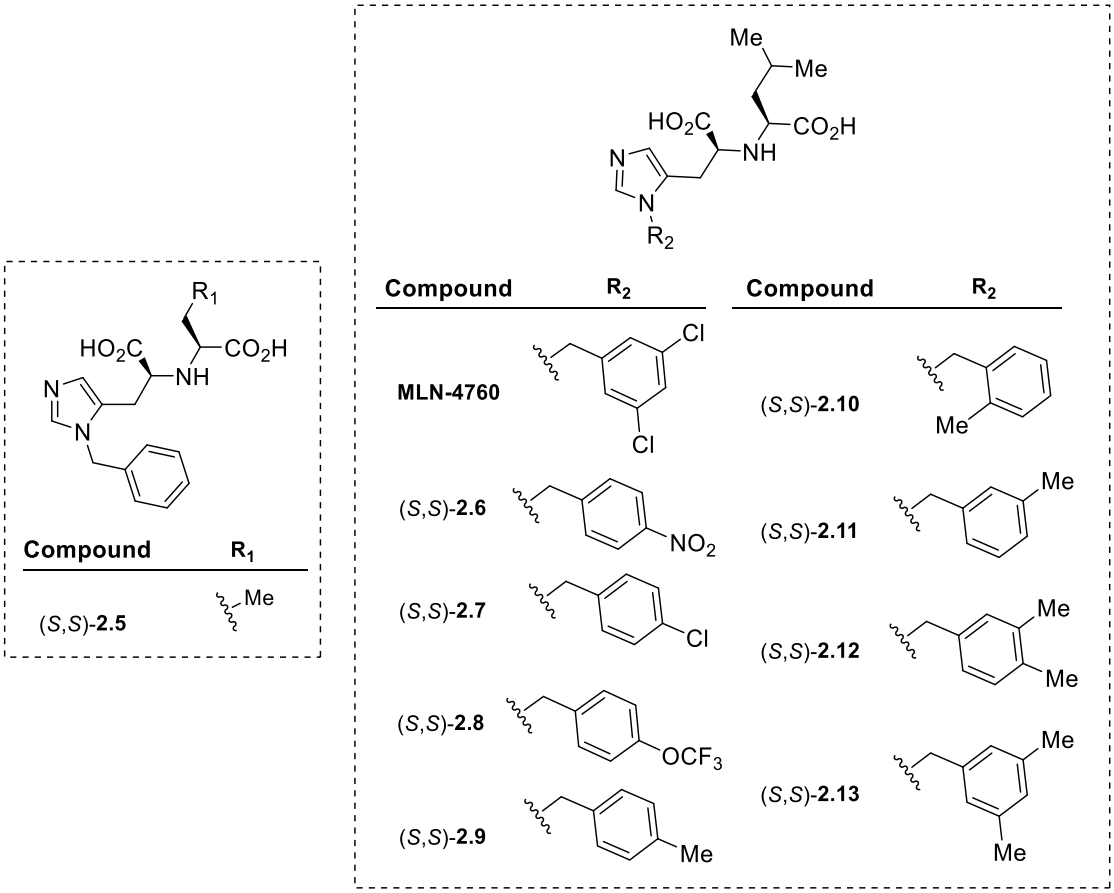

Compound	Reported pIC_{50}	Experimental pIC_{50}	Error
MLN-4760	9.36	8.19	1.17
(*S*,*S*)-**2.5**	6.52	7.40	0.87
(*S*,*S*)-**2.6**	7.12	7.46	0.34
(*S*,*S*)-**2.7**	7.68	7.92	0.24
(*S*,*S*)-**2.8**	7.28	6.84	0.44
(*S*,*S*)-**2.9**	7.49	8.00	0.51
(*S*,*S*)-**2.10**	7.54	7.48	0.06
(*S*,*S*)-**2.11**	8.38	7.94	0.44
(*S*,*S*)-**2.12**	8.00	8.73	0.73
(*S*,*S*)-**2.13**	8.85	8.26	0.59

Table 2.1: Retrospectively modelled MLN-4760 analogues with reported pIC_{50} values[1] and estimated pIC_{50} values measured by the linear regression model of $Glide_{Evdw}$ energy.

2.2.2 Molecular Dynamics and RBFE Analysis

To improve the reliability of the docking predictions and assess the dynamic stability of the ligand–ACE2 complexes, molecular dynamics (MD) simulations were carried out. All MD simulations were performed using GROMACS 2020.2 with standard force-field parameterisation for protein and ligand topology files.[4] It was first validated using the X-ray crystal structure of MLN-4760 bound to ACE2 (PDB ID: 1R4L) as a benchmark. Throughout the simulations, the ligand maintained stable binding within the ACE2 active site, with conserved hydrogen bonding networks and metal coordination to the catalytic Zn^{2+} centre across the S1 and S1′ subsites. The consistency of ligand poses across MD trajectories provided strong support for refinement of analogue selection.

Following validation, a subset of 14 analogues was shortlisted for relative binding free energy (RBFE) calculations to obtain a more accurate thermodynamic evaluation of binding affinity which is detailed in Table 2.2. Alchemical free energy perturbation methods were applied using the ProtoCaller RBFE protocol.[5] The same receptor model, force fields, and simulation parameters were used as in the benchmark to ensure consistency across all calculations. These RBFE simulations accounted for solvent effects, conformational flexibility, and entropic contributions that are not captured by static docking models. The Gibbs free energy differences (ΔΔG) obtained from the RBFE simulations were first corrected using the previously established linear regression model, yielding adjusted ΔΔG* values. These

corrected values were then used in Equation 2 to estimate the predicted pIC_{50} of each analogue relative to the reference compound MLN-4760 or its known analogue. The resulting predicted pIC_{50} values for the 14 selected MLN-4760 analogues are summarised in Table 2.2.

$$\Delta\Delta G = \Delta G_{bound} - \Delta G_{unbound}$$

$$\Delta\Delta G^{*} = \beta \times \Delta\Delta G + \alpha \qquad (2)$$

$$pIC_{50} \cong pIC_{50\,ref} - \Delta\Delta G^{*}$$

All 14 fluorinated analogues demonstrated predicted pIC_{50} values between 6.81 and 9.58, indicative of sufficient binding affinity to ACE2 to justify further evaluation. From this series, four fluorinated MLN-4760 analogues, (*S*,*S*)-**2.1**–(*S*,*S*)-**2.4** shown in Figure 2.4, were prioritised for synthesis based on a combined factors of predicted inhibitory potency, chemical accessibility, and structural diversity. Among these, the 4-fluorobenzyl analogue (*S*,*S*)-**2.1** was selected as a model compound for initial synthetic validation due to its relatively simple structure and ease of derivatisation.

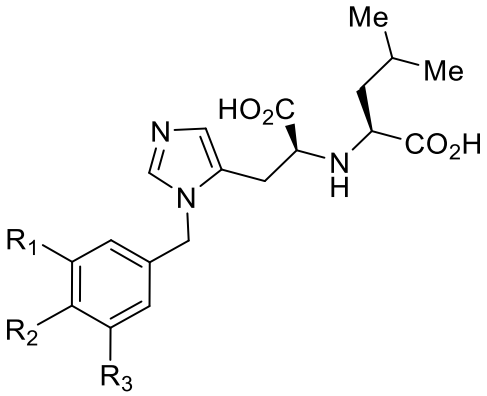

	R_1	R_2	R_3	Predicted IC_{50}
MLN-4760	Cl	H	Cl	6.53 nM
(*S*,*S*)-**2.1**	H	F	H	73.1 nM
(*S*,*S*)-**2.2**	Me	H	F	11.5 nM
(*S*,*S*)-**2.3**	Cl	H	F	10.3 nM
(*S*,*S*)-**2.4**	OMe	H	OC_2H_4F	1.32 nM

Figure 2.4: Structural analogues of MLN-4760 ((*S*,*S*)-**2.1**–(*S*,*S*)-**2.4**) selected for synthesis and their predicted IC_{50} values.

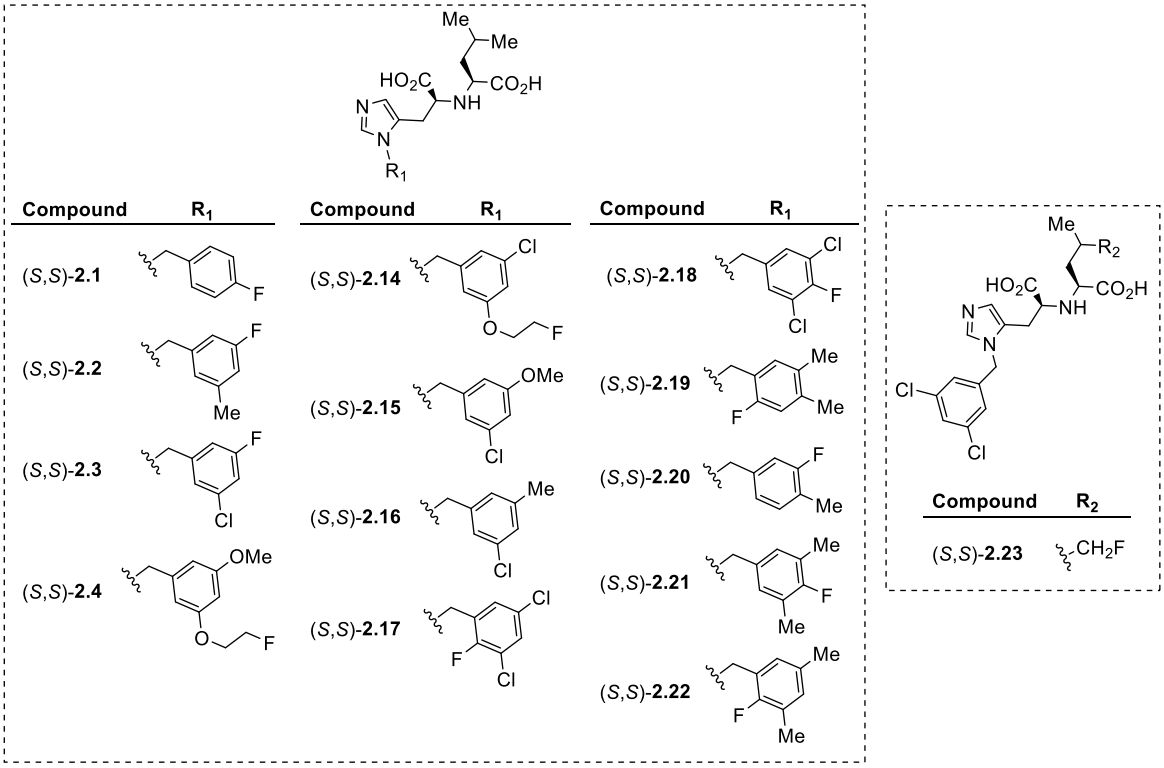

Compound	Predicted ΔΔG	Predicted pIC_{50}
(*S*,*S*)-**2.1**	0.364 (± 0.03)	7.56 (± 1.34)
(*S*,*S*)-**2.2**	1.958 (± 0.04)	8.45 (± 1.41)
(*S*,*S*)-**2.3**	1.497 (± 0.03)	8.68 (± 1.39)
(*S*,*S*)-**2.4**	-0.566 (± 0.04)	9.58 (± 1.36)
(*S*,*S*)-**2.14**	-0.550 (± 0.06)	9.58 (± 1.35)
(*S*,*S*)-**2.15**	1.203 (± 0.04)	8.71 (± 1.38)
(*S*,*S*)-**2.16**	1.285 (± 0.02)	8.78 (± 1.38)
(*S*,*S*)-**2.17**	2.387 (± 0.02)	8.83 (± 1.37)
(*S*,*S*)-**2.18**	0.268 (± 0.02)	9.28 (± 1.33)
(*S*,*S*)-**2.19**	1.484 (± 0.04)	6.81 (± 1.39)
(*S*,*S*)-**2.20**	0.001 (± 0.02)	7.54 (± 1.32)
(*S*,*S*)-**2.21**	-0.393 (± 0.02)	9.10 (± 1.30)
(*S*,*S*)-**2.22**	1.698 (± 0.02)	8.49 (± 1.36)
(*S*,*S*)-**2.23**	0.631 (± 0.02)	9.10 (± 1.35)

Table 2.2: Predicted relative binding free energies ($\Delta\Delta G$) and pIC_{50} values for radiotracer candidates determined by RBFE simulations.

2.3 Synthesis of Fluorinated MLN-4760 Analogues

2.3.1 Validation of the Existing Synthetic Route with Analogue (*S,S*)-2.1

The synthetic route to MLN-4760 illustrated in Scheme 2.1, was developed by Millennium Pharmaceuticals in 2002, and was first adapted to synthesise compound (*S,S*)-**2.1**, selected based on in silico predictions.[1] The synthesis consisted of four main steps: (a) di-*tert*-butoxycarbonyl (di-Boc) group protection, (b) selective imidazole N3-benzylation, (c) reductive amination and (d) basic ester hydrolysis followed by purification to afford compound (*S,S*)-**2.1**.

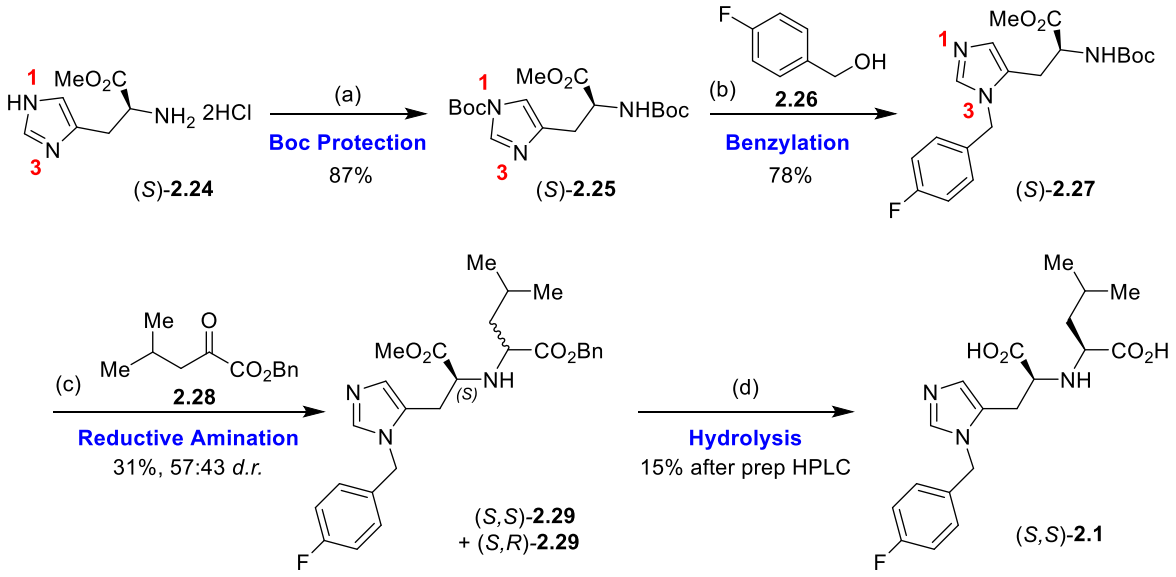

Scheme 2.1: Synthesis of the model MLN-4760 analogue (*S,S*)-**2.1**. Reagents and conditions: (a) (*S*)-**2.24** (1.0 equiv.), Boc_2O (2.0 equiv.), Et_3N (2.0 equiv.), MeOH, rt, 16 h, 87%; (b) $(CF_3SO_2)_2O$ (1.0 equiv.), DIPEA (1.2 equiv.), **2.26** (1.0 equiv.), CH_2Cl_2, -78 °C, 20 min, then (*S*)-**2.25** (1.1 equiv.), CH_2Cl_2, rt, 24 h, 78%; (c) (*S*)-**2.27** (1.0 equiv.), HCl (4 M in dioxane, excess), 2 h, rt, triturated, then Et_3N (2.0 equiv.), CH_2Cl_2, rt, 1 h, then **2.28** (1.5 equiv.), AcOH (1.0 equiv.), 4Å MS, rt, 2 h, then $NaB(OAc)_3H$ (3.0 equiv.), CH_2Cl_2, 24 h, 31%, 57:43 *d.r.*; (d) NaOH (1.0 M, 3.0 equiv.), MeOH, rt, 1 h, work up with HCl (1.0 M), rt, 30 min, 35%, 57:43 *d.r.*, after preparative HPLC, 15%.

Step (a) involved the regioselective protection of commercially available (*S*)-histidine methyl ester (*S*)-**2.24** with two equivalents of di-*tert*-butyl dicarbonate (Boc_2O), yielding the di-Boc-protected intermediate (*S*)-**2.25** in 87% yield. Regioselectivity for N1 protection over N3 is attributed to the lower steric hindrance at the N1 position.[6, 7] This selective protection was essential for directing the subsequent benzylation step to the desired N3 position. Without Boc protection, alkylation predominantly occurs at N1, yielding an isomer with reduced ACE2 inhibition. Structure–activity relationship studies of MLN-4760 analogues confirmed that the N3-benzylated imidazole exhibits potent ACE2 inhibition (IC_{50} = 0.024 μM), whereas the N1-benzylated analogue is over 400-fold less active (IC_{50} = 10 μM).[1]

In step (b), selective N3-benzylation was achieved by *in situ* generation of 4-fluorobenzyl triflate from 4-fluorobenzyl alcohol (**2.26**) using trifluoromethanesulfonic anhydride. The resulting triflate was directly reacted with (*S*)-**2.25** to yield the N3-benzylated intermediate (*S*)-**2.27** in 78% yield. Two regioisomers were formed and separated by silica gel chromatography. Structural assignment was performed using two-dimensional (2D) ^{1}H-^{15}N heteronuclear multiple bond correlation (HMBC) NMR spectroscopy. This technique is useful for elucidating nitrogen-containing molecular structures by detecting two- or three-bond ^{1}H-^{15}N couplings, confirming site-selective functionalisation.[8] The major isomer was unambiguously identified as N3-benzylated, and the minor as N1-benzylated as illustrated in Figures 2.5 and 2.6. Reducing the reaction time for benzyl triflate generation from 30 minutes to 20 minutes improved the yield of the desired N3-benzylated product from 55% to 78%. This is likely due

to the partial decomposition of benzyl triflate upon prolonged reaction times. The resulting trifluoromethanesulfonic acid can cleave the Boc protecting group on N1 and result in the formation of undesired N1-benzylation products.

In the spectrum of the N3-benzylated compound (*S*)-**2.27** presented in Figure 2.5, three discrete nitrogen resonances were observed at ^{15}N chemical shift of 87, 174, and 245 ppm. The signal at 87 ppm was assigned to the Boc-protected amide nitrogen N8, based on its exclusive correlation with the methylene protons H_d and H_d', located three bonds away, and the absence of long-range couplings to the imidazole ring protons H_e and H_f. The nitrogen signal at 245 ppm was assigned to N1. It showed correlations with H_e and H_f, consistent with its position on the imidazole ring. The absence of long-range coupling to H_d and H_d' is also in agreement with its electronic environment and spatial separation from methylene protons. The remaining resonance at 174 ppm was attributed to N3. This assignment was supported by multiple long-range correlations to H_d and H_d' and the imidazole ring protons H_e and H_f, indicating its position within the aromatic system. The differential correlation pattern with the H_d and H_d' protons thus provide a clear basis for distinguishing N1 from N3. Critically, N3 also exhibited correlation with the benzylic methylene protons H_g, confirming the attachment of the benzyl group at the N3 position. Collectively, these correlations confirmed the assignment of the spectrum to the N3-benzylated regioisomer of (*S*)-**2.27**.

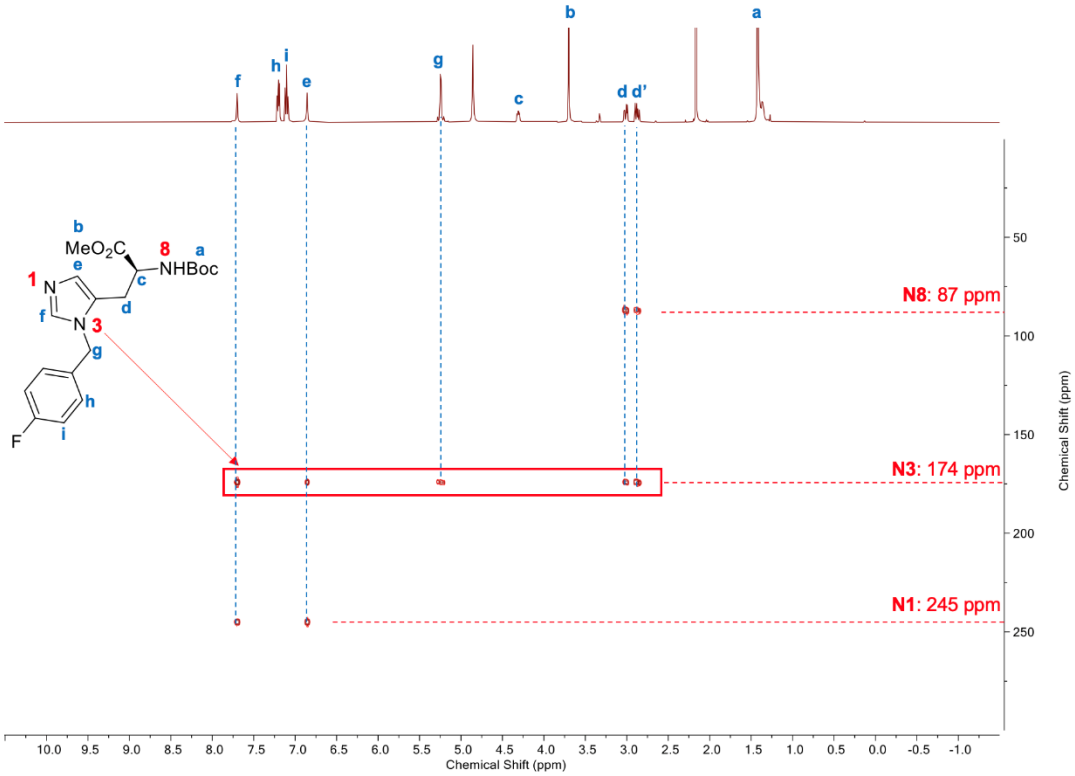

Figure 2.5: 2D ^{1}H-^{15}N HMBC NMR spectrum of N3-benzylated product (*S*)-**2.27**.

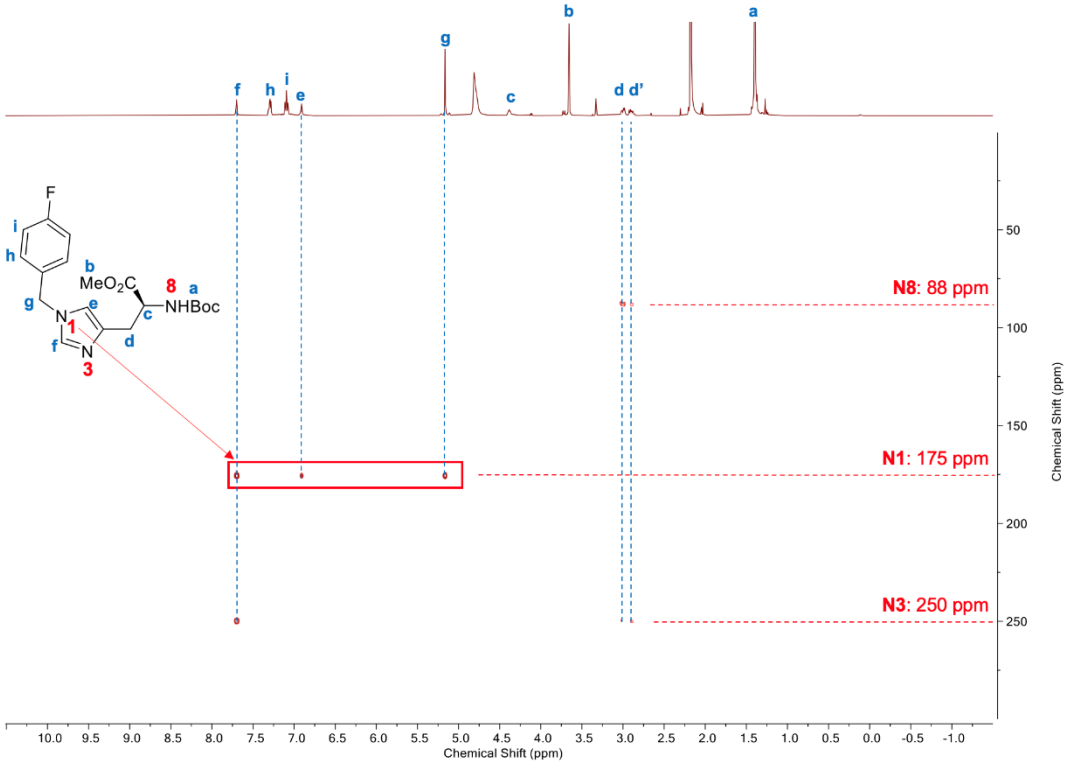

Figure 2.6: 2D ^{1}H-^{15}N HMBC NMR spectrum of N1-benzylated regioisomer of (*S*)-**2.27**.

The 2D ^{1}H-^{15}N HMBC NMR spectrum of the N1-benzylated regioisomer of (*S*)-**2.27** displayed a different correlation pattern, as illustrated in Figure 2.6. Nitrogen resonances were assigned following the same rationale as for the N3-benzylated isomer. In this spectrum, the benzylic methylene proton H_g displayed a clear long-range coupling with the N1 nitrogen, alongside correlations between N1 and the imidazole protons H_e and H_f. In this case, N3 showed no detectable correlation with H_g, indicating that benzylation had occurred at the N1 position.

Following isolation of the N3-benzylated intermediate (*S*)-**2.27**, Boc deprotection was carried out using HCl in dioxane. Without isolating the deprotected amine intermediate, the crude product was directly subjected to reductive amination with benzyl 4-methyl-2-oxopentanoate (**2.28**) to afford the histidine–leucine dipeptide derivative **2.29**. This reductive amination step proved particularly challenging. While the original synthesis of MLN-4760 reported a yield of 65% with a 67:33 diastereomeric ratio (*d.r.*), attempts to reproduce these conditions yielded **2.29** in only 10% with 55:45 *d.r.* (Table 2.3, Entry 1).

To address this limitation, the reductive amination protocol was optimised. Reaction parameters including solvent, reducing agent, and additives were varied in order to improve yield and selectivity. The most productive conditions employed triethylamine (Et_3N) as a base, sodium triacetoxyborohydride ($NaB(OAc)_3H$) as the reducing agent, and dichloromethane (CH_2Cl_2) as the solvent. The addition of acetic acid and 4 Å molecular sieves further enhanced the outcome, improving the yield of **2.29** to 31%

with a 57:43 *d.r.* in Table 2.3, Entry 7. The *d.r.* was determined by ^{1}H NMR spectroscopy through integration of distinct methyl proton singlet signals corresponding to each diastereomer as illustrated in Figure 2.7. At this stage, the stereochemistry of each diastereomer could not be assigned based on the available characterisation data. As a result, the product was quantified as a combined mixture of (*S*,*S*)-**2.29** and (*S*,*R*)-**2.29**.

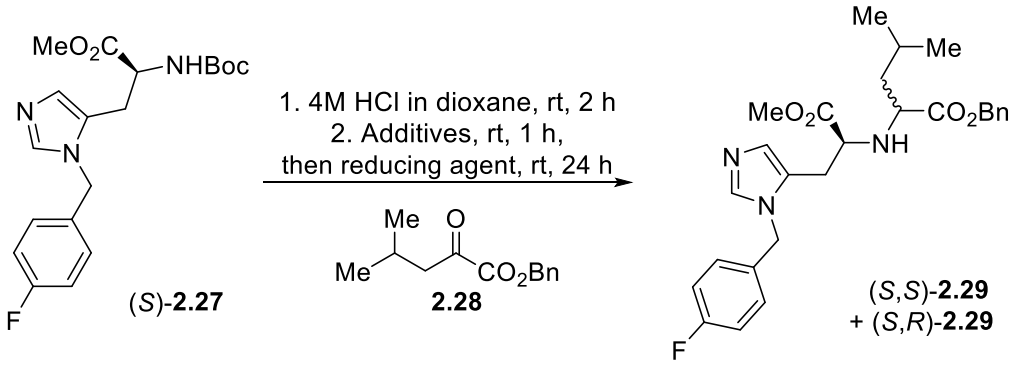

Entry	Solvent	Reducing Agent	Additives	(*S*,*S*)-2.29 + (*S*,*R*)-2.29 Yield[a]	*d.r.*[b]
1[c]	DCE	$NaB(OAc)_3H$	none	10%	55:45
2	DCE	$NaBH_4$	none	n.d.	N/A
3	DCE	$NaBH_3CN$	none	n.d.	N/A
4	THF	$NaB(OAc)_3H$	none	6%	56:44
5	CH_2Cl_2	$NaB(OAc)_3H$	none	12%	55:45
6	CH_2Cl_2	$NaB(OAc)_3H$	AcOH + 4Å MS	15%	51:49
7	CH_2Cl_2	$NaB(OAc)_3H$	Et_3N[d], then AcOH + 4Å MS	31%	57:43

Table 2.3: Reaction optimisation of the reductive amination step. [a]Isolated, combined yields of two non-separable diastereomers. [b]Diastereomeric ratio (*d.r.*) determined by ^{1}H NMR of the mixture. [c]Literature conditions.[1] [d]2.0 equiv. were used. n.d. = not determined. Reagents: (*S*)-**2.27** (1.0 equiv.), **2.28** (1.5 equiv.), HCl (4 M in dioxane, excess), solvent (0.1 M), reducing agent (3.0 equiv.), additives (1.0 equiv.). DCE = dichloroethane, THF = tetrahydrofuran, $NaB(OAc)_3H$ = sodium triacetoxyborohydride, $NaBH_4$ = sodium borohydride, $NaBH_3CN$ = sodium borocyanohydride, Et_3N = triethylamine.

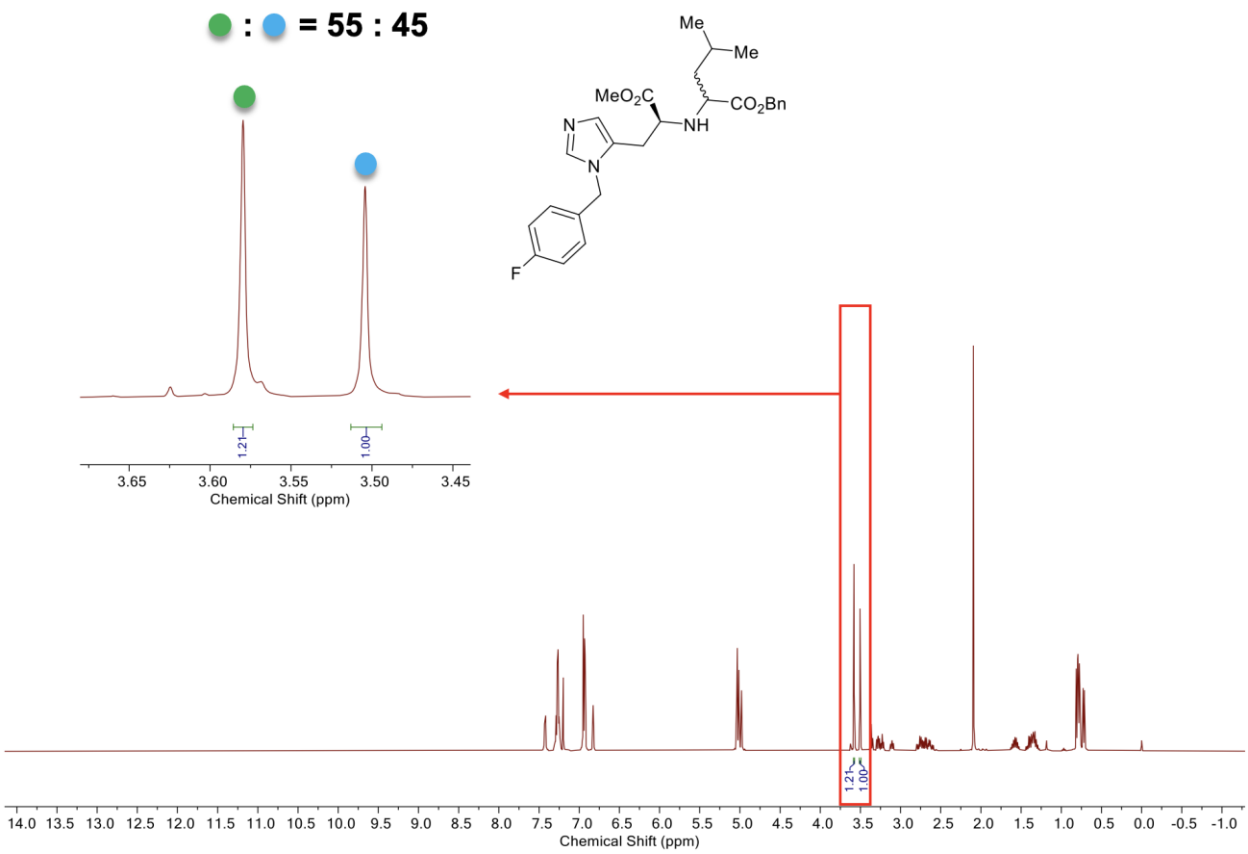

Figure 2.7: Determination of the diastereomeric ratio by ^{1}H NMR using the methyl proton singlet peak ratio of the two diastereomers in the mixture.

The yield of the reductive amination step remained suboptimal and the separation of the diastereomers proved particularly challenging. The diastereomers (*S*,*S*)-**2.29** and (*S*,*R*)-**2.29** co-eluted upon silica gel chromatography under several eluent systems and could also not be separated by thin-layer chromatography. The final step (d) involved ester hydrolysis using sodium hydroxide, followed by isolation and purification of the (*S*,*S*)-diastereomer (*S,S*)-**2.1** via preparative high-performance liquid chromatography (HPLC). This process was labour-intensive and time-consuming, requiring extensive optimisation of chromatographic conditions, including the use of acid additives, to achieve acceptable peak shape and resolution.

Despite these efforts, the isolated yield of (*S,S*)-**2.1** of this step was low (15%), limiting the efficiency of the approach.

Although the reported synthesis of MLN-4760 was successfully reproduced with the analogue (*S,S*)-**2.1**, the strategy proved suboptimal for radiotracer development. This route positions the benzylation step, which installs the benzyl group identified by in silico modelling as the most suitable site for radiolabelling, early in the synthesis (Figure 2.4). For the evaluation of analogues that are radiolabelled at different positions, this approach therefore requires several multi-step syntheses of their separate precursors and non-radioactive reference standards, an approach that would be complex and time-consuming.[9, 10] Additionally, as the reductive amination step lacked stereoselectivity, this necessitates separation of diastereomers by preparative HPLC. Together, these challenges motivated the development of a more efficient synthetic route to support ACE2-targeted PET radiotracer discovery.

2.3.2 Development of an Optimised Synthetic Strategy for MLN-4760 Analogues

2.3.2.1 Retrosynthetic Strategy

A retrosynthetic strategy for fluorinated MLN-4760 analogues was developed, focusing on two key C–N bond disconnections: regioselective N3-benzylation of the imidazole ring and stereoselective formation of the central C–N bond connecting leucine- and histidine-derived fragments as depicted in Scheme 2.2. The N3-

benzylation could be achieved using a Boc-protection followed by benzylation sequence, as validated in the synthesis of (*S,S*)-**2.1**. For the stereoselective C–N bond formation, the Fukuyama–Mitsunobu amination was selected as an alternative to the original reductive amination step, due to its high stereospecificity. This revised approach introduced stereochemical control and maintained regioselectivity, enabling the synthesis of analogues from readily available chiral building blocks, including (*S*)-histidine methyl ester (*S*)-**2.24**, (*R*)-*α*-hydroxy ester (*R*)-**2.30**, and various commercial fluorinated alcohols.

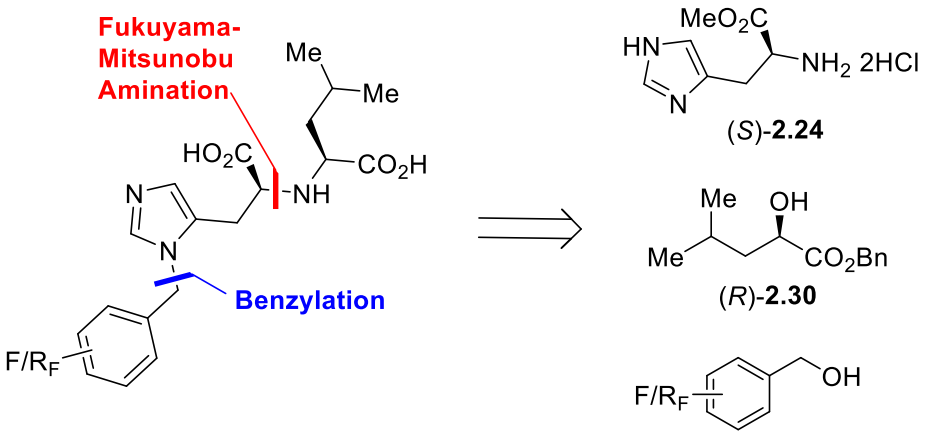

Scheme 2.2: Retrosynthesis of fluorinated MLN-4760 analogues highlighting key disconnections.

2.3.2.2 Fukuyama-Mistunobu Amination

The Fukuyama–Mitsunobu amination is a variant of the Mitsunobu reaction adapted for nitrogen nucleophiles through the use of a sulfonamide protecting group to enhance both reactivity and selectivity. In the Mitsunobu reaction, an alcohol **2.31** is converted to a more reactive intermediate **2.33** via *in situ* activation with triphenylphosphine (PPh_3) and diethyl azodicarboxylate (DEAD) or diisopropyl

azodicarboxylate (DIAD). This enables nucleophilic substitution by a pronucleophile **2.32** under mild conditions, proceeding with inversion of configuration under an S_N2 mechanism, to afford the product **2.34** as illustrated in Scheme 2.3.[11]

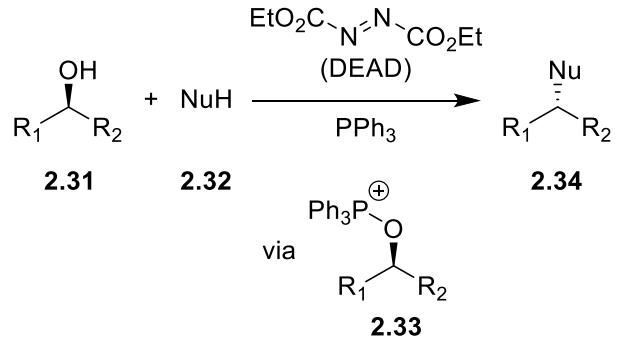

Scheme 2.3: The Mitsunobu reaction.

In 1995, Fukuyama and co-workers expanded the scope of the Mitsunobu reaction by introducing a protecting group strategy, which enabled the efficient synthesis of secondary amines via Mitsunobu coupling of protected primary amines as shown in Scheme 2.4.[12, 13] In this approach, a primary amine **2.35** is first protected with 2-nitrobenzenesulfonyl chloride (NsCl) to afford the Ns-protected amine **2.36**, enhancing the acidity of the N–H proton. Upon activation with PPh_3 and DEAD, a betaine intermediate is formed that deprotonates **2.36**, generating a nucleophilic sulfonamide anion. This anion undergoes efficient S_N2-type displacement of the activated alcohol **2.37**, affording the alkylated sulfonamide intermediate **2.38** with inversion of stereochemistry. While the 2-nitrobenzenesulfonyl (Ns) group is most commonly employed, alternative sulfonylating agents such as 4-nitrobenzenesulfonyl chloride (*p*-NsCl) and 2,4-dinitrobenzenesulfonyl chloride (DNsCl) are also compatible with the Fukuyama–Mitsunobu reaction.[12-14] Following

substitution, the Ns group is selectively removed under mild conditions using thiolates, affording the desired secondary amine product **2.39**.

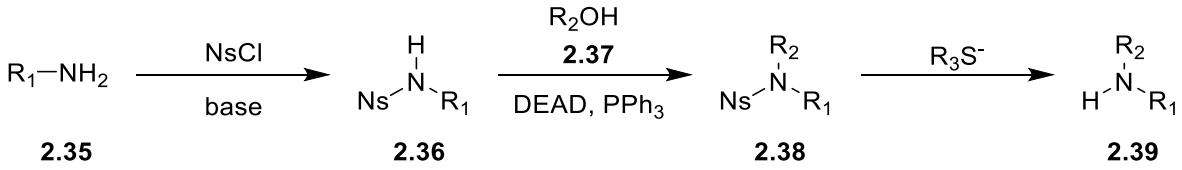

Scheme 2.4: The Fukuyama-Mitsunobu reaction.

The Fukuyama–Mitsunobu amination is widely applied in pharmaceutical synthesis and polymer chemistry as represented in Scheme 2.5.[15] A notable example is its use in the synthesis of oseltamivir **2.43**, an antiviral agent used in the treatment of influenza and marketed as Tamiflu, where Raghavan and Babu employed it for stereospecific *N*-alkylation to efficiently construct the Tamiflu scaffold **2.42** with high stereochemical control.[16] Furthermore, the reaction is applied in macromolecular synthesis. Broussy and colleagues utilised the Fukuyama–Mitsunobu amination to construct 13-membered macrocyclic peptides **2.47** using solid-phase techniques.[17] Its high yields, mild conditions, and good stereochemical control make the Fukuyama–Mitsunobu amination a versatile reaction.

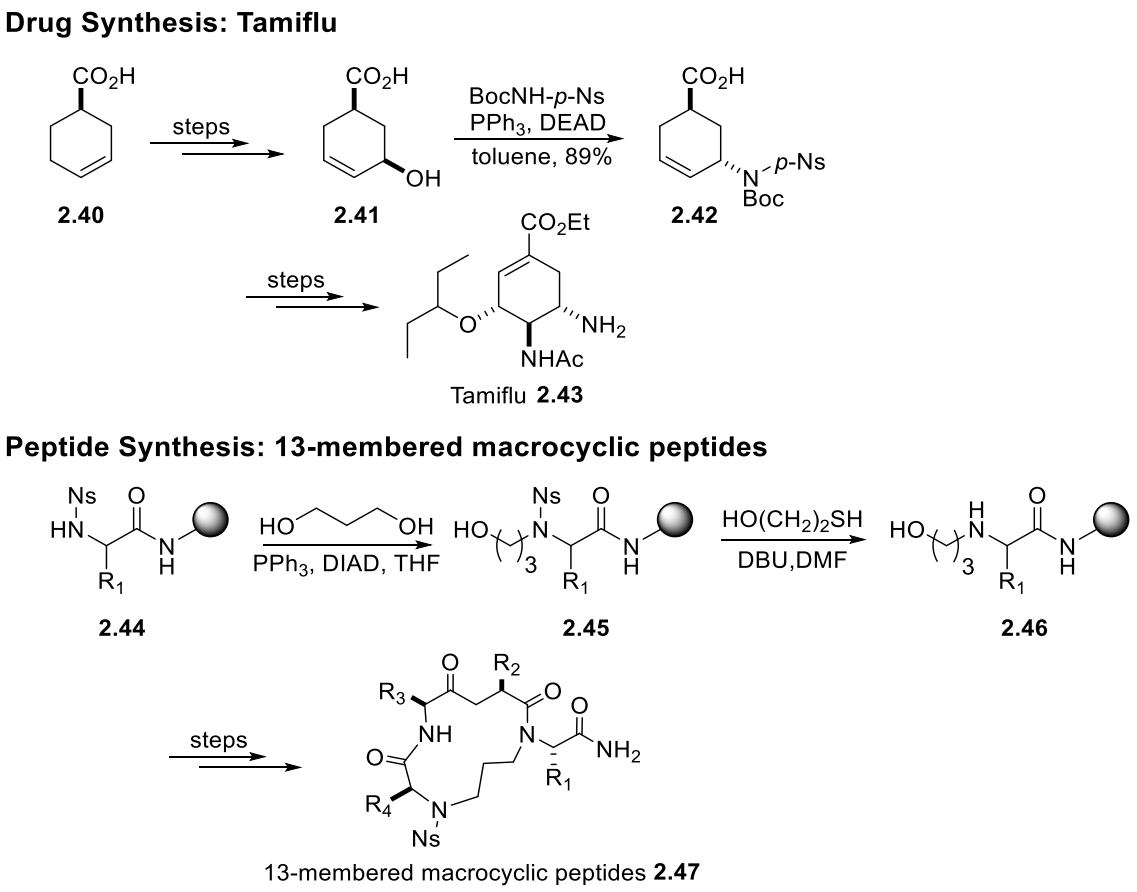

Scheme 2.5: Selected applications of the Fukuyama-Mitsunobu amination.

2.3.2.3 Synthesis of MLN-4760 Analogues via Fukuyama–Mitsunobu Amination

The compatibility of the Fukuyama–Mitsunobu amination with MLN-4760 analogues was evaluated using three protected histidine derivatives as presented in Scheme 2.6. Initial attempts focused on intermediates from our previous synthetic route, including the di-Boc-protected histidine derivative (*S*)-**2.25** and the Boc-protected N3-benzylated histidine derivative (*S*)-**2.27**. Under standard Fukuyama–Mitsunobu conditions, neither substrate afforded the desired product, as indicated by analysing

the NMR spectra of the crude reaction mixtures. In both cases, the starting materials were largely recovered. In contrast, product formation was observed when the Ns-protected histidine derivative (*S*)-**2.50** was employed. The benzylated Ns-protected histidine-leucine derivative product (*S*)-**2.51** was synthesised in 31% yield. This outcome supports literature reports that highlight the enhanced reactivity of Ns-protected amines due to increased N–H acidity, facilitating the formation of more nucleophilic anionic species and undergo nucleophilic substitution under Mitsunobu-type conditions.[12-14]

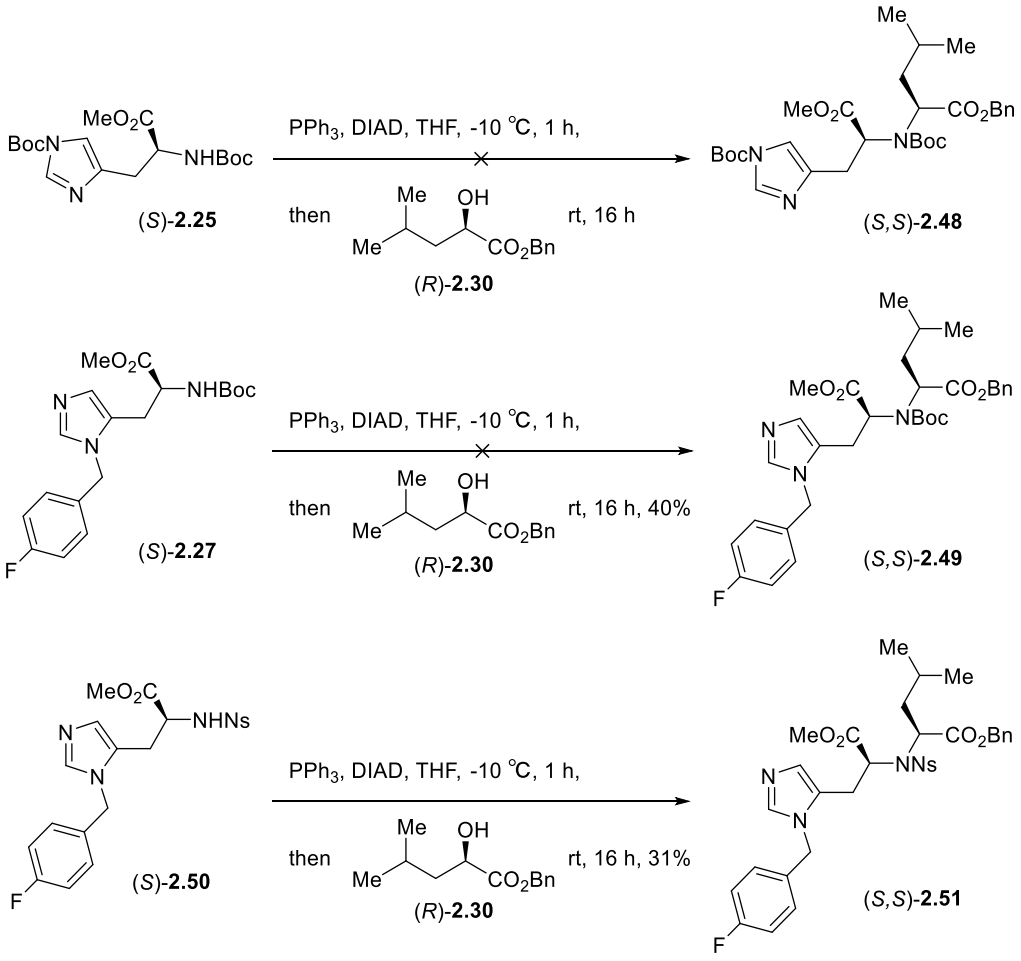

Scheme 2.6: Preliminary evaluation of the Fukuyama–Mitsunobu amination. Ns = 2-nitrobenzenesulfonyl, DIAD = diisopropyl azodicarboxylate.

Based on these findings, we revised the synthetic route to incorporate the Ns group as a key activating element, enabling successful Fukuyama–Mitsunobu amination. Scheme 2.7 details the synthesis of the (*S,S*)-**2.1** and (*S,R*)-**2.1** diastereomers of the 4-fluorobenzyl MLN-4760 analogue applying this route.

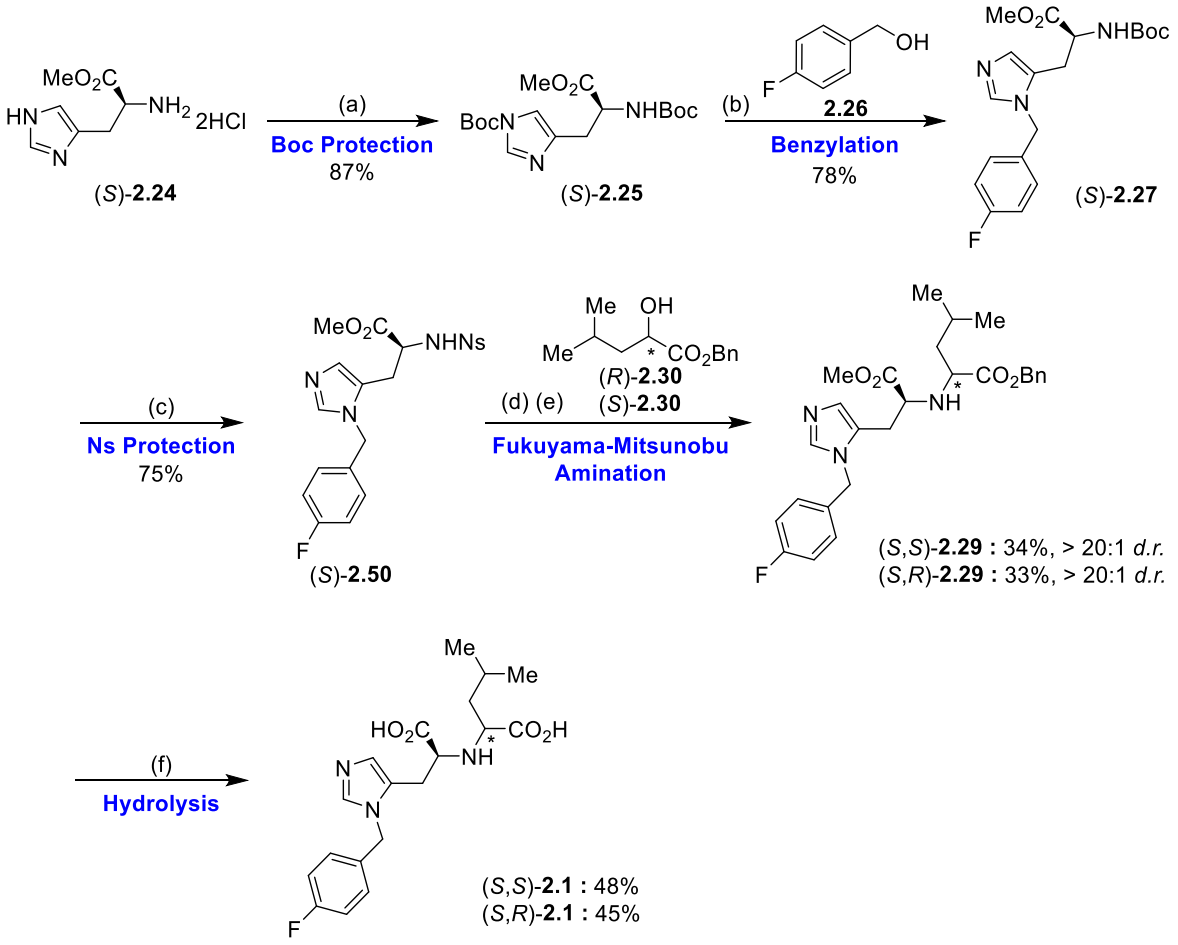

Scheme 2.7: Synthesis of (*S,S*)-**2.1** and (*S,R*)-**2.1** via Fukuyama–Mitsunobu amination**.** Reagents and conditions: (a) Boc_2O (2.0 equiv.), Et_3N (2.0 equiv.), MeOH, rt, 16 h, 87%; (b) $(CF_3SO_2)_2O$ (1.0 equiv.), DIPEA (1.2 equiv.), **2.26** (1.0 equiv.), CH_2Cl_2, -78 ℃, 20 min, then (*S*)-**2.25** (1.1 equiv.), CH_2Cl_2, rt, 24 h, 78%; (c) HCl (4.0 M in dioxane, 5.0 equiv.), 2 h, rt; then Et_3N (3.0 equiv.), CH_2Cl_2, rt, 1 h; then NsCl (1.5 equiv.), CH_2Cl_2, rt, 18 h, 75%; (d) PPh_3 (1.0 equiv.), DIAD (1.0 equiv.), THF, -10 ℃, 1 h, then (*R*)-**2.30**/(*S*)-**2.30** (1.0 equiv.), THF, rt, 2 h, then (*S*)-**2.50** (1.5 equiv.), THF, rt, 16 h, isolated as crude, then (e) PhSH (1.5 equiv.), K_2CO_3 (1.5 equiv.), DMF, rt, 1 h, (*S,S*)-**2.29** (34%, > 20:1 *d.r.*), (*S,R*)-**2.29** (33%, > 20:1 *d.r.*); (f) NaOH (1.0 M, 3.0 equiv.), MeOH/H_2O, rt, 1 h, work up with HCl (1.0 M), rt, 30 min, then preparative HPLC purification, (*S,S*)-**2.1** (48%) (*S,R*)-**2.1** (45%).

The revised route retained step (a) Boc protection of the histidine core and step (b) N3-selective benzylation of the imidazole ring from the original synthesis (Scheme 2.1). A key divergence was introduced at step (c), where the Boc group was replaced with the 2-nitrobenzenesulfonyl (Ns) group. Following Boc deprotection with HCl in dioxane, the crude amine was directly treated with triethylamine and NsCl in dichloromethane, affording the Ns-protected histidine derivative (*S*)-**2.50** in 75% yield.

Fukuyama–Mitsunobu amination was performed in step (d), where the Ns-protected histidine derivative (*S*)-**2.50** was reacted with the enantiomeric benzyl 2-hydroxy-4-methylpentanoates, (*R*)-**2.30** and (*S*)-**2.30**, respectively, to evaluate the stereoselectivity of this transformation. This step was optimised by varying the azo reagent, stoichiometry, and timing of reagent addition (Table 2.4). DIAD proved superior to DEAD, yielding higher conversions as determined by the ^{1}H NMR analysis of crude reaction mixtures (Table 2.4, Entry 3). Increasing the number of equivalents of (*S*)-**2.50** from 1.0 to 1.5 equiv. resulted in a noticeable improvement in conversion (Table 2.4, Entry 5 and 6). Optimal conditions were established by initially combining PPh_3 and DIAD in THF at −10 °C, followed by sequential addition of 1.5 equivalents of (*S*)-**2.50** and 1.0 equivalent of (*R*)-**2.30** to the reaction mixture after stirring for 1 hour and 2 hours at room temperature, respectively. This protocol afforded (*S,S*)-**2.51** in 51% yield with a diastereomeric ratio >20:1, as determined by ^{1}H NMR (Table 2.4, Entry 6). This optimisation significantly enhanced the reproducibility and overall efficiency of this synthetic route.

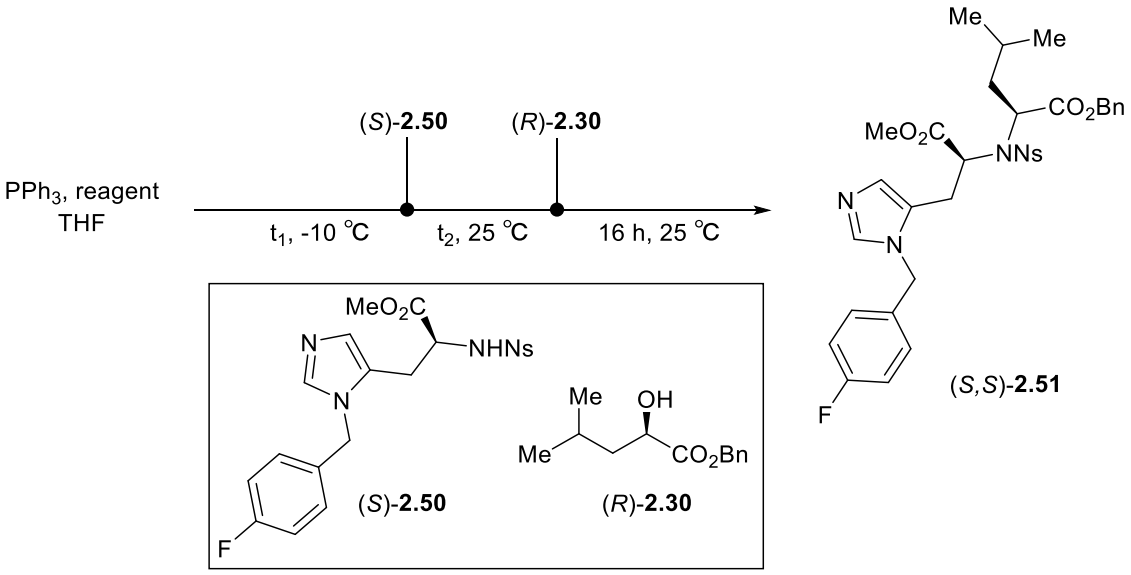

Entry	Reagent	(*S*)-2.50 loading	t_1/ h	t_2/ h	Yield of (*S,S*)-2.51[a]
1	DEAD	1.0 equiv.	0	0	traces
2	DEAD	1.0 equiv.	0	2	8%
3	DIAD	1.0 equiv.	0	2	21%
4	DIAD	1.0 equiv.	1	2	35%
5	DIAD	1.5 equiv.	0	2	41%
6	DIAD	1.5 equiv.	1	2	51%

Table 2.4: Optimisation of the Fukuyama-Mitsunobu amination. PPh_3 = 1.0 equiv., DIAD/ DEAD = 1.0 equiv., (*R*)-**2.30** = 1.0 equiv. [a]Yields determined by quantitative ^{19}F NMR spectroscopy with 4-fluoroanisole as internal standard.

Following the Fukuyama–Mitsunobu amination, the intermediate (*S,S*)-**2.51** was directly subjected to thiophenol-mediated removal of the Ns group using thiophenol (PhSH), affording the histidine–leucine derivatives (*S,S*)-**2.29** and (*S,R*)-**2.29** in 34% and 33% yield and *d.r.* >20:1, respectively. In the final step (f), hydrolysis of the ester groups with aqueous NaOH yielded the MLN-4760 analogues (*S,S*)-**2.1** and (*S,R*)-**2.1** in 48% and 45% yield, respectively.

To confirm the structures of the fluorinated MLN-4760 analogues (*S,S*)-**2.1** and (*S,R*)-**2.1**, we performed a comparative structural analysis. Single-crystal X-ray diffraction unambiguously established the configuration of (*S,R*)-**2.1**. The two diastereomers were then distinguished by ^{1}H, ^{19}F and ^{13}C NMR spectroscopy and analytical HPLC, with clear differences in chemical shifts, coupling patterns, and retention times confirming their identities.

X-ray Crystallography Analysis

Single-crystal X-ray diffraction (SCXRD) enables determination of spatial atomic positions within a crystal lattice by analysing diffraction patterns produced when X-rays interact with the crystal. Crystallisation trials for both diastereomers were performed using slow solvent evaporation and vapour diffusion across various systems, including ethyl acetate/hexanes, methanol/water, acetone/diethyl ether.

While (*S,R*)-**2.1** yielded crystals suitable for SCXRD, repeated attempts with (*S,S*)-**2.1** under varied conditions consistently produced amorphous or microcrystalline material unsuitable for analysis. Diastereomers, while sharing the same connectivity, differ in three-dimensional spatial arrangement, which can significantly influence crystal lattice formation.[18, 19] This disparity likely reflects distinct molecular packing behaviours whereas (*S,R*)-**2.1** adopts a conformation conducive to regular packing and intermolecular interactions, (*S,S*)-**2.1** may favour disordered arrangements that hinder nucleation. SCXRD of (*S,R*)-**2.1** unambiguously confirmed its configuration in

Figure 2.8. The stereochemistry of (*S,S*)-**2.1** was subsequently assigned by comparison with spectroscopic data.

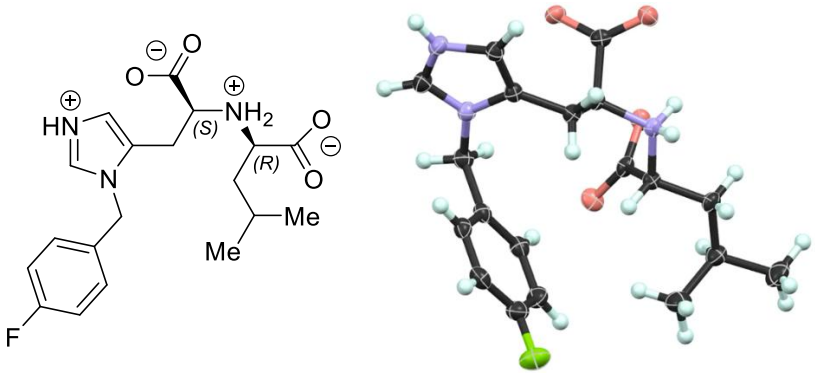

Figure 2.8: Single-crystal X-ray structure of (*S,R*)-**2.1**, confirming its stereochemistry. The structure is depicted in ball-and-stick form, with nitrogen in purple, oxygen in red, fluorine in green, carbon in black, and hydrogen in light blue.

NMR Spectroscopy Analysis

The ^{1}H NMR spectra of (*S,R*)-**2.1** and (*S,S*)-**2.1** showed clear differences in the chemical shifts and splitting patterns of key resonances, particularly in regions associated with protons near the stereocentres. An enlarged section of the spectrum from 0.5 to 1.8 ppm revealed distinct variations in the overlapping peaks corresponding to aliphatic protons, as shown in Figure 2.9. These included methyl and methylene protons on the isopropyl and adjacent alkyl chains. Further differences were observed in the region between 3.0 and 3.6 ppm, where CH and CH_2 protons adjacent to heteroatoms such as nitrogen and the imidazole ring showed distinguishable chemical shifts in Figure 2.10. These observations suggest differing local electronic environments between (*S,R*)-**2.1** and (*S,S*)-**2.1**, consistent with their unique three-dimensional arrangements of the two diastereomers.

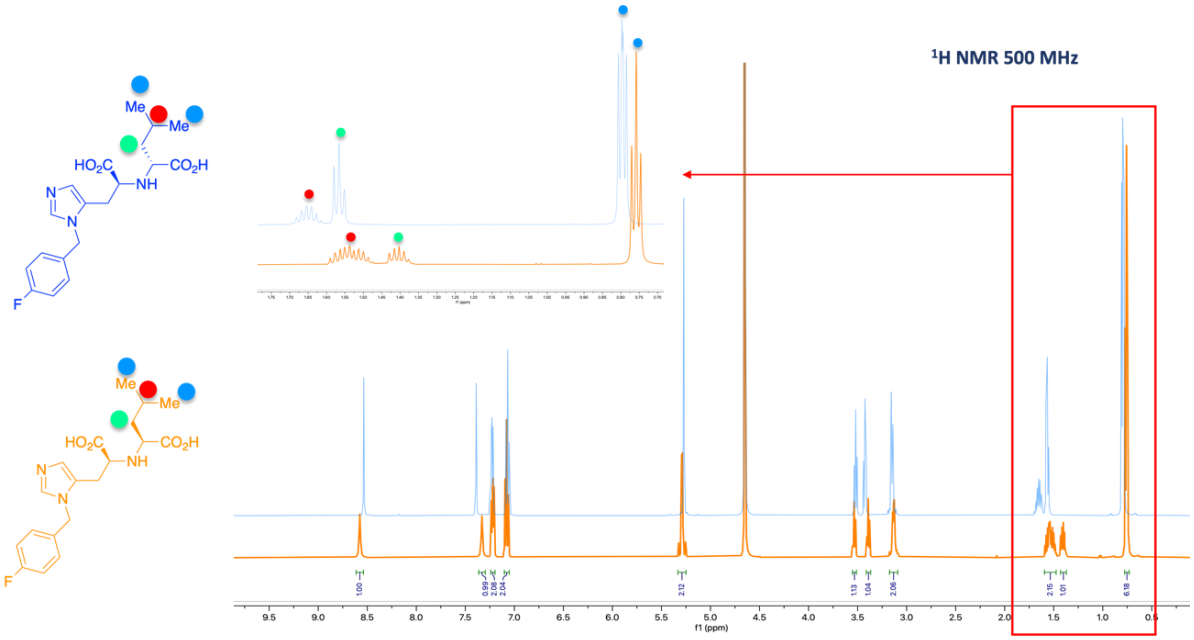

Figure 2.9: Overlapped ^{1}H NMR spectra of (*S,R*)-**2.1** (blue) and (*S,S*)-**2.1** (orange), expanded in the region of 0.5 to 1.8 ppm.

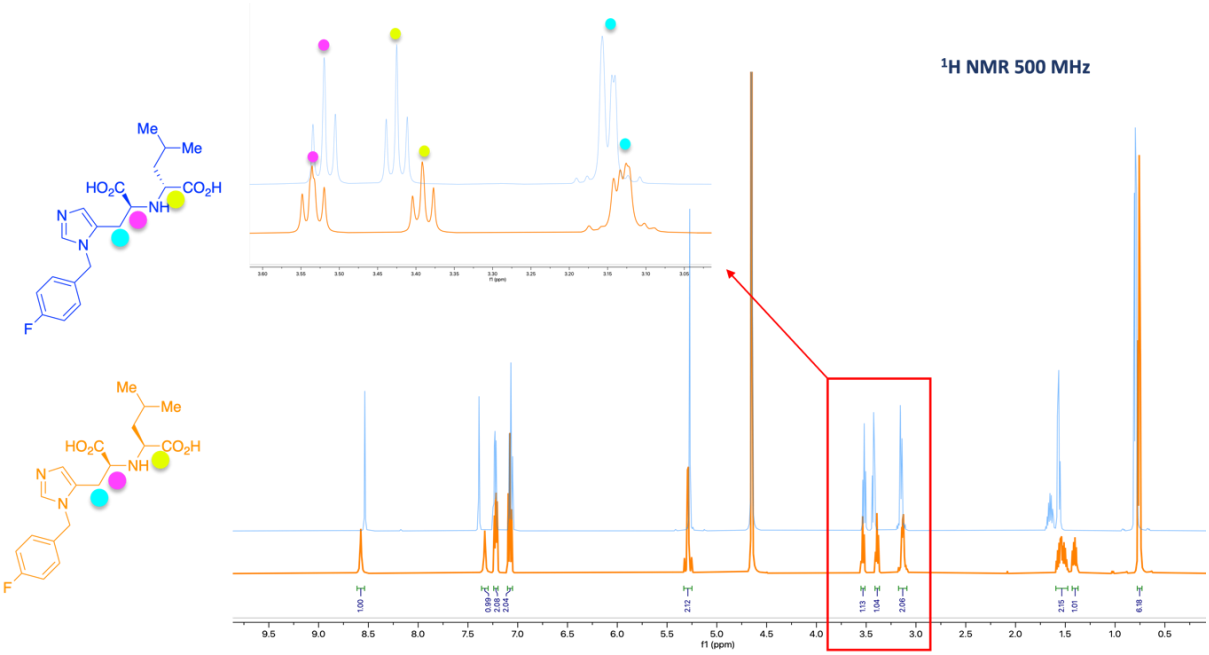

Figure 2.10: Overlapped ^{1}H NMR spectra of (*S,R*)-**2.1** (blue) and (*S,S*)-**2.1** (orange), expanded in the region of 3.0 to 3.6 ppm.

^{19}F NMR provided additional evidence of diastereomeric differentiation in Figure 2.11. The fluorine resonance of the *para*-fluorobenzyl group appeared at -113.06 ppm for (*S,R*)-**2.1** and -112.94 ppm for (*S,S*)-**2.1**, indicating distinct chemical environments and different stereochemistry.

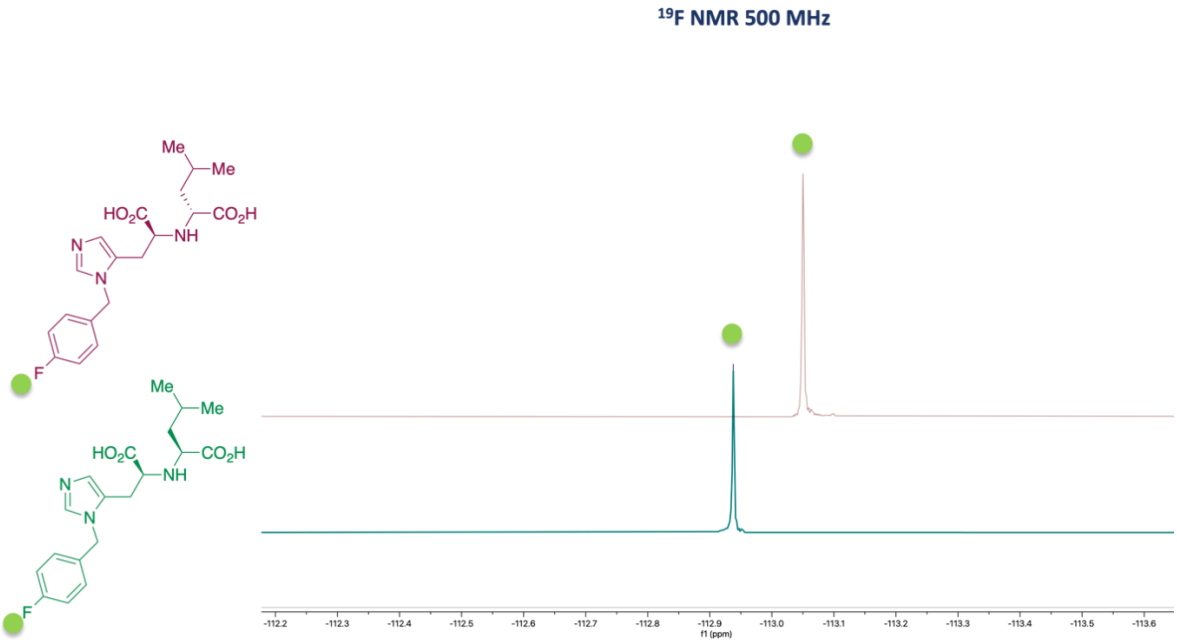

Figure 2.11: Overlapped ^{19}F NMR spectra of (*S,R*)-**2.1** (maroon) and (*S,S*)-**2.1** (green).

The ^{13}C NMR spectra showed distinct chemical shifts, especially of the resonances for carbon atoms near the stereocentres, further confirming the non-equivalent conformations of (*S,R*)-**2.1** and (*S,S*)-**2.1** in Figure 2.12.

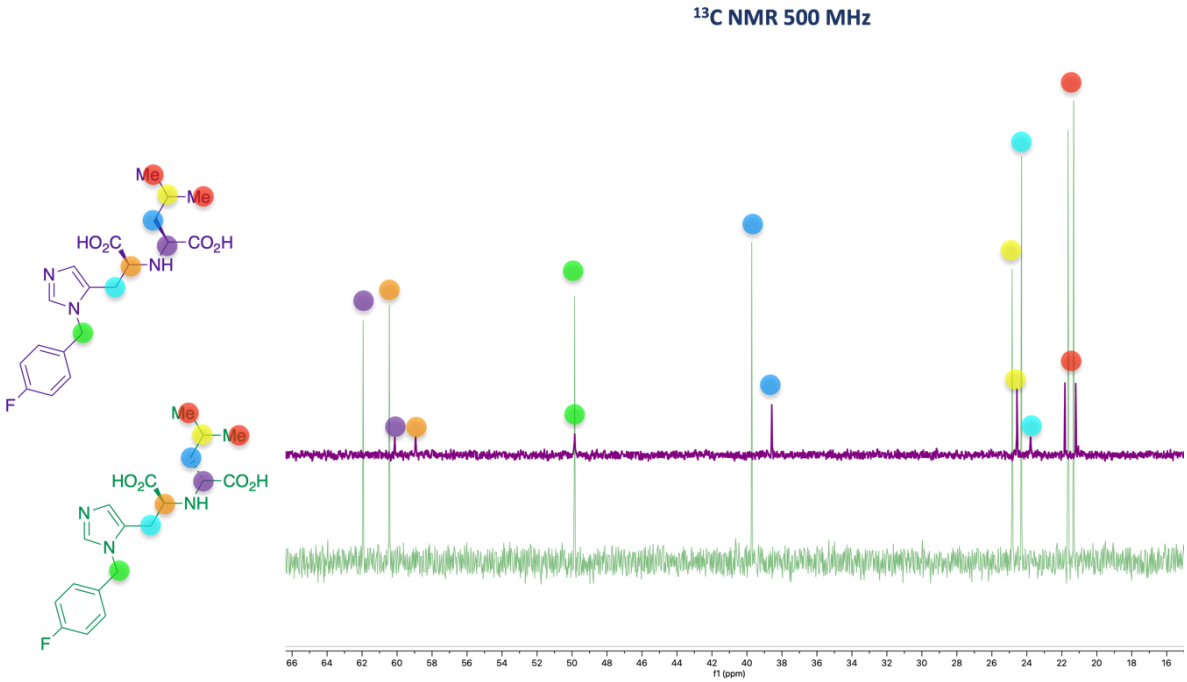

Figure 2.12: Overlapped ^{13}C NMR spectra of (*S,R*)-**2.1** (green) and (*S,S*)-**2.1** (purple).

HPLC Analysis

Reverse-phase HPLC analysis under identical conditions (10% acetonitrile in water with 0.1% trifluoroacetic acid) clearly resolved the diastereomers with different retention times (t_R), where (*S,S*)-**2.1** eluted at t_R = 11.6 min and (*S,R*)-**2.1** eluted at t_R = 13.9 min as shown in Figure 2.13. These distinct retention times reflect their differences in polarity, shape, and interaction with the stationary phase, consistent with diastereomeric compounds. Alongside single-crystal X-ray analysis of (*S,R*)-**2.1** and comparative ^{1}H, ^{19}F, and ^{13}C NMR data, these findings confirm the identity of both diastereomers and validate the enhanced stereochemical control achieved through the revised synthetic strategy.

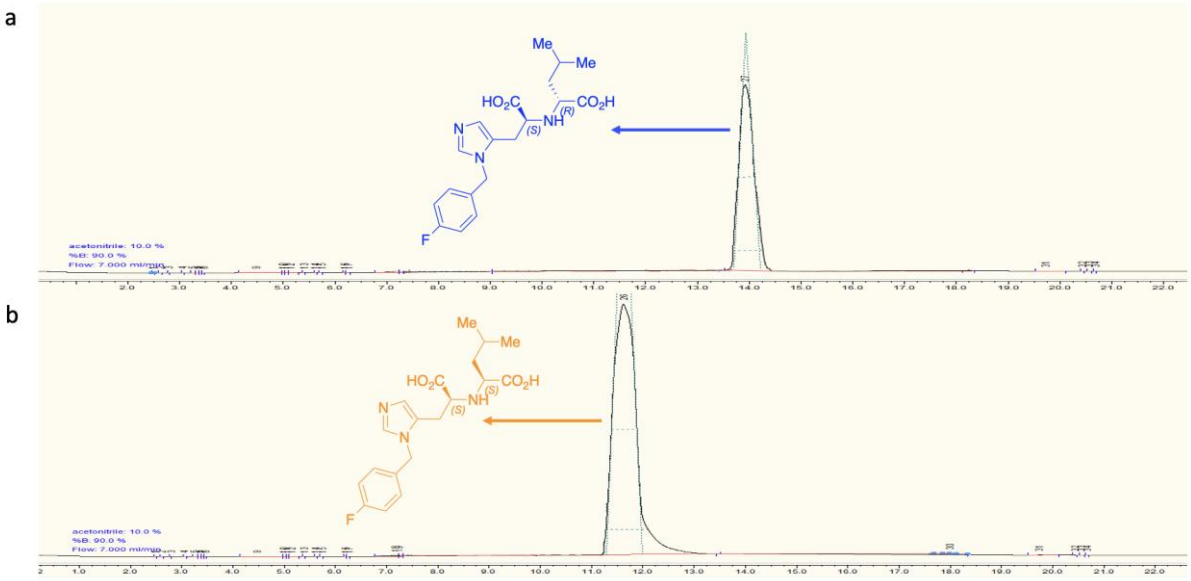

Figure 2.13: HPLC traces for a) (*S,R*)-**2.1**; b) (*S,S*)-**2.1**. Reverse phase HPLC details: Phenomenex Kinetex® 5 µm C18 100 Å, 250 x 4.6 mm, flow rate = 7 mL/min, column temperature = 25 °C, eluent = 10% MeCN (0.1% TFA) and 90% H_2O (0.1% TFA) for 25 min.

2.3.2.3 Refinement of the Synthetic Route for MLN-4760 Analogues

To improve efficiency and enable late-stage diversification, the synthetic route via Fukuyama–Mitsunobu amination was further modified by resequencing the amination and benzylation steps. This optimised strategy allows for the introduction of various benzyl groups at a later stage from a common intermediate, reducing the need to repeat early synthetic steps for each analogue. This approach was successfully applied to the synthesis of (*S*,*S*)-**2.1**–(*S*,*S*)-**2.4** as depicted in Scheme 2.8.

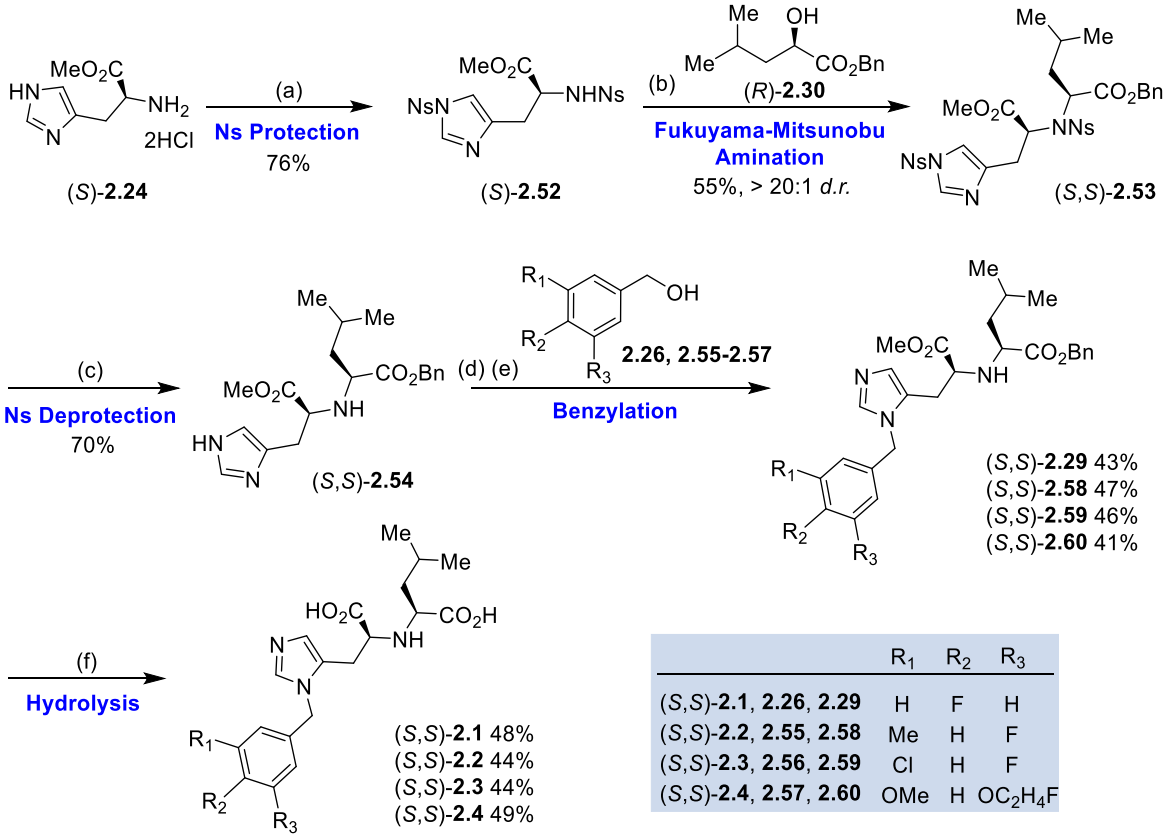

	R_1	R_2	R_3
(*S*,*S*)-**2.1**, **2.26**, **2.29**	H	F	H
(*S*,*S*)-**2.2**, **2.55**, **2.58**	Me	H	F
(*S*,*S*)-**2.3**, **2.56**, **2.59**	Cl	H	F
(*S*,*S*)-**2.4**, **2.57**, **2.60**	OMe	H	OC_2H_4F

Scheme 2.8: Synthesis of fluorinated MLN-4760 analogues (*S*,*S*)-**2.1**–(*S*,*S*)-**2.4**. Reagents and conditions: (a) Et_3N (3.0 equiv.), CH_2Cl_2, rt, 1 h, then NsCl (2.2 equiv.), rt, 18 h, 76%; (b) PPh_3 (1.0 equiv.), DIAD (1.0 equiv.), THF, -10 ℃, 1 h, then (*S*)-**2.52** (1.5 equiv.), THF, rt, 2 h, then (*R*)-**2.30** (1.0 equiv.), THF, rt, 16 h, 55%, > 20:1 *d.r.*; (c) PhSH (2.2 equiv.), K_2CO_3 (3.0 equiv.), DMF, rt, 1 h, 70%, > 20:1 *d.r.*; (d) (*S,S*)-**2.54** (1.1 equiv.), Boc_2O (2.2 equiv.), DIPEA (2.0 equiv.), CH_2Cl_2, rt, 24 h, isolated as crude, then (e) $(CF_3SO_2)_2O$ (1.0 equiv.), **2.26**, **2.55**–**2.57** (1.0 equiv.), DIPEA (1.5 equiv.), -78 ℃ to rt, 24 h, then HCl (4.0 M in dioxane, 1.1 equiv.), rt, 1 h, (*S,S*)-**2.29** (43%, > 20:1 *d.r.*), (*S,S*)-**2.58** (47%, >20:1 *d.r.*), (*S,S*)-**2.59** (46%, > 20:1 *d.r.*), (*S,S*)-**2.60** (41%, > 20:1 *d.r.*); (f) NaOH (1.0 M, 3.0 equiv.), MeOH/H_2O, rt, 1 h, work up with HCl (1 M), rt, 30 min, then preparative HPLC purification, (*S,S*)-**2.1** (48%), (*S,S*)-**2.2** (44%), (*S,S*)-**2.3** (44%), (*S,S*)-**2.4** (49%).

The synthesis began with the histidine derivative (*S*)-**2.24**. The Ns group was introduced at both the imidazole N1-position and the primary amine using NsCl and triethylamine in dichloromethane. This yielded the doubly Ns-protected intermediate (*S*)-**2.52** in 76% yield. In step (b), the Fukuyama–Mitsunobu amination between (*S*)-

2.52 and benzyl (*R*)-2-hydroxy-4-methylpentanoate ((*R*)-**2.30**) was performed under previously optimised conditions, employing DIAD and PPh_3 in THF at room temperature as shown in Table 2.5. Further optimisation of reagent stoichiometry and addition sequence revealed that the sequential addition of 1.5 equivalents of (*S*)-**2.52** followed by 1.0 equivalent of (*R*)-**2.30** to a pre-stirred mixture of DIAD and PPh_3 in THF, after delays of 1 h and 2 h respectively, led to the highest yield for this step in Table 2.5, Entry 6. Under these conditions, the histidine–leucine derivative (*S,S*)-**2.53** was obtained in 55% yield with high diastereoselectivity (>20:1 *d.r.*, determined by ^{1}H NMR).

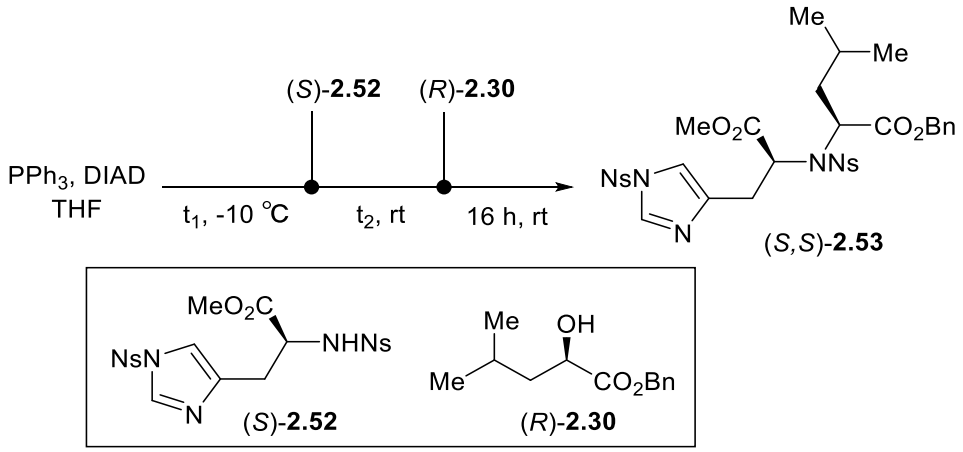

Entry	(*S*)-2.52 loading	t_1/ h	t_2/ h	Yield of (*S,S*)-2.53
1	1.0 equiv.	0	0	traces [a]
2	1.0 equiv.	0	1	12% [a]
3	1.0 equiv.	0	2	21% [a]
4	1.0 equiv.	1	2	35%
5	1.5 equiv.	0	2	42%
6	1.5 equiv.	1	2	55%

Table 2.5: Optimisation of the Fukuyama-Mitsunobu amination. PPh_3 = 1.0 equiv., DIAD = 1.0 equiv., (*R*)-**2.30** = 1.0 equiv. [a] Yields determined by quantitative ^{19}F NMR spectroscopy with 4-fluoroanisole as internal standard.

In steps (c) to (e), initial attempts of a direct benzylation of di-Ns-protected compound (*S*,*S*)-**2.53** was unsuccessful, likely due to the electron-withdrawing nature of the Ns groups which reduced the nucleophilicity of the substrate as illustrated in Scheme 2.9. As a workaround, selective deprotection of the Ns groups with thiophenol (PhSH) was employed, yielding the histidine-leucine derivative (*S,S*)-**2.54** in 70% yield. To enable regioselective N3-benzylation, the imidazole N1-position and the secondary amine of the leucine residue were protected with Boc groups. The resulting intermediate was directly subjected to benzylation using 4-fluorobenzyl alcohol (**2.26**) in the presence of trifluoromethanesulfonic anhydride. Subsequent one-pot Boc deprotection with HCl in dioxane yielded (*S,S*)-**2.29** in 43% yield with >20:1 *d.r.* (determined by ^{1}H NMR).

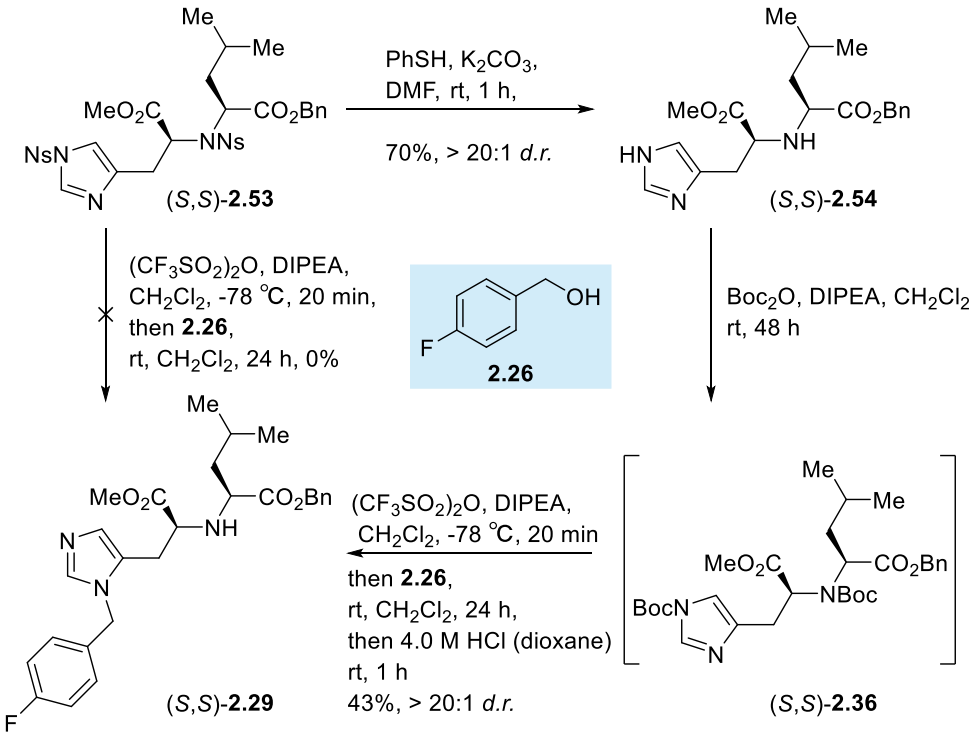

Scheme 2.9: Synthesis of (*S*,*S*)-**2.53** via a three-step Ns group cleavage-Boc protection-benzylation sequence to yield (*S*,*S*)-**2.29**.

Using the modified conditions, the common intermediate (*S,S*)-**2.54** was benzylated with four different fluorinated benzyl alcohols (**2.26**, **2.55–2.57**), yielding intermediates (*S,S*)-**2.29** and (*S,S*)-**2.58**–(*S,S*)-**2.60** in 41–47% yield and >20:1 *d.r.* as determined by ^{1}H NMR. Subsequent hydrolysis of the ester groups under basic conditions using NaOH afforded the target MLN-4760 analogues (*S,S*)-**2.1** to (*S,S*)-**2.4** in 44–49% yield as isolated and pure diastereomers. Notably, this strategy avoided the need for laborious preparative HPLC separation of diastereomers and final purification was achieved by reverse-phase chromatography. This remained necessary due to the high polarity and zwitterionic nature of the final histidine–leucine dipeptide derivatives, with the histidine side chain (pK_a ≈ 6.0) remaining protonated at near physiological p*H*. Overall, this optimised route employed Fukuyama–Mitsunobu amination to achieve stereocontrol and late-stage benzylation to enable structural diversification, offering a versatile strategy for accessing MLN-4760 analogues.

2.4 In Vitro ACE2 Inhibition Analysis

The ACE2 inhibitory potency of the synthesised fluorinated MLN-4760 analogues was determined using a commercially available Abcam ACE2 Inhibitor Screening Kit, ab273373 as illustrated in Figure 2.14 and Table 2.6. The kit quantitatively evaluates inhibition of recombinant human ACE2 activity using a fluorometric assay in which active ACE2 cleaves a synthetic 7-methoxycoumarin-4-acetic acid (MCA)–based peptide substrate, releasing a fluorophore detectable at 320/420 nm. Inhibitor-induced reductions in fluorescence allow determination of inhibitory potency. Each potency measurement was obtained from three independent runs, with each concentration tested in triplicate wells. The measured potency is expressed as pIC_{50}, the negative logarithm of the half-maximal inhibitory concentration (IC_{50}) value, where higher pIC_{50} values correspond to stronger inhibitory activity. In Figure 2.14, reported pIC_{50} values represent the mean of nine technical replicates per concentration, and error bars indicate the corresponding standard deviation. To account for potential discrepancies arising from variations in assay conditions compared with those used in the literature, the inhibitory activity of MLN-4760 was first evaluated. This measurement produced an experimental pIC_{50} (pIC^{exp}_{50}) value of 8.19, which is lower than the literature-reported value of 9.36.[1] All analogue pIC_{50} values were subsequently compared relative to this experimentally determined reference, enabling consistent assessment under identical assay conditions as shown in Table 2.6.

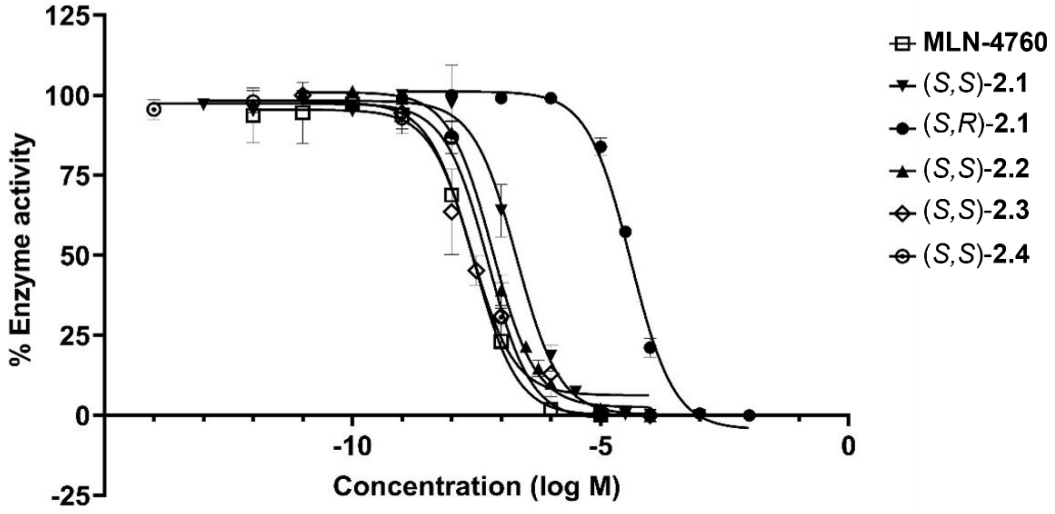

Figure 2.14: Inhibitory activity of MLN-4760 and analogues (*S*,*S*)-**2.1**–(*S*,*S*)-**2.4**, and (*S*,*R*)-**2.1**. Data points represent mean ± standard deviation (n = 9).

Compound	pIC^{pr}_{50}	$pIC^{pr\text{-}MLN}_{50} - pIC^{pr}_{50}$	pIC^{exp}_{50}	$pIC^{exp\text{-}MLN}_{50} - pIC^{exp}_{50}$
MLN-4760	8.19	0.00	7.54 ± 0.06	0.00
(*S*,*S*)-2.1	7.14	1.05	6.69 ± 0.05	0.85
(*S*,*R*)-2.1	n.d.	n.d.	4.39 ± 0.04	3.15
(*S*,*S*)-2.2	7.94	0.25	7.18 ± 0.04	0.36
(*S*,*S*)-2.3	7.99	0.20	7.61 ± 0.09	–0.07
(*S*,*S*)-2.4	8.88	–0.69	7.27 ± 0.05	0.27

Table 2.6: In vitro ACE2 inhibition study for MLN-4760 analogues ((*S*,*S*)-**2.1**–(*S*,*S*)-**2.4**) and comparison to in silico predictions. pIC_{50} determined using Abcam ACE2 inhibitor screening kit. pIC^{exp}_{50} values represent mean ± standard deviation (n = 9). $pIC_{50} = -\log_{10}(IC_{50})$, n.d. = not determined, pIC^{pr}_{50} = predicted pIC_{50}, $pIC^{pr\text{-}MLN}_{50}$ = predicted MLN-4760 pIC_{50}, pIC^{exp}_{50} = experimental pIC_{50}, $pIC^{exp\text{-}MLN}_{50}$ = experimental MLN-4760 pIC_{50}.

The stereochemical configuration exerted significant influence on the inhibitory potency of the MLN-4760 analogues. The (*S,S*)-**2.1** analogue demonstrated markedly higher activity, with a pIC_{50} value of 6.69 ± 0.05, compared to 4.39 ± 0.04 for its (*S,R*)-**2.1** counterpart, corresponding to an approximately 100-fold difference

in potency. This disparity is consistent with literature indicating that the (*S*,*S*)-configuration of MLN-4760 is preferred for ACE2 inhibition.[1] Figure 2.15 illustrates the X-ray crystallographic analysis by Towler and co-workers, which showed that the (*S*,*S*)-configuration enables optimal occupancy of the S1 subsite and coordination with the catalytic zinc ion, whereas the (*S*,*R*)-configuration may result in suboptimal positioning within the active site.[3]

Another indication of the influence of spatial arrangement on ACE2 inhibition is observed when comparing the 3,5-disubstituted benzyl derivatives to their *para*-substituted counterpart. Among the fluorinated MLN-4760 analogues, the 3,5-disubstituted derivatives (*S,S*)-**2.2**, (*S,S*)-**2.3**, and (*S,S*)-**2.4** exhibited pIC_{50} values ranging from 7.18 to 7.61, which were higher than that of the *para*-fluorobenzyl substituted derivative (*S,S*)-**2.1** (pIC^{exp}_{50} = 6.69 ± 0.05) and closely matched the potency of MLN-4760 ($pIC^{exp\text{-}MLN}_{50}$ = 7.54 ± 0.06). Analogue (*S,S*)-**2.3** displayed the highest potency within this series (pIC^{exp}_{50} = 7.61 ± 0.09), confirming its strong inhibitory activity in Table 2.6. A strong correlation was observed between the experimentally determined pIC^{exp}_{50} values and the in silico predicted pIC_{50} (pIC^{pr}_{50}) values relative to MLN-4760. For all 3,5-disubstituted benzyl analogues (*S,S*)-**2.2–**(*S,S*)-**2.4**, the pIC^{pr}_{50} values were lower than that of the *para*-substituted (*S,S*)-**2.1**, mirroring the trend observed in the experimental pIC^{exp}_{50} data. This is consistent with literature, which highlights the that ACE2 binding affinity is improved by substitution at the 3- and 5-positions on the benzylimidazole scaffold.[1] Structural analysis of the MLN-4760–ACE2 complex reveals that the 3,5-dichlorobenzylimidazole moiety is

positioned to occupy the S1' subsite, where it forms favourable hydrophobic and electrostatic contacts with residues Asn149, Glu145, Cys344, Cys361, Met360, and Asp368. The spatial arrangement of these amino acid side-chains creates a pocket that is geometrically and electronically complementary to the 3,5-substitution pattern. In contrast, *para*-substituted analogues, such as (*S,S*)-**2.1**, may provide only a single-point interaction within this subsite, which appears insufficient to maximise binding within the binding pocket, resulting in comparatively lower potency.

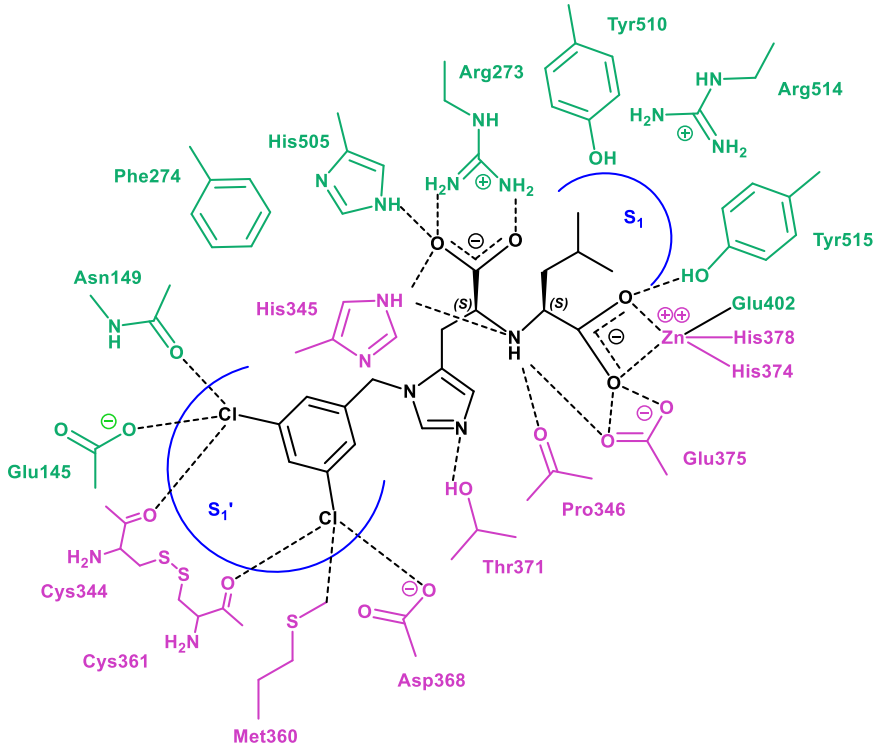

Figure 2.15: A schematic representation of the binding interactions between MLN-4760 and ACE2. MLN-4760 is shown in black, with residues from subdomain I in purple and those from subdomain II in green. *Figure reproduced with permission of P. Towler et al., ACE2 X-ray structures reveal a large hinge-bending motion important for inhibitor binding and catalysis, J. Bio. Chem., 2004, Vol. 279, Issue 17, Pages 17996-18007;*[3] *permission conveyed through Copyright Clearance Center, Inc.*

Müller and co-workers recently investigated fluorinated analogues of MLN-4760 as potential PET imaging agents, demonstrating that substitution of one chlorine atom in MLN-4760 with fluorine preserves its binding mode within the ACE2 active site.[20] Co-crystallisation of the fluorinated analogue with hACE2, and comparison to the hACE2–MLN-4760 complex (PDB: 1R4L), revealed a highly similar binding pose as presented in Figure 2.16. In both structures, the 3,5-substituted benzyl moiety, bearing either dichloro or chlorofluoro substitution, occupies the S1' subsite and engages in favourable interactions with Asn149 and Asp368. The carboxylate group coordinates to the catalytic zinc ion within the closed conformation of the hACE2 peptidase domain, and the fluorinated analogue adopts the same (*S*,*S*)-stereochemistry as the parent MLN-4760.

Guided by in vitro pIC^{exp}_{50} measurements and structural analyses, (*S,S*)-**2.1**–(*S,S*)-**2.4** exhibited high ACE2 inhibition potency, with (*S,S*)-**2.3** emerging as the most active analogue and a compelling candidate for future studies.

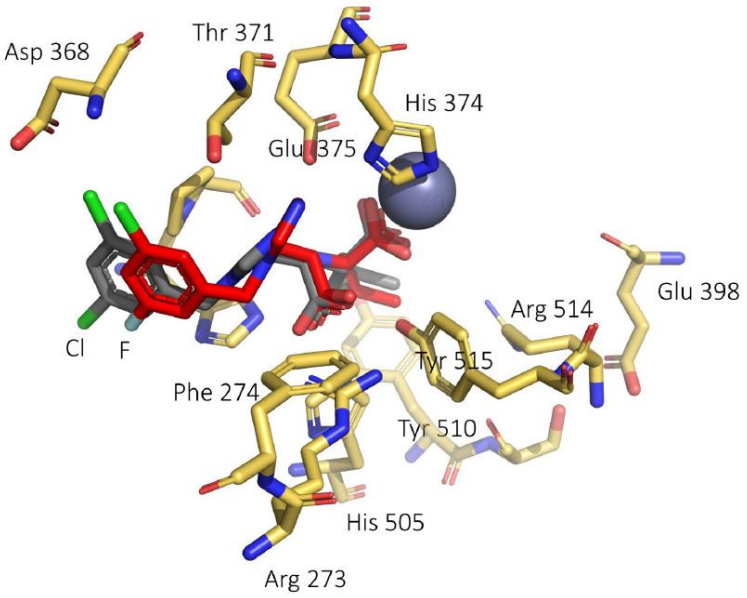

Figure 2.16: Structural overlay of the hACE2–MLN-4760 complex (PDB ID: 1R4L) and the hACE2 complex with the fluorinated MLN-4760 analogue. Key ACE2 active-site residues are shown with yellow carbon atoms. MLN-4760 is represented in grey, and the fluorinated analogue in red, with atom colours as follows: nitrogen (blue), oxygen (red), chlorine (light green), and fluorine (light blue). *Figure reproduced under CC BY 4.0 license from J. Wang, D. Beyer, C. Vaccarin, Y. He, M. Tanriver, R. Benoit, C. Müller, et al., Development of Radiofluorinated MLN-4760 Derivatives for PET Imaging of the SARS-CoV-2 Entry Receptor ACE2, EJNMMI, 2024, pp. 1–13 (http://creativecommons.org/licenses/by/4.0).*

2.5 Conclusion and Future Outlook

This chapter describes the discovery of four potent and selective ACE2 PET radiotracer candidates (*S,S*)-**2.1** to (*S,S*)-**2.4**. In silico screening of MLN-4760 analogues guided their design, followed by development of a novel synthetic route featuring a Fukuyama–Mitsunobu reaction and late-stage benzylation. In vitro assays confirmed their strong ACE2 inhibition, displaying potencies comparable to MLN-4760, highlighting them as priority candidates for ^{18}F-radiolabelling and PET imaging studies.

Future work could leverage this versatile synthetic route to explore additional MLN-4760 analogues, systematically tuning the electronic and steric properties of the benzyl substituent to optimise ACE2 binding affinity and pharmacological profile. The strategy is also well-suited for PET tracer development, offering straightforward incorporation of fluorine-18, either directly (e.g. via copper-mediated radiofluorination) or via prosthetic groups (e.g. benzylation), to enable the translation of potent ACE2 inhibitors into radiolabelled imaging agents. This application to radiolabelling is further developed in Chapter 3.

2.6 Reference

(1) Dales, N. A.; Gould, A. E.; Brown, J. A.; Calderwood, E. F.; Guan, B.; Minor, C. A.; Gavin, J. M.; Hales, P.; Kaushik, V. K.; Stewart, M. Substrate-based design of the first class of angiotensin-converting enzyme-related carboxypeptidase (ACE2) inhibitors. *J. Am. Chem. Soc.* **2002**, *124* (40), 11852–11853.

(2) Wang, X.; He, J.; Hosseini-Gerami, L.; Thomas, M.; Thompson, S.; Ford, J.; Ortalli, S.; Chen, Z.; Destro, G.; Bender, A. Synthesis and Inhibitory Assessment of ACE2 Inhibitors for SARS-CoV-2: An In Silico and In Vitro Study. *J. Org. Chem.* **2025**, *90* (30), 10941–10947.

(3) Towler, P.; Staker, B.; Prasad, S. G.; Menon, S.; Tang, J.; Parsons, T.; Ryan, D.; Fisher, M.; Williams, D.; Dales, N. A. ACE2 X-ray structures reveal a large hinge-bending motion important for inhibitor binding and catalysis. *J. Biol. Chem.* **2004**, *279* (17), 17996–18007.

(4) Abraham, M. J.; Murtola, T.; Schulz, R.; Páll, S.; Smith, J. C.; Hess, B.; Lindahl, E. GROMACS: High performance molecular simulations through multi-level parallelism from laptops to supercomputers. *SoftwareX* **2015**, *1*, 19–25.

(5) Suruzhon, M.; Senapathi, T.; Bodnarchuk, M. S.; Viner, R.; Wall, I. D.; Barnett, C. B.; Naidoo, K. J.; Essex, J. W. ProtoCaller: robust automation of binding free energy calculations. *J. Chem. Inf. Model.* **2020**, *60* (4), 1917–1921.

(6) Hodges, J. C. Regiospecific synthesis of 3-substituted L-histidines. *Synthesis* **1987**, *1987* (01), 20–24.

(7) Van Den Berge, E.; Robiette, R. Development of a regioselective N-methylation of (benz) imidazoles providing the more sterically hindered isomer. *J. Org. Chem.* **2013**, *78* (23), 12220–12223.

(8) Claridge, T. D. *High-Resolution NMR Techniques in Organic Chemistry*; Elsevier, 2016.

(9) Rong, J.; Haider, A.; Jeppesen, T. E.; Josephson, L.; Liang, S. H. Radiochemistry for positron emission tomography. *Nat. Commun.* **2023**, *14* (1), 3257.

(10) Halder, R.; Ritter, T. ^{18}F-Fluorination: Challenge and Opportunity for Organic Chemists. *J. Org. Chem.* **2021**, *86* (20), 13873–13884.

(11) Mitsunobu, O. The use of diethyl azodicarboxylate and triphenylphosphine in synthesis and transformation of natural products. *Synthesis* **1981**, *1981* (01), 1–28.

(12) Fukuyama, T.; Jow, C.-K.; Cheung, M. 2-and 4-Nitrobenzenesulfonamides: Exceptionally versatile means for preparation of secondary amines and protection of amines. *Tetrahedron Lett.* **1995**, *36* (36), 6373–6374.

(13) Fukuyama, T.; Cheung, M.; Jow, C.-K.; Hidai, Y.; Kan, T. 2, 4-Dinitrobenzenesulfonamides: A simple and practical method for the preparation of a variety of secondary amines and diamines. *Tetrahedron Lett.* **1997**, *38* (33), 5831–5834.

(14) Kan, T.; Fukuyama, T. Ns strategies: a highly versatile synthetic method for amines. *Chem. Commun.* **2004**, (4), 353–359.

(15) Sikandar, S.; Zahoor, A. F.; Naheed, S.; Parveen, B.; Ali, K. G.; Akhtar, R. Fukuyama reduction, Fukuyama coupling and Fukuyama–Mitsunobu alkylation: recent developments and synthetic applications. *Mol. Divers.* **2022**, 1–40.

(16) Raghavan, S.; Babu, V. S. Enantioselective synthesis of oseltamivir phosphate. *Tetrahedron* **2011**, *67* (11), 2044–2050.

(17) Wang, L.; Liu, W.-Q.; Saraux, N.; Vidal, M.; Broussy, S. Solid phase synthesis of constrained 13-membered peptide macrocycles employing Fukuyama–Mitsunobu alkylations. *Tetrahedron Lett.* **2015**, *56* (19), 2456–2459.

(18) Brittain, H. G. Crystallographic consequences of molecular dissymmetry. *Pharm. Res.* **1990**, *7*, 683–690.

(19) Tyson, B.; Pask, C. M.; George, N.; Simone, E. Crystallization behavior and crystallographic properties of DL-arabinose and DL-xylose diastereomer sugars. *Cryst. Growth Des.* **2022**, *22* (2), 1371–1383.

(20) Wang, J.; Beyer, D.; Vaccarin, C.; He, Y.; Tanriver, M.; Benoit, R.; Deupi, X.; Mu, L.; Bode, J. W.; Schibli, R. Development of radiofluorinated MLN-4760 derivatives for PET imaging of the SARS-CoV-2 entry receptor ACE2. *Eur. J. Nucl. Med. Mol. Imag.* **2024**, 1–13.

Chapter 3: Development of Radiolabelled [^{18}F]MLN-4760 Analogues

3.1 Introduction

This chapter focuses on the ^{18}F-radiolabelling of two MLN-4760 analogues, (*S*,*S*)-**3.1** and (*S*,*S*)-**3.2**, as shown in Figure 3.1. Section 3.1 begins with a review of current PET radiotracers for ACE2, including their design, radiolabelling strategies, and imaging performance. This is followed by a discussion of radiochemical methods for (hetero)aromatic ^{18}F-fluorination, with a focus on nucleophilic ^{18}F-labelling via Cu(II)-mediated radiofluorination of boronic ester precursors. Section 3.2 describes the radiosynthesis of two [^{18}F]MLN-4760 analogues. It begins with spiking experiments to assess stability under radiolabelling conditions, and outlines the synthesis of boronic ester precursors. Subsequent fluorine-18 incorporation via Cu(II)-mediated radiofluorination, followed by post-labelling hydrolysis afforded the [^{18}F]MLN-4760 analogues in good radiochemical yields.

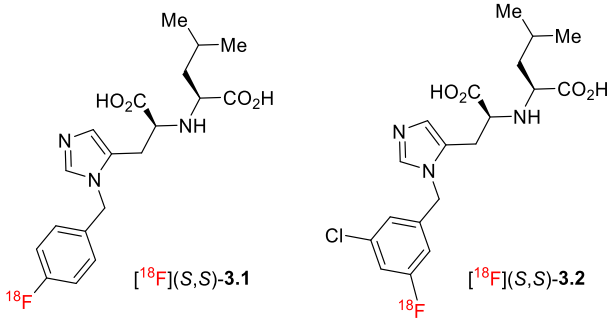

Figure 3.1: Target [^{18}F]MLN-4760 analogues.

All radiochemistry experiments were carried out in collaboration with Dr. Joseph Ford and Dr. Sebastiano Ortalli at the University of Oxford and Cardiff University. The work described in this chapter forms the basis of a paper published in the *Journal of Organic Chemistry* on 21 July 2025 (DOI: 10.1021/acs.joc.5c00918).[1]

3.1.1 Current PET Radiotracers for ACE2 Imaging

3.1.1.1 DX600-Based Radiotracers

Various methods have been explored for monitoring ACE2 expression, including immunoprecipitation, western blotting, immunohistochemistry, and quantitative reverse transcription polymerase chain reaction (RT-PCR).[2-5] While these techniques provide valuable insights into ACE2 distribution at the molecular level, they rely on single-cell ribonucleic acid (RNA) sequencing and protein databases, making it hard to visualise dynamic changes in vivo.[2-5] In contrast, PET imaging offers a non-invasive, highly sensitive, and quantitative approach for real-time visualisation of ACE2 expression in vivo.[6]

Early developments of PET radiotracers for ACE2 imaging focused on modifying DX600, a peptide inhibitor of ACE2, at its N-terminal for radiolabelling with ^{18}F, ^{64}Cu, and ^{68}Ga, yielding tracers such as ^{68}Ga-NOTA-PEP4, ^{68}Ga-HZ20 (^{68}Ga-cyc-DX600), ^{64}Cu-HZ20 and [^{18}F]AlF-DX600-BCH (Table 3.1).[7-16] Wilson and co-workers introduced ^{68}Ga-NOTA-PEP4 **3.3** in 2021, conjugating the DX600 peptide to a 1,4,7-triazacyclononane-1,4,7-triacetic acid (NOTA) chelator for ^{68}Ga coordination.[14] The cyclic structure of NOTA-PEP4 showed enhanced inhibitory potency, achieving a half-maximal inhibitory concentration (IC_{50}) of 67.6 nM, compared to 118.2 nM for the parent DX600 peptide in ACE2 inhibition assays. In vivo PET imaging using transgenic K18-hACE2 mice showed rapid clearance from circulation, with primary accumulation in the kidneys.

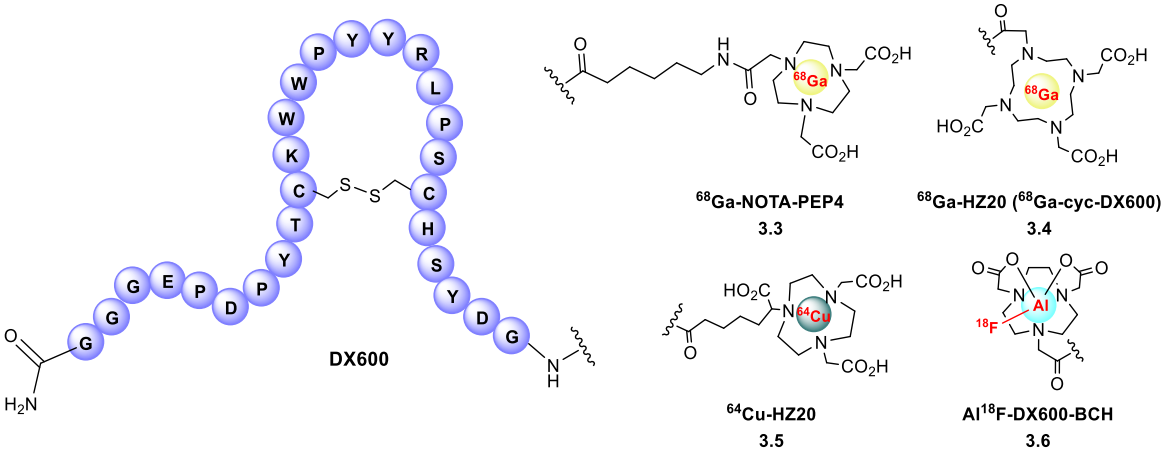

Radiotracer	Binding Affinity	RCY	Molar Activity	Ref.
^{68}Ga-NOTA-PEP4	IC_{50} = 67.6 nM	63.2% ± 6.4% (decay corrected)	≥15.6 GBq/μmol	14
^{68}Ga-HZ20 (^{68}Ga-cyc-DX600)	K_d = 100.0 nM	59.9% ± 3.9% (non-decay corrected)	60 GBq/μmol	7-13, 15
^{64}Cu-HZ20	K_d = 66 ± 1 nM (4 °C), 143 ± 1 nM (37 °C)	Not reported	Not reported	7
[^{18}F]AlF-DX600-BCH	K_d = 69.8 μM	20.4% ± 5.2% (non-decay corrected)	13.5–27 GBq/μmol	16

Table 3.1: DX600-derived PET radiotracers: ^{68}Ga-NOTA-PEP4, ^{68}Ga-HZ20 (DOTA chelator), ^{64}Cu-HZ20 (NODAGA chelator), and Al^{18}F-DX600-BCH (NOTA chelator). NODAGA = 1,4,7-triazacyclononane,1-glutaric acid-4,7-acetic acid; NOTA = 1,4,7-triazacyclononane-1,4,7-triacetic acid; DOTA = 1,4,7,10-tetraazacyclododecane-1,4,7,10-tetraacetic acid; IC_{50} = half-maximal inhibitory concentration; K_d = dissociation constant; RCY = radiochemical yield. GBq = gigabecquerel.

In 2021, Zhu and co-workers developed two DX600-based PET tracers, ^{68}Ga-HZ20 **3.4** (also referred to as ^{68}Ga-cyc-DX600) and ^{64}Cu-HZ20 **3.5**, designed as cyclic DX600 analogues to enhance ACE2 binding stability and pharmacokinetic properties.[7] In vitro studies demonstrated strong binding affinity for ACE2, with dissociation constants (K_d) in the nanomolar range. In vivo blocking experiments

using unlabelled DX600 further confirmed ACE2 specificity, as tracer uptake was significantly reduced in the presence of the parent peptide. Preclinical PET imaging in HEK293-hACE2 xenograft mice revealed selective accumulation in ACE2-expressing tissues, with high renal uptake, consistent with the known physiological distribution of ACE2. This study also included a first in-human evaluation of ^{68}Ga-HZ20 (NCT04422457), providing key translational insights into ACE2 PET imaging. In healthy volunteers, PET imaging showed prominent tracer uptake in the renal cortex and reproductive system, while pulmonary uptake remained low, reflecting the ACE2 expression profile in human tissues. Additionally, PET imaging of a recovered COVID-19 patient revealed altered tracer biodistribution, with decreased renal uptake and increased accumulation in the gallbladder and testes compared to healthy controls as illustrated in Figure 3.2. These findings suggest potential dysregulation of ACE2 expression following SARS-CoV-2 infection.

Beyond its applications in COVID-19 research, tracing ACE2 expression is also critical in oncology. PET imaging in xenograft tumour models has demonstrated reduced ACE2 expression in cancerous tissues.[8, 13] Moreover, in a patient with liver metastases from rectal cancer, ^{68}Ga-cyc-DX600 uptake was significantly lower in metastatic lesions than in normal liver tissue, supporting the association between ACE2 expression and tumour progression.[9]

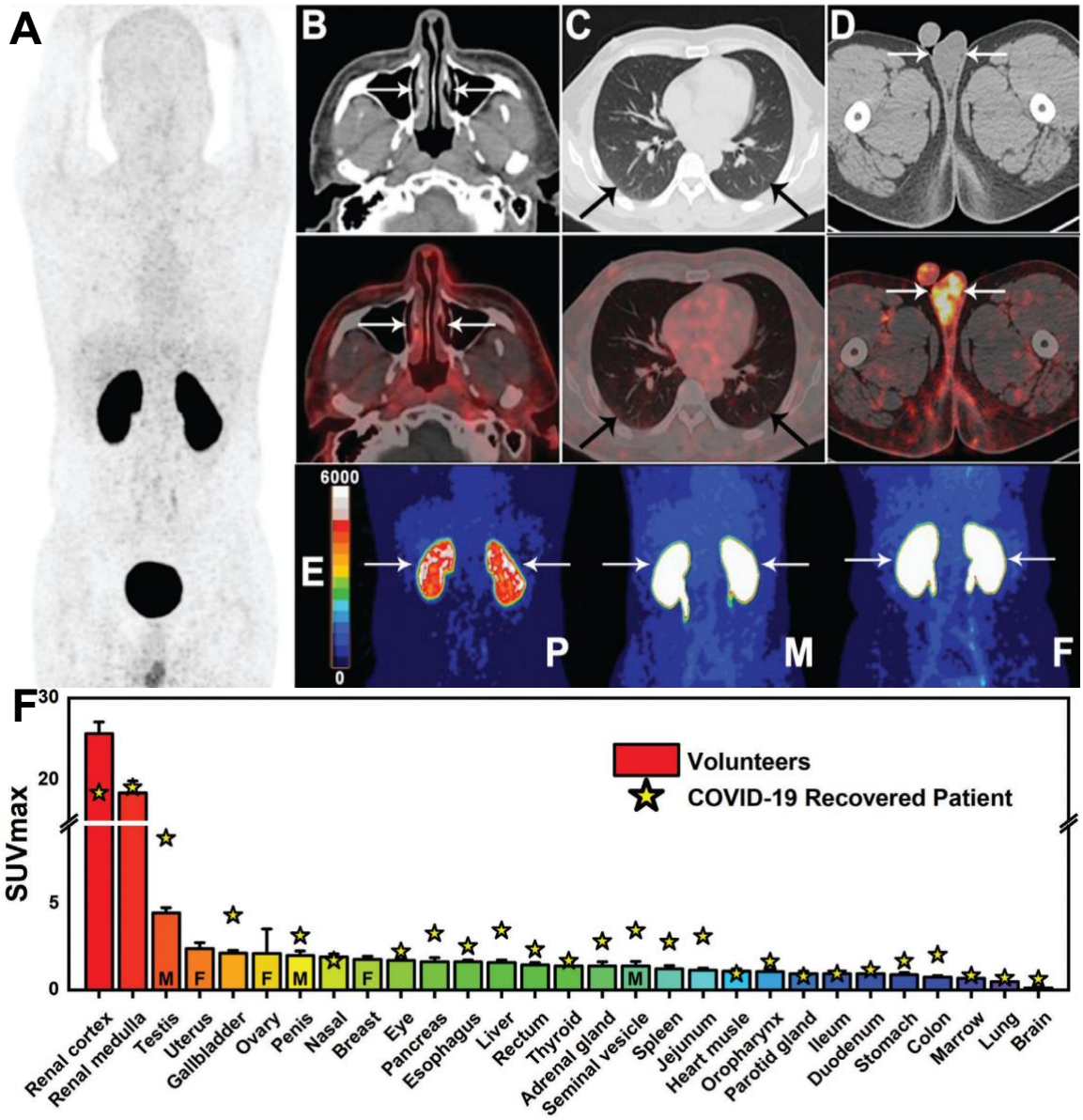

Figure 3.2: A-E) Representative PET images of ^{68}Ga-HZ20 in a volunteer recovered from COVID-19 and F) ranked organ ACE2 expression. A) Whole-body PET scan. B–D) axial PET/CT images highlighting tracer uptake in the nasal cavity, lungs, and testes at 90 minutes post-injection. E) Renal uptake of ^{68}Ga-HZ20 is compared among a recovered COVID-19 patient (P), a healthy male (M), and a healthy female (F) volunteer. F) The table presents the average SUV_{max} at 90 minutes post-injection from 20 healthy volunteers, and stars indicate SUV_{max} values from the COVID-19 recovered patient, with specific values for only males (M) and females (F) where applicable. SUV_{max} = maximum standardised uptake value. *Figure reproduced under CC BY 4.0 license from H. Zhu, H. Zhang, N. Zhou, J. Ding, J. Jiang, T. Liu, Z. Liu, F. Wang, Q. Zhang, Z. Zhang, et al., Molecular PET/CT Profiling of ACE2 Expression In Vivo: Implications for Infection and Outcome from SARS-CoV-2, Adv. Sci., 2021, Vol. 8, e2100965 (http://creativecommons.org/licenses/by/4.0).*

Zhu and co-workers developed [^{18}F]AlF-DX600-BCH **3.6**, employing an aluminium-[^{18}F]fluoride chelation strategy.[16] Clinical evaluation (NCT04542863) demonstrated high nasal mucosa uptake, consistent with elevated ACE2 expression in the upper respiratory tract. Its ability to enable non-invasive, quantitative detection of ACE2 expression makes this imaging approach valuable for investigating ACE2 dynamics in infection and disease progression.

3.1.1.2 MLN-4760-Based Radiotracers

Research on MLN-4760-based PET tracers remains limited, but in parallel with our work, two studies published in 2024 have explored MLN-4760-derived radiotracers as presented in Table 3.2.[17, 18] Wang and co-workers reported [^{18}F]F-MLN-4760 **3.2**, prepared by copper-mediated radiofluorination of an arylstannane precursor, and [^{18}F]F-Aza-MLN-4760 **3.8**, obtained through nucleophilic substitution of a chlorinated precursor.[17] In both cases, radiofluorination was followed by ester hydrolysis, yielding the final radiotracers in radiochemical yields (RCY) of 5.3% and 2.1%, respectively. In vitro assays in HEK-ACE2 and HEK-ACE cells demonstrated their selective binding to ACE2-expressing cells, with negligible uptake in ACE-negative controls. In vivo PET imaging in HEK-ACE2 and HEK-ACE xenograft mouse models confirmed their specificity, with preferential uptake in ACE2-positive tumours. Both tracers showed physiological accumulation in the kidneys, gallbladder, intestines, and urinary bladder, with pronounced retention in the gallbladder and intestinal tract at 1 and 3 hours post-injection as shown in Figure 3.3.

Zhou and co-workers also reported the synthesis of [^{18}F]MLN-4760 **3.7** via an ^{18}F/Cl exchange reaction under phase-transfer catalysis, achieving a radiochemical yield of 30% but with a radiochemical purity of only 30%.[18] It is worth noting that the characterisation of the product presented was limited, and, in the absence of definitive analytical data, the possibility that the radiochemical product contained contributions from both **3.2** and **3.7** could not be excluded. In vivo PET imaging in a humanised ACE2 mouse model revealed selective accumulation in ACE2-rich tissues, including the heart, liver, lungs, and kidneys, with stable retention over 120 minutes. Immunohistochemical analysis corroborated these findings, confirming ACE2 expression in the major organs.

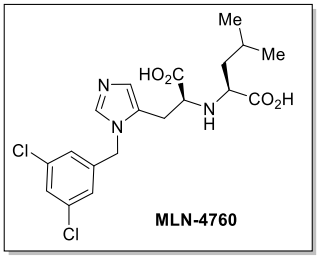

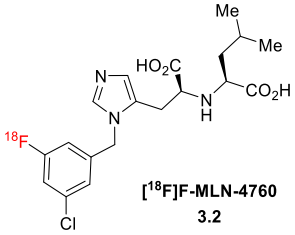

[^{18}F]F-MLN-4760
3.2

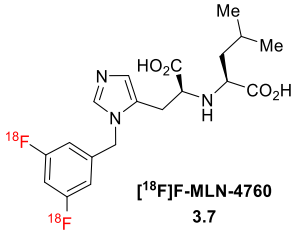

[^{18}F]F-MLN-4760
3.7

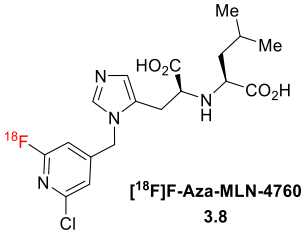

[^{18}F]F-Aza-MLN-4760
3.8

Radiotracer	Binding Affinity	RCY	Molar Activity	Ref.
[^{18}F]F-MLN-4760 **3.2**	IC_{50} = 150 nM	5.3% (decay corrected)	21–38 GBq/μmol	[17]
[^{18}F]F-MLN-4760 **3.7**	Not reported	30% (non-decay corrected)	3.7 GBq/μmol	[18]
[^{18}F]F-Aza-MLN-4760 **3.8**	IC_{50} = 387 nM	1.2% (decay corrected)	78–81 GBq/μmol	[17]

Table 3.2: Reported MLN-4760-derived radiotracers: [^{18}F]F-MLN-4760 and [^{18}F]F-Aza-MLN-4760. IC_{50} = half-maximal inhibitory concentration; RCY = radiochemical yield; GBq = giga becquerel.

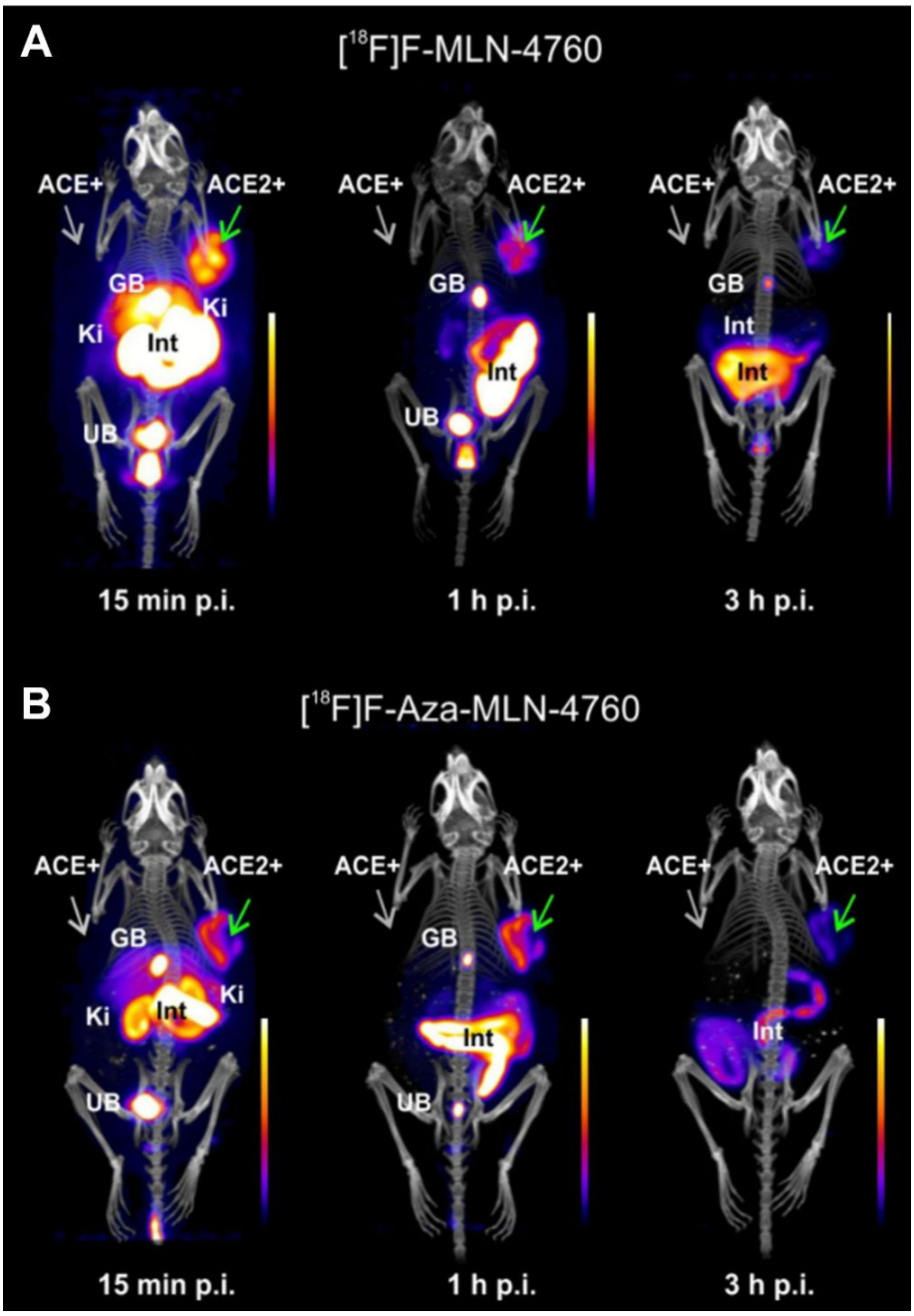

Figure 3.3: PET/CT images of nude mice bearing HEK-ACE2 and HEK-ACE xenografts. Images were acquired at 15 minutes, 1 hour, and 3 hours post-injection following administration of (A) [^{18}F]F-MLN-4760 and (B) [^{18}F]F-Aza-MLN-4760. Green arrows indicate HEK-ACE2 xenografts (ACE2^{+}), while grey arrows indicate HEK-ACE xenografts (ACE^{+}). GB = gallbladder; Ki = kidney; Int = intestines; UB = urinary bladder. *Figure reproduced under CC BY 4.0 license from J. Wang, D. Beyer, C. Vaccarin, Y. He, M. Tanriver, R. Benoit, C. Müller, et al., Development of Radiofluorinated MLN-4760 Derivatives for PET Imaging of the SARS-CoV-2 Entry Receptor ACE2, EJNMMI, 2024, pp. 1–13 (http://creativecommons.org/licenses/by/4.0).*

3.1.2 Aromatic ^{18}F-Fluorination

3.1.2.1 Copper-mediated ^{18}F-Fluorination

In developing our PET radiotracers, which require fluorine incorporation into an aromatic ring, we identified copper-mediated ^{18}F-fluorination as a particularly promising labelling strategy. This approach offers broad substrate scope, high functional group tolerance, and proven compatibility with heteroaromatic systems.[19, 20] The methodology builds on advances in non-radioactive ^{19}F-fluorination, which established copper as a useful reagent for late-stage C–F bond formation. In the radiochemical context, copper-mediated ^{18}F-fluorination enables the regioselective introduction of fluorine into (hetero)aromatic frameworks from nucleophilic [^{18}F]fluoride ([^{18}F]F^-).

Ribas and co-workers reported the first Cu(I)-mediated fluorination of aryl halides **3.9** in 2011, demonstrating that nucleophilic fluorides such as KF and AgF could generate aryl fluorides **3.10** through a Cu(I)/Cu(III) catalytic cycle.[21] The reaction proceeded via oxidative addition of aryl halides to Cu(I), halide exchange, and reductive elimination, establishing a fundamental pathway for Cu-mediated fluorination as illustrated in Scheme 3.1A. Building on this, Wang and co-workers isolated a Cu(III)-F complex **3.12** generated through copper(II) perchlorate ($Cu(ClO_4)_2$)-mediated C–H activation, validating the role of Cu(III)-fluoride intermediates in C–F bond formation as shown in Scheme 3.1B.[22] Shortly after, Hartwig and co-workers expanded the scope by demonstrating a Cu(I)-mediated

fluorination of aryl pinacol boronic esters (Bpin) **3.14** with electrophilic fluorine sources, enabling functionalisation of structurally diverse arenes (Scheme 3.1C).[23] In 2013, Sanford and co-workers demonstrated that arylboron derivatives **3.16** could undergo Cu(II)-mediated fluorination using nucleophilic fluoride sources such as KF, with excess copper(II) triflate ($Cu(OTf)_2$) (Scheme 3.1D).[24] Among the substrates tested, aryltrifluoroborates **3.18** and aryl pinacol boronic esters **3.19** exhibited the highest fluorination yields (70% and 56%, respectively). In contrast, arylboronic acids **3.20** and aryl *N*-methyliminodiacetic acid boronates **3.21** resulted in significantly lower yields (3% and 9%), limiting their utility in this transformation.

Scheme 3.2 details the proposed mechanism, which involves an initial Cu(II)-aryl complex **3.23** and undergoes oxidation by $Cu(OTf)_2$ to generate a Cu(III)–aryl species **3.24**, followed by reductive elimination to afford the desired aryl fluoride **3.25**. This methodology provided a practical and regioselective approach for late-stage fluoroarene synthesis.

A) Cu(I)-mediated fluorination of aryl halides

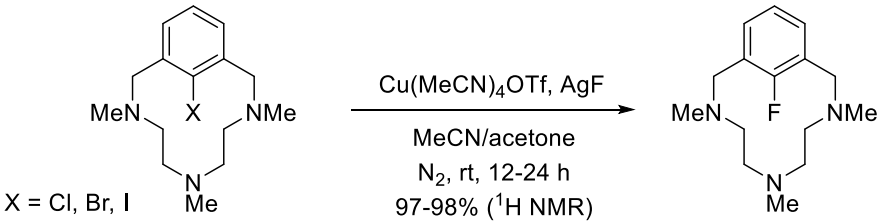

3.9 **3.10**

B) Fluorination of aryl Cu(III) complex

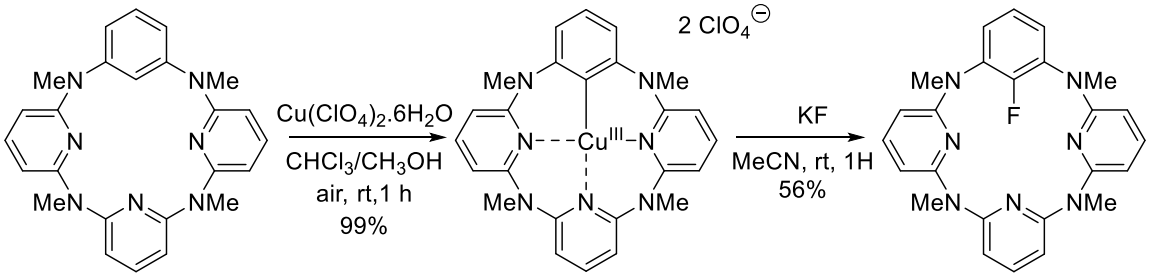

3.11 **3.12** **3.13**

C) Cu(I)-mediated fluorination of arylboronic esters

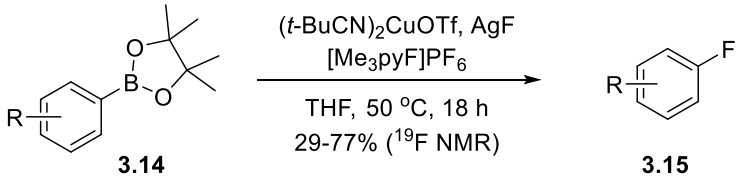

3.14 **3.15**

D) Cu(II)-mediated fluorination of arylboron derivatives

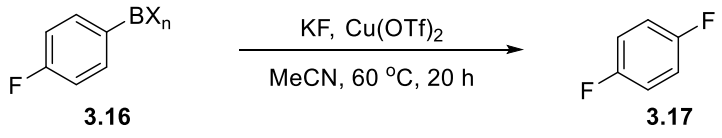

3.16 **3.17**

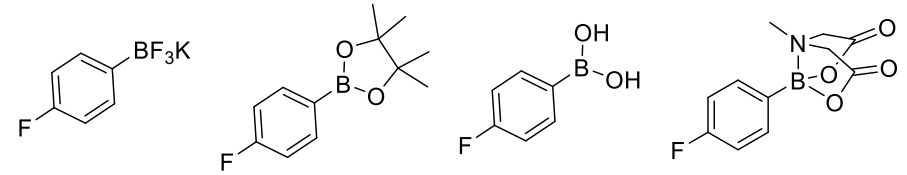

3.18 70%

3.19 56%

3.20 3%

3.21 9%

Scheme 3.1: Development of Cu-mediated ^{19}F-fluorination. A) Cu(I)-mediated fluorination of aryl halides; B) fluorination of aryl Cu(III) complexes; C) Cu(I)-mediated fluorination of aryl pinacol boronic esters; D) Cu(II)-mediated fluorination of arylboron derivatives.

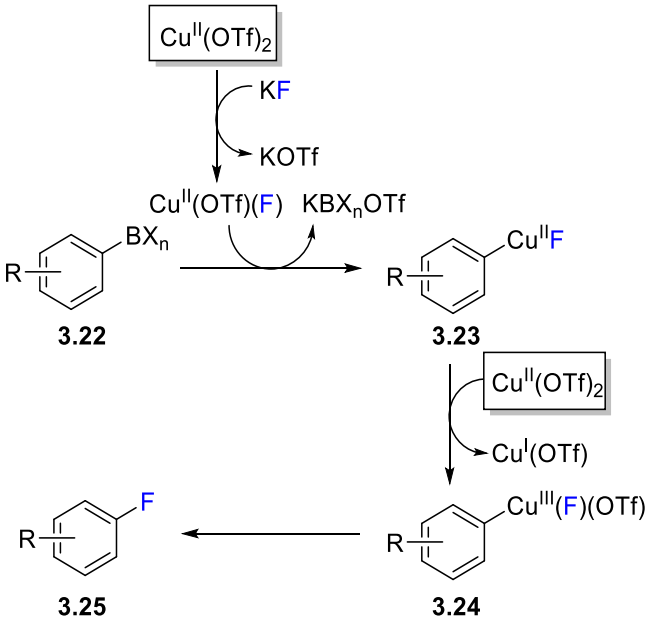

Scheme 3.2: Proposed mechanism of fluorination of aryl boron derivatives.

The development of copper-mediated ^{18}F-fluorination has bridged the synthetic gap between established ^{19}F-fluorination methodologies and their radiochemical applications. In 2014, Gouverneur and co-workers introduced a Cu(II)-mediated ^{18}F-fluorination protocol for (hetero)aryl pinacol boronic esters (Bpin) **3.26** as depicted in Scheme 3.3.[19] Using [^{18}F]KF/K_{222} as the fluoride source and catalytic tetrakis(pyridine)copper(II) triflate ($Cu(OTf)_2(py)_4$), they demonstrated selective ^{18}F-labelling of both electron-rich and electron-deficient arenes. In the same year, Sanford and Scott reported Cu(II)-mediated fluorination of arylboronic acids **3.28** and arylstannanes **3.30**, respectively, using [^{18}F]KF as the fluoride source with a stoichiometric amount of $Cu(OTf)_2$.[25, 26] These developments broadened the scope of Cu(II)-mediated ^{18}F-fluorination, demonstrating tolerance to a wide range of functional groups and both electron-rich and electron-deficient arenes.

In June 2025, Gouverneur and co-workers reported a protocol for Cu(II)-mediated ^{18}F-fluorination of (hetero)aryl boronic 1,1,2,2-tetraethylethylene glycol ester (BEpin) reagents **3.32** as shown in Scheme 3.3D.[27] BEpin precursors are an alternative precursor class to address the practical challenges often encountered during isolation and purification of certain (hetero)aryl-Bpin precursors, including streaking, over-adsorption, and degradation on silica gel. Sharing close structural and electronic similarity with their Bpin counterparts, BEpin precursors can be synthesised analogously from commercially available reagents. Building on established Cu(II)-mediated ^{18}F-fluorination of Bpin precursors, the BEpin protocol employed [^{18}F]KF/K_{222} with an optimised condition incorporating 1 equivalent of $Cu(OTf)_2(py)_4$ and 1,3-dimethyl-2-imidazolidinone (DMI) as solvent. Across a series of 20 examples, this approach delivered ^{18}F-fluoro(hetero)arenes in radiochemical yields of 65–98%. Collectively, these advancements reinforced Cu(II)-mediated ^{18}F-fluorination as a powerful strategy for accessing ^{18}F-labelled tracers for PET imaging applications.

A) Cu(II)-mediated ^{18}F-Fluorination of (hetero)aryl pinacol boronic esters (Bpin)

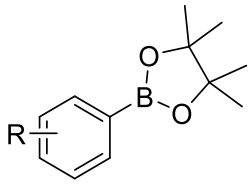

3.26

$[^{18}F]KF/K_{222}$
$Cu(OTf)_2(py)_4$ (9 mol%)
DMF,110 °C, 20 min

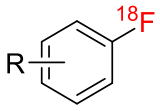

[^{18}F]3.27
RCY = 5% - 83%
31 examples

B) Cu(II)-mediated ^{18}F-Fluorination of aryl boronic acid

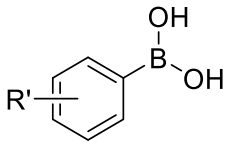

3.28

$[^{18}F]KF$, $KOTf/K_2CO_3$
$Cu(OTf)_2$ (2.0 equiv.)
pyridine, DMF,
110 °C, 20 min

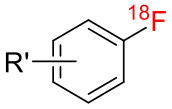

[^{18}F]3.29
RCY = 8% - 73%
18 examples

C) Cu(II)-mediated ^{18}F-Fluorination of arylstannanes

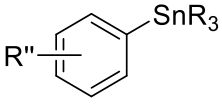

3.30

$[^{18}F]KF$, $KOTf/K_2CO_3$
$Cu(OTf)_2$ (5.0 equiv.)
pyridine, DMA,
100-140 °C, 5-30 min

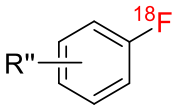

[^{18}F]3.31
RCY = 7% - 64%
18 examples

D) Cu(II)-mediated ^{18}F-Fluorination of (hetero)aryl boronic 1,1,2,2-tetraethylethylene glycol ester (BEpin)

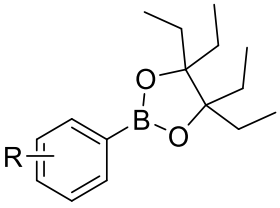

3.32

$[^{18}F]KF/K_{222}$
$Cu(OTf)_2(py)_4$ (1.0 equiv.)
DMI,110 °C, 20 min

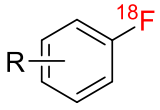

[^{18}F]3.33
RCY = 65% - 98%
20 examples

Scheme 3.3: Cu(II)-mediated ^{18}F-fluorination of A) (hetero)aryl pinacol boronic esters (Bpin), B) aryl boronic acids, C) arylstannanes and D) (hetero)aryl boronic 1,1,2,2-tetraethylethylene glycol esters (BEpin).

3.2 Radiosynthesis of [^{18}F]MLN-4760 Analogues

3.2.1 Robustness Screening Experiments for [^{18}F]MLN-4760 Analogues

The ^{18}F-fluorination of a target molecule of interest must be validated experimentally to ascertain the feasibility of radiolabelling. Late-stage ^{18}F-incorporation is generally preferred due to the short half-life of fluorine-18 (110 min), as extensive synthetic modifications following ^{18}F-fluorination lead to radioactive decay and a reduction in molar activity prior to in vivo administration for PET imaging. However, not all molecules are amenable to ^{18}F-fluorination, as the functional group compatibility of different radiolabelling technologies varies.

To mitigate these risks, Gouverneur and co-workers introduced a derisking strategy for Cu(II)-mediated ^{18}F-fluorination in 2017. This approach employs robustness screening of key structural motifs to assess functional group and heterocycle tolerance as shown in Scheme 3.4.[28] As illustrated, direct ^{18}F-fluorination of a molecule containing multiple heterocycles (A, B, C, D) poses a high risk of failure. If, for example, heterocycle A is incompatible while heterocycles B, C, and D are tolerated, and the full ABCD system fails due to A, an alternative strategy would be to introduce A after ^{18}F-labelling.

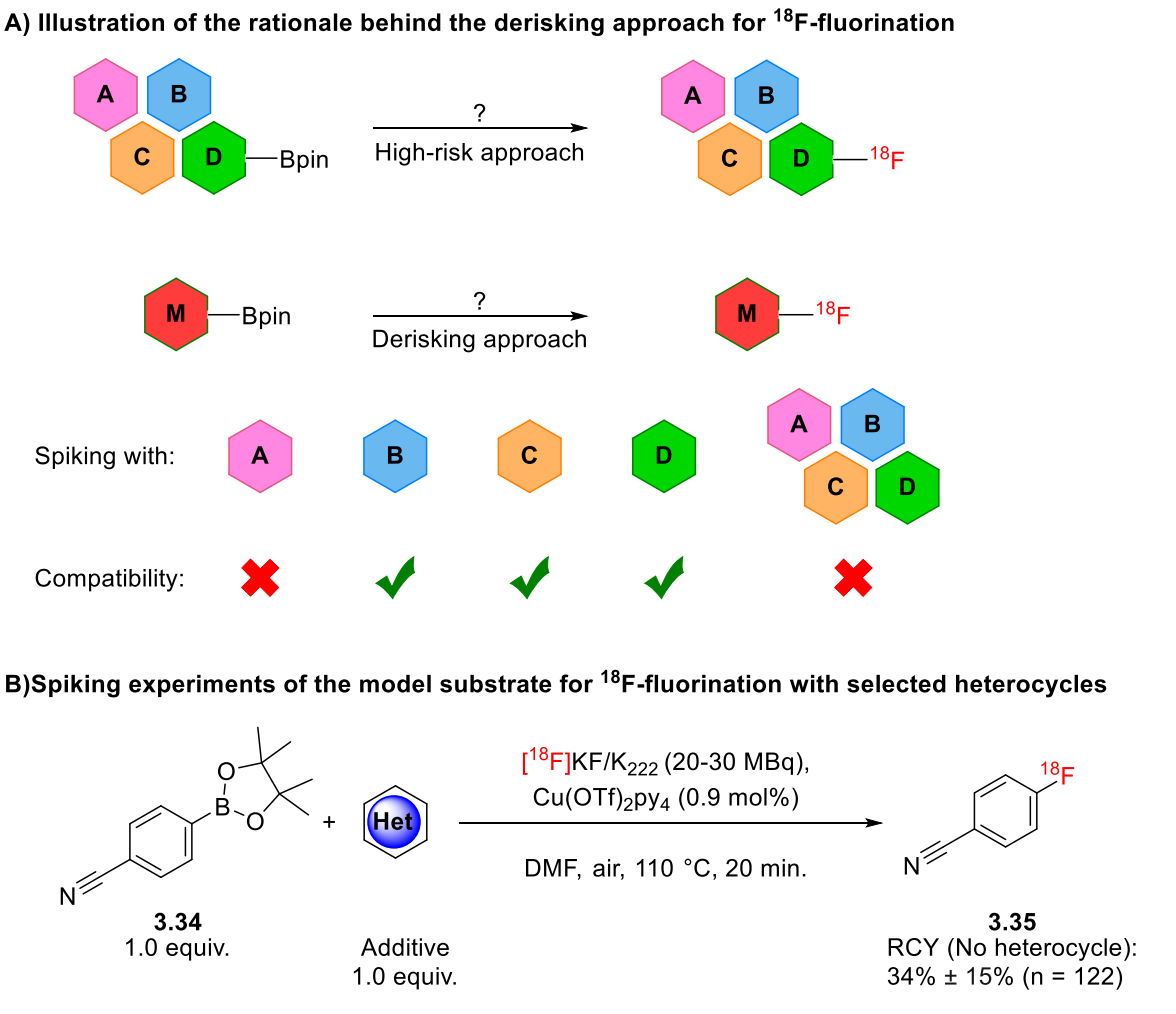

Scheme 3.4: Derisking approach for Cu(II)-mediated ^{18}F-fluorination. A) Illustration of the rationale behind the derisking approach for ^{18}F-fluorination; B) Spiking experiments of the model substrate for ^{18}F-fluorination with selected heterocycles.

In this study, the model reaction with 4-(4,4,5,5-tetramethyl-1,3,2-dioxaborolan-2-yl)benzonitrile **3.34** as a representative aryl Bpin affords an RCY of 34% ± 15%

across 122 trials without additives as illustrated in Scheme 3.4B.[28] Late-stage ^{18}F-fluorination may be feasible if additives do not significantly compromise RCY. To assess whether a heterocycle is tolerated, one equivalent of the heterocycle is added to the reaction mixture, and its impact on RCY is evaluated. Among 90+ heterocycles studied, imidazole and benzimidazole derivatives were selected here due to their relevance to our target MLN-4760 analogues. RCY data show that unprotected imidazole and benzimidazole are not tolerated, while *N*-methyl imidazole improves RCY to 7% ± 0% (unsubstituted), 30% ± 1% (C2-substituted), and 70% ± 8% (C4-substituted). Benzimidazole remains incompatible, with *N*-methyl protection ineffective and Boc protection yielding only 8% ± 1%.

These findings informed the design of our target precursor, prompting a series of robustness screening experiments using MLN-4760 analogue motifs as presented in Scheme 3.5. The benchmark Cu(II)-mediated ^{18}F-fluorination, performed without additives, proceeded efficiently, affording a radiochemical yield of 98% ± 1% (n = 2). In contrast, spiking with the histidine derivative bearing an unprotected primary amine (*S*)-**3.36** markedly suppressed fluorination, consistent with the high nucleophilicity and strong coordinating ability of primary amines, which can sequester copper or competitively bind to the organocopper intermediate, thereby disrupting the process.[24] To mitigate this, amine protection strategies were evaluated. Both the *N*-Boc-protected ((*S*)-**3.37**, RCY = 97% ± 2%) and N-Ns-protected ((*S*)-**3.38**, RCY = 95% ± 1%) histidine derivatives preserved fluorination efficiency, confirming that suitable protection preserves reaction efficiency. Furthermore, spiking with the

protected fluorinated MLN-4760 analogue (*S*,*S*)-**3.39** also had no adverse effect (RCY = 96% ± 2%). In this case, the secondary amine remained unprotected, yet as it is substituted with large substituents this likely minimised its ability to coordinate to copper, thereby maintaining high yields. This is particularly advantageous, as attempts to protect the secondary amine were challenging due to facile deprotection and degradation during silica gel chromatography, which complicated purification. Avoiding this step also reduced the number of synthetic steps required.

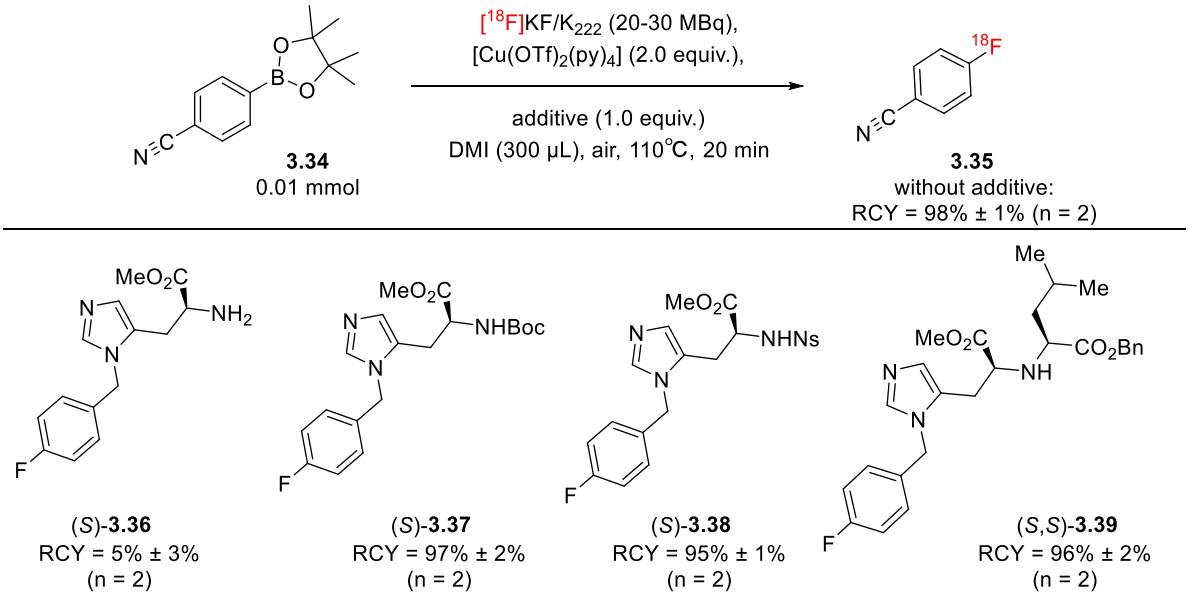

Scheme 3.5: Robustness screening experiments of MLN-4760 analogue motifs as additives in a model ^{18}F-fluorination reaction.

Building on these results, we proposed a retrosynthetic strategy depicted in Scheme 3.6 for the [^{18}F]MLN-4760 analogues, illustrated with the *para*-^{18}F-fluorinated analogue [^{18}F](*S*,*S*)-**3.1**. The route comprises Cu(II)-mediated ^{18}F-fluorination of the boronic ester precursor (*S*,*S*)-**3.41** to afford the protected intermediate [^{18}F](*S*,*S*)-**3.40**, followed by post-labelling hydrolysis to yield the target radiotracer.

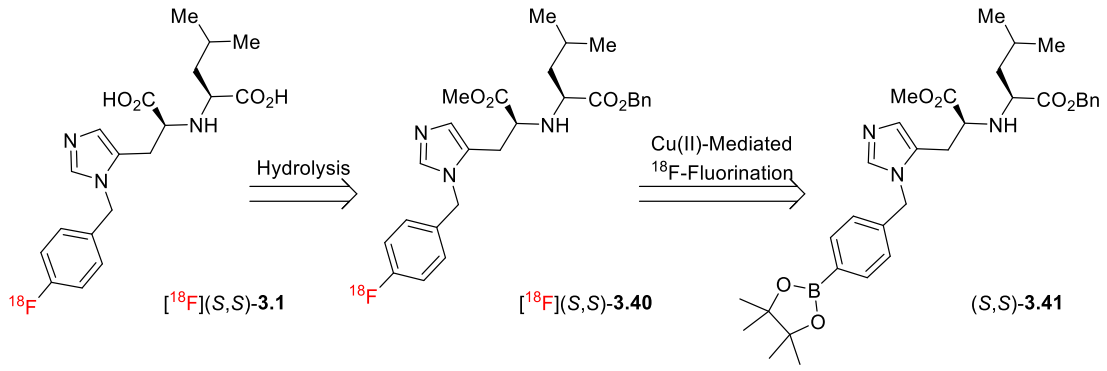

Scheme 3.6: Proposed retrosynthesis of [^{18}F]MLN-4760 analogue (*S*,*S*)-**3.1**.

3.2.2 Synthesis of Bpin Precursors for ^{18}F-Fluorination

The synthesis of aryl pinacol boronic ester (Bpin) precursors for radiofluorination was adapted from the novel MLN-4760 analogue synthesis described in Chapter 2 and is detailed in Scheme 3.7. The *para*-Bpin precursor (*S*,*S*)-**3.41** was selected as an initial target owing to its structural simplicity, while the *meta*-chloro-Bpin precursor (*S*,*S*)-**3.49** was prioritised due to the high in vitro potency of its corresponding fluorinated analogue (*S*,*S*)-**2.3** as described in Chapter 2. Both syntheses commenced from the common intermediate (*S*,*S*)-**3.44**, obtained in three steps from (*S*)-**3.42** and (*R*)-**3.43**. Benzylation with 4-bromobenzyl alcohol **3.45** or 3-bromo-5-chlorobenzyl alcohol **3.46** afforded (*S*,*S*)-**3.47** in 44% yield and (*S*,*S*)-**3.48** in 40% yield, respectively.

Final Miyaura borylation reaction conditions were optimised for each target. For (*S*,*S*)-**3.41**, a more efficient reaction protocol using $Pd(OAc)_2$, 2-dicyclohexylphosphino-2',4',6'-triisopropylbiphenyl (XPhos), and KOAc produced the *para*-Bpin precursor in 30% yield after preparative HPLC. In contrast, for (*S*,*S*)-

3.49, the presence of both chlorine and bromine substituents necessitated milder conditions to avoid diborylation.[29] Using Pd(dppf)Cl_2 instead of the Pd(OAc)$_2$/XPhos system enabled selective borylation of the bromide, affording the *meta*-chloro-Bpin precursor (*S*,*S*)-**3.49** in 67% yield.

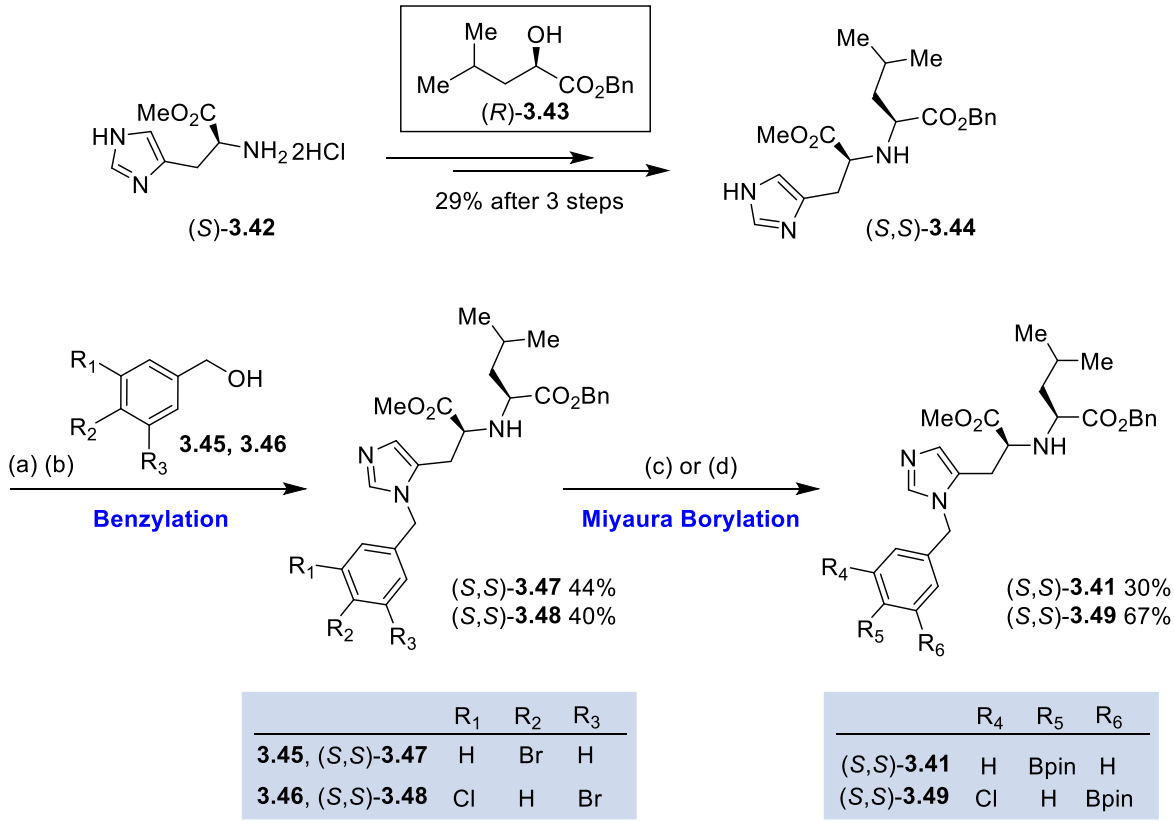

	R_1	R_2	R_3
3.45, (*S*,*S*)-**3.47**	H	Br	H
3.46, (*S*,*S*)-**3.48**	Cl	H	Br

	R_4	R_5	R_6
(*S*,*S*)-**3.41**	H	Bpin	H
(*S*,*S*)-**3.49**	Cl	H	Bpin

Scheme 3.7: Synthesis of aryl pinacol boronic ester precursors. Reagents and conditions: (a) (*S,S*)-**3.44** (1.1 equiv.), Boc_2O (2.2 equiv.), DIPEA (2.0 equiv.), CH_2Cl_2, rt, 24 h, isolated as crude, then (b) $(CF_3SO_2)_2O$ (1.0 equiv.), **3.45** or **3.46** (1.0 equiv.), DIPEA (1.5 equiv.), -78 °C to rt, 24 h, then HCl (4.0 M in dioxane, 1.1 equiv.), rt, 1 h, (*S,S*)-**3.47** 44%, (*S,S*)-**3.48** 40%; (c) (*S,S*)-**3.47** (1.0 equiv.), bis(pinacolato)diboron (2.2 equiv.), Pd(OAc)$_2$ (2 mol%), XPhos (4 mol%), KOAc (3.0 equiv.). degassed 1,4-dioxane, 110 °C, 20 minutes, then preparative HPLC purification, (*S,S*)-**3.41** 30%; (d) (*S,S*)-**3.48** (1.0 equiv.), bis(pinacolato)diboron (2.2 equiv.), Pd(dppf)Cl_2 (2 mol%), KOAc (3.0 equiv.), degassed 1,4-dioxane, 110 °C, 30 min, (*S,S*)-**3.49** 67%. XPhos = 2-dicyclohexylphosphino-2',4',6'-triisopropylbiphenyl.

3.2.3 Radiosynthesis of the [^{18}F]MLN-4760 Analogues

3.2.3.1 Radiosynthesis of Analogue [^{18}F](*S*,*S*)-3.1

The radiofluorination of the Bpin precursors was performed using the Cu(II)-mediated ^{18}F-fluorination approach. [^{18}F]Fluoride was first isolated from [^{18}O]water via an anion exchange quaternary methylammonium (QMA) cartridge. The cartridge was pre-activated with 10 mL of water and subsequently eluted with a solution containing K_{222} (7.5 mg) and K_2CO_3 (1.5 mg) in a 4:1 mixture of acetonitrile (MeCN) and water (0.75 mL). The eluate was transferred to the reactor and dried azeotropically with additional MeCN at 110 °C to remove any residual water. The resulting dry residue was re-dissolved in MeCN and dispensed into a 3 mL syringe. An aliquot of the [^{18}F]KF.K_{222} solution (5-20 MBq) in MeCN (approximately 20 µL) was then added to a 3 mL vial containing a solution (300 µL) of (*S*,*S*)-**3.41** and $Cu(OTf)_2py_4$ in either 1,3-dimethyl-2-imidazolidinone (DMI) or *N*,*N*-dimethylacetamide (DMA). The reaction vessel was purged with air to create an aerobic environment, and the mixture was stirred at 110 °C for 20 minutes. After the reaction, the mixture was cooled to room temperature, and an aliquot was taken for analysis by radioHPLC to determine the product identity and its radiochemical yield.

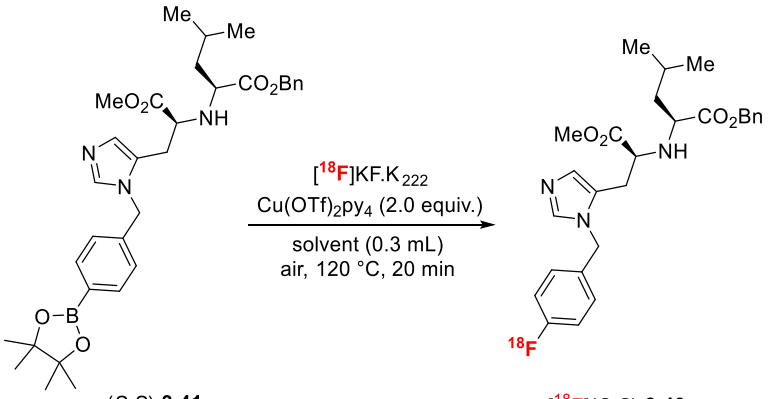

(*S*,*S*)-**3.41** [^{18}F](*S*,*S*)-**3.40**

Entry	(*S*,*S*)-3.41 loading	Solvent	RCY_{HPLC} of [^{18}F](*S*,*S*)-3.40
1	5.0 µmol	DMI	24% ± 7% (*n* = 2)
2	5.0 µmol	DMA	18% (*n* = 1)
3	3.3 µmol	DMI	17% (*n* = 1)

Table 3.3: Cu(II)-mediated ^{18}F-radiolabelling of (*S*,*S*)-**3.41** to obtain [^{18}F](*S*,*S*)-**3.40**. RCY_{HPLC}= radiochemical yield, determined by radio-HPLC analysis of the crude reaction mixture; DMI = 1,3-dimethyl-2-imidazolidinone; DMA = *N*,*N*-dimethylacetamide.

Initial radiolabelling efforts targeted the protected analogue [^{18}F](*S*,*S*)-**3.40** to validate the synthetic route. Table 3.3 illustrates the reaction optimisation which focused on precursor loading and solvent choice. Reducing (*S*,*S*)-**3.41** loading from 5.0 µmol to 3.3 µmol lowered the HPLC radiochemical yield (RCY_{HPLC}) from 24% to 17%. Substituting DMI with DMA decreased the RCY_{HPLC} from 24% to 18%, confirming DMI as the optimal solvent for Cu(II)-mediated radiofluorination. Under the optimised conditions using 5.0 µmol of (*S*,*S*)-**3.41** with 2.0 equivalents of $Cu(OTf)_2py_4$ in DMI, the highest RCY_{HPLC} achieved was 24% ± 7% (n = 2).

The identity of [^{18}F](*S*,*S*)-**3.40** was confirmed by radioHPLC, with its chromatographic profile matching that of the authentic [^{19}F](*S*,*S*)-**3.40** reference

under identical analytical conditions as shown in Figure 3.4. The detection of a distinct product peak by radioHPLC, with a retention time well-aligned to the non-radioactive reference, confirms the successful formation of [^{18}F](*S*,*S*)-**3.40**.

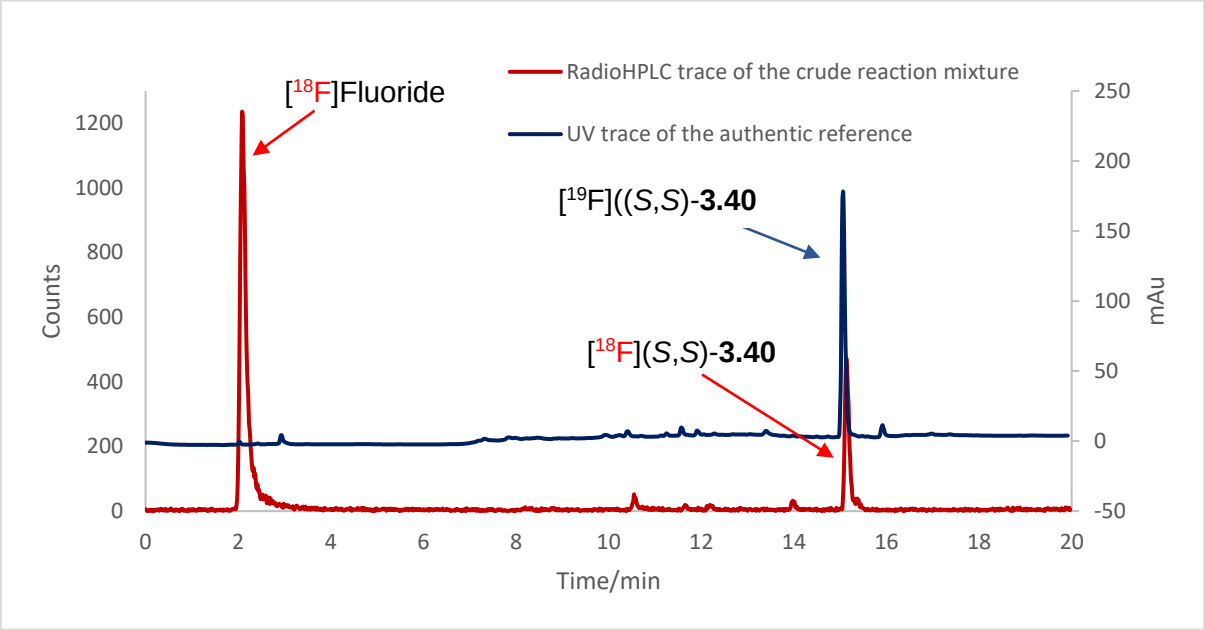

Figure 3.4: Radiochromatogram (red) obtained from the radioHPLC analysis of [^{18}F](*S*,*S*)-**3.40** overlaid with the UV chromatogram of the reference standard (*S*,*S*)-**3.40** (blue, λ = 220 nm).

Following the validation of ^{18}F-fluorination of the protected Bpin precursor (*S*,*S*)-**3.40**, we investigated a two-step, one-pot radiofluorination strategy to synthesise the [^{18}F]MLN-4760 analogue [^{18}F](*S*,*S*)-**3.1**, incorporating a post-labelling deprotection step of [^{18}F](*S*,*S*)-**3.40** as presented in Table 3.4. After completion of the initial ^{18}F-fluorination, the reaction mixture was cooled to room temperature, and an aqueous solution of NaOH (1.0 M, 0.1 mL) was added. The mixture was subsequently heated at 65 °C for 20 minutes to induce basic hydrolysis. Upon cooling, the reaction was neutralised with aqueous HCl (1.0 M, 0.1 mL). An aliquot was then taken for analysis

by radio-HPLC (Phenomenex Kinetex C18 column, MeCN/H_2O with 0.1% TFA) to confirm product identity and determine the radiochemical yield. The results indicate that no residual intermediate ([^{18}F](*S*,*S*)-**3.40**) was detected, suggesting complete conversion to [^{18}F](*S*,*S*)-**3.1**. The average RCY_{HPLC} over the two-step process was 18% ± 8% (*n* = 2). As shown in Figure 3.5, the overlay of the radiochromatogram of [^{18}F](*S*,*S*)-**3.1** and the UV chromatogram of its authentic ^{19}F reference both exhibit the same retention time under identical elution conditions, confirming its identity.

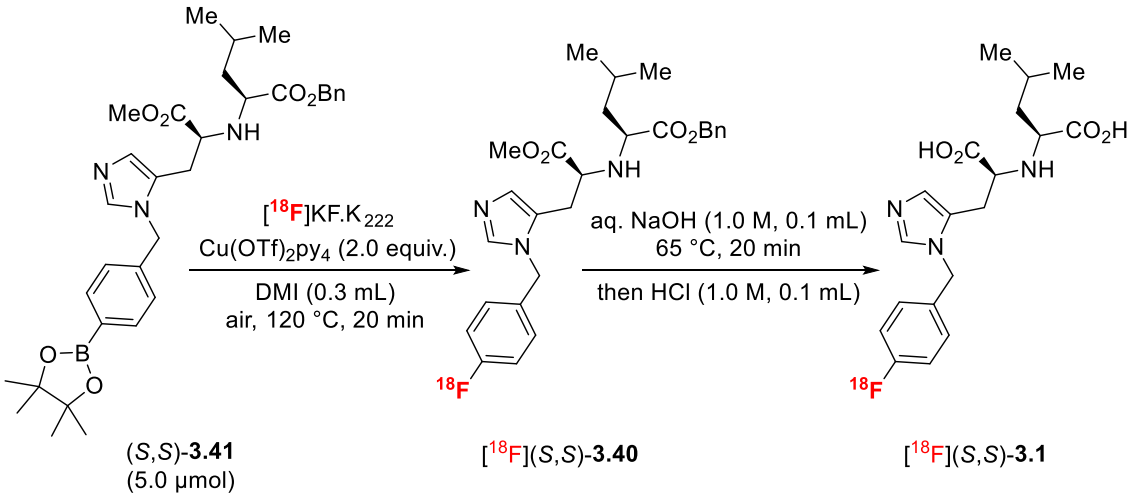

Entry	[^{18}F](*S*,*S*)-3.40 remaining	RCY_{HPLC} of [^{18}F](*S*,*S*)-3.1 (over two steps)
1	0%	25%
2	0%	10%
Average	0% (*n* = 2)	18% ± 8% (*n* = 2)

Table 3.4: Cu(II)-mediated ^{18}F-radiolabelling of (*S*,*S*)-**3.40** followed by a basic hydrolysis to obtain [^{18}F](*S*,*S*)-**3.1**. RCY_{HPLC}= radiochemical yield, determined by radio-HPLC analysis of the crude reaction mixture; DMI = 1,3-dimethyl-2-imidazolidinone.

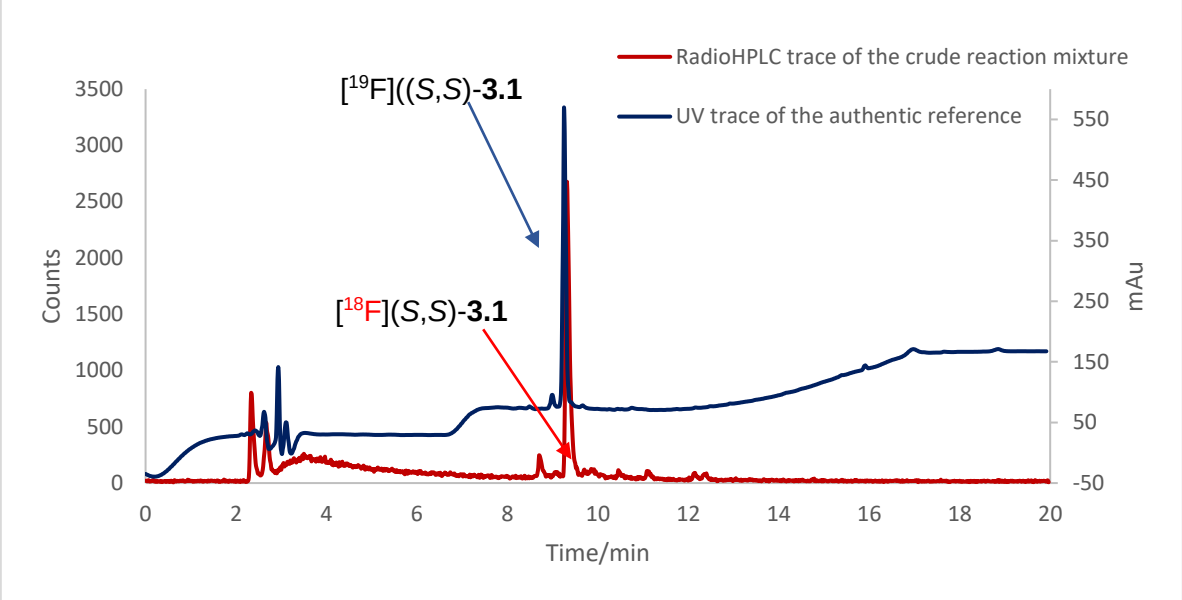

Figure 3.5: Radiochromatogram (red) obtained from the radioHPLC analysis of [^{18}F](*S*,*S*)-**3.1** overlaid with the UV chromatogram of the reference standard [^{19}F](*S*,*S*)-**3.1** (blue, λ = 220 nm).

3.2.3.1 Radiosynthesis of Analogue [^{18}F](*S*,*S*)-3.2

Applying the validated two-step radiofluorination with post-labelling deprotection optimised for [^{18}F](*S*,*S*)-**3.1**, the [^{18}F]MLN-4760 analogue [^{18}F](*S*,*S*)-**3.2** was then synthesised (Table 3.5). As previously observed for [^{18}F](*S*,*S*)-**3.1,** no residual intermediate ([^{18}F](*S*,*S*)-**3.50**) was observed in the deprotection step, indicating complete conversion. The mean RCY_{HPLC} over two steps was 8% ± 3% (n = 2). Identity of [^{18}F](*S*,*S*)-**3.2** was confirmed in Figure 3.6 by the overlap of the product radiochromatogram with the UV chromatogram of the non-radioactive reference under identical conditions.

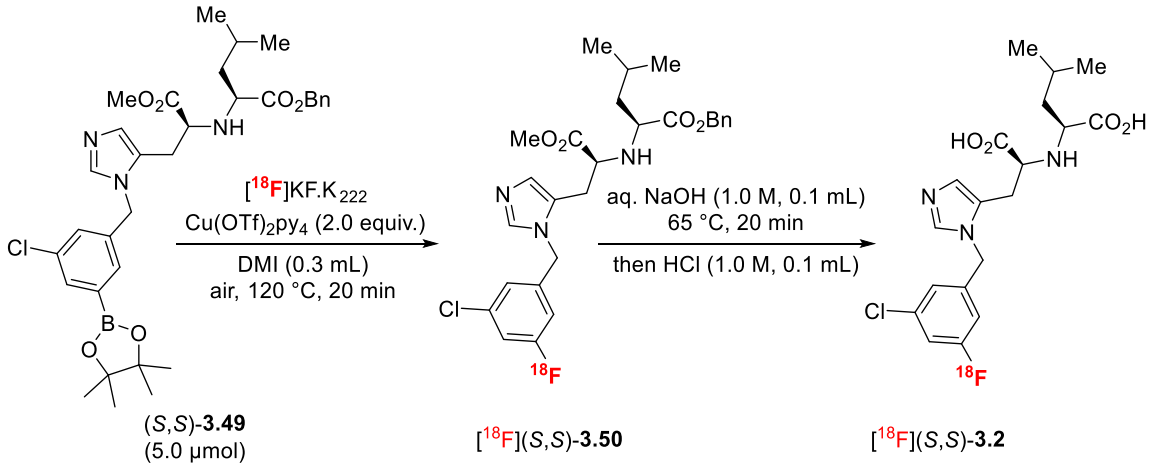

(*S*,*S*)-**3.49** (5.0 µmol)

[^{18}F](*S*,*S*)-**3.50**

[^{18}F](*S*,*S*)-**3.2**

Entry	[^{18}F](*S*,*S*)-3.50 remaining	RCY$_{HPLC}$ of [^{18}F](*S*,*S*)-3.2 (over two steps)
1	0%	10%
2	0%	5%
Average	0% (*n* = 2)	8% ± 3% (*n* = 2)

Table 3.5: Cu(II)-mediated ^{18}F-radiolabelling of (*S*,*S*)-**3.50** followed by a basic hydrolysis to obtain [^{18}F](*S*,*S*)-**3.2**. RCY$_{HPLC}$= radiochemical yield, determined by radio-HPLC analysis of the crude reaction mixture; DMI = 1,3-dimethyl-2-imidazolidinone.

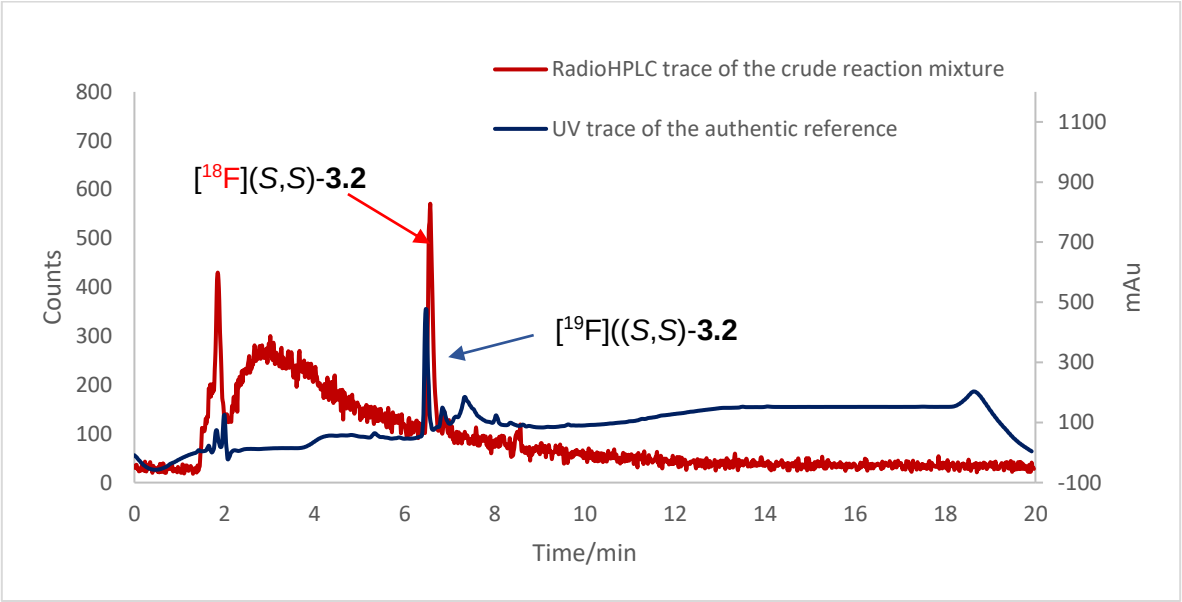

Figure 3.6: Radiochromatogram (red) obtained from the radioHPLC analysis of [^{18}F](*S*,*S*)-**3.2** overlaid with the UV chromatogram of the reference standard [^{19}F](*S*,*S*)-**3.2** (blue, λ = 220 nm).

3.3 Conclusion and Future Outlook

In this chapter, we synthesised two [^{18}F]MLN-4760 analogues, [^{18}F](*S*,*S*)-**3.1** and [^{18}F](*S*,*S*)-**3.2**. Their Bpin precursors were prepared using our novel synthetic route incorporating an optimised Miyaura borylation, followed by a two-step Cu(II)-mediated ^{18}F-fluorination and post-labelling deprotection sequence to afford the radiolabelled products. The method proved robust and reproducible, enabling efficient incorporation of fluorine-18 into MLN-4760 analogues. These advances provide a foundation for developing ACE2 PET tracers.

Ongoing radiolabelling efforts aim to label additional analogues, refine synthesis conditions, and improve radiochemical yields in the process. Beyond tracer development, in vivo PET imaging studies could be used to evaluate the pharmacokinetics, biodistribution, and target specificity of these ^{18}F-labelled ACE2 inhibitors. These studies will provide essential data on the tracer's uptake, clearance, and specificity in relevant disease models.

3.4 References

(1) Wang, X.; He, J.; Hosseini-Gerami, L.; Thomas, M.; Thompson, S.; Ford, J.; Ortalli, S.; Chen, Z.; Destro, G.; Bender, A. Synthesis and Inhibitory Assessment of ACE2 Inhibitors for SARS-CoV-2: An In Silico and In Vitro Study. *J. Org. Chem.* **2025**, *90* (30), 10941–10947.

(2) García-Ayllón, M. S.; Moreno-Pérez, O.; García-Arriaza, J.; Ramos-Rincón, J. M.; Cortés-Gómez, M. Á.; Brinkmalm, G.; Andrés, M.; León-Ramírez, J. M.; Boix, V.; Gil, J. Plasma ACE2 species are differentially altered in COVID-19 patients. *FASEB J.* **2021**, *35* (8), e21745.

(3) Wijnant, S. R.; Jacobs, M.; Van Eeckhoutte, H. P.; Lapauw, B.; Joos, G. F.; Bracke, K. R.; Brusselle, G. G. Expression of ACE2, the SARS-CoV-2 receptor, in lung tissue of patients with type 2 diabetes. *Diabetes* **2020**, *69* (12), 2691–2699.

(4) Beyerstedt, S.; Casaro, E. B.; Rangel, É. B. COVID-19: angiotensin-converting enzyme 2 (ACE2) expression and tissue susceptibility to SARS-CoV-2 infection. *Eur. J. Clin. Microbiol. Infect. Dis.* **2021**, *40* (5), 905–919.

(5) Su, H.; Yang, M.; Wan, C.; Yi, L.-X.; Tang, F.; Zhu, H.-Y.; Yi, F.; Yang, H.-C.; Fogo, A. B.; Nie, X. Renal histopathological analysis of 26 postmortem findings of patients with COVID-19 in China. *Kidney Int.* **2020**, *98* (1), 219–227.

(6) Xu, W.; Langhans, S. A.; Johnson, D. K.; Stauff, E.; Kandula, V. V.; Kecskemethy, H. H.; Averill, L. W.; Yue, X. Radiotracers for Molecular Imaging of Angiotensin-Converting Enzyme 2. *Int. J. Mol. Sci.* **2024**, *25* (17), 9419.

(7) Zhu, H.; Zhang, H.; Zhou, N.; Ding, J.; Jiang, J.; Liu, T.; Liu, Z.; Wang, F.; Zhang, Q.; Zhang, Z. Molecular PET/CT profiling of ACE2 expression in vivo: implications for infection and outcome from SARS-CoV-2. *Adv. Sci.* **2021**, *8* (16), 2100965.

(8) Ren, F.; Jiang, H.; Shi, L.; Zhang, L.; Li, X.; Lu, Q.; Li, Q. 68Ga-cyc-DX600 PET/CT in ACE2-targeted tumor imaging. *Eur. J. Nucl. Med. Mol. Imag.* **2023**, *50* (7), 2056–2067.

(9) Li, R.; Xu, A.; Cheng, C.; Chen, J.; Wang, M.; Luo, X.; Liang, S.; Hou, W.; Cui, B.; Feng, Y. ACE2 PET in healthy and diseased conditions. *View* **2023**, *4* (5), 20230009.

(10) Li, X.; Yin, W.; Li, A.; Li, D.; Gao, X.; Wang, R.; Cui, B.; Qiu, S.; Li, R.; Jia, L. ACE2 PET to reveal the dynamic patterns of ACE2 recovery in an infection model with pseudocorona virus. *J. Med. Virol.* **2023**, *95* (2), e28470.

(11) Wang, Z.; Liu, Z.; Yang, L.; Ding, J.; Wang, F.; Liu, T.; Yang, Z.; Wang, C.; Zhu, H.; Liu, Y. Noninvasive mapping of angiotensin converting enzyme-2 in pigeons using micro positron emission tomography. *Life* **2022**, *12* (6), 793.

(12) Wang, Z.; Zhao, C.; Li, C.; Liu, S.; Ding, J.; He, C.; Liu, J.; Dong, B.; Yang, Z.; Liu, Q. Molecular PET/CT mapping of rhACE2 distribution and quantification in organs to aid in SARS-CoV-2 targeted therapy. *J. Med. Virol.* **2023**, *95* (11), e29221.

(13) Zhang, Q.; Liu, T.; Ding, J.; Zhou, N.; Yu, Z.; Ren, Y.; Qin, X.; Du, P.; Yang, Z.; Zhu, H. Evaluation of 68Ga-and 177Lu-labeled HZ20 angiotensin-converting enzyme 2-targeting peptides for tumor-specific imaging. *Mol. Pharm.* **2022**, *19* (11), 4149–4156.

(14) Parker, M. F.; Blecha, J.; Rosenberg, O.; Ohliger, M.; Flavell, R. R.; Wilson, D. M. Cyclic 68Ga-labeled peptides for specific detection of human angiotensin-converting enzyme 2. *J. Nucl. Med.* **2021**, *62* (11), 1631–1637.

(15) Li, X.; Li, J.; Zhou, P.; Li, D.; Wang, M.; Tong, Q.; Chen, J.; Zuo, C.; Zhang, L.; Li, R. The functional views on response of host rabbit post coronavirus vaccination via ACE2 PET. *Am. J. Nucl. Med. Mol. Imaging* **2023**, *13* (1), 43.

(16) Ding, J.; Zhang, Q.; Jiang, J.; Zhou, N.; Yu, Z.; Wang, Z.; Meng, X.; Daggumati, L.; Liu, T.; Wang, F. Preclinical evaluation and pilot clinical study of 18F-labeled inhibitor peptide for noninvasive positron emission tomography mapping of angiotensin converting enzyme 2. *ACS Pharmacol. Transl. Sci.* **2024**, *7* (6), 1758–1769.

(17) Wang, J.; Beyer, D.; Vaccarin, C.; He, Y.; Tanriver, M.; Benoit, R.; Deupi, X.; Mu, L.; Bode, J. W.; Schibli, R. Development of radiofluorinated MLN-4760 derivatives for PET imaging of the SARS-CoV-2 entry receptor ACE2. *Eur. J. Nucl. Med. Mol. Imag.* **2024**, *52* (1), 9–21.

(18) Zhou, P.; Ning, K.; Xue, S.; Li, Q.; Li, D.; Yang, H.; Liang, Z.; Li, R.; Yang, J.; Li, X. An ACE2 PET imaging agent derived from 18F/Cl exchange of MLN-4760 under phase transfer catalysis. *EJNMMI Radiopharm. Chem.* **2024**, *9* (1), 1–11.

(19) Tredwell, M.; Preshlock, S. M.; Taylor, N. J.; Gruber, S.; Huiban, M.; Passchier, J.; Mercier, J.; Génicot, C.; Gouverneur, V. A general copper-mediated nucleophilic 18F fluorination of arenes. *Angew. Chem. Int. Ed.* **2014**, *53* (30), 7751–7755.

(20) Javier, A.; Gianluca, D.; Cornelissen, B.; Véronique, G. Closing the gap between 19F and 18F chemistry. *EJNMMI Radiopharm. Chem.* **2021**, *6* (1).

(21) Casitas, A.; Canta, M.; Sola, M.; Costas, M.; Ribas, X. Nucleophilic aryl fluorination and aryl halide exchange mediated by a CuI/CuIII catalytic cycle. *J. Am. Chem. Soc.* **2011**, *133* (48), 19386–19392.

(22) Yao, B.; Wang, Z.-L.; Zhang, H.; Wang, D.-X.; Zhao, L.; Wang, M.-X. Cu (ClO4) 2-mediated arene C–H bond halogenations of azacalixaromatics using alkali metal halides as halogen sources. *J. Org. Chem.* **2012**, *77* (7), 3336–3340.

(23) Fier, P. S.; Luo, J.; Hartwig, J. F. Copper-mediated fluorination of arylboronate esters. Identification of a copper (III) fluoride complex. *J. Am. Chem. Soc.* **2013**, *135* (7), 2552–2559.

(24) Ye, Y.; Schimler, S. D.; Hanley, P. S.; Sanford, M. S. Cu (OTf) 2-mediated fluorination of aryltrifluoroborates with potassium fluoride. *J. Am. Chem. Soc.* **2013**, *135* (44), 16292–16295.

(25) Mossine, A. V.; Brooks, A. F.; Makaravage, K. J.; Miller, J. M.; Ichiishi, N.; Sanford, M. S.; Scott, P. J. Synthesis of [18F] arenes via the copper-mediated [18F] fluorination of boronic acids. *Org. Lett.* **2015**, *17* (23), 5780–5783.

(26) Makaravage, K. J.; Brooks, A. F.; Mossine, A. V.; Sanford, M. S.; Scott, P. J. Copper-mediated radiofluorination of arylstannanes with [18F] KF. *Org. Lett.* **2016**, *18* (20), 5440–5443.

(27) Hadjipaschalis, N.; Ortalli, S.; Chen, Z.; Paton, R. S.; Ford, J.; Tredwell, M.; Gouverneur, V. Ethyl pinacol boronates as advantageous precursors for copper-mediated radiofluorination. *Org. Lett.* **2025**.

(28) Taylor, N. J.; Emer, E.; Preshlock, S.; Schedler, M.; Tredwell, M.; Verhoog, S.; Mercier, J.; Genicot, C.; Gouverneur, V. Derisking the Cu-mediated ^{18}F-fluorination

of heterocyclic positron emission tomography radioligands. *J. Am. Chem. Soc.* **2017**, *139* (24), 8267–8276.

(29) Ishiyama, T.; Murata, M.; Miyaura, N. Palladium (0)-catalyzed cross-coupling reaction of alkoxydiboron with haloarenes: a direct procedure for arylboronic esters. *J. Org. Chem.* **1995**, *60* (23), 7508–7510.

Chapter 4. Experimental

4.1 General Information

Reagents were obtained from commercial suppliers (Sigma-Aldrich, Alfa Aesar, Fluorochem, Apollo Scientific) and were used as received without further purification. For reactions to be carried out under inert conditions, reaction flasks and magnetic stirrers were flame-dried under vacuum and refilled with nitrogen. Dry solvents were obtained from commercial suppliers and dried using an MBRAUN-SPS solvent purification system. Reaction progress was tracked via thin-layer chromatography (TLC) using silica gel-coated aluminium sheets (Merck Kieselgel 60 F_{254} plates). TLC plates were visualised using ultraviolet light at 254 nm, and using ninhydrin as a stain for amino acid derivatives. Flash column chromatography was conducted with Merck silica gel (60, particle size 0.040-0.063 mm). Nuclear magnetic resonance (NMR) analyses were performed at 298 K, unless otherwise specified, using Bruker AVIIIHD 400, AVIIIHD 500, AVII 500 and NEO 600 spectrometers, and the data were processed using MestreNova 14.0 software or higher. Chemical shifts (δ) for ^{1}H, ^{19}F and ^{13}C NMR spectral data are reported in parts per million (ppm), referenced to the solvent peak using Bruker's internal referencing procedure (edlock), with ^{19}F NMR chemical shifts externally referenced to $CFCl_3$. Coupling constants (*J*) are reported in Hertz (Hz) to the nearest 0.1 Hz. ^{13}C spectra are recorded with proton decoupling, and the reported coupling constants correspond to ^{19}F–^{13}C heteronuclear coupling, unless stated otherwise. Peak multiplicities are described as s (singlet), d (doublet), t (triplet), q (quartet), pent (pentet), sept (septet), br (broad), or m (multiplet). High-resolution mass spectra (HRMS, m/z) were obtained using a Thermo Exactive mass

spectrometer combined with a Waters Acquity liquid chromatography system, utilising either the heated electrospray (HESI-II) probe for positive electrospray ionization (ESI+) or an atmospheric pressure chemical ionization (APCI) probe. Infrared spectra were taken either of neat samples or an evaporated solution (thin layer film) using a Bruker Tensor 27 FT-IR spectrometer, with absorptions reported in wavenumbers (cm^{-1}). Melting points for solid compounds were obtained using a Griffin apparatus and are uncorrected. Optical rotations were measured with a Schmidt-Haensch Autopol L 2000 polarimeter at 25 °C, with measurements at λ_{max} = 589 nm recorded as $[\alpha]_D^{25\ ^\circ C}$, with the concentration (in units of g/100 ml) and solvent specified.

4.2 Procedures and Characterisation for Chapter 2

((*S*)-1-Carboxy-2-(1-(4-fluorobenzyl)-1*H*-imidazol-5-yl)ethyl)-*L*-leucine ((*S*,*S*)-2.1)

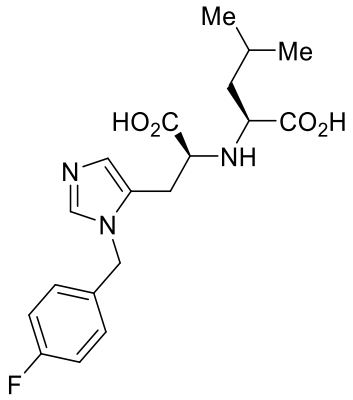

(*S,S*)-**2.29** and (*S,R*)-**2.29** mixture (100 mg, 0.208 mmol, 1.0 equiv.) was subjected to hydrolysis using NaOH (24.9 mg, 0.623 mmol, 3.0 equiv.) in H_2O and MeOH (1:1, 0.415 mL, 0.5 M). The resulting mixture was stirred for 1 hour at room temperature, followed by the addition of aqueous HCl (1.0 M) to adjust the pH to 7.0. The mixture was stirred for an additional 30 minutes and then concentrated under reduced pressure and obtained the crude mixture (27.5 mg, 0.073 mmol, 35%, 57:43 *d.r.*). The crude product was separated and purified using preparative HPLC to obtain (*S,S*)-**2.1** as a white solid (12.0 mg, 31.8 µmol, 15%).

Alternative modified procedure: (*S,S*)-**2.29** (100 mg, 0.208 mmol, 1.0 equiv.) was subjected to hydrolysis using NaOH (24.9 mg, 0.623 mmol, 3.0 equiv.) in H_2O and MeOH (1:1, 0.415 mL, 0.5 M). The resulting mixture was stirred for 1 hour at room temperature, followed by the addition of aqueous HCl (1.0 M) to adjust the pH to 7.0.

The mixture was stirred for an additional 30 minutes and then concentrated under reduced pressure and obtained the crude product (74.0 mg, 0.196 mmol, 94%, > 20:1 d.r.). The crude product was further purified using preparative HPLC to obtain (*S,S*)-**2.1** as a white solid (38.0 mg, 101 μmol, 48%).

Reverse phase HPLC details: Phenomenex Kinetex® 5 μm C18 100 Å, 250 x 4.6 mm, flow rate = 7 mL/min, column temperature = 25 °C, eluent = 10% MeCN (0.1% TFA) and 90% H_2O (0.1% TFA) for 25 min, retention time = 11.6 min.

^{1}H NMR (500 MHz, D_2O) δ 8.67 (d, *J* = 1.7 Hz, 1H), 7.53 (d, *J* = 1.5 Hz, 1H), 7.41 – 7.33 (m, 2H), 7.24 – 7.18 (m, 2H), 5.43 – 5.39 (m, 2H), 3.69 – 3.63 (m, 1H), 3.58 – 3.55 (m, 1H), 3.31 – 3.29 (m, 1H), 3.29 – 3.27 (m, 1H), 1.83 – 1.75 (m, 1H), 1.73 – 1.68 (m, 2H), 0.94 (d, *J* = 4.4 Hz, 3H), 0.93 (d, *J* = 4.6 Hz, 3H).

^{13}C{^{1}H} NMR (126 MHz, D_2O) δ 173.8, 171.0, 162.8 (d, *J* = 246.1 Hz), 135.6, 130.3 (d, *J* = 8.6 Hz), 129.0, 128.6 (d, *J* = 3.2 Hz), 119.2, 116.2 (d, *J* = 21.8 Hz), 61.9, 60.4, 49.9, 39.7, 24.8, 24.3, 21.7, 21.3.

^{19}F NMR (471 MHz, D_2O) δ -115.60 (tt, *J* = 10.4, 5.2 Hz).

HRMS (ESI^+) m/z: $[M+H]^+$ Calcd for $C_{19}H_{25}FN_3O_4$ 378.1824; Found 378.1821.

IR (thin layer film) ν (cm^{-1}) 3449, 3125, 3051, 2971, 2943, 2879, 1744, 1682, 1620, 1514, 1465, 1436, 1388, 1304, 1187, 1041, 939, 841, 825, 798, 724, 687, 657.

MP 198–200 °C.

$[\alpha]_D^{25\,°C}$ +32.2 (c 0.015, H_2O).

((*S*)-1-Carboxy-2-(1-(4-fluorobenzyl)-1*H*-imidazol-5-yl)ethyl)-*D*-leucine ((*S*,*R*)-2.1)

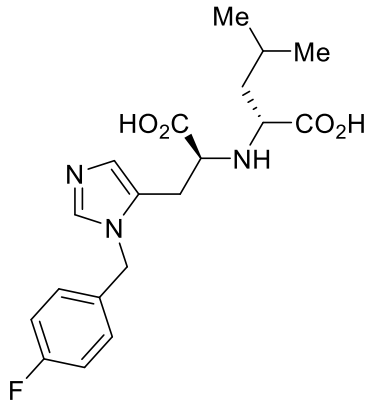

(*S*,*R*)-**2.29** (100 mg, 0.208 mmol, 1.0 equiv.) was subjected to hydrolysis using NaOH (24.9 mg, 0.623 mmol, 3.0 equiv.) in H_2O and MeOH (1:1, 0.415 mL, 0.5 M). The resulting mixture was stirred for 1 hour at room temperature, followed by the addition of aqueous HCl (1.0 M) to adjust the pH to 7.0. The mixture was stirred for an additional 30 minutes and then concentrated under reduced pressure and obtained the crude product (62.0 mg, 0.164 mmol, 79%, > 20:1 d.r.). The crude product was further purified using preparative HPLC to obtain the desired product as a white solid (35.0 mg, 92.7 μmol, 45%).

Reverse phase HPLC details: Phenomenex Kinetex® 5 μm C18 100 Å, 250 x 4.6 mm, flow rate = 7 mL/min, column temperature = 25 °C, eluent = 10% MeCN (0.1% TFA) and 90% H_2O (0.1% TFA) for 25 min, retention time = 13.9 min.

^{1}H NMR (500 MHz, D_2O) δ 8.73 – 8.70 (m, 1H), 7.49 – 7.45 (m, 1H), 7.40 – 7.32 (m, 2H), 7.26 – 7.18 (m, 2H), 5.48 – 5.38 (m, 2H), 3.71 – 3.64 (m, 1H), 3.56 – 3.50 (m,

1H), 3.33 – 3.21 (m, 2H), 1.75 – 1.60 (m, 2H), 1.59 – 1.50 (m, 1H), 0.93 – 0.87 (m, 6H).

$^{13}C\{^{1}H\}$ NMR (126 MHz, D_2O) δ 173.7, 171.1, 162.8 (d, *J* = 246.1 Hz), 135.6, 130.0 (d, *J* = 9.1 Hz), 129.2 (d, *J* = 2.8 Hz), 128.7 (d, *J* = 3.2 Hz), 119.1, 116.3 (d, *J* = 22.0 Hz), 60.1, 58.9, 49.9, 38.6, 24.6, 23.8, 21.8, 21.2.

^{19}F NMR (471 MHz, D_2O) δ -112.93 (tt, *J* = 10.4, 5.2 Hz, 1F).

HRMS (ESI$^+$) m/z: $[M+H]^+$ Calcd for $C_{19}H_{25}FN_3O_4$ 378.1824; Found 378.1825.

IR (thin layer film) v (cm^{-1}) 3449, 3124, 3046, 2971, 2943, 2880, 1744, 1676, 1621, 1515, 1464, 1436, 1388, 1304, 1188, 939, 841, 825, 798, 724, 636.

MP 198 - 200 °C.

$[\alpha]_D^{25\,°C}$ +3.5 (c 0.050, H_2O).

((*S*)-1-Carboxy-2-(1-(3-fluoro-5-methylbenzyl)-1*H*-imidazol-5-yl)ethyl)-*L*-leucine ((*S,S*)-2.2)

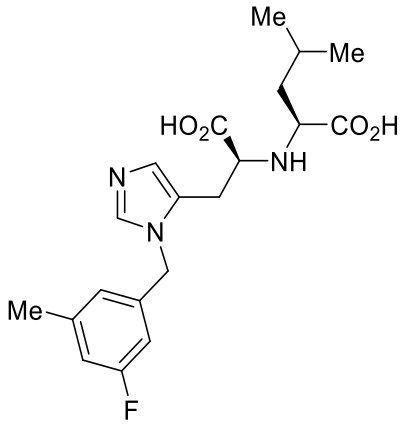

(*S,S*)-**2.58** (100 mg, 0.202 mmol, 1.0 equiv.) was subjected to hydrolysis using NaOH (24.2 mg, 0.606 mmol, 3.0 equiv.) in H_2O and MeOH (1:1, 0.404 mL, 0.5 M).

The resulting mixture was stirred for 1 hour at room temperature, followed by the addition of aqueous HCl (1.0 M) to adjust the pH to 7.0. The mixture was stirred for an additional 30 minutes and then concentrated under reduced pressure and obtained the crude product (68.0 mg, 0.174 mmol, 86%, > 20:1 d.r.). The crude product was further purified using preparative HPLC to obtain desired (*S,S*)-**2.2** as a white solid (35.0 mg, 89.4 μmol, 44%).

Reverse phase HPLC details: NUCLEODUR® RP-Säulen 5 μm C18 110 Å, 250 x 4.6 mm, flow rate = 15 mL/min, column temperature = 25 °C, eluent = gradient 2% - 55% MeCN/ H_2O (0.1% TFA) over 40 min, retention time = 17.9 min.

^{1}H NMR (500 MHz, D_2O) δ 8.77 (d, *J* = 1.7 Hz, 1H), 7.56 (d, *J* = 1.5 Hz, 1H), 7.09 – 7.01 (m, 1H), 6.98 – 6.95 (m, 1H), 6.92 – 6.86 (m, 1H), 5.45 – 5.41 (m, 2H), 3.78 – 3.68 (m, 2H), 3.31 – 3.29 (m, 1H), 3.29 – 3.27 (m, 1H), 2.35 (s, 3H), 1.86 – 1.78 (m, 1H), 1.77 – 1.68 (m, 2H), 0.97 – 0.93 (m, 6H).

^{13}C{^{1}H} NMR (126 MHz, D_2O) δ 173.7, 171.0, 162.8 (d, *J* = 246.1 Hz), 158.6, 135.6, 130.3 (d, *J* = 8.6 Hz), 128.9, 128.6 (d, *J* = 3.2 Hz), 119.2, 116.3, 116.2, 64.0, 61.9, 60.4, 49.9, 39.7, 24.8, 24.3, 21.6, 21.3.

^{19}F NMR (471 MHz, D_2O) δ -112.80 – -112.89 (m).

HRMS (ESI$^+$) m/z: $[M+H]^+$ Calcd for $C_{20}H_{27}FN_3O_4$ 392.1980; Found 392.1982.

IR (thin layer film) ν (cm^{-1}) 3657, 3343, 2980, 2972, 2887, 1770, 1636, 1471, 1463, 1380, 1252, 1160, 1130, 952, 817, 692.

MP 195 - 197 °C.

$[\alpha]_D^{25\,°C}$ +29.5 (c 0.070, H_2O).

((*S*)-1-Carboxy-2-(1-(3-chloro-5-fluorobenzyl)-1*H*-imidazol-5-yl)ethyl)-*L*-leucine ((*S,S*)-2.3)

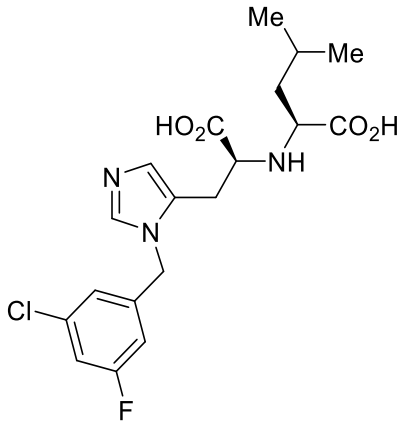

(*S,S*)-**2.59** (100 mg, 0.194 mmol, 1.0 equiv.) was subjected to hydrolysis using NaOH (23.3 mg, 0.581 mmol, 3.0 equiv.) in H_2O and MeOH (1:1, 0.388 mL, 0.5 M). The resulting mixture was stirred for 1 hour at room temperature, followed by the addition of aqueous HCl (1.0 M) to adjust the pH to 7.0. The mixture was stirred for an additional 30 minutes and then concentrated under reduced pressure and obtained the crude product (68.0 mg, 0.165 mmol, 85%, > 20:1 d.r.). The crude product was further purified using preparative HPLC to obtain desired (*S,S*)-**2.3** as a white solid (35.0 mg, 85.0 µmol, 44%).

Reverse phase HPLC details: NUCLEODUR® RP-Säulen 5 µm C18 110 Å, 250 x 4.6 mm, flow rate = 15 mL/min, column temperature = 25 °C, eluent = gradient 2% - 55% MeCN/ H_2O (0.1% TFA) over 40 min, retention time = 16.0 min.

^{1}H NMR (500 MHz, D_2O) δ 8.77 (d, *J* = 1.7 Hz, 1H), 7.43 (d, *J* = 1.5 Hz, 1H), 7.25 – 7.18 (m, 1H), 7.09 – 7.05 (m, 1H), 6.97 – 6.91 (m, 1H), 5.43 (d, *J* = 16.2 Hz, 1H), 5.37 (d, *J* = 16.2 Hz, 1H), 3.69 – 3.62 (m, 2H), 3.21 – 3.16 (m, 2H), 1.71 – 1.63 (m,

1H), 1.63 – 1.56 (m, 1H), 1.50 – 1.41 (m, 1H), 0.82 (d, *J* = 6.6 Hz, 3H), 0.80 (d, *J* = 6.6 Hz, 3H).

$^{13}C\{^{1}H\}$ NMR (126 MHz, D_2O) δ 173.1, 170.7, 163.8 (d, *J* = 245.1 Hz), 136.5 (d, *J* = 9.2 Hz), 136.0, 135.5 (d, *J* = 12.1 Hz), 129.0, 123.7, 119.4, 116.8 (d, *J* = 25.0 Hz), 113.5 (d, *J* = 22.7 Hz), 61.1, 60.1, 49.4, 39.5, 24.7, 24.3, 21.6, 21.3.

^{19}F NMR (471 MHz, D_2O) δ -110.03 – -110.15 (m, 1F).

HRMS (ESI^+) m/z: $[M+H]^+$ Calcd for $C_{19}H_{24}{}^{35}ClFN_3O_4$ 412.1434; Found 412.1435.

IR (thin layer film) v (cm^{-1}) 3568, 3216, 3122, 2980, 2928, 2889, 2859, 1677, 1622, 1515, 1436, 1387, 1189, 1141, 938, 798, 723, 656.

MP 201–203 °C.

$[\alpha]_D^{25\,°C}$ +27.4 (c 0.025, H_2O).

((*S*)-1-Carboxy-2-(1-(3-(2-fluoroethoxy)-5-methoxybenzyl)-1*H*-imidazol-5-yl)ethyl)-*L*-leucine ((*S,S)*-2.4)

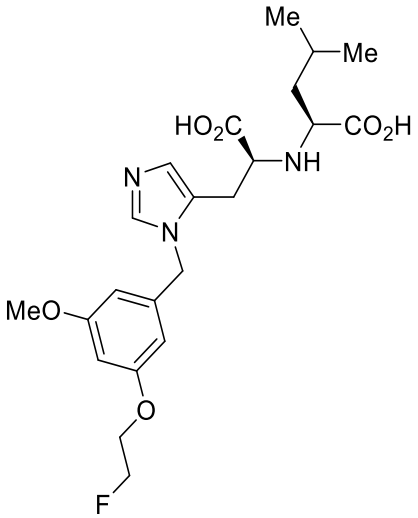

The protected (*S,S*)-**2.60** (100 mg, 0.180 mmol, 1.0 equiv.) was subjected to hydrolysis using NaOH (21.6 mg, 0.540 mmol, 3.0 equiv.) in H_2O and MeOH (1:1, 0.415 mL, 0.5 M). The resulting mixture was stirred for 1 hour at room temperature, followed by the addition of HCl (1.0 M) to adjust the pH to 7.0. The mixture was stirred for an additional 30 minutes and then concentrated under reduced pressure and obtained the crude product (67.0 mg, 0.148 mmol, 82%, > 20:1 *d.r.*). The crude product was further purified using preparative HPLC to obtain desired (*S,S*)-**2.4** as a white solid (40.0 mg, 88.6 µmol, 49%).

Reverse phase HPLC details: NUCLEODUR® RP-Säulen 5 µm C18 110 Å, 250 x 4.6 mm, flow rate = 15 mL/min, column temperature = 25 °C, eluent = gradient 2% - 55% MeCN/ H_2O (0.1% TFA) over 40 min, retention time = 24.0 min.

^{1}H NMR (500 MHz, D_2O) δ 8.75 (d, *J* = 1.5 Hz, 1H), 7.55 (d, *J* = 1.5 Hz, 1H), 6.67 (dd, *J* = 2.3, 2.3 Hz, 1H), 6.60 – 6.43 (m, 2H), 5.41 – 5.38 (m, 2H), 4.87 – 4.82 (m, 1H), 4.77 – 4.72 (m, 1H), 4.36 – 4.31 (m, 1H), 4.30 – 4.25 (m, 1H), 3.81 (s, 3H), 3.77 (dd, *J* = 7.2, 7.2 Hz, 1H), 3.71 (dd, *J* = 7.5, 6.1 Hz, 1H), 3.32 – 3.27 (m, 2H), 1.84 – 1.77 (m, 1H), 1.76 – 1.68 (m, 2H), 0.96 – 0.90 (m, 6H).

^{13}C{^{1}H} NMR (126 MHz, D_2O) δ 163.1, 162.8, 161.0, 159.8, 135.8, 135.5, 128.7, 119.4, 117.5, 115.2, 114.0, 106.9 (d, *J* = 6.8 Hz), 101.4, 82.6 (d, *J* = 164.4 Hz), 67.7 (d, *J* = 18.6 Hz), 55.6, 50.3, 39.2, 24.6, 24.3, 21.4, 21.2.

^{19}F NMR (471 MHz, D_2O) δ -223.30 – -223.49 (m, 1F).

HRMS (ESI$^+$) m/z: $[M+H]^+$ Calcd for $C_{22}H_{31}FN_3O_6$ 452.2191; Found 452.2192.

IR (thin layer film) ν (cm^{-1}) 3356, 3125, 2965, 2936, 1618, 1592, 1447, 1387, 1347, 1270, 1099, 1047, 986, 855, 670, 637.

MP 186–188 °C.

$[\alpha]_D^{25\,°C}$ +24.5 (c 0.015, H_2O).

Tert-butyl (*S*)-4-(2-((*tert*-butoxycarbonyl)amino)-3-methoxy-3-oxopropyl)-1*H*-imidazole-1-carboxylate ((*S*)-2.25)

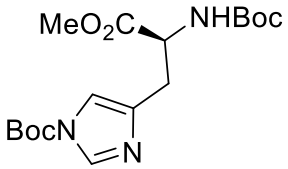

Di-*tert*-butyl dicarbonate (Boc_2O, 18.0 g, 82.6 mmol, 2.0 equiv.) in MeOH (20.0 mL) was added slowly via an addition funnel to a solution of (*S*)-histidine methyl ester dihydrochloride ((*S*)-**2.24**) (10.0 g, 41.3 mmol, 1.0 equiv.) and triethylamine (14.4 mL, 103 mmol, 2.5 equiv.) in MeOH (82.6 mL, 0.5 M). After 16 hours, the reaction mixture was concentrated *in vacuo*, and the residue was redissolved in dichloromethane (CH_2Cl_2) and H_2O (1:1, 40 mL). After separation, the organic phase was washed with brine (25 mL), dried over Na_2SO_4, filtered and concentrated to yield a colourless oil, which was then triturated with hexane, and further purified using flash column chromatography (35% EtOAc in pentane) to obtain the di-Boc protected imidazole (*S*)-**2.25** as white powder (13.3 g, 36.0 mmol, 87%).

R_f 0.33 (35% EtOAc/pentane).

^{1}H NMR (500 MHz, $CDCl_3$) δ 7.96 (d, *J* = 1.3 Hz, 1H), 7.12 (d, *J* = 1.3 Hz, 1H), 5.70 (d, *J* = 8.4 Hz, 1H), 4.59 – 4.52 (m, 1H), 3.71 (s, 3H), 3.08 – 2.97 (m, 2H), 1.58 (s, 9H), 1.42 (s, 9H).

^{13}C{^{1}H} NMR (126 MHz, $CDCl_3$) δ 172.4, 155.6, 147.0, 138.8, 137.0, 114.7, 85.7, 79.8, 53.3, 52.4, 30.4, 28.4, 28.0.

Characterisation data were in accordance with those found in the literature.[1]

Methyl *N*$^{\alpha}$-(*tert*-butoxycarbonyl)-*N*$^{\pi}$-(4-fluorobenzyl)-*L*-histidinate ((*S*)-2.27)

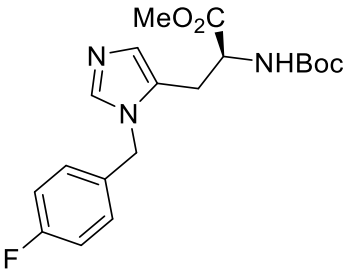

The synthesis of (*S*)-**2.27** was performed using a modified literature procedure.[2] Under anhydrous conditions, a solution of (4-fluorophenyl)methanol **2.26** (3.11 g, 24.7 mmol, 1.0 equiv.) and diisopropylethylamine (DIPEA, 4.59 mL, 29.6 mmol, 1.2 equiv.) in CH_2Cl_2 (10.6 mL) was added to a cooled (-78 °C) solution of trifluoromethanesulfonic anhydride (Tf_2O, 4.15 mL, 24.7 mmol, 1.0 equiv.) in CH_2Cl_2 (80.0 mL, 0.25 M). After stirring for 20 minutes at -78 °C, a solution of (*S*)-**2.25** (10.0 g, 27.1 mmol, 1.1 equiv.) in CH_2Cl_2 (8.0 mL) was then added to the reaction mixture and was left to stir at room temperature for 24 h. The reaction mixture was then concentrated under reduced pressure and was transferred to a separatory funnel

containing EtOAc (25 mL) and H_2O (25 mL). This was extracted with EtOAc (2 × 25 mL) and the combined organics were washed with brine (25 mL), dried over Na_2SO_4, and concentrated under reduced pressure to yield the crude product. The crude product was further purified using flash column chromatography (gradient 0– 5% MeOH in CH_2Cl_2) to obtain (*S*)-**2.27** as a viscous yellow oil (7.28 g, 19.3 mmol, 78%).

R_f 0.37 (5% MeOH/CH_2Cl_2).

^{1}H NMR (500 MHz, MeOD) δ 7.70 – 7.66 (m, 1H), 7.22 – 7.15 (m, 2H), 7.12 – 7.06 (m, 2H), 6.85 – 6.82 (m, 1H), 5.28 – 5.17 (m, 2H), 4.32 – 4.26 (m, 1H), 3.68 (s, 3H), 2.99 (dd, *J* = 15.5, 5.3 Hz, 1H), 2.85 (dd, *J* = 15.5, 9.1 Hz, 1H), 1.40 (s, 9H).

^{13}C{^{1}H} NMR (126 MHz, MeOD) δ 173.3, 163.8 (d, *J* = 245.3 Hz), 157.6, 139.3, 133.9 (d, *J* = 3.2 Hz), 130.1 (d, *J* = 8.2 Hz), 129.1, 128.5, 116.8 (d, *J* = 21.9 Hz), 80.7, 54.2, 52.8, 30.7, 28.7, 27.2.

^{19}F NMR (471 MHz, MeOD) δ -117.68 – -118.00 (m).

HRMS (ESI$^+$) m/z: $[M+H]^+$ Calcd for $C_{19}H_{25}FN_3O_4$ 378.1824; Found 378.1821.

IR (thin layer film) ν (cm^{-1}) 3119, 2981, 2955, 1745, 1709, 1607, 1513, 1438, 1366, 1276, 1255, 1225, 1161, 1101, 1056, 1031, 831, 771, 639.

$[\alpha]_D^{25\,°C}$ +13.1 (c 0.150, $CHCl_3$).

Benzyl 4-methyl-2-oxopentanoate (2.28)

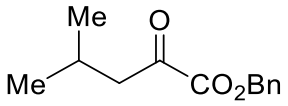

Benzyl alcohol (2.16 g, 20.0 mmol, 2.0 equiv.), 4-methyl-2-oxopentanoic acid (1.30 g, 10.0 mmol, 1.0 equiv.), and pyridine (2.0 mL, 25.0 mmol, 2.5 equiv.) were dissolved in anhydrous tetrahydrofuran (THF, 50 mL, 0.2 M) and the reaction mixture was cooled to 0 °C under inert atmosphere. Mesyl chloride (MsCl, 0.93 mL, 12.0 mmol, 1.2 equiv.) was added dropwise and the reaction mixture was warmed to room temperature and stirred for 18 hours. The reaction was quenched with water (20 mL) and extracted with Et_2O (3 × 20 mL). The organic layers were combined and dried over Na_2SO_4, filtered, and concentrated under reduced pressure. The resulting crude product was purified by flash column chromatography (5% ethyl acetate in pentane) to produce **2.28** as a colourless viscous oil (1.75 g, 7.94 mmol, 80%).

R_f 0.31 (10% diethyl ether/pentane).

^{1}H NMR (500 MHz, $CDCl_3$) δ 7.38 – 7.26 (m, 5H), 5.22 (s, 2H), 2.74 (d, *J* = 7.4 Hz, 2H), 2.30 – 2.23 (m, 1H), 0.93 (d, *J* = 7.3 Hz, 6H).

^{13}C{^{1}H} NMR (126 MHz, $CDCl_3$) δ 194.6, 162.0, 135.4, 128.6, 128.2, 128.2, 67.3, 47.5, 24.5, 22.4.

Characterisation data were in accordance with those found in the literature.[3]

Benzyl ((*S*)-3-(1-(4-fluorobenzyl)-1*H*-imidazol-5-yl)-1-methoxy-1-oxopropan-2-yl)leucinate((*S*,*S*)-2.29 + (*S*,*R*)-2.29)

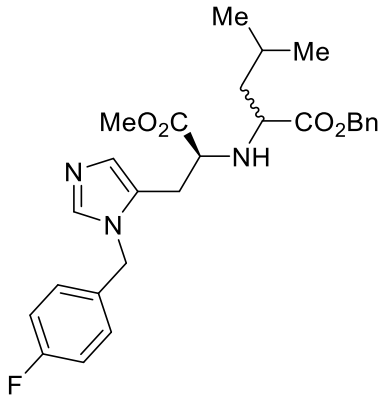

4N HCl in dioxane (50 mL, 20 equiv.) was added to (*S*)-**2.27** (3.77g, 10.0 mmol, 1.0 equiv.) and stirred for 2 hours at room temperature. Then the solution was concentrated under reduced pressure and the resulting di-HCl salt was triturated with ethyl acetate (EtOAc, 3 × 10 mL) to afford a white solid which was suspended in CH_2Cl_2 (100 mL, 0.1 M). triethylamine Et_3N (1.39 mL, 30.0 mmol, 3.0 equiv.) was added to the solution and stirred for 1 hour at room temperature. Subsequently, the 1,2-keto ester **2.28** (3.30 g, 15 mmol, 1.5 equiv.), acetic acid (572 mmL, 10.0 mmol, 1.0 equiv.) and 4Å molecular sieves were added and the mixture was stirred for another 2 hours. Sodium triacetoxyborohydride ($NaB(OAc)_3H$, 1.89 g, 30.0 mmol, 3.0 equiv.) was added slowly and stirred overnight. After 24 hours, saturated aqueous $NaHCO_3$ solution was added to raise the pH of the reaction mixture to 8 and was stirred for 1 hour. After phase separation, the aqueous phase was extracted with EtOAc (3 × 10 mL). The combined organic phases were dried over Na_2SO_4, filtered and concentrated under reduced pressure, and purified by flash column

chromatography (gradient 10-0% EtOAc in pentane, then gradient 0-5% MeOH in EtOAc) to afford the mixture (*S*,*S*)-**2.29** and (*S*,*R*)-**2.29** as a viscous yellow oil (1.49 g, 31%, 57:43 *d.r.*)

Benzyl ((*S*)-3-(1-(4-fluorobenzyl)-1*H*-imidazol-5-yl)-1-methoxy-1-oxopropan-2-yl)-*L*-leucinate ((*S*,*S*)-2.29)

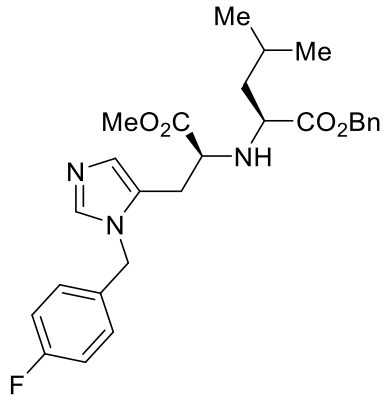

Triphenylphosphine (PPh_3, 189 mg, 0.720 mmol, 1.0 equiv.) and diisopropyl azodicarboxylate (DIAD, 141 µL, 0.720 mmol, 1.0 equiv.) was mixed in THF (3.60 mL, 0.2 M) at -10 °C under inert atmosphere and the mixture was left to stir for 60 minutes. Subsequently, (*R*)-**2.30** (160 mg, 0.720 mmol, 1.0 equiv.) was added and stirred for 2 hours. Then (*S*)-**2.50** (500 mg, 1.08 mmol 1.5 equiv.) was added and the reaction mixture was warmed to room temperature and stirred overnight. After 16 hours, the mixture was concentrated *in vacuo*, and the resulting residue was redissolved in EtOAc and H_2O (1:1, 20 mL). The aqueous layer was extracted with EtOAc (3 × 10 mL), and the combined organic layer was washed with brine (25 mL), dried over Na_2SO_4 and concentrated under reduced pressure. The resulting crude

product was used directly in the next step. Then potassium carbonate (K_2CO_3, 149 mg, 1.08 mmol, 1.5 equiv.) was added to this crude intermediate in *N*,*N*-dimethylformamide (3.60 mL, 0.2 M) at room temperature, thiophenol (PhSH, 111 µL, 1.08 mmol, 1.5 equiv.) was added and the resulting mixture was stirred for 1 hour at room temperature. The solution was then partitioned between equal volumes of EtOAc and H_2O, and the aqueous layer was further extracted with EtOAc (3 × 20 mL). The combined organic layer was washed with brine (25 mL), dried over Na_2SO_4 and concentrated under reduced pressure. The resulting residue was purified by flash column chromatography (2% MeOH in EtOAc) to afford the product as a viscous cream oil (118 mg, 0.245 mmol, 34%, > 20:1 *d*.*r*.).

Alternative resequenced procedure: Di-*tert*-butyl dicarbonate (Boc_2O, 350 mg, 1.60 mmol, 2.2 equiv.) in CH_2Cl_2 (0.65 mL) was slowly added to a solution of (*S,S*)-**2.54** (300 mg, 0.802 mmol, 1.1 equiv.) and DIPEA (254 µL, 1.46 mmol, 2.0 equiv.) in CH_2Cl_2 (3.00 mL, 0.2 M) at room temperature. After stirring for 24 hours, the reaction mixture was concentrated under reduced pressure, and the residue was redissolved in dichloromethane (CH_2Cl_2) and H_2O (1:1, 10 mL). After separation, and the organic phase was washed with brine, dried over Na_2SO_4, filtered, and concentrated to obtain a crude intermediate. Separately, a solution of trifluoromethanesulfonic anhydride (Tf_2O, 122 µL, 0.729 mmol, 1.0 equiv.) in CH_2Cl_2 (3.00 mL, 0.2 M) was cooled to -78 °C. To this solution, (4-fluorophenyl)methanol (**2.26**, 92.0 mg, 0.729 mmol, 1.0 equiv.) and diisopropylethylamine (DIPEA, 191 µL, 1.09 mmol, 1.5 equiv.) in CH_2Cl_2 (0.35 mL) were added. After stirring for 20 minutes, to this solution was

added a solution of the crude intermediate in CH_2Cl_2 (0.30 mL) was added, and the reaction mixture was slowly brought to room temperature and stirred overnight. Thereafter, HCl (0.201 mL, 4.0 M in dioxane, 1.1 equiv.) was added to the reaction mixture and stirred for 1 hour. The reaction mixture was then concentrated and the organic phase was extracted with EtOAc (3 × 25 mL), washed with brine (25 mL), dried over Na_2SO_4, and concentrated to yield the crude product. The crude product was further purified using flash column chromatography (gradient 0 - 10% MeOH in EtOAc) to obtain the product as a viscous cream oil (150 mg, 0.311 mmol, 43%, > 20:1 *d.r.*).

R_f 0.32 (2% MeOH/EtOAc).

^{1}H NMR (500 MHz, $CDCl_3$) δ 8.60 – 8.56 (m, 1H), 7.41 – 7.30 (m, 6H), 7.23 – 7.16 (m, 2H), 7.14 – 7.07 (m, 2H), 5.38 – 5.28 (m, 2H), 5.14 – 5.11 (m, 2H), 3.74 (s, 3H), 3.56 – 3.50 (m, 1H), 3.47 (dd, *J* = 8.2, 5.5 Hz, 1H), 3.01 (dd, *J* = 15.5, 5.6 Hz, 1H), 2.88 (dd, *J* = 15.6, 6.8 Hz, 1H), 1.72 – 1.61 (m, 1H), 1.57 (ddd, *J* = 13.7, 8.2, 5.6 Hz, 1H), 1.46 (ddd, *J* = 13.9, 8.2, 6.1 Hz, 1H), 0.91 (d, *J* = 6.6 Hz, 3H), 0.89 (d, *J* = 6.5 Hz, 3H).

^{13}C{^{1}H} NMR (126 MHz, $CDCl_3$) δ 174.1, 172.6, 163.4 (d, *J* = 250.0 Hz), 135.5, 130.6, 130.0 (d, *J* = 8.5 Hz), 128.9, 128.8, 128.5, 128.2 (d, *J* = 3.3 Hz), 119.7, 117.0 (d, *J* = 21.9 Hz), 67.2, 59.0, 58.9, 53.0, 50.5, 42.2, 27.6, 24.9, 22.9, 21.9.

^{19}F NMR (471 MHz, $CDCl_3$) δ -110.86 – -110.95 (m).

HRMS (ESI^+) m/z: $[M+H]^+$ Calcd for $C_{27}H_{33}FN_3O_4$ 482.2450; Found 482.2451.

IR (thin layer film) ν (cm^{-1}) 3335, 2968, 2358, 1619, 1598, 1505, 1426, 1379, 1277, 1176, 1135, 888, 813, 750, 700, 682.

$[\alpha]_D^{25\,°C}$ -16.3 (c 0.020, $CHCl_3$).

Benzyl ((*S*)-3-(1-(4-fluorobenzyl)-1*H*-imidazol-5-yl)-1-methoxy-1-oxopropan-2-yl)-*D*-leucinate ((*S*,*R*)-2.29)

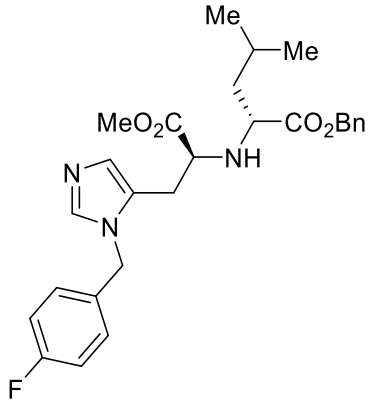

Triphenylphosphine (PPh_3, 113 mg, 0.432 mmol, 1.0 equiv.) and diisopropyl azodicarboxylate (DIAD, 84.8 µL, 0.432 mmol, 1.0 equiv.) was mixed in THF (2.16 mL, 0.2 M) at -10 °C under inert atmosphere and the mixture was left to stir for 60 minutes. Subsequently, (*S*)-**2.30** (96.0 mg, 0.432 mmol, 1.0 equiv.) was added and stirred for 2 hours. Then (*S*)-**2.50** (300 mg, 0.648 mmol 1.5 equiv.) were added and the reaction mixture was warmed to room temperature and stirred overnight. After 16 hours, the mixture was concentrated *in vacuo*, and the resulting residue was redissolved in EtOAc and H_2O (1:1, 20 mL). The aqueous layer was extracted with EtOAc (3 × 10 mL), and the combined organic layer was washed with brine (25 mL), dried over Na_2SO_4 and concentrated under reduced pressure. The resulting crude product was used directly in the next step. Then potassium carbonate (K_2CO_3, 89.5 mg, 0.648 mmol, 1.5 equiv.) was added to this crude intermediate in *N*,*N*-

dimethylformamide (2.16 mL, 0.2 M) at room temperature, thiophenol (PhSH, 66.3 µL, 0.648 mmol, 1.5 equiv.) was added and the resulting mixture was stirred for 1 hour at room temperature. The solution was then partitioned between equal volumes of EtOAc and H_2O, and the aqueous layer was further extracted with EtOAc (3 × 10 mL). The combined organic layer was washed with brine (25 mL), dried over Na_2SO_4 and concentrated under reduced pressure. The resulting residue was purified by flash column chromatography (2% MeOH in EtOAc) to afford the product as a viscous cream oil (68.0 mg, 0.141 mmol, 33%, > 20:1 d.r.).

R_f 0.32 (2% MeOH/EtOAc).

^{1}H NMR (500 MHz, $CDCl_3$) δ 8.62 – 8.58 (m, 1H), 7.40 – 7.31 (m, 6H), 7.18 – 7.14 (m, 2H), 7.14 – 7.08 (m, 2H), 5.31 – 5.27 (m, 2H), 5.13 – 5.10 (m, 2H), 3.63 (s, 3H), 3.42 – 3.36 (m, 1H), 3.24 (dd, *J* = 8.1, 6.3 Hz, 1H), 2.93 – 2.81 (m, 2H), 1.67 – 1.54 (m, 1H), 1.53 – 1.46 (m, 1H), 1.46 – 1.37 (m, 1H), 0.87 (d, *J* = 6.6 Hz, 3H), 0.80 (d, *J* = 6.6 Hz, 3H).

^{13}C{^{1}H} NMR (126 MHz, $CDCl_3$) δ 174.1, 172.7, 163.4 (d, *J* = 249.8 Hz), 135.5, 130.6, 130.0 (d, *J* = 8.6 Hz), 128.9, 128.8, 128.5, 128.3 (d, *J* = 3.2 Hz), 119.7, 117.0 (d, *J* = 21.8 Hz), 67.2, 59.0, 59.0, 53.0, 50.5, 42.2, 27.7, 25.0, 22.9, 21.9.

^{19}F NMR (471 MHz, $CDCl_3$) δ -110.67 – -110.76 (m).

HRMS (ESI^+) m/z: $[M+H]^+$ Calcd for $C_{27}H_{33}FN_3O_4$ 482.2450; Found 482.2452.

IR (thin layer film) ν (cm^{-1}) 3332, 2971, 2659, 1768, 1467, 1411, 1379, 1309, 1161, 1129, 952, 817, 701, 675.

$[\alpha]_D^{25\,°C}$ +6.3 (c 0.010, $CHCl_3$).

Benzyl (*R*)-2-hydroxy-4-methylpentanoate ((*R*)-2.30)

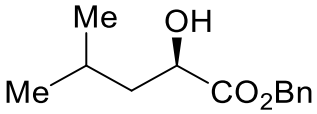

To a solution of (*R*)-2-hydroxy-4-methylpentanoic acid (4.00 g, 30.3 mmol, 1.0 equiv.) in H_2O (10.0 mL) and MeOH (110 mL), Cs_2CO_3 (9.86 g, 30.3 mmol, 1.0 equiv.) was added and stirred for 30 minutes. The reaction mixture was then concentrated *in vacuo* and redissolved in *N*,*N*-dimethylformamide (DMF) (120 mL, 0.25 M) and cooled to 0 °C. Benzyl bromide (5.18 g, 30.3 mmol, 1.0 equiv.) was added to the reaction mixture and stirred at room temperature for 12 hours. The reaction was quenched with NH_4Cl, extracted with EtOAc (3 × 20 mL), washed with brine (25 mL), dried over Na_2SO_4, and concentrated under reduced pressure. The crude product was purified by flash column chromatography (5% EtOAc in pentane) to yield the product as a colourless liquid (5.50 g, 24.7 mmol, 82%).

R_f 0.45 (5% EtOAc/pentane).

^{1}H NMR (400 MHz, $CDCl_3$) δ 7.41 – 7.32 (m, 5H), 5.23 – 5.19 (m, 2H), 4.25 (ddd, *J* = 7.9, 6.7, 5.4 Hz, 1H), 2.85 – 2.78 (m, 1H), 1.95 – 1.84 (m, 1H), 1.61 – 1.56 (m, 2H), 1.00 – 0.89 (m, 6H).

^{13}C{^{1}H} NMR (101 MHz, $CDCl_3$) δ 175.8, 135.4, 128.7, 128.6, 128.4, 69.3, 67.3, 43.5, 24.5, 23.3, 21.7.

HRMS (ESI$^+$) m/z: $[M+Na]^+$ Calcd for $C_{13}H_{18}O_3Na$ 245.1148; Found 245.1154.

IR (thin layer film) ν (cm^{-1}) 3492, 3035, 2958, 2871, 1737, 1499, 1469, 1457, 1386, 1369, 1269, 1214, 1141, 1088, 1005, 962, 850, 804, 749, 698.

[α]$_D^{25\,°C}$ +11.4 (c 0.010, $CHCl_3$).

Benzyl (*S*)-2-hydroxy-4-methylpentanoate ((*S*)-2.30)

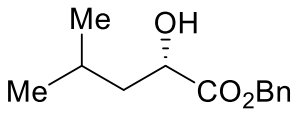

To a solution of *(S)*-2-hydroxy-4-methylpentanoic acid (2.00 g, 15.1 mmol, 1.0 equiv.) in H_2O (5.50 mL) and MeOH (55.0 mL, 0.25 M), Cs_2CO_3 (4.93 g, 15.1 mmol, 1.0 equiv.) was added and stirred for 30 minutes. The reaction mixture was then concentrated *in vacuo* and redissolved in *N*,*N*-dimethylformamide (DMF, 60.5 mL, 0.25 M) and cooled to 0 °C. Benzyl bromide (BnBr, 2.59 g, 15.1 mmol, 1.0 equiv.) was added to the solution and stirred at room temperature for 12 hours. The reaction was quenched with NH_4Cl, extracted with EtOAc (3 × 10 mL), washed with brine (25 mL), dried over Na_2SO_4, and concentrated under reduced pressure. The crude product was purified by flash column chromatography (5% EtOAc in pentane) to yield the product as a colourless liquid (3.00 g, 13.5 mmol, 89%).

R_f 0.42 (5% EtOAc/pentane).

^{1}H NMR (500 MHz, $CDCl_3$) δ 7.42 – 7.31 (m, 5H), 5.22 (d, *J* = 12.3 Hz, 1H), 5.19 (d, *J* = 12.4 Hz, 1H), 4.24 (ddd, *J* = 8.5, 6.0, 4.7 Hz, 1H), 2.67 – 2.61 (m, 1H), 1.95 – 1.83 (m, 1H), 1.64 – 1.51 (m, 2H), 0.94 (d, *J* = 5.5 Hz, 3H), 0.93 (d, *J* = 5.8 Hz, 3H).

^{13}C{^{1}H} NMR (126 MHz, $CDCl_3$) δ 175.9, 135.4, 128.8, 128.7, 128.5, 69.3, 67.4, 43.6, 24.6, 23.4, 21.7.

HRMS (ESI$^+$) m/z: $[M+Na]^+$ Calcd for $C_{13}H_{18}O_3Na$ 245.1148; Found 245.1159.

IR (thin layer film) v (cm^{-1}) 3469, 3035, 2958, 2871, 1737, 1499, 1469, 1456, 1386, 1369, 1270, 1214, 1141, 1088, 1004, 962, 850, 749, 698.

$[\alpha]_D^{25\,°C}$ -11.2 (c 0.025, $CHCl_3$).

Methyl N^{π}-(4-fluorobenzyl)-N^{α}-((2-nitrophenyl)sulfonyl)-*L*-histidinate ((*S*)-2.50)

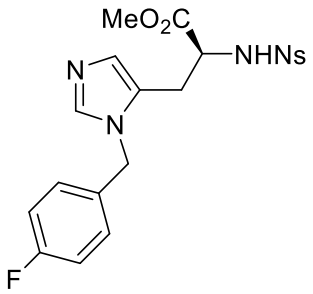

Excess HCl (3.98 mL, 4.0 M in dioxane, 5.0 equiv.) was added to (*S*)-**2.27** (1.20 g, 3.18 mmol, 1.0 equiv.) and the resulting mixture was stirred for 2 hours. The reaction mixture was then concentrated under reduced pressure and the obtained di-HCl salt was triturated with EtOAc (10 mL) to yield a white solid. This solid was suspended in CH_2Cl_2 (15.9 mL, 0.2 M) and Et_3N (1.33 mL, 9.54 mmol, 3.0 equiv.) was added and stirred for 1 hour. Subsequently, 2-nitrobenzenesulfonyl chloride (1.06 g, 4.77 mmol, 1.5 equiv.) was added to the reaction mixture and stirred overnight at room temperature for 18 hours. The reaction was then quenched with NH_4Cl, and extracted with EtOAc (3 × 20 mL), washed with brine (25 mL), dried over Na_2SO_4, and concentrated under reduced pressure. The crude product was purified via flash

column chromatography (2% MeOH in EtOAc) to obtain the product as a viscous yellow oil (1.10 g, 2.38 mmol, 75%).

R_f 0.25 (2% MeOH/EtOAc).

^{1}H NMR (500 MHz, $CDCl_3$) δ 8.01 – 7.97 (m, 1H), 7.91 – 7.87 (m, 1H), 7.76 – 7.68 (m, 2H), 7.48 – 7.44 (m, 1H), 7.10 – 7.03 (m, 4H), 6.81 – 6.78 (m, 1H), 5.21 (d, *J* = 16.0 Hz, 1H), 5.14 (d, *J* = 16.0 Hz, 1H), 4.31 – 4.25 (m, 1H), 3.56 (s, 3H), 3.07 – 3.04 (m, 2H).

^{13}C{^{1}H} NMR (126 MHz, $CDCl_3$) δ 170.2, 162.6 (d, *J* = 247.4 Hz), 147.8, 138.7, 134.0, 133.7, 133.0, 131.8 (d, *J* = 3.2 Hz), 130.6, 129.3, 128.7 (d, *J* = 8.3 Hz), 125.8, 125.7, 116.2 (d, *J* = 21.6 Hz), 56.6, 53.0, 48.3, 28.2.

^{19}F NMR (471 MHz, $CDCl_3$) δ -113.61 – -113.72 (m).

HRMS (ESI^+) m/z: $[M+H]^+$ Calcd for $C_{20}H_{20}FN_4O_6S$ 463.1082; Found 463.1084.

IR (thin layer film) v (cm^{-1}) 3327, 2981, 2950, 2833, 1451, 1393, 1252, 1150, 1119, 1026, 956, 689.

$[\alpha]_D^{25\,°C}$ -31.4 (c 0.015, $CHCl_3$).

Methyl *N*$^{\pi}$-(4-fluorobenzyl)-*N*$^{\alpha}$-((2-nitrophenyl)sulfonyl)-*L*-histidinate ((*S*)-2.52)

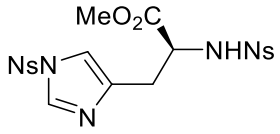

(*S*)-histidine methyl ester dihydrochloride ((*S*)-**2.24**, 2.00 g, 8.26 mmol, 1.0 equiv.) was stirred with triethylamine (Et_3N, 3.68 mL, 26.4 mmol, 3.0 equiv.) in dichloromethane (CH_2Cl_2, 33.0 mL, 0.25 M) for 60 minutes at room temperature. 2-Nitrobenzenesulfonyl chloride (4.03 g, 18.2 mmol, 2.2 equiv.) was added to the solution, and the reaction mixture was stirred overnight at room temperature for 18 hours. After completion of the reaction, the mixture was concentrated and extracted with EtOAc (3 × 20 mL), and the combined organic layer was washed with brine (25 mL), dried over Na_2SO_4, and concentrated under reduced pressure. The resulting crude product was purified using flash column chromatography (20% pentane in EtOAc) to afford the product as a yellow solid (3.40 g, 6.30 mmol, 76%).

R_f = 0.33 (20% pentane/EtOAc).

^{1}H NMR (400 MHz, $CDCl_3$) δ 8.07 – 8.02 (m, 1H), 8.02 – 7.98 (m, 1H), 7.96 (d, *J* = 1.3 Hz, 1H), 7.91 – 7.80 (m, 4H), 7.75 – 7.69 (m, 2H), 7.22 – 7.20 (m, 1H), 6.52 (d, *J* = 8.4 Hz, 1H), 4.53 (ddd, *J* = 8.4, 6.3, 5.0 Hz, 1H), 3.54 (s, 3H), 3.14 – 3.08 (m, 2H).

^{13}C{^{1}H} NMR (101 MHz, $CDCl_3$) [overlapping signals] δ 170.8, 139.1, 137.7, 136.2, 134.5, 133.7, 133.5, 133.0, 131.2, 130.9, 130.5, 125.7, 125.6, 116.1, 55.9, 52.8, 31.4.

HRMS (ESI^+) m/z: $[M+H]^+$ Calcd for $C_{19}H_{18}N_5O_{10}S_2$ 540.0490; Found 540.0480.

IR (thin layer film) ν (cm^{-1}) 3657, 2981, 2889, 1746, 1543, 1473, 1462, 1442, 1390, 1252, 1165, 1081, 955, 854, 762, 743, 655, 613.

MP 72–74 °C.

$[\alpha]_D^{25\,°C}$ -42.2 (c 0.015, $CHCl_3$).

Benzyl *N*-((*S*)-1-methoxy-3-(1-((4-nitrophenyl)sulfonyl)-1*H*-imidazol-4-yl)-1-oxopropan-2-yl)-*N*-((4-nitrophenyl)sulfonyl)-*L*-leucinate ((*S*,*S*)-2.53)

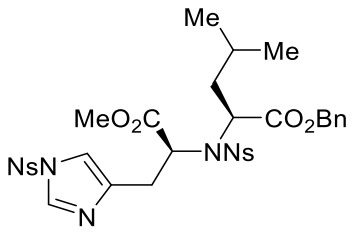

A mixture of diisopropyl azodicarboxylate (DIAD, 121 µL, 0.618 mmol, 1.0 equiv.) and triphenylphosphine (PPh_3, 162 mg, 0.618 mmol, 1.0 equiv.) was mixed in tetrahydrofuran (THF, 3.09 mL, 0.2 M) under an inert atmosphere at -10 °C. The mixture was left to stir for 60 minutes. Subsequently, (*S*)-**2.52** (500 mg, 0.927 mmol, 1.5 equiv.) were added to the reaction mixture and stirred for another 2 hours at room temperature. Then (*R*)-**2.30** (137 mg, 0.618 mmol, 1.0 equiv.) was added and the reaction mixture was stirred overnight for 16 hours. After that, the mixture was concentrated *in vacuo*, and the resulting residue was redissolved in EtOAc and H_2O (1:1, 20 mL). The aqueous layer was extracted with EtOAc (3 × 10 mL), and the combined organic layer was washed with brine (25 mL), dried over Na_2SO_4 and concentrated under reduced pressure. The residue was purified using flash column chromatography (2% MeOH in EtOAc) to yield the product as a viscous yellow oil (252 mg, 0.339 mmol, 55%, > 20:1 *d.r.*).

R_f 0.27 (2% MeOH/EtOAc).

^{1}H NMR (500 MHz, $CDCl_3$) δ 8.19 (dd, *J* = 7.9, 1.3 Hz, 1H), 8.11 (dd, *J* = 7.7, 1.7 Hz, 1H), 8.06 (d, *J* = 1.4 Hz, 1H), 7.90 – 7.82 (m, 2H), 7.79 (dd, *J* = 7.5, 1.7 Hz, 1H), 7.77 – 7.68 (m, 1H), 7.49 (ddd, *J* = 8.3, 7.3, 1.3 Hz, 1H), 7.47 – 7.43 (m, 1H), 7.34 – 7.29 (m, 3H), 7.28 (d, *J* = 1.4 Hz, 1H), 7.18 – 7.15 (m, 2H), 5.00 – 4.94 (m, 1H), 4.92 – 4.80 (m, 2H), 4.43 (dd, *J* = 10.1, 5.1 Hz, 1H), 3.59 (s, 3H), 3.50 (dd, *J* = 14.7, 7.0 Hz, 1H), 3.31 (dd, *J* = 14.8, 7.8 Hz, 1H), 1.78 (ddd, *J* = 13.3, 10.1, 5.2 Hz, 1H), 0.98 – 0.83 (m, 2H), 0.77 (d, *J* = 6.6 Hz, 3H), 0.74 (d, *J* = 6.6 Hz, 3H).

^{13}C{^{1}H} NMR (126 MHz, $CDCl_3$) δ 170.6, 169.8, 149.1, 148.1, 140.4, 137.1, 136.2, 135.0, 133.9, 133.4, 133.2, 132.6, 131.7, 131.4, 131.3, 128.6, 128.5, 128.5, 125.2, 123.4, 116.8, 67.2, 59.1, 58.2, 52.7, 39.6, 31.2, 25.0, 23.1, 21.6.

HRMS (ESI^+) m/z: $[M+H]^+$ Calcd for $C_{32}H_{34}N_5O_{12}S_2$ 744.1640; Found 744.1634.

IR (thin layer film) ν (cm^{-1}) 2958, 2927, 2855, 1738, 1713, 1546, 1468, 1287, 1183, 1082, 924, 852, 779, 697, 655.

$[\alpha]_D^{25\,°C}$ -12.8 (c 0.050, $CHCl_3$).

Benzyl ((*S*)-3-(1*H*-imidazol-4-yl)-1-methoxy-1-oxopropan-2-yl)-*L*-leucinate ((*S*,*S*)-2.54)

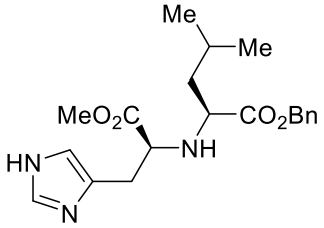

Thiophenol (60.4 µL, 0.592 mmol, 2.2 equiv.) was added to a solution of (*S,S*)-**2.53** (200 mg, 0.269 mmol, 1.0 equiv.) and potassium carbonate (K_2CO_3, 111 mg, 0.807 mmol, 3.0 equiv.) in *N,N*-dimethylformamide (DMF, 2.69 mL, 0.1 M) at room temperature and stirred for 1 hour. The resulting solution was partitioned between equal volumes of EtOAc and H_2O. The aqueous layer was extracted with EtOAc (3 × 20 mL), and the combined organic layer was washed with brine (25 mL), dried over Na_2SO_4 and concentrated under reduced pressure. The residue was purified by flash column chromatography (2% MeOH in EtOAc) to afford the product as a viscous colourless oil (70.0 mg, 0.187 mmol, 70 %, > 20:1 *d.r.*).

R_f = 0.22 (2% MeOH/CH_2Cl_2).

^{1}H NMR (500 MHz, $CDCl_3$) δ 7.47 – 7.43 (m, 1H), 7.39 – 7.27 (m, 5H), 6.81 – 6.77 (m, 1H), 5.13 – 5.11 (m, 2H), 3.70 (s, 3H), 3.50 (dd, *J* = 8.7, 3.8 Hz, 1H), 3.41 (dd, *J* = 7.9, 6.0 Hz, 1H), 2.99 (dd, *J* = 15.3, 3.8 Hz, 1H), 2.82 (ddd, *J* = 15.3, 8.7, 1.0 Hz, 1H), 1.77 – 1.66 (m, 1H), 1.62 – 1.49 (m, 2H), 0.96 – 0.88 (m, 6H).

^{13}C{^{1}H} NMR (126 MHz, $CDCl_3$) δ 175.5, 174.1, 135.5, 134.9, 128.8, 128.6, 128.4, 67.0, 59.9, 58.8, 52.3, 42.9, 25.0, 23.0, 22.1. *note: broad peaks at 122 ppm and 129 ppm were found by HSQC and HMBC experiments.*

HRMS (ESI^+) m/z: $[M+H]^+$ Calcd for $C_{20}H_{28}N_3O_4$ 374.2074; Found 374.2074.

IR (thin layer film) ν (cm^{-1}) 3502, 3153, 3050, 2880, 1749, 1632, 1561, 1474, 1446, 1282, 1251, 1180, 1032, 963, 944, 765, 644.

$[\alpha]_D^{25\,°C}$ -14.6 (c 0.010, $CHCl_3$).

Benzyl ((*S*)-3-(1-(3-fluoro-5-methylbenzyl)-1*H*-imidazol-5-yl)-1-methoxy-1-oxopropan-2-yl)-*L*-leucinate ((*S*,*S*)-2.58)

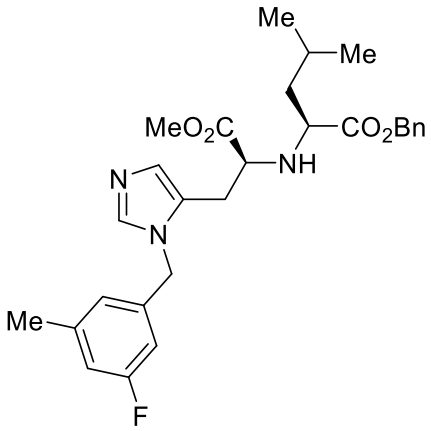

Di-*tert*-butyl dicarbonate (Boc_2O, 350 mg, 1.60 mmol, 2.2 equiv.) in CH_2Cl_2 (0.65 mL) was slowly added to a solution of (*S,S*)-**2.54** (300 mg, 0.802 mmol, 1.1 equiv.) and DIPEA (254 µL, 1.46 mmol, 2.0 equiv.) in CH_2Cl_2 (3.00 mL, 0.2 M) at room temperature. After stirring for 24 hours, the reaction mixture was concentrated in *vacuo*, and the residue was redissolved in CH_2Cl_2 and H_2O (1:1, 10 mL). After separation, and the organic phase was washed with brine, dried over Na_2SO_4, filtered, and concentrated to obtain a crude intermediate. Separately, a solution of trifluoromethanesulfonic anhydride (Tf_2O, 122 µL, 0.729 mmol, 1.0 equiv.) in CH_2Cl_2 (3.00 mL, 0.2 M) was cooled to -78 °C. To this solution, (3-fluoro-5-methylphenyl)methanol (**2.55**, 102 mg, 0.729 mmol, 1.0 equiv.) and diisopropylethylamine (DIPEA, 191 µL, 1.09 mmol, 1.5 equiv.) in CH_2Cl_2 (0.35 mL) were added. After stirring for 20 minutes, the crude intermediate obtained previously was dissolved in CH_2Cl_2 (0.30 mL) was added, and the reaction mixture was slowly brought to room temperature and stirred for 24 hours. Thereafter, HCl (0.201 mL,

4.0 M in dioxane, 1.1 equiv.) was added to the reaction mixture and stirred for 1 hour. The reaction mixture was then concentrated and the organic phase was extracted with EtOAc (3 × 25 mL), washed with brine (25 mL), dried over Na_2SO_4, and concentrated to yield the crude product. The crude product was further purified using flash column chromatography (gradient 0 - 10% MeOH in EtOAc) to obtain product as a viscous cream oil (170 mg, 0.343 mmol, 47%, > 20:1 d.r.).

R_f 0.30 (5% MeOH/EtOAc).

^{1}H NMR (500 MHz, $CDCl_3$) δ 8.63 – 8.59 (m, 1H), 7.41 – 7.30 (m, 6H), 6.97 – 6.83 (m, 1H), 6.76 – 6.73 (m, 1H), 6.72 – 6.67 (m, 1H), 5.33 – 5.29 (m, 2H), 5.14 (d, *J* = 12.4 Hz, 1H), 5.11 (d, *J* = 12.5 Hz, 1H), 3.75 (s, 3H), 3.57 – 3.52 (m, 1H), 3.49 (dd, *J* = 8.3, 5.6 Hz, 1H), 3.02 (dd, *J* = 15.9, 5.7 Hz, 1H), 2.90 (dd, *J* = 15.6, 6.9 Hz, 1H), 2.35 (s, 3H), 1.70 – 1.62 (m, 1H), 1.61 – 1.54 (m, 1H), 1.52 – 1.43 (m, 1H), 0.91 (d, *J* = 6.6 Hz, 3H), 0.89 (d, *J* = 6.6 Hz, 3H).

^{13}C{^{1}H} NMR (126 MHz, $CDCl_3$) δ 174.6, 173.2, 163.1 (d, *J* = 248.9 Hz), 136.0, 135.7, 130.3 (d, *J* = 27.2 Hz), 129.8 (d, *J* = 8.6 Hz), 129.5 (d, *J* = 8.6 Hz), 129.3 (d, *J* = 3.2 Hz), 128.8, 128.8, 128.7, 128.5, 116.7 (d, *J* = 21.8 Hz), 116.6 (d, *J* = 22.3 Hz), 66.9, 58.7 (d, *J* = 16.3 Hz), 52.7, 50.0, 42.4, 27.9, 24.9, 23.0, 22.7, 22.1, 21.9.

^{19}F NMR (471 MHz, $CDCl_3$) δ -112.21 – -112.30 (m).

HRMS (ESI^+) m/z: $[M+H]^+$ Calcd for $C_{28}H_{35}FN_3O_4$ 496.2606; Found 496.2610.

IR (thin layer film) ν (cm^{-1}) 3493, 3468, 3091, 3067, 3035, 2957, 2871, 1734, 1618, 1456, 1369, 1267, 1213, 1140, 1087, 1029, 1004, 850, 805, 748, 697.

$[\alpha]_D^{25\,°C}$ -12.7 (c 0.005, $CHCl_3$).

Benzyl ((*S*)-3-(1-(3-chloro-5-fluorobenzyl)-1*H*-imidazol-5-yl)-1-methoxy-1-oxopropan-2-yl)-*L*-leucinate ((*S*,*S*)-2.59)

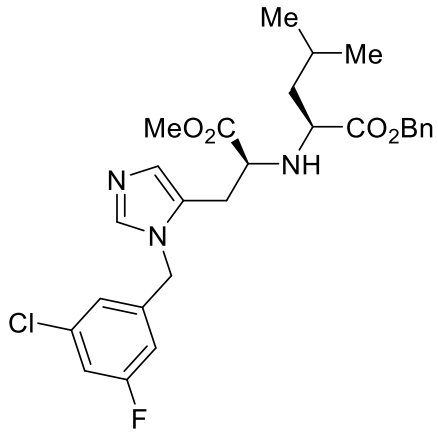

Di-*tert*-butyl dicarbonate (Boc_2O, 350 mg, 1.60 mmol, 2.2 equiv.) in CH_2Cl_2 (0.65 mL) was slowly added to a solution of (*S,S*)-**2.54** (300 mg, 0.802 mmol, 1.1 equiv.) and DIPEA (254 µL, 1.46 mmol, 2.0 equiv.) in CH_2Cl_2 (3.00 mL, 0.2 M) at room temperature. After stirring for 24 hours, the reaction mixture was concentrated *in vacuo*, and the residue was redissolved in CH_2Cl_2 and H_2O (1:1, 10 mL). After separation, the organic phase was washed with brine, dried over Na_2SO_4, filtered, and concentrated to obtain a crude intermediate. Separately, a solution of trifluoromethanesulfonic anhydride (Tf_2O, 122 µL, 0.729 mmol, 1.0 equiv.) in CH_2Cl_2 (3.00 mL, 0.2 M) was cooled to -78 °C. To this solution, (3-chloro-5-fluorophenyl)methanol (**2.56**, 117 mg, 0.729 mmol, 1.0 equiv.) and diisopropylethylamine (DIPEA, 191 µL, 1.09 mmol, 1.5 equiv.) in CH_2Cl_2 (0.35 mL) were added. After stirring for 20 minutes, the crude intermediate obtained previously was dissolved in CH_2Cl_2 (0.30 mL) was added, and the reaction mixture was slowly brought to room temperature and stirred for 24 hours. Thereafter, HCl (0.201 mL,

4.0 M in dioxane, 1.1 equiv.) was added to the reaction mixture and stirred for 1 hour. The reaction mixture was then concentrated and the organic phase was extracted with EtOAc (3 × 25 mL), washed with brine (25 mL), dried over Na_2SO_4, and concentrated to yield the crude product. The crude product was further purified using flash column chromatography (gradient 0 - 10% MeOH in EtOAc) to obtain the product as a viscous cream oil (172 mg, 0.333 mmol, 46%, > 20:1 d.r.).

R_f 0.28 (5% MeOH/EtOAc).

^{1}H NMR (500 MHz, $(CD_3)_2CO$) δ 8.84 – 8.80 (m, 1H), 7.37 – 7.33 (m, 1H), 7.29 – 7.24 (m, 3H), 7.22 – 7.19 (m, 2H), 7.15 – 7.09 (m, 1H), 7.04 – 7.00 (m, 1H), 6.93 – 6.88 (m, 1H), 5.41 – 5.37 (m, 2H), 5.02 – 4.92 (m, 2H), 3.56 (s, 3H), 3.32 – 3.25 (m, 1H), 3.22 – 3.16 (m, 1H), 2.99 (dd, *J* = 15.6, 6.3 Hz, 1H), 2.86 (dd, *J* = 15.8, 7.9 Hz, 1H), 1.46 – 1.37 (m, 1H), 1.36 – 1.24 (m, 2H), 0.73 – 0.65 (m, 6H).

^{13}C{^{1}H} NMR (126 MHz, $(CD_3)_2CO$) δ 175.2, 173.9, 164.0 (d, *J* = 249.3 Hz), 140.2, 137.4, 137.0, 136.4 (d, *J* = 10.9 Hz), 132.2, 129.5, 129.2, 129.1, 125.0 (d, *J* = 3.6 Hz), 120.9, 117.1 (d, *J* = 25.0 Hz), 114.7 (d, *J* = 22.7 Hz), 67.1, 59.5, 59.2, 52.6, 49.9, 43.0, 28.1, 25.5, 23.3, 22.3.

^{19}F NMR (471 MHz, $(CD_3)_2CO$) δ -112.25 – -112.35 (m, 1F).

HRMS (ESI$^+$) m/z: $[M+H]^+$ Calcd for $C_{27}H_{32}{}^{35}ClFN_3O_4$ 516.2060; Found 516.2060.

IR (thin layer film) ν (cm^{-1}) 3457, 3067, 3040, 2957, 2871, 1737, 1677, 1512, 1439, 1388, 1282, 1260, 1226, 1181, 1113, 937, 807, 755, 663.

$[\alpha]_D^{25\,°C}$ -12.0 (c 0.010, $CHCl_3$).

Methyl 3-hydroxy-5-methoxybenzoate (S1)

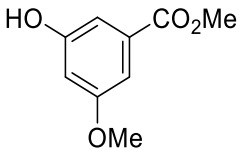

A solution of methyl 3,5-dihydroxybenzoate (1.00 g, 5.97 mmol, 1.1 equiv.) in anhydrous DMF (7.00 mL) was added to a solution of sodium hydride (60% dispersion in mineral oil, 217 mg, 5.43 mmol, 1.0 equiv.) in DMF (20.0 mL) at 0˚C and stirred for 20 minutes. Therafter, iodomethane (0.372 mL, 5.97 mmol, 1.1 equiv.) was added dropwise over 10 minutes. The resulting mixture was slowly brought to room temperature and stirred for 1.5 hours, quenched with distilled H_2O (20 mL) at 0 ˚C and acidified with cold aqueous hydrochloric acid (1 M, 7.00 mL). After extraction with diethyl ether (3 × 25 mL), the combined organic phase was washed with brine (25 mL), dried over Na_2SO_4, and concentrated under reduced pressure. The crude product was further purified using flash column chromatography (10% EtOAc in pentane) to afford the desired product as a white solid (586 mg, 3.22 mmol, 59%).

R_f 0.35 (10% EtOAc/pentane).

^{1}H NMR (400 MHz, $CDCl_3$) δ 7.21 (dd, *J* = 2.3, 1.3 Hz, 1H), 7.12 (dd, *J* = 2.4, 1.4 Hz, 1H), 6.78 (br s, 1H), 6.64 (dd, *J* = 2.4, 2.4 Hz, 1H), 3.90 (s, 3H), 3.78 (s, 3H).

^{13}C{^{1}H} NMR (101 MHz, $CDCl_3$) δ 167.7, 160.9, 157.2, 131.8, 109.6, 107.0, 107.0, 55.7, 52.6.

Characterisation data were in accordance with those found in the literature.[4]

3-(Hydroxymethyl)-5-methoxyphenol (S2)

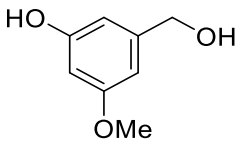

Lithium aluminium hydride solution in dry THF (2.4 M, 11.4 mL, 27.5 mmol, 5.0 equiv.) was added dropwise to a solution of methyl 3-hydroxy-5-methoxybenzoate (**S1**, 1.00 g, 5.49 mmol, 1.0 equiv.) in dry tetrahydrofuran (THF, 54.9 mL) at 0˚C. After stirring for 10 minutes, the reaction mixture was slowly heated to reflux and stirred for overnight. After 16 hours, the reaction mixture was quenched by adding EtOAc (10 mL) and distilled H_2O (10 mL) dropwise at 0 ˚C, followed by the addition of aqueous HCl (1.0 M) to adjust the pH to 7.0. After concentration, the resulting residue was redissolved in EtOAc and H_2O (1:1, 30 mL). The aqueous layer was extracted with EtOAc (3 × 10 mL), and the combined organic layer was washed with brine (25 mL), dried over Na_2SO_4 and concentrated under reduced pressure. The crude product was further purified using flash column chromatography (30% EtOAc in pentane) to afford product **S2** as a yellow oil (721 mg, 4.68 mmol, 85%).

R_f 0.30 (30% EtOAc/pentane).

^{1}H NMR (500 MHz, $(CD_3)_2CO$) δ 8.39 (s, 1H), 6.49 (dd, *J* = 2.3, 1.4 Hz, 1H), 6.46 (dd, *J* = 2.3, 1.4 Hz, 1H), 6.31 (dd, *J* = 2.3, 2.3 Hz, 1H), 4.57 (br s, 2H), 3.71 (s, 3H).

^{13}C{^{1}H} NMR (126 MHz, $(CD_3)_2CO$) δ 161.8, 159.1, 145.3, 106. 8, 104.1, 100.7, 64.6, 55.3.

Characterisation data were in accordance with those found in the literature.[5]

(3-(2-Fluoroethoxy)-5-methyoxyphenyl)methanol (2.57)

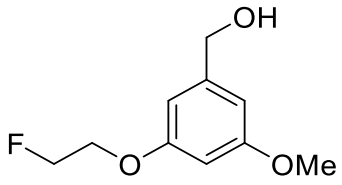

To a solution of **S2** (1.00 g, 6.49 mmol, 1.0 equiv.) dissolved in DMF (32.4 mL, 0.2 M) at room temperature, 2-fluoroethyl 4-methylbenzenesulfonate (1.42 g, 6.49 mmol, 1.0 equiv.) and caesium carbonate (4.23 g, 13.0 mmol, 2.0 equiv.) were added sequentially. After heating to 80 ˚C, the reaction mixture was stirred for 2 hours and subsequently quenched with distilled H_2O (30 mL) and EtOAc (30 mL) at room temperature, followed by neutralization with aqueous HCl (1.0 M). The concentrated mixture was then partitioned between equal volumes of EtOAc and H_2O, and the aqueous layer was further extracted with EtOAc (3 × 20 mL). The combined organic layer was washed with brine (25 mL), dried over Na_2SO_4 and concentrated under reduced pressure. The resulting residue was purified by flash column chromatography (50% EtOAc in pentane) to afford the product as a light brown solid (816 mg, 4.08 mmol, 63%).

R_f 0.32 (50% EtOAc/pentane).

^{1}H NMR (500 MHz, $CDCl_3$) δ 6.58 – 6.53 (m, 2H), 6.42 (dd, *J* = 2.4, 2.4 Hz, 1H), 4.75 (dt, *J* = 47.4, 4.0 Hz, 2H), 4.65 (d, *J* = 6.0 Hz, 2H), 4.21 (dt, *J* = 27.9, 4.1 Hz, 2H), 3.80 (s, 3H), 1.62 (t, *J* = 6.0 Hz, 1H).

^{13}C{^{1}H} NMR (126 MHz, $CDCl_3$) δ 161.2, 160.0, 143.6, 105.4, 105.1, 100.5, 82.0 (d, *J* = 170.8 Hz), 67.3 (d, *J* = 20.0 Hz), 65.5, 55.5.

^{19}F NMR (471 MHz, $CDCl_3$) δ -223.87 (tt, *J* = 46.8, 27.7 Hz).

HRMS (ESI^+) m/z: $[M+H]^+$ Calcd for $C_{10}H_{14}FO_3$ 201.0921; Found 201.0919.

IR (thin layer film) ν (cm^{-1}) 3391, 2997, 2954, 2873, 2842, 1599, 1469, 1438, 1348, 1322, 1296, 1238, 1198, 1165, 1053, 930, 886, 836, 688.

MP 44–45 °C.

Benzyl ((*S*)-3-(1-(3-(2-fluoroethoxy)-5-methoxybenzyl)-1*H*-imidazol-5-yl)-1-methoxy-1-oxopropan-2-yl)-*L*-leucinate ((*S*,*S*)-2.60)

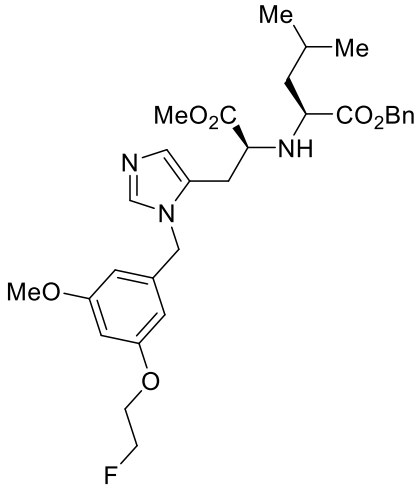

Di-*tert*-butyl dicarbonate (Boc_2O, 350 mg, 1.60 mmol, 2.2 equiv.) in CH_2Cl_2 (0.65 mL) was slowly added to a solution of (*S,S*)-**2.54** (300 mg, 0.802 mmol, 1.1 equiv.) and DIPEA (254 µL, 1.46 mmol, 2.0 equiv.) in CH_2Cl_2 (3.00 mL, 0.2 M) at room temperature. After stirring for 24 hours, the reaction mixture was concentrated under reduced pressure, and the residue was redissolved in CH_2Cl_2 and H_2O (1:1, 10 mL). After separation, and the organic phase was washed with brine (25 mL), dried over Na_2SO_4, filtered, and concentrated to obtain a crude intermediate. Separately, a

solution of trifluoromethanesulfonic anhydride (Tf_2O, 122 µL, 0.729 mmol, 1.0 equiv.) in CH_2Cl_2 (3.00 mL, 0.2 M) was cooled to -78 °C. To this solution, the benzyl alcohol **2.57** (146 mg, 0.729 mmol, 1.0 equiv.) and diisopropylethylamine (DIPEA, 191 µL, 1.09 mmol, 1.5 equiv.) in CH_2Cl_2 (0.35 mL) were added. After stirring for 20 minutes, a solution of the previously obtained crude intermediate in CH_2Cl_2 (0.30 mL) was added, and the reaction mixture was slowly brought to room temperature and stirred for 24 hours. After that, HCl (0.201 mL, 4.0 M in dioxane, 1.1 equiv.) was added to the reaction mixture and stirred for 1 hour. The reaction mixture was then concentrated and the organic phase was extracted with EtOAc (3 × 25 mL), washed with brine (25 mL), dried over Na_2SO_4, and concentrated to yield the crude product. The crude product was further purified using flash column chromatography (gradient 50 - 0% pentane in EtOAc) to obtain the product as a viscous cream oil (165 mg, 0.297 mmol, 41%, > 20:1 *d.r.*).

R_f 0.33 (10% pentane/EtOAc).

^{1}H NMR (500 MHz, $CDCl_3$) δ 7.53 – 7.49 (m, 1H), 7.41 – 7.28 (m, 5H), 6.83 – 6.77 (m, 1H), 6.58 – 6.53 (m, 2H), 6.42 (dd, *J* = 2.4, 2.4 Hz, 1H), 5.15 – 5.11 (m, 2H), 4.81 – 4.67 (m, 2H), 4.64 (s, 3H), 4.26 – 4.15 (m, 2H), 3.79 (s, 3H), 3.74 – 3.70 (m, 2H), 3.48 (dd, *J* = 8.9, 3.5 Hz, 1H), 3.42 (dd, *J* = 8.1, 5.8 Hz, 1H), 2.99 (dd, *J* = 15.4, 3.5 Hz, 1H), 2.81 (ddd, *J* = 15.6, 8.9, 1.1 Hz, 1H), 1.78 – 1.67 (m, 1H), 1.65 – 1.52 (m, 2H), 0.93 (d, *J* = 6.6 Hz, 3H), 0.92 (d, *J* = 6.6 Hz, 3H).

^{13}C{^{1}H} NMR (126 MHz, $CDCl_3$) δ 175.6, 174.0, 161.2, 159.9, 143.7, 135.5, 134.7, 128.8, 128.7 (d, *J* = 2.3 Hz), 128.5, 127.8, 127.1, 105.4, 105.1, 100.5, 82.0 (d, *J* =

170.8 Hz), 67.3 (d, *J* = 20.4 Hz), 67.2, 65.4, 59.8, 58.9, 55.5, 52.4, 42.9, 29.2, 25.0, 23.0, 22.1.

^{19}F NMR (471 MHz, $CDCl_3$) δ -224.23 (tt, *J* = 46.8, 27.7 Hz, 1F).

HRMS (ESI^+) m/z: $[M+H]^+$ Calcd for $C_{30}H_{39}FN_3O_6$ 556.2817; Found 556.2817.

IR (thin layer film) v (cm^{-1}) 3349, 3128, 3065, 3038, 2965, 2939, 2877, 1740, 1679, 1611, 1593, 1449, 1275, 1205, 1140, 954, 867, 801, 752, 722, 700.

$[\alpha]_D^{25\,°C}$ -14.2 (c 0.010, $CHCl_3$).

4.3 X-ray Crystallography Data for Chapter 2

((*S*)-1-Carboxy-2-(1-(4-fluorobenzyl)-1*H*-imidazol-5-yl)ethyl)-*D*-leucine ((*S*,*R*)-2.1)

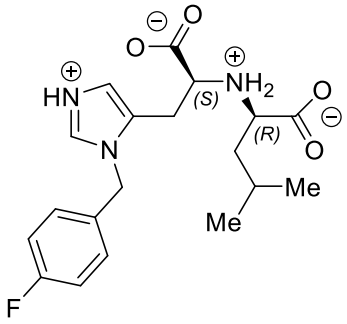

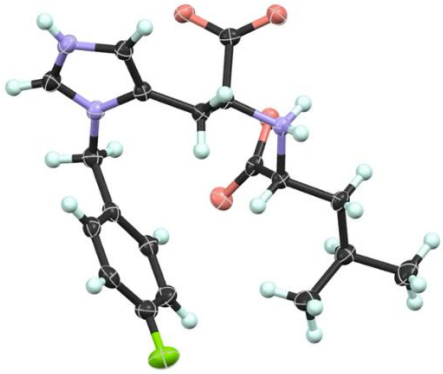

Parameter	Value
Empirical Formula	$C_{19}H_{24}FN_3O_4$
Formula Weight (g/mol)	377.42
Temperature (K)	150.0(2)
Crystal System	Monoclinic
Space Group	$P2_1/n$
a (Å)	5.18070(8)
b (Å)	8.99559(15)
c (Å)	21.0860(3)
α (°)	90.0
β (°)	95.0007(15)
γ (°)	90.0

Volume (Å³)	978.94(3)
Z (Formula Units per Cell)	4
Density (g/cm³)	1.514
Absorption Coefficient (μ, mm⁻¹)	0.219
Crystal Size (mm³)	0.530 × 0.480 × 0.360
Radiation	Cu Kα (λ = 1.54184 Å)
Theta Range (°)	4.1760 to 75.6700
Index Ranges	-6 ≤ h ≤ 6, -11 ≤ k ≤ 10, -26 ≤ l ≤ 26
Reflections Collected	21595
Independent Reflections	12661 [Rint = 0.0484]
Goodness-of-Fit on F²	1.048
Final R Indexes [I ≥ 2σ(I)]	R_1 = 0.0524, wR_2 = 0.1433
Software Used	CrysAlisPro 1.171.42.72a (Rigaku OD, 2022)
Absorption Correction Method	Multi-scan, Empirical absorption correction using spherical harmonics (SCALE3 ABSPACK)
Radiation Source	Micro-focus sealed X-ray tube (SuperNova, Cu X-ray)
Detector Type	CCD plate (Atlas)
Measurement Environment	N_2 (Nitrogen)

Table 4.1: Crystal data and structure refinement.

4.4 In Silico Experimental Procedure for Chapter 2 (Conducted by Dr. L. Hosseini-Gerami and Dr. M. Thomas)

4.3.1 Protein and Ligand Preparation

An X-ray structure of MLN-4760 co-crystallised with ACE2 (PDB: 1R4L) was utilised as the model system in this work.[6] The complex was prepared with Maestro's (Schrödinger, LLC, New York, NY) Protein Preparation Wizard. Four missing side chain residues were rebuilt with Prime, H-bonds were assigned and their orientations optimised using PROPKA,[7] finally the protein-ligand complex was minimised with the default heavy atom constraint of 0.3 Å as per default in Protein Preparation Wizard. This complex was used to build the receptor grid for docking that was centred on the ligand using default parameters. All molecules docked against the system were prepared and embedded into 3D from SMILES using LigPrep (Schrödinger, LLC, New York, NY), including assignment of charges at pH 7 ± 2.

4.3.2 Validation of Computational Docking for ACE2

First, MLN-4760 was re-docked into its original X-ray co-crystal structure with ACE2 to provide a sanity check that computational docking correctly predicted the bioactive conformation of MLN-4760.[6] MLN-4760 was prepared from SMILES and then re-docked using the prepared grid, using GlideXP without nitrogen inversion or ring

conformation sampling, which resulted in the most accurate pose. The top-ranked docked pose identified the correct bioactive conformation with an RMSD of 1.88 Å to the co-crystallised MLN-4760 compound.

Following the validation of accurate bioactive conformation prediction of MLN-4760, known analogues published in the original report were docked using the same protocol as shown in Figure 4.1.[8] The GlideXP docking score, and other calculated properties were compared to their published ACE2 binding affinity. The strongest correlation identified was between the $Glide_{evdw}$, or Van der Waals energy, which showed a Pearson correlation of -0.76 and Spearman rank correlation of -0.83 with compound pIC_{50} values as shown in Figure 4.2. A simple linear model was fit between experimental pIC_{50} and $Glide_{evdw}$ (Eq. 1) with $\beta = -2.12$ and $\alpha = -14.77$. An interpolation of the fitted data using this equation is shown in Table 4.2.

$$pIC_{50} = \beta \times Glide_{evdw} + \alpha \quad (1)$$

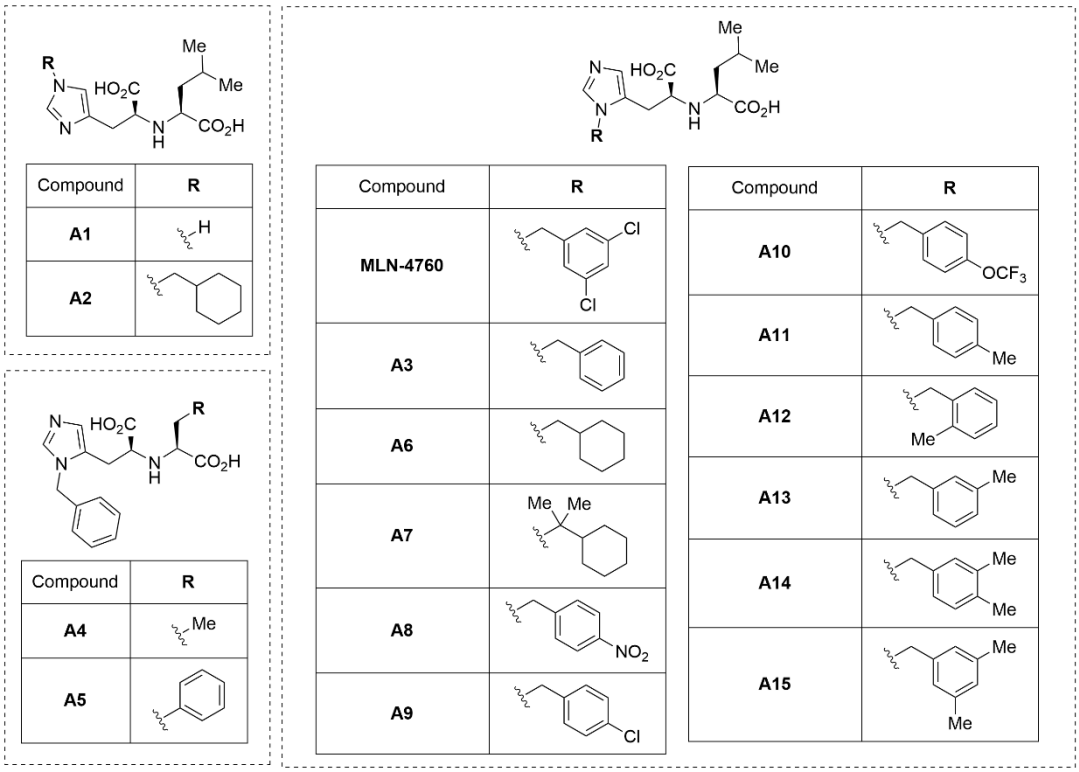

Figure 4.1: Structures of MLN-4760 and analogues thereof reported by Dales *et al*.[8]

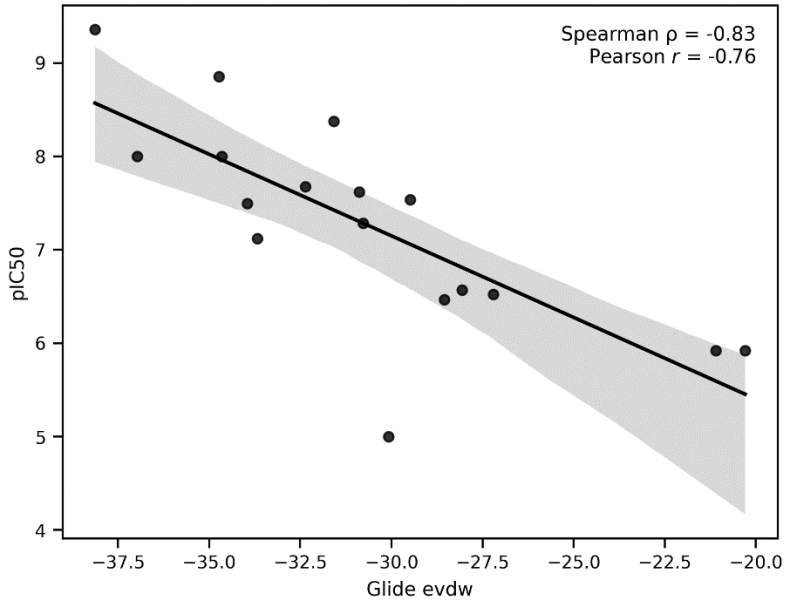

Figure 4.2: Scatterplot showing experimental pIC_{50} vs calculated evdw of MLN-4760 and known analogues.

Compound	Reported pIC_{50}	Estimated pIC_{50}	Error
MLN-4760	9.36	8.19	1.17
A4	6.52	7.40	0.87
A8	7.12	7.46	0.34
A9	7.68	7.92	0.24
A10	7.28	6.84	0.44
A11	7.49	8.00	0.51
A12	7.54	7.48	0.06
A13	8.38	7.94	0.44
A14	8.00	8.73	0.73
A15	8.85	8.26	0.59

Table 4.2: Retrospectively modelled analogues of MLN-4760 including reported pIC_{50} and interpolated estimated pIC_{50} using the linear model of $Glide_{evdw}$ energy.

4.3.3 Estimation of Analogue Binding Affinity by Docking

A selection of 31 possible analogues of MLN-4760 as illustrated in Figure 4.3 were docked using the same protocol as previously described. The $Glide_{evdw}$ of the top-ranked pose and the linear model fit on known analogue pIC_{50} values was used to estimate the pIC_{50} of the analogues. As the radiolabel was assumed to have no effect of protein binding, the effect of this was not modelled.

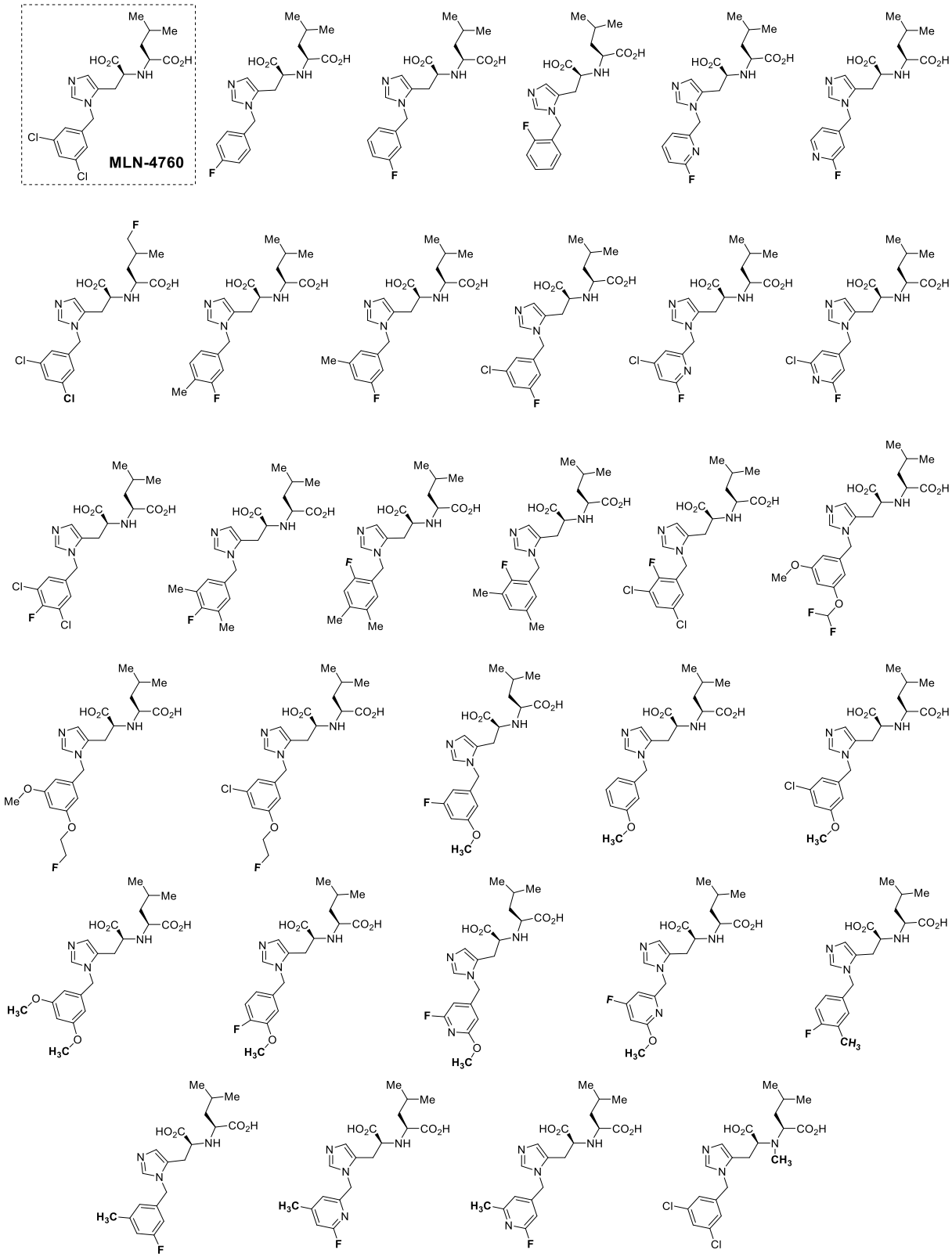

Figure 4.3: 31 possible analogues of MLN-4760 considered for in silico prioritisation.

4.3.4 Validation of Molecular Dynamics for ACE2

ACE2 is a challenging system to run relative binding free energy (RBFE) calculations on, due to the binding of the ligand to a coordinated Zn^{2+} ion. This should require bespoke parameterisation of the forcefield that was beyond the resources available in this work. However, as the Zn^{2+} site as shown in Figure 4.4 in the S1 site is relatively distant from the proposed analogue changes to the ligand in the S1' site, hence we here assumed that poor force-field parameterisation of the Zn ion should have marginal effects in the calculation. To ensure the simulation was still stable a control simulation was conducted. GROMACS 2020.2 was used as the molecular dynamics (MD) engine.[9] The prepared X-ray crystal structure of ACE2 bound to MLN-4760 (PDB: 1R4L) was taken from the docking protocol.[6] The receptor complex was parameterised using the amber99sb force field with a TIP3P forcefield model for water.[10, 11] The ligand complex was parameterised using the GAFF force field *via* antechamber[12, 13] and parameter files generated using tleap before using parmed[14] and ProtoCaller[15] to convert the files back into GROMACS. BioSimSpace was then used to merge the receptor and ligand into a complex and then solvate a box of $90Å^3$.[16] The complex was energy minimised for 50,000 steps before undergoing equilibration in NVT and then NPT conditions for 100 ps each. Then with the system equilibrated, production simulation was run for 50 ns with a timestep of 2 fs. Over the course of the simulation the zinc ion did not move more than 2 Å relative to the protein backbone. Concluding that the force field would be sufficient for the complex

to remain stable over the timescale of the RBFE simulations used in this work of 1 ns (1/50th of the control simulation).

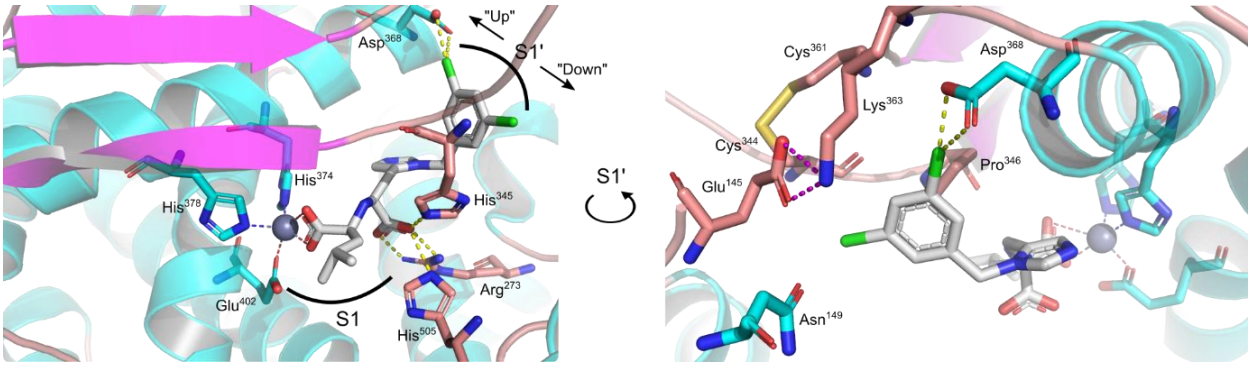

Figure 4.4: X-ray crystal structure of ACE2 bound to inhibitor MLN-4760 (PDB: 1R4L). Sub pockets S_1 and S_1' are annotated alongside orientation annotation used in this work for rotamers of asymmetric substructures in the S_1' sub-pocket. Left: view through the S1 subsite at zinc coordination of MLN-4760. Right: view through the S1' subsite and nearby residues, notably Asp368 interacting with the 3,5-dichlorobenzyl moiety.

4.3.5 Relative binding free energy protocol

RBFE simulations were run following the ProtoCaller default protocol with GROMACS 2020.2 as the MD engine.[15] The same receptor parameterisation and files were used as for the MD control. Ligand molecules were edited directly from the MLN-4760 reference ligand in PyMol, any sub-optimal geometries are minimised during energy minimising before MD simulation. Similarly, the ligand molecules were parameterised as in the molecular dynamics control. Then, provided the ligand structures, ProtoCaller was used to generate morph structure and topology files. Following the suggested protocol on GitHub,[17] 40 λ windows were used to scale Lennard-Jones, bonded and Coulomb values. Each λ window consisted of energy minimisation for 25,000 steps, NVT and NPT equilibration for 50 ps respectively,

followed by a final production simulation for 1 ns. For further information, the reader is referred to Suruzhon *et al*.[15] Note that non-symmetric aryl analogues with ambiguous orientation in the S1' site were run in both the 'up' (towards Asp368) and 'down' orientation, and the result averaged as shown in Figure 4.4.

To calculate relative change in free energy, the alchemical-analysis package[18] was utilised to run MBAR estimations of the energy difference states.[19] Convergence of the free energy was visually assessed in both the forward and reverse directions. This was corrected using a simple linear model between real pIC_{50} and predicted pIC_{50} for analogue compounds. The final absolute predicted pIC_{50} has then been taken as the difference between the reference compound and the predicted, corrected change in free energy ($\Delta\Delta G^{*}$) (Eq. 2). This is approximately equal to pIC_{50} because we are neglecting the small difference between binding free energy and binding constants which are typically calculated in binding assays, not withholding expected error associated with the assay.

$$\Delta\Delta G = \Delta G_{\mathrm{bound}} - \Delta G_{\mathrm{unbound}}$$

$$\Delta\Delta G^{*} = \beta \times \Delta\Delta G + \alpha \qquad (2)$$

$$pIC_{50} \cong pIC_{50\,ref} - \Delta\Delta G^{*}$$

An error value is calculated for the prediction. First the error calculated by MBAR for the bound and unbound legs is summed ($\Delta\Delta G_{error}$). This is then propagated with the errors in the linear model (Eq. 3).

$$pIC_{50error} = pIC_{50} \times \sqrt[2]{\left(\frac{\beta_{error}}{\beta}\right)^2 + \left(\frac{\Delta\Delta G_{error}}{\Delta\Delta G}\right)^2} + \sqrt[2]{\left(\frac{\alpha_{error}}{\alpha}\right)^2} \quad (3)$$

4.3.6 Validation of relative binding free energy for ACE2

RBFE calculations were first validated on a subset of known analogues published alongside MLN-4760, similar to validation of the docking protocol and is displayed in Figure 4.5. Due to the increased computational expense of the simulations, a subset of the analogues most similar to MLN-4760 were chosen. Single perturbations between matched molecular pairs of the analogues were run. Most perturbations were predicted within 1 kcal/mol of the real difference in free energy, however, two were notably inaccurate (A8→A3, A10→A3) to the extent of incorrect relative classification i.e., stronger, or weaker binder relative to the reference. Upon further inspection, the two incorrectly classified perturbations and MLN-4760→A9 contained at least one artefact during the simulation of either the first or last λ window, such as, free solvent ion coordination to the binding site or a significant change in binding mode. Due to the limited resources available, simulations with such artefacts were omitted. A simple linear model similar to Equation 1 was fit on the remaining perturbations, resulting in a linear regression fit of α = -0.0552, β = 0.4926 with Spearman rank correlation of 0.87 and Pearson correlation of 0.96, albeit from a

small dataset. This model was subsequently used as a correction term between the RBFE predicted delta free energy of binding (Pred. $\Delta\Delta G$) and the experimental (Exp. $\Delta\Delta G$) assumed from the difference in pIC_{50}.

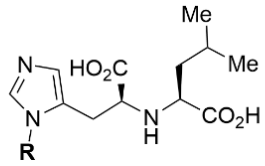

Compound	R	ACE2 IC50 (μM)	ACE IC50 (μM)
MLN-4760	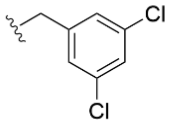	0.00044	>100
A3	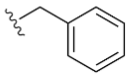	0.024	>100
A8	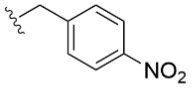	0.076	
A9	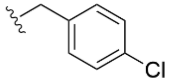	0.021	
A10	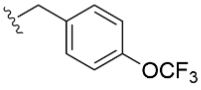	0.052	
A11	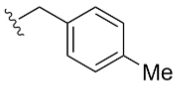	0.032	>10
A13	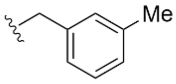	0.0042	>10
A14	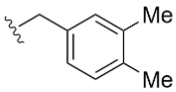	0.010	>10
A15	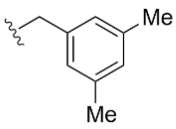	0.0014	>10

Figure 4.5: Analogues to MLN-4760 with reported binding affinity to ACE2 used for RBFE validation studies.

4.3.7 Estimation of radiolabelled analogue binding affinity by RBFE

A smaller subset of more promising radiolabelled analogues based on the results of docking simulations and estimated ease of synthesis were subject to RBFE simulations. In total, 14 out of the initial 31 compounds were carried forward for more computationally expensive RBFE calculations. Table 4.3 shows the predicted binding affinity of the proposed analogues according to single perturbation simulations from MLN-4760 or its analogues based on minimal alchemical changes. Most corresponded to structural changes in the S1' sub-pocket of ACE2. In cases where a structural modification resulted in an asymmetric sub-structure, both 'up' and 'down' orientations in the S1' sub-pocket was run and averaged if possible.

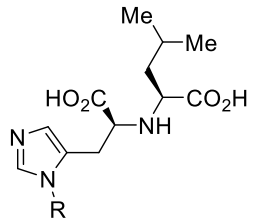

Reference Compound	Reference Structure (R =)	Proposed Structure (R =)	Predicted ΔΔG	Reference pIC_{50}	Predicted pIC_{50}
MLN-4760	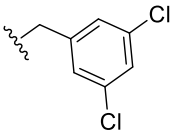	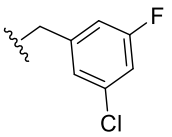	1.497 (± 0.03)	9.36	8.68 (± 1.39)
MLN-4760	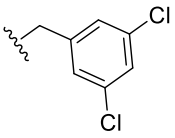	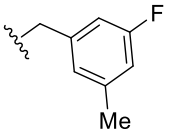	1.958 (± 0.04)	9.36	8.45 (± 1.41)
MLN-4760	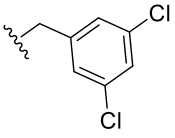	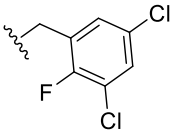	2.387 (± 0.02)	9.36	8.83 (± 1.37)
MLN-4760	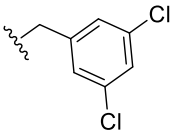	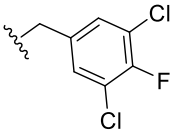	0.268 (± 0.02)	9.36	9.28 (± 1.33)
MLN-4760	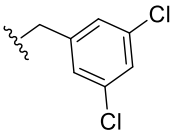	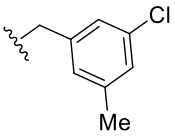	1.285 (± 0.02)	9.36	8.78 (± 1.38)
MLN-4760	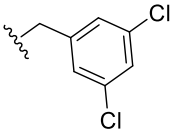	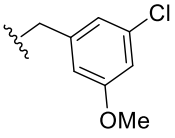	1.203 (± 0.04)	9.36	8.71 (± 1.38)
MLN-4760	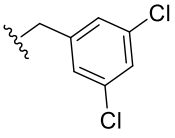	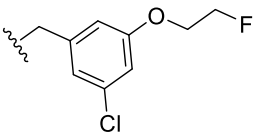	-0.550 (± 0.06)	9.36	9.58 (± 1.35)
MLN-4760	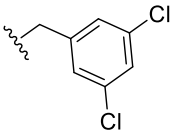	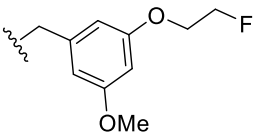	-0.566 (± 0.04)	9.36	9.58 (± 1.36)

(*S*,*S*)-**2.59**	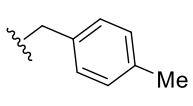	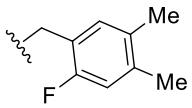	1.484 (± 0.04)	7.49	6.81 (± 1.39)
(*S*,*S*)-**2.59**	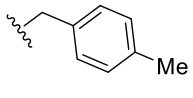	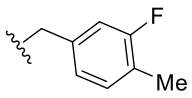	0.001 (± 0.02)	7.49	7.54 (± 1.32)
(*S*,*S*)-**2.63**	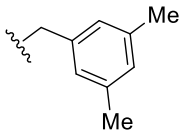	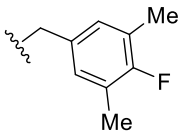	-0.393 (± 0.02)	8.85	9.10 (± 1.30)
(*S*,*S*)-**2.63**	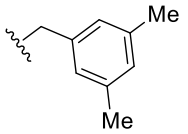	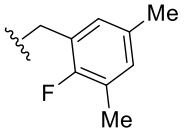	1.698 (± 0.02)	8.85	8.49 (± 1.36)
(*S*,*S*)-**2.57**	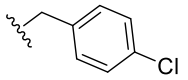	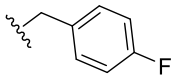	0.364 (± 0.03)	7.68	7.56 (± 1.34)

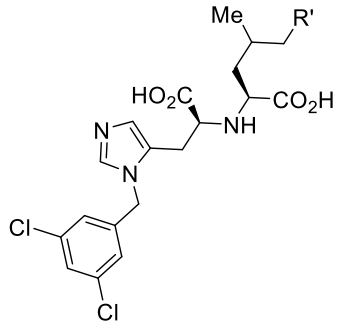

Reference Compound	Reference Structure (R' =)	Proposed Structure (R' =)	Predicted ΔΔG	Reference pIC_{50}	Predicted pIC_{50}
MLN-4760			0.631 (± 0.02)	9.36	9.10 (± 1.35)

Table 4.3: Predicted relative binding free energies ($\Delta\Delta G$) and pIC_{50} values for radiotracer candidates determined by RBFE simulations.

4.5 In Vitro Experimental Procedure for Chapter 2 (Conducted by J. He)

The ACE2 inhibition assay was performed using a commercial ACE2 inhibitor screening kit (Abcam/BioVision, catalogue no. ab273373). The kit components provided for each set of reactions included: Assay Buffer XI/ACE2 Assay Buffer (~25 mL), formulated to maintain optimal enzyme activity; ACE2 Dilution Buffer (~1.5 mL) for preparation of enzyme and test compound solutions; Recombinant ACE2 Enzyme (20 µL) representing the catalytic domain of human ACE2; ACE2 Substrate (~200 µL), a fluorogenic MCA-tagged peptide that is specifically recognised and cleaved by ACE2; ACE2 Inhibitor (0.5 mM) (5 µL), a positive control inhibitor to validate assay performance.

All kit reagents were stored at −20 °C prior to use and equilibrated to room temperature before assay setup. Test compounds were serially diluted from a 5 mg/mL stock in dimethyl sulfoxide (DMSO) into the ACE2 dilution buffer to yield the desired concentration series. Assays were conducted in half-area, black, flat-bottom 96-well microplates (Greiner Bio-One International) at ambient temperature (set to 23.5 °C) in a final volume of 100 µL per well. Fluorescence signals were measured kinetically following substrate addition, and inhibitory potency was calculated relative to appropriate controls.

Diluted ACE2 enzyme solution was prepared by diluting ACE2 enzyme (20 µL, provided in the kit) with dilution buffer (198 µL, provided in the kit) and was aliquoted and stored at -20 ˚C. Diluted ACE2 enzyme solution (2 µL) was added to assay buffer (48 µL) to make ACE2 enzyme working solution. Inhibitor solution was prepared by adding the control inhibitors (5 µL, 0.5 mM) to dilution buffer (50 µL) and was aliquoted and stored at -20 ˚C. The ACE2 substrate was aliquoted and stored at -20 ˚C. ACE2 substrate solution was prepared by diluting substrate (2 µL) to assay buffer (38 µL).

Five controls were prepared: enzyme control (positive control, inhibition free reaction), inhibitor control (negative control to test inhibition), background control (to remove fluorescence from the background), test compound control (to test whether the test compounds react with the substrate) and vehicle control (to test the effect of solvent DMSO on ACE2 enzyme activity).

For enzyme control, inhibitor control and vehicle control, and test compounds, ACE2 enzyme working solution (50 µL) was added. For background control and test compound control, assay buffer (50 µL) was added. Then, assay buffer (10 µL) was added to enzyme control and background control. DMSO solution in assay buffer (10 µL) was added to vehicle control. Inhibitor solution (10 µL) was added to inhibitor control. Test compound solution (10 µL) was added to the test compound control. For the test compound, compound solution (10 µL) with the different concentrations were added. An example of preparation can be found on Table 4.4. The mixture and

substrate were incubated separately at room temperature for 15 minutes before substrate (40 µL) was added to each test and mixed evenly to start the reaction. Fluorescence was monitored over 61-minutes (excitation = 320 nm, emission = 420 nm) using a Tecan microplate reader (Infinite® 200 PRO NanoQuant Microplate Reader). Fluorescence spectra were measured using the fluorescence intensity mode (excitation = 320 nm). To ensure reproducibility and statistical robustness, each potency measurement was performed in three independent experimental runs, and within each run, every concentration point was measured in triplicate wells. Thus, each reported value reflects the mean of nine technical replicates per concentration across three independent assay sets.

Test	Component 1	Component 2	Component 3
Vehicle control	50 µL enzyme[a]	10 µL DMSO (0.1 mM)	40 µL substrate[b]
Background control	50 µL assay buffer	10 µL assay buffer	40 µL substrate
Enzyme control	50 µL enzyme	10 µL assay buffer	40 µL substrate
Inhibitor control	50 µL enzyme	10 µL inhibitor solution	40 µL substrate
Test compound control	50 µL enzyme	10 µL MLN (0.1 mM)	40 µL substrate
LogM = -5	50 µL enzyme	10 µL MLN (0.1 mM)	40 µL substrate
LogM = -6	50 µL enzyme	10 µL MLN (10 µM)	40 µL substrate
LogM = -7	50 µL enzyme	10 µL MLN (1 µM)	40 µL substrate
LogM = -8	50 µL enzyme	10 µL MLN (0.1µM)	40 µL substrate
LogM = -9	50 µL enzyme	10 µL MLN (10 nM)	40 µL substrate
LogM = -10	50 µL enzyme	10 µL MLN (1 nM)	40 µL substrate
LogM = -11	50 µL enzyme	10 µL MLN (0.1 nM)	40 µL substrate
LogM = -12	50 µL enzyme	10 µL MLN (10 pM)	40 µL substrate

Table 4.4: An example of preparing the control and the test compounds. [a]Enzyme working solution (2 µL) + assay buffer (48 µL). [b]Substrate solution (2 µL) + assay buffer (38 µL)

4.6 Procedures and Characterisation for Chapter 3

Benzyl ((*S*)-3-(1-(4-bromobenzyl)-1*H*-imidazol-5-yl)-1-methoxy-1-oxopropan-2-yl)-*L*-leucinate ((*S*,*S*)-3.47)

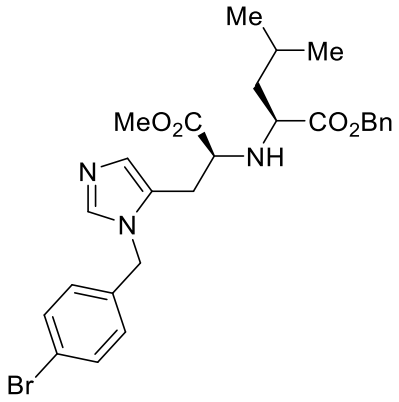

Di-*tert*-butyl dicarbonate (Boc_2O, 350 mg, 1.60 mmol, 2.2 equiv.) in CH_2Cl_2 (0.65 mL) was slowly added to a solution of (*S,S*)-**3.44** (300 mg, 0.802 mmol, 1.1 equiv.) and DIPEA (254 µL, 1.46 mmol, 2.0 equiv.) in CH_2Cl_2 (3.00 mL, 0.2 M) at room temperature. After stirring for 24 hours, the reaction mixture was concentrated under reduced pressure, and the residue was redissolved in dichloromethane (CH_2Cl_2) and H_2O (1:1, 10 mL). After separation, and the organic phase was washed with brine, dried over Na_2SO_4, filtered, and concentrated to obtain a crude intermediate. Separately, a solution of trifluoromethanesulfonic anhydride (Tf_2O, 122 µL, 0.729 mmol, 1.0 equiv.) in CH_2Cl_2 (3.00 mL, 0.2 M) was cooled to -78 °C. To this solution, (4-bromophenyl)methanol (**3.45**, 136 mg, 0.729 mmol, 1.0 equiv.) and diisopropylethylamine (DIPEA, 191 µL, 1.09 mmol, 1.5 equiv.) in CH_2Cl_2 (0.35 mL) were added. After stirring for 20 minutes, to this solution was added a solution of the crude intermediate in CH_2Cl_2 (0.30 mL) was added, and the reaction mixture was

slowly brought to room temperature and stirred overnight. Thereafter, HCl (0.201 mL, 4.0 M in dioxane, 1.1 equiv.) was added to the reaction mixture and stirred for 1 hour. The reaction mixture was then concentrated and the organic phase was extracted with EtOAc (3 × 25 mL), washed with brine (25 mL), dried over Na_2SO_4, and concentrated to yield the crude product. The crude product was further purified using flash column chromatography (gradient 0 - 10% MeOH in EtOAc) to obtain the product as a viscous cream oil (173 mg, 0.319 mmol, 44%, > 20:1 *d.r.*).

R_f 0.35 (2% MeOH/EtOAc).

^{1}H NMR (500 MHz, $CDCl_3$) δ 8.66 – 8.63 (m, 1H), 7.57 – 7.55 (m, 1H), 7.55 – 7.53 (m, 1H), 7.40 – 7.30 (m, 6H), 7.08 – 7.06 (m, 1H), 7.06 – 7.03 (m, 1H), 5.38 – 5.29 (m, 2H), 5.16 – 5.09 (m, 2H), 3.74 (s, 3H), 3.52 (dd, *J* = 6.9, 5.6 Hz, 1H), 3.47 (dd, *J* = 8.2, 5.5 Hz, 1H), 2.99 (dd, *J* = 15.6, 5.8 Hz, 1H), 2.87 (dd, *J* = 15.7, 6.7 Hz, 1H), 1.70 – 1.61 (m, 1H), 1.57 (ddd, *J* = 13.7, 8.2, 5.6 Hz, 1H), 1.46 (ddd, *J* = 14.0, 8.3, 6.1 Hz, 1H), 0.91 (d, *J* = 6.6 Hz, 3H), 0.89 (d, *J* = 6.6 Hz, 3H).

^{13}C{^{1}H} NMR (126 MHz, $CDCl_3$) δ 174.1, 172.6, 135.6, 135.4, 133.0, 131.5, 130.7, 129.4, 128.9, 128.8, 128.5, 124.0, 119.8, 67.2, 59.1, 59.0, 53.0, 50.6, 42.1, 27.6, 25.0, 22.9, 21.9.

HRMS (ESI^+) m/z: $[M+H]^+$ Calcd for $C_{27}H_{33}{}^{79}BrN_3O_4$ 542.1649; Found 542.1648.

IR (thin layer film) ν (cm^{-1}) 3389, 2984, 2951, 2684, 1640, 1541, 1475, 1397, 1222, 1025, 838, 670.

$[\alpha]_D^{25\,°C}$ -16.5 (c 0.015, $CHCl_3$).

Benzyl ((*S*)-3-(1-(3-bromo-5-chlorobenzyl)-1*H*-imidazol-5-yl)-1-methoxy-1-oxopropan-2-yl)-*L*-leucinate ((*S*,*S*)-3.48)

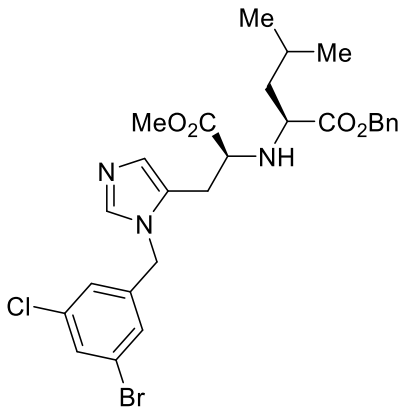

Di-*tert*-butyl dicarbonate (Boc_2O) (350 mg, 1.60 mmol, 2.2 equiv.) in CH_2Cl_2 (0.65 mL) was slowly added to a solution of (*S,S*)-**3.44** (300 mg, 0.802 mmol, 1.1 equiv.) and DIPEA (254 µL, 1.46 mmol, 2.0 equiv.) in CH_2Cl_2 (3.00 mL, 0.2 M) at room temperature. After stirring for 24 hours, the reaction mixture was concentrated under reduced pressure, and the residue was redissolved in dichloromethane (CH_2Cl_2) and H_2O (1:1, 10 mL). After separation, the organic phase was washed with brine, dried over Na_2SO_4, filtered, and concentrated to obtain a crude intermediate. Separately, a solution of trifluoromethanesulfonic anhydride (Tf_2O, 122 µL, 0.729 mmol, 1.0 equiv.) in CH_2Cl_2 (3.00 mL, 0.2 M) was cooled to -78 °C. To this solution, (3-bromo-5-chlorophenyl)methanol (**3.46**, 162 mg, 0.729 mmol, 1.0 equiv.) and diisopropylethylamine (DIPEA, 191 µL, 1.09 mmol, 1.5 equiv.) in CH_2Cl_2 (0.35 mL) were added. After stirring for 20 minutes, to this solution was added a solution of the crude intermediate in CH_2Cl_2 (0.30 mL) was added, and the reaction mixture was slowly brought to room temperature and stirred overnight. Thereafter, HCl (0.201 mL,

4.0 M in dioxane, 1.1 equiv.) was added to the reaction mixture and stirred for 1 hour. The reaction mixture was then concentrated and the organic phase was extracted with EtOAc (3 × 25 mL), washed with brine (25 mL), dried over Na_2SO_4, and concentrated to yield the crude product. The crude product was further purified using flash column chromatography (gradient 0 - 10% MeOH in EtOAc) to obtain the product as a viscous cream oil (170 mg, 0.295 mmol, 40%, > 20:1 *d.r.*).

R_f 0.30 (2% MeOH/EtOAc).

^{1}H NMR (500 MHz, $CDCl_3$) δ 7.45 – 7.42 (m, 2H), 7.37 – 7.30 (m, 5H), 7.06 – 7.03 (m, 1H), 6.93 – 6.91 (m, 1H), 6.90 – 6.88 (m, 1H), 5.12 – 5.09 (m, 2H), 5.06 – 5.04 (m, 2H), 3.67 (s, 3H), 3.43 – 3.39 (m, 1H), 3.35 (dd, *J* = 8.3, 5.9 Hz, 1H), 2.82 (ddd, *J* = 15.1, 6.7, 0.8 Hz, 1H), 2.74 (ddd, *J* = 15.1, 6.6, 0.8 Hz, 1H), 1.69 – 1.62 (m, 1H), 1.51 – 1.44 (m, 1H), 1.44 – 1.36 (m, 1H), 0.90 – 0.83 (m, 6H).

^{13}C{^{1}H} NMR (126 MHz, $CDCl_3$) δ 174.7, 173.7, 140.2, 138.3, 136.0, 135.8, 131.2, 129.2, 128.8, 128.5, 128.4, 128.1, 127.2, 125.7, 123.6, 66.7, 59.4, 58.5, 52.3, 47.4, 42.4, 28.3, 24.9, 23.0, 22.0.

HRMS (ESI^+) m/z: $[M+H]^+$ Calcd for $C_{27}H_{32}{}^{79}Br^{35}ClN_3O_4$ 576.1259; Found 576.1249.

IR (thin layer film) ν (cm^{-1}) 3422, 2957, 1736, 1710, 1591, 1565, 1496, 1432, 1366, 1222, 1153, 1112, 971, 753, 699, 668.

$[\alpha]_D^{25\,°C}$ -12.1 (c 0.020, $CHCl_3$).

Benzyl ((*S*)-1-methoxy-1-oxo-3-(1-(4-(4,4,5,5-tetramethyl-1,3,2-dioxaborolan-2-yl)benzyl)-1*H*-imidazol-5-yl)propan-2-yl)-*L*-leucinate ((*S*,*S*)-3.41)

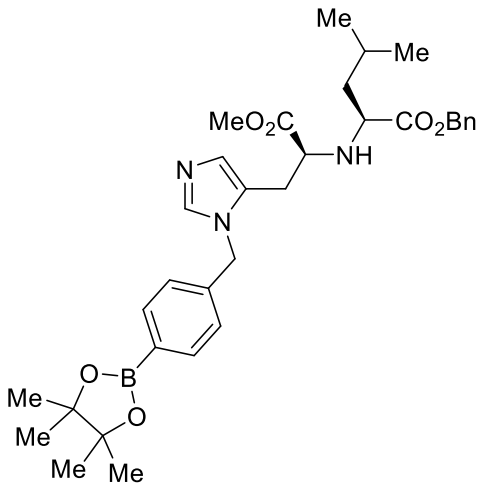

An oven-dried Schlenk tube was charged with (*S,S*)-**3.47** (80 mg, 148 µmol, 1.0 equiv.), bis(pinacolato)diboron (82.4 mg, 324 µmol, 2.2 equiv.), $Pd(OAc)_2$ (0.662 mg, 2.95 µmol, 2 mol%), XPhos (2.81 mg, 5.90 µmol, 4 mol%), and potassium acetate (43.4 mg, 442 µmol, 3.0 equiv.). The tube was sealed with a rubber septum, evacuated, and backfilled with argon (repeated twice). Degassed 1,4-dioxane (1.47 mL, 0.1 M) was added via syringe, and the reaction mixture was stirred at 110 °C for 20 minutes. The mixture was then cooled to room temperature, filtered through a pad of celite, and concentrated under reduced pressure. The organic phase was extracted with EtOAc (3 × 10 mL), washed with brine (10 mL), dried over Na_2SO_4, and purified using flash column chromatography (gradient 0–5% MeOH in EtOAc) to afford the crude product (62.0 mg, 105 µmol, 71% yield). The crude product was

further purified using preparative HPLC to obtain desired (*S,S*)-**3.41** as a viscous colourless oil (26.0 mg, 44.1 μmol, 30%).

Reverse phase HPLC details: NUCLEODUR® RP-Säulen 5 μm C18 110 Å, 250 x 4.6 mm, flow rate = 12 mL/min, column temperature = 25 °C, eluent = gradient 50% - 98% MeCN/ H_2O (0.1% TFA) over 40 min, retention time = 31.8 min;

^{1}H NMR (500 MHz, $(CD_3)_2CO$) δ 8.84 – 8.77 (m, 1H), 7.48 – 7.29 (m, 8H), 7.22 – 7.14 (m, 2H), 5.67 – 5.62 (m, 2H), 5.16 – 5.11 (m, 2H), 3.68 (s, 3H), 3.62 (dd, *J* = 7.7, 5.3 Hz, 1H), 3.48 (dd, *J* = 8.2, 6.0 Hz, 1H), 3.15 – 3.08 (m, 1H), 3.02 – 2.93 (m, 1H), 1.75 – 1.65 (m, 1H), 1.55 – 1.41 (m, 2H), 1.21 (s, 12H), 0.90 – 0.84 (m, 6H).

^{13}C{^{1}H} NMR (126 MHz, $(CD_3)_2CO$) δ 175.0, 173.8, 164.6, 162.7, 137.2, 131.1, 131.0, 129.4, 129.1, 129.0, 116.9, 116.7, 83.7, 66.9, 59.4, 59.3, 59.0, 52.4, 50.3, 42.9, 25.4, 24.9, 23.2, 22.2.

HRMS (ESI$^+$) m/z: $[M+H]^+$ Calcd for $C_{33}H_{45}BN_3O_6$ 590.3396; Found 590.3391.

IR (thin layer film) ν (cm^{-1}) 3348, 2971, 2932, 2884, 1739, 1675, 1467, 1379, 1341, 1306, 1161, 1129, 952, 817, 722, 698, 650, 618.

$[\alpha]_D^{25\,°C}$ -21.8 (c 0.010, $CHCl_3$).

Benzyl ((*S*)-3-(1-(3-chloro-5-(4,4,5,5-tetramethyl-1,3,2-dioxaborolan-2-yl)benzyl)-1*H*-imidazol-5-yl)-1-methoxy-1-oxopropan-2-yl)-*L*-leucinate ((*S*,*S*)-3.49)

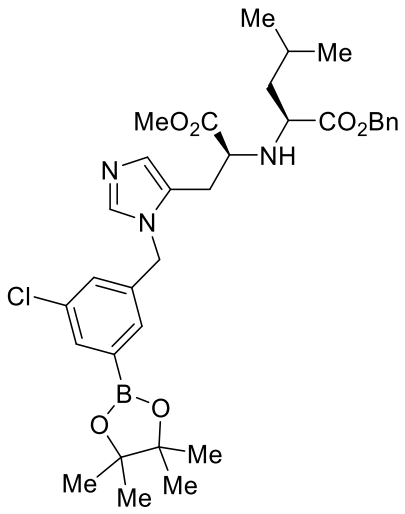

An oven-dried Schlenk tube was charged with (*S,S*)-**3.48** (50 mg, 86.7 μmol, 1.0 equiv.), bis(pinacolato)diboron (48.4 mg, 191 μmol, 2.2 equiv.), (1,1'-bis(diphenylphosphino)ferrocene)palladium(II) dichloride ($Pd(dppf)Cl_2$, 1.27 mg, 1.73 μmol, 2 mol%), and potassium acetate (25.5 mg, 260 μmol, 3.0 equiv.). The tube was sealed with a rubber septum, evacuated, and backfilled with argon (repeated twice). Degassed 1,4-dioxane (867 μL, 0.1 M) was added via syringe, and the reaction mixture was stirred at 110 °C for 30 minutes. The mixture was then cooled to room temperature, filtered through a pad of celite, and concentrated under reduced pressure. The organic phase was extracted with EtOAc (3 × 10 mL), washed with brine (10 mL), dried over Na_2SO_4, and purified using flash column chromatography (gradient 0–5% MeOH in EtOAc) to afford the product a viscous colourless oil (36.0 mg, 57.7 μmol, 67% yield).

^{1}H NMR (500 MHz, $(CD_3)_2CO$) δ 7.65 – 7.62 (m, 1H), 7.58 – 7.55 (m, 1H), 7.41 – 7.34 (m, 5H), 7.27 – 7.25 (m, 1H), 7.16 – 7.14 (m, 1H), 6.84 – 6.82 (m, 1H), 5.37 – 5.33 (m, 2H), 5.15 – 5.11 (m, 2H), 3.65 (s, 3H), 3.53 – 3.49 (m, 1H), 3.41 (dd, *J* = 8.4, 6.0 Hz, 1H), 2.91 (ddd, *J* = 15.3, 6.6, 0.9 Hz, 1H), 2.79 (ddd, *J* = 15.3, 6.7, 0.9 Hz, 1H), 1.77 – 1.66 (m, 1H), 1.48 – 1.37 (m, 2H), 1.23 (s, 12H), 0.89 – 0.84 (m, 6H).

^{13}C{^{1}H} NMR (126 MHz, $(CD_3)_2CO$) δ 175.1, 174.2, 143.2, 139.1, 137.3, 136.1, 131.1, 129.3, 129.3, 129.0, 129.0, 128.3, 126.8, 123.7, 83.7, 66.8, 60.0, 58.9, 52.1, 47.5, 43.0, 28.5, 25.4, 24.9, 23.2, 22.2.

HRMS (ESI^+) m/z: $[M+H]^+$ Calcd for $C_{33}H_{44}B^{35}ClN_3O_6$ 624.3006; Found 624.3016.

IR (thin layer film) ν (cm^{-1}) 3355, 2972, 1731, 1468, 1378, 1303, 1253, 1162, 1131, 1048, 953, 817, 620.

$[\alpha]_D^{25\,°C}$ -14.6 (c 0.010, $CHCl_3$).

4.7 Radiosynthesis Procedure for Chapter 3

4.7.1 General Information

[^{18}F]Fluoride was produced in an IBA Cyclon 18/9 cyclotron using the ^{18}O(p,n)^{18}F reaction in PETIC (UK). Analytical HPLC runs were performed with an Agilent 1200 equipped with a UV detector and LabLogic gamma-RAM Model 4 detector (approximate radio-UV detector offset = 0.1 min).

Conditions A:

Flow rate = 1.0 mL/min

Temperature = 25 °C

Wavelength = 220 nm (unless otherwise specified)

HPLC gradient: water/MeCN or water + 0.1% TFA/MeCN + 0.1% TFA

0-1 min (5% MeCN) isocratic

1-10 min (5% MeCN to 95% MeCN) linear increase

10-16 min (95% MeCN) isocratic

16-18 min (95% MeCN to 5% MeCN) linear decrease

18-20 min (5% MeCN) isocratic

Conditions B:

Flow rate = 1.0 mL/min

Temperature = 25 °C

Wavelength = 220 nm (unless otherwise specified)

HPLC gradient: water/MeCN or water + 0.1% TFA/MeCN + 0.1% TFA

0-1 min (25% MeCN) isocratic

1-10 min (25% MeCN to 95% MeCN) linear increase

10-16 min (95% MeCN) isocratic

16-18 min (95% MeCN to 25% MeCN) linear decrease

18-20 min (25% MeCN) isocratic

4.7.2 Radiochemistry protocols

4.7.2.1 Preparation of [^{18}F]Fluoride

The following procedure was performed using a Trasis AllinOne automated synthesizer. [^{18}F]Fluoride was first separated from [^{18}O]water using an anion exchange cartridge (Waters Sep-Pak AccellPlus QMA Carbonate Plus Light Cartridge), activated with H_2O (10 mL) prior to use and released with a solution of Kryptofix (7.5 mg), and K_2CO_3 (1.5 mg) in MeCN/H_2O (0.75 mL, 4:1, v/v). The eluate was transferred to the reactor and dried azeotropically with additional MeCN at 110 °C. The dry residue was redissolved in MeCN and transferred into a 3 mL syringe for dispensing.

4.7.2.2 Cu-mediated ^{18}F-Fluorination

To an oven-dried 3 mL v-vial equipped with a magnetic stir bar was added the relevant Bpin precursor, $Cu(OTf)_2py_4$ (2 equiv.) and DMI (300 µL). To the vial was then added an aliquot of the [^{18}F]KF.K_{222} solution (5-20 MBq) in MeCN (approx. 20

μL) (*vide supra*). The reaction vial was purged with air (20 mL) and reaction mixture was stirred at the given temperature for 20 minutes. The reaction mixture was cooled to rt. An aliquot of this mixture was subsequently analysed by radioHPLC (gradient: MeCN/H_2O) for radiochemical yield (RCY) and product identity.

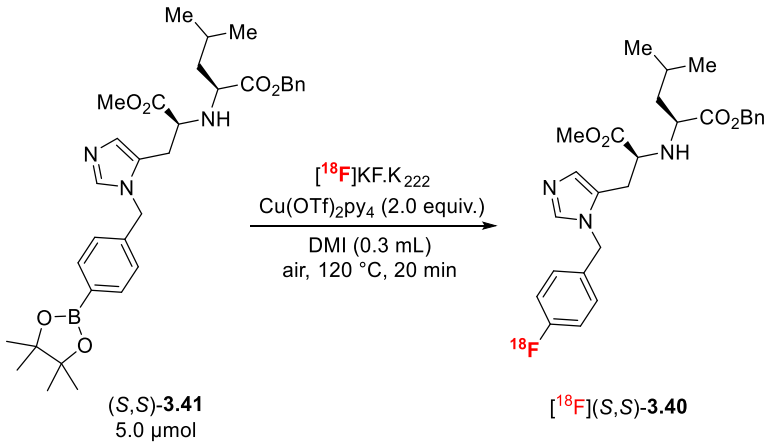

Scheme 4.1: Copper-mediated radiofluorination of pinacol boronic ester (*S*,*S*)-**3.41**.

RCY_{HPLC}: radiochemical yield, determined by radio-HPLC analysis (Conditions A, column: Phenomenex Kinetex C18 250 x 4.6 mm) of the crude reaction mixture is displayed in Table 4.5. Product identity confirmed by comparison of retention time to an authentic reference standard ((*S*,*S*)-**3.40**) by UV-HPLC as shown in Figure 4.6.

Entry	RCY_{HPLC} of [^{18}F](S,S)-3.40
1	31%
2	17%
Average	24% ± 7% (*n* = 2)

Table 4.5: Cu(II)-mediated ^{18}F-radiolabelling of (*S*,*S*)-**3.41** to obtain [^{18}F](*S*,*S*)-**3.40**.

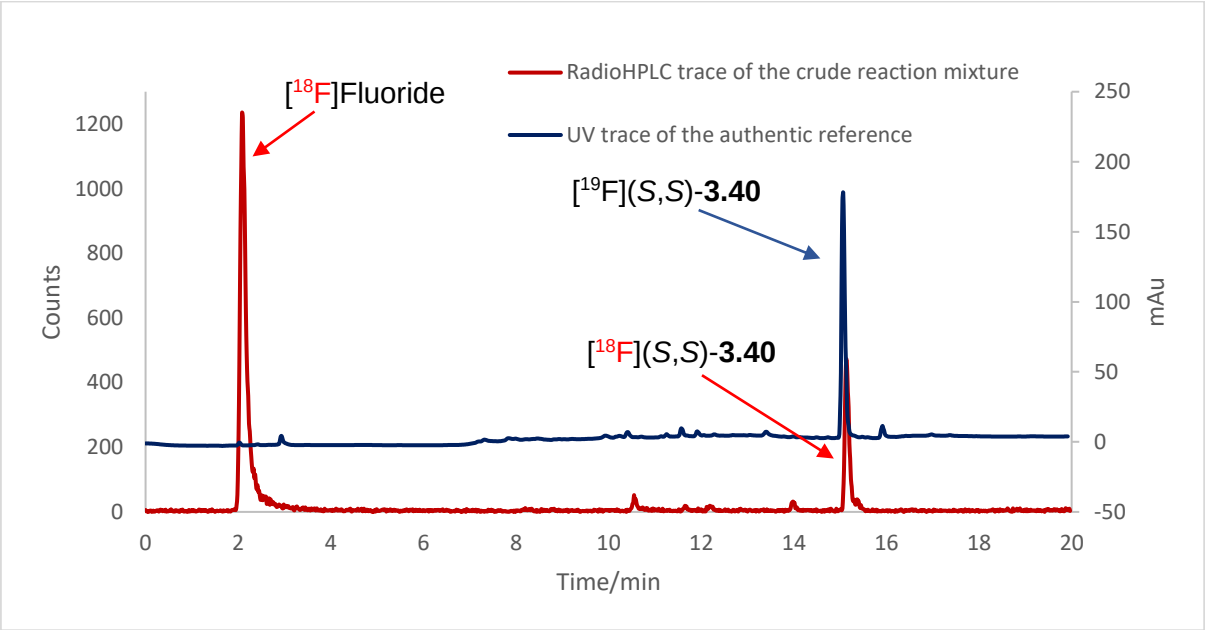

Figure 4.6: Radiochromatogram (red) obtained from the radioHPLC analysis of [^{18}F](*S*,*S*)-**3.40** overlaid with the UV chromatogram of the reference standard [^{19}F](*S*,*S*)-**3.40** (blue, λ = 220 nm).

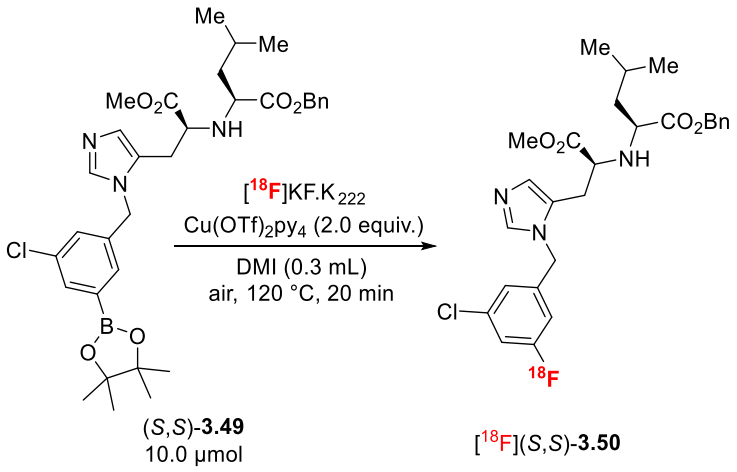

(*S*,*S*)-**3.49**
10.0 μmol

[^{18}F](*S*,*S*)-**3.50**

Scheme 4.2: Copper-mediated radiofluorination of pinacol boronic ester (*S*,*S*)-**3.49**.

RCY_{HPLC}: radiochemical yield, determined by radio-HPLC analysis (Conditions B, column: Agilent C18 Eclipse Plus 80 Å 150 x 4.6 mm) of the crude reaction mixture is displayed in Table 4.6. Product identity confirmed by comparison of retention time to an authentic reference standard ((*S*,*S*)-**3.50**) by UV-HPLC as shown in Figure 4.7.

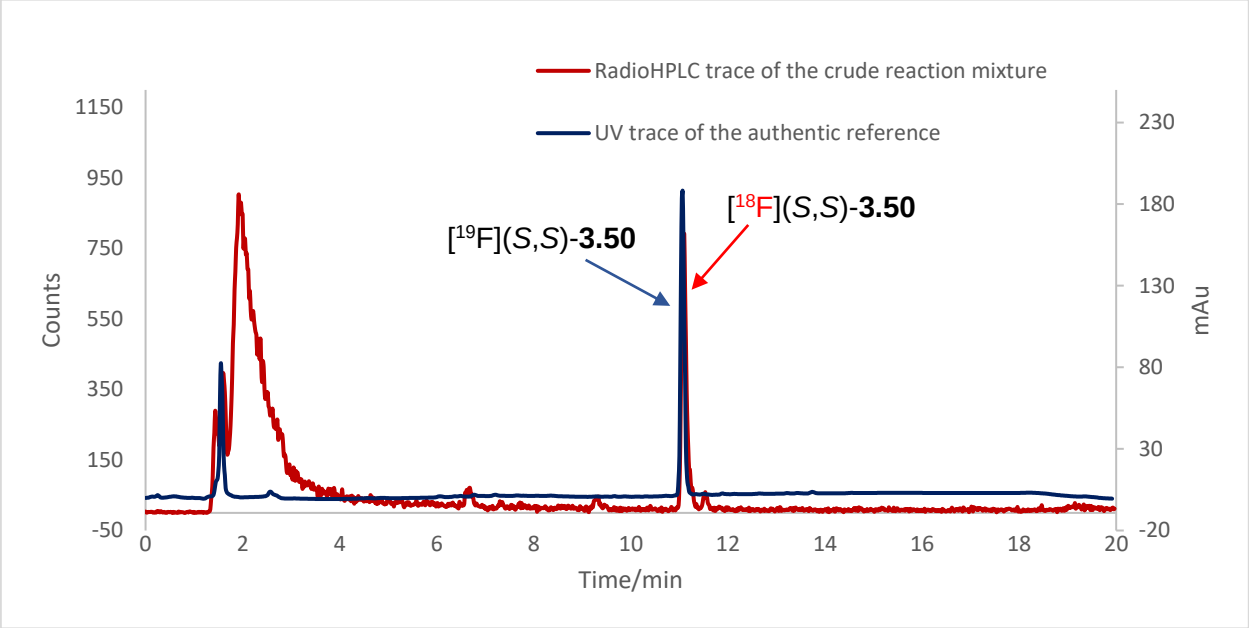

Figure 4.7: Radiochromatogram (red) obtained from the radioHPLC analysis of [^{18}F](*S*,*S*)-**3.50** overlaid with the UV chromatogram of the reference standard [^{19}F](*S*,*S*)-**3.50** (blue, λ = 220 nm).

Entry	RCY_{HPLC} of [^{18}F](S,S)-3.50
1	12%
2	6%
Average	9% ± 3% (*n* = 2)

Table 4.6: Cu(II)-mediated ^{18}F-radiolabelling of (*S*,*S*)-**3.49** to obtain [^{18}F](*S*,*S*)-**3.50**.

4.7.2.3 Radiosynthesis of [^{18}F](*S*,*S*)-3.1

To an oven-dried 3 mL v-vial equipped with a magnetic stir bar was added (*S*,*S*)-**3.41** (5 µmol), $Cu(OTf)_2py_4$ (2 equiv.) and DMI (300 µL). To the vial was then added an aliquot of the [^{18}F]KF.K_{222} solution (5-20 MBq) in MeCN (approx. 20 µL) (*vide supra*). The reaction vial was purged with air (20 mL) and reaction mixture was stirred at 120 °C for 20 minutes. The reaction mixture was cooled to rt and NaOH (aq., 1 M, 0.1 mL) was added. This mixture was heated at 65 °C for 20 minutes. Once cooled, the reaction mixture was neutralised with HCl (aq., 1 M, 0.1 mL). An aliquot of this mixture was subsequently analysed by radioHPLC for radiochemical yield (RCY) and product identity as shown in Table 4.7.

RCY_{HPLC}: radiochemical yield, determined by radio-HPLC analysis (Conditions A, Phenomenex Kinetex C18 250 x 4.6 mm, gradient: MeCN +0.1% TFA/H_2O +0.1% TFA) of the crude reaction mixture. Product identity confirmed by comparison of retention time to an authentic reference standard ((*S*,*S*)-**3.1**) by UV-HPLC as shown in Figure 4.8.

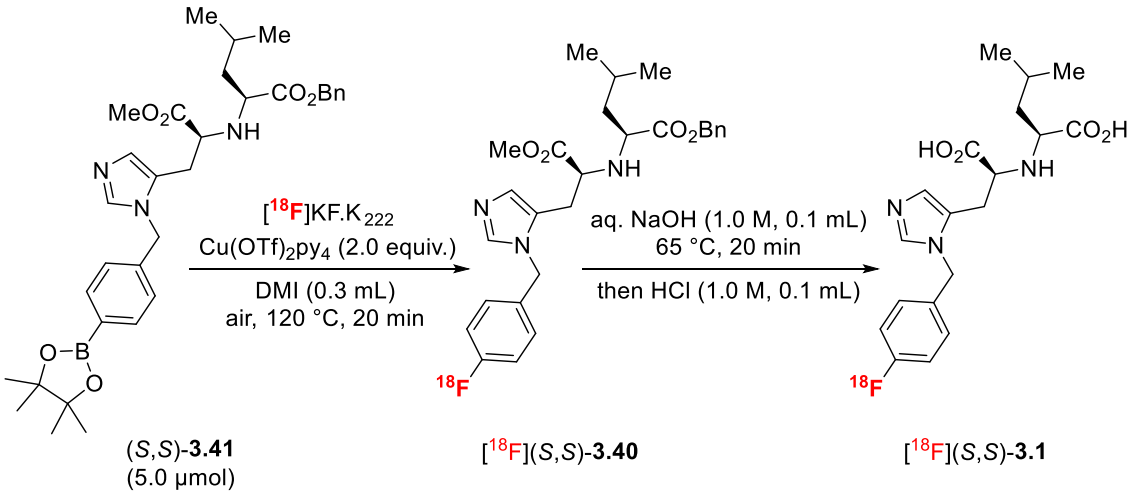

(*S*,*S*)-**3.41** (5.0 μmol) | [^{18}F](*S*,*S*)-**3.40** | [^{18}F](*S*,*S*)-**3.1**

Entry	[^{18}F](*S*,*S*)-3.40 remaining	RCY$_{HPLC}$ of [^{18}F](*S*,*S*)-3.1 (over two steps)
1	0%	25%
2	0%	10%
Average	0% (*n* = 2)	18% ± 8% (*n* = 2)

Table 4.7: Cu(II)-mediated ^{18}F-radiolabelling of (*S*,*S*)-**3.40** followed by a basic hydrolysis to obtain [^{18}F](*S*,*S*)-**3.1**.

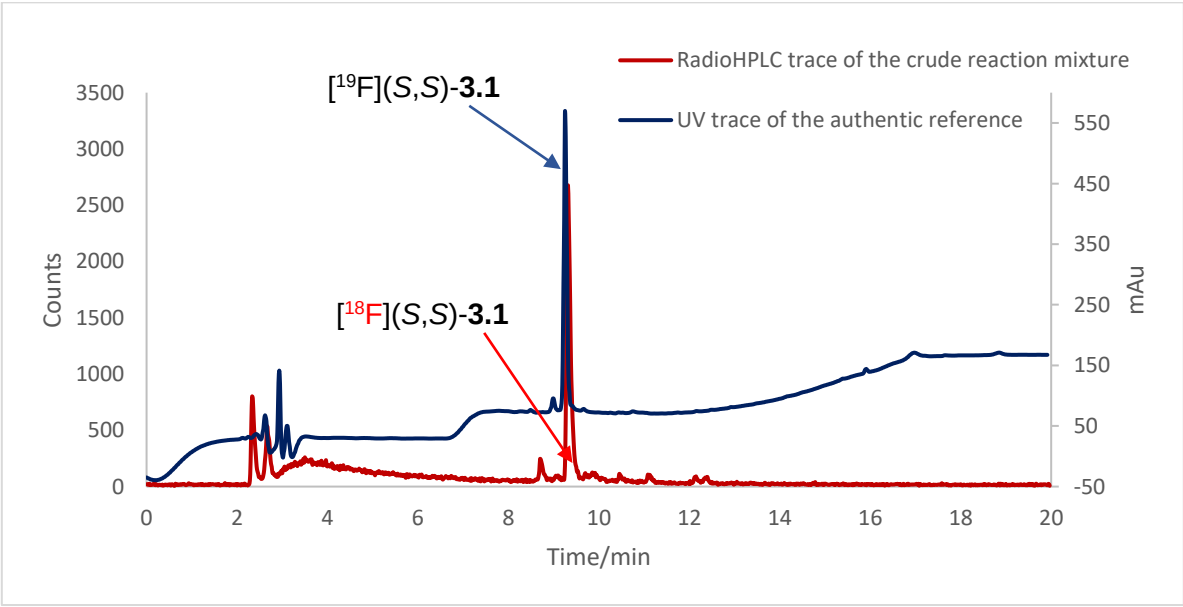

Figure 4.8: Radiochromatogram (red) obtained from the radioHPLC analysis of [^{18}F](*S*,*S*)-**3.1** overlaid with the UV chromatogram of the reference standard [^{19}F](*S*,*S*)-**3.1** (blue, λ = 220 nm).

4.7.2.4 Radiosynthesis of [^{18}F](*S*,*S*)-3.2

To an oven-dried 3 mL v-vial equipped with a magnetic stir bar was added (*S*,*S*)-**3.49** (10 µmol), $Cu(OTf)_2py_4$ (2 equiv.) and DMI (300 µL). To the vial was then added an aliquot of the [^{18}F]KF.K_{222} solution (5-20 MBq) in MeCN (approx. 20 µL) (*vide supra*). The reaction vial was purged with air (20 mL) and reaction mixture was stirred at 120 °C for 20 minutes. The reaction mixture was cooled to rt and NaOH (aq., 1 M, 0.1 mL) was added. This mixture was heated at 65 °C for 20 minutes. Once cooled, the reaction mixture was neutralised with HCl (aq., 1 M, 0.1 mL). An aliquot of this mixture was subsequently analysed by radioHPLC for radiochemical yield (RCY) and product identity as displayed in Table 4.8.

RCY_{HPLC}: radiochemical yield, determined by radio-HPLC analysis (Conditions A, Agilent C18 Eclipse Plus 80 Å 150 x 4.6 mm, gradient: MeCN +0.1% TFA/H_2O +0.1% TFA) of the crude reaction mixture. Product identity confirmed by comparison of retention time to an authentic reference standard ((*S*,*S*)-**3.2**) by UV-HPLC as shown in Figure 4.9.

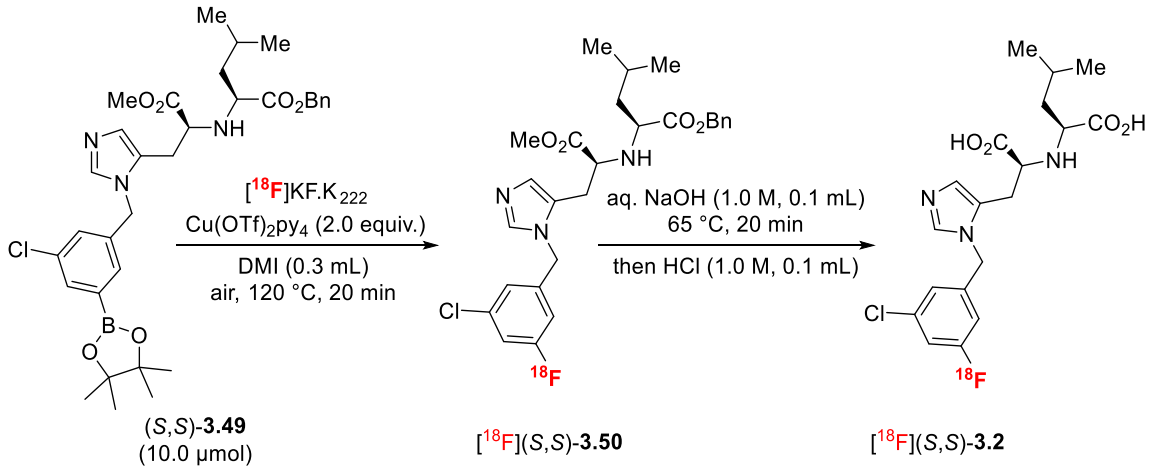

(*S*,*S*)-**3.49** (10.0 µmol)

[^{18}F](*S*,*S*)-**3.50**

[^{18}F](*S*,*S*)-**3.2**

Entry	[^{18}F](*S*,*S*)-3.50 remaining	RCY$_{HPLC}$ of [^{18}F](*S*,*S*)-3.2 (over two steps)
1	0%	10%
2	0%	5%
Average	0% (*n* = 2)	8% ± 3% (*n* = 2)

Table 4.8: Cu(II)-mediated ^{18}F-radiolabelling of (*S*,*S*)-**3.50** followed by a basic hydrolysis to obtain [^{18}F](*S*,*S*)-**3.2**. RCY$_{HPLC}$= radiochemical yield, determined by radio-HPLC analysis of the crude reaction mixture; DMI = 1,3-dimethyl-2-imidazolidinone.

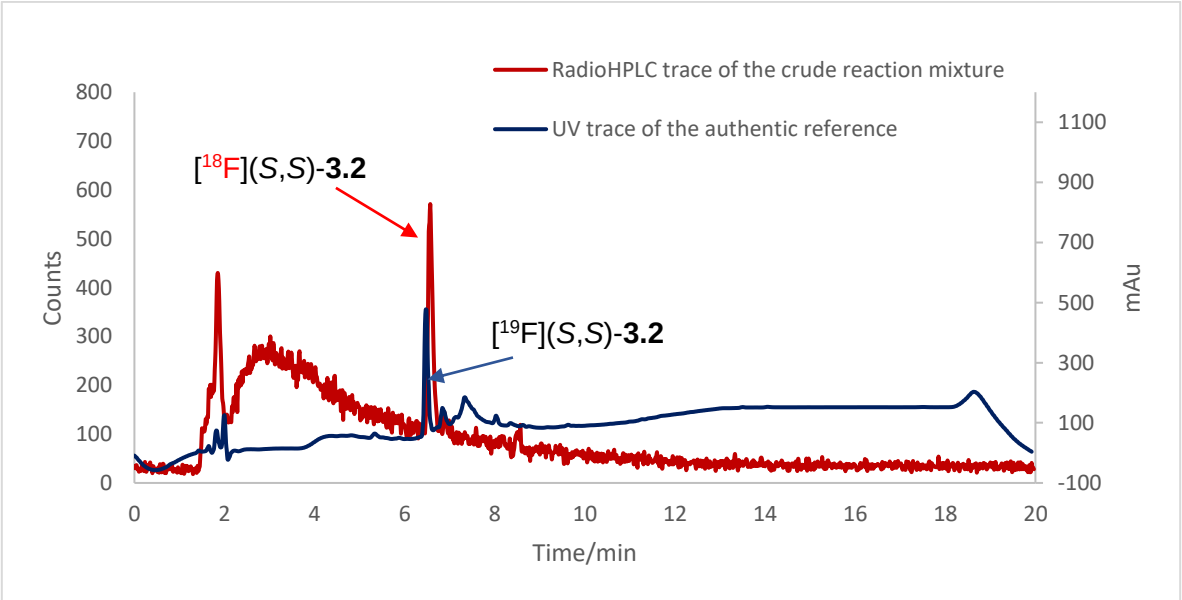

Figure 4.9: Radiochromatogram (red) obtained from the radioHPLC analysis of [^{18}F](*S*,*S*)-**3.2** overlaid with the UV chromatogram of the reference standard [^{19}F](*S*,*S*)-**3.2** (blue, λ = 220 nm).

4.8 References

(1) Xu, J.; Yadan, J. C. Synthesis of L-(+)-ergothioneine. *J. Org. Chem.* **1995**, *60* (20), 6296–6301.

(2) Blankley, C. J.; Hodges, J. C.; Klutchko, S. R.; Himmelsbach, R. J.; Chucholowski, A.; Connolly, C. J.; Neergaard, S. J.; Van Nieuwenhze, M. S.; Sebastian, A. Synthesis and structure-activity relationships of a novel series of non-peptide angiotensin II receptor binding inhibitors specific for the AT2 subtype. *J. Med. Chem.* **1991**, *34* (11), 3248–3260.

(3) Raimondi, W.; Basle, O.; Constantieux, T.; Bonne, D.; Rodriguez, J. Activation of 1, 2-Keto Esters with Takemoto's Catalyst toward Michael Addition to Nitroalkenes. *Adv. Synth. Catal.* **2012**, *354* (4), 563–568.

(4) Iino, T.; Tsukahara, D.; Kamata, K.; Sasaki, K.; Ohyama, S.; Hosaka, H.; Hasegawa, T.; Chiba, M.; Nagata, Y.; Eiki, J.-i. Discovery of potent and orally active 3-alkoxy-5-phenoxy-N-thiazolyl benzamides as novel allosteric glucokinase activators. *Biorg. Med. Chem.* **2009**, *17* (7), 2733–2743.

(5) Jia, F.; Li, D. H.; He, S.; Yang, L. P.; Jiang, W. Conformational Effects on the Threading Kinetics of Dumbbell-Shaped Guests into the Cavity of Oxatub [4] arene. *Angew. Chem. Int. Ed.* **2022**, *134* (45), e202212305.

(6) Towler, P.; Staker, B.; Prasad, S. G.; Menon, S.; Tang, J.; Parsons, T.; Ryan, D.; Fisher, M.; Williams, D.; Dales, N. A. ACE2 X-ray structures reveal a large hinge-bending motion important for inhibitor binding and catalysis. *J. Biol. Chem.* **2004**, *279* (17), 17996–18007.

(7) Søndergaard, C. R.; Olsson, M. H.; Rostkowski, M.; Jensen, J. H. Improved treatment of ligands and coupling effects in empirical calculation and rationalization of p K a values. *J. Chem. Theory Comput.* **2011**, *7* (7), 2284–2295.

(8) Dales, N. A.; Gould, A. E.; Brown, J. A.; Calderwood, E. F.; Guan, B.; Minor, C. A.; Gavin, J. M.; Hales, P.; Kaushik, V. K.; Stewart, M. Substrate-based design of the first class of angiotensin-converting enzyme-related carboxypeptidase (ACE2) inhibitors. *J. Am. Chem. Soc.* **2002**, *124* (40), 11852–11853.

(9) Abraham, M. J.; Murtola, T.; Schulz, R.; Páll, S.; Smith, J. C.; Hess, B.; Lindahl, E. GROMACS: High performance molecular simulations through multi-level parallelism from laptops to supercomputers. *SoftwareX* **2015**, *1*, 19–25.

(10) Ponder, J. W.; Case, D. A. Force fields for protein simulations. *Adv. Protein Chem.* **2003**, *66*, 27–85.

(11) Jorgensen, W. L.; Chandrasekhar, J.; Madura, J. D.; Impey, R. W.; Klein, M. L. Comparison of simple potential functions for simulating liquid water. *J. Chem. Phys.* **1983**, *79* (2), 926–935.

(12) Wang, J.; Wolf, R. M.; Caldwell, J. W.; Kollman, P. A.; Case, D. A. Development and testing of a general amber force field. *J. Comput. Chem.* **2004**, *25* (9), 1157–1174.

(13) Wang, J.; Wang, W.; Kollman, P. A.; Case, D. A. Automatic atom type and bond type perception in molecular mechanical calculations. *J. Mol. Graph. Model.* **2006**, *25* (2), 247–260.

(14) Shirts, M. R.; Klein, C.; Swails, J. M.; Yin, J.; Gilson, M. K.; Mobley, D. L.; Case, D. A.; Zhong, E. D. Lessons learned from comparing molecular dynamics engines on the SAMPL5 dataset. *J. Comput. Aided Mol. Des.* **2017**, *31*, 147–161.

(15) Suruzhon, M.; Senapathi, T.; Bodnarchuk, M. S.; Viner, R.; Wall, I. D.; Barnett, C. B.; Naidoo, K. J.; Essex, J. W. ProtoCaller: robust automation of binding free energy calculations. *J. Chem. Inf. Model.* **2020**, *60* (4), 1917–1921.

(16) Hedges, L. O.; Mey, A. S.; Laughton, C.; Gervasio, F. L.; Mulholland, A. J.; Woods, C. J.; Michel, J. BioSimSpace: An interoperable Python framework for biomolecular simulation. *J. Open Source Softw.* **2019**, *4*, 1831.

(17) ProtoCaller: Full automation of relative protein-ligand binding free energy calculations in GROMACS. In: GitHub. https://github.com/protocaller/protocaller. (accessed 20 Jan 2024).

(18) Klimovich, P. V.; Shirts, M. R.; Mobley, D. L. Guidelines for the analysis of free energy calculations. *J. Comput. Aided Mol. Des.* **2015**, *29*, 397–411.

(19) Bennett, C. H. Efficient estimation of free energy differences from Monte Carlo data. *J. Comput. Phys.* **1976**, *22* (2), 245–268.